

UNIVERSITY OF STRATHCLYDE

DOCTORAL THESIS

Dynamical models for novel diffraction techniques in SEM

Author:

Elena PASCAL

Supervisor:

Dr. Ben HOURAHINE

Dr. Carol TRAGER-COWAN

*A thesis submitted in fulfilment of the requirements
for the degree of Doctor of Philosophy*

in the

Semiconductor Spectroscopy and Devices Group
Department of Physics
2019

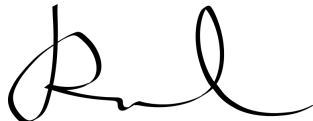
Declaration of Authorship

I, Elena PASCAL, declare that this thesis titled, "Dynamical models for novel diffraction techniques in SEM" and the work presented in it are my own. I confirm that:

- This thesis is the result of the author's original research. It has been composed by the author and has not been previously submitted for examination which has led to the award of a degree.
- Where I have consulted the published work of others, this is always clearly attributed.
- I have acknowledged all main sources of help.
- Where the thesis is based on work done by myself jointly with others, I have made clear exactly what was done by others and what I have contributed myself.

The copyright of this thesis belongs to the author under the terms of the United Kingdom Copyright Acts as qualified by University of Strathclyde Regulation 3.50. Due acknowledgement must always be made of the use of any material contained in, or derived from, this thesis.

Signed:



Date: November 24, 2019

"The way the creative process works is that you first say something, and later, sometimes years later, you understand what you said."

Daniel Kahneman

UNIVERSITY OF STRATHCLYDE

Abstract

Science
Department of Physics

Doctor of Philosophy

Dynamical models for novel diffraction techniques in SEM

by Elena PASCAL

The scanning electron microscope is a powerful nanocharacterisation tool for a variety of materials including semiconductors and metals. Less known for its diffraction abilities than its transmission counterpart, scanning electron microscopy (SEM) can be used in a number of diffraction modalities to provide information on crystal imperfections at the nanoscale level. This comes with the added benefit of SEM requiring minimal sample preparation. Models for diffraction in the SEM are still being developed and improved, hence in this work I explore the physics and implementations of such models. I focus on the two main branches of SEM diffraction techniques: incident beam channelling, or *diffraction in*, powerful when it comes to resolving individual dislocations close to the surface; and back(/forward)scattering diffraction, or *diffraction out*, which provides a variety of information about grain distribution, orientation and strain. Both of these diffraction modalities involve the same physical processes, so it makes sense to use the same models, namely dynamical scattering in the column approximation. I use the two beam Bloch waves approach for electron channelling contrast imaging (ECCI) of threading dislocations (TDs) normal to the surface in wurtzite group-III nitride materials. I also introduce and use the notion of ECC-strain to study crystal features and to predict the behaviour of TDs contrast. For the electron back(/forward)scatter modality, I show the first application of the new energy-weighted dynamical scattering capabilities of EMsoft to study the novel transmission mode (TKD) of the SEM.

Acknowledgements

I want to thank the entire SSD group for being welcoming and generous with their time and for all the science and non-science conversations. I am thankful for all my wonderful office mates, Nouf for kindly teaching me basics when I started, Paul for unlimited wisdom, James for welcomed distractions. I also have to mention Stefano for taking me under his wing in the first two years, and trying to pass his polymath knowledge onto me; I only wish I made more of your time here. I do hold fond memories of our electron diffraction (sometimes heated) discussions.

I am incredibly indebted to my supervisors for guiding me at every step on this long and sometimes challenging journey. I have to thank Carol for taking me on the program and giving me a chance to do research. I am grateful to her for always being available to hear any concerns I might have. I think I struggled with a lot of impostor's syndrome, and while I still do, I know that having Ben as a supervisor helped a lot. I am truly indebted for Ben's patience of framing the work I did in a way that made it sound meaningful even when we both knew that PhD work is rarely impactful. I am also thankful for all the very last minute revisions and feedback.

Gratitude must undoubtedly be extended to Marc for replying, always promptly, to my emails from the other side of the pond even though he was under no obligation to do so. I have only recently realised that the skill of answering and clarifying naive and sometimes confused, if not incoherent questions, is indeed very rare. Thank you for always making me feel like my understanding of a concept or idea is worth your time. And thank you for welcoming my visit.

I am extremely grateful for the support of my partner, Gunnar, without whom I don't think this manuscript would exist. Thank you for believing I am strong all the times I did not. Thank you for not doubting for a second I will hand in a Thesis for all the times I did.

Most importantly, I would like to thank my mother, who, despite having been denied further education, or perhaps because of it, values it so greatly that it took surprisingly little convincing work to let me leave ten years ago, with only a precarious survival plan, for a foreign land in the pursuit of it.

Contributions and Awards

Papers:

- **E Pascal**, S Singh, P G Callahan, B Hourahine, C Trager-Cowan, M De Graef, *Energy-weighted dynamical scattering simulations of electron diffraction modalities in the scanning electron microscope*, Ultramicroscopy, **187**, 2018, 98-106.
- **E Pascal**, B Hourahine, G Naresh-Kumar, K Mingard, C Trager-Cowan, *Dislocation contrast in electron channelling contrast images as projections of strain-like components*, Materials Today: Proceedings, **5**, 2018.
- **E Pascal**, S Singh, B Hourahine, C Trager-Cowan, M De Graef *Dynamical Simulations of Transmission Kikuchi Diffraction (TKD) Patterns*, Microscopy and Microanalysis, **23** (S1), 2017, 540-541.

Invited Talk:

- *When do electrons channel in the SEM?* 2018
Heimbach International workshop on physics of III-nitrides, Mansfeld, Germany.

Prizes and Awards:

- **Corbett prize** 2017
for *Modelling of ECCI strain-like profiles as a method of TD identification*.
Awarded every two years for an outstanding contribution at the International Conference of Defects in Semiconductors, Matsue, Japan.
- **Poster prize** 2017
for *Dynamical modelling of channelling contrast in ECCI*.
Best poster contribution at the EBSD conference, Oxford, UK.
- **Poster prize** 2016
for *Modelling of defect characterisation in the SEM*.
Best poster contribution at the National Physics Lab PhD conference, UK.
- **Young researcher SUPA exchange travel funding** 2016
for *International collaboration on energy filtering dynamical electron diffraction model*.

Contents

| | |
|---|-------------|
| List of Figures | x |
| List of Tables | xiii |
| List of Abbreviations | xiv |
| Physical Constants | xv |
| List of Symbols | xvi |
| 1 Introduction | 1 |
| 1.1 The big picture | 1 |
| 1.2 Diffraction and the SEM | 4 |
| 1.2.1 Diffraction | 5 |
| 1.2.2 The scanning electron microscope | 6 |
| 1.3 ECCI and the characterisation of TDs in nitrides | 10 |
| 1.3.1 Modelling of diffraction-in | 14 |
| 1.4 TKD and the study of truly nanostructured materials | 14 |
| 1.4.1 Modelling of diffraction-out | 15 |
| 2 Background and Basics | 16 |
| 2.1 Primer | 17 |
| 2.1.1 Crystal structure | 17 |
| 2.1.2 Debye-Waller correction factor | 17 |
| 2.1.3 hP Bravais lattice and the hexagonal crystal system | 20 |
| 2.1.4 Lattice planes and directions in the hexagonal system | 23 |
| 2.1.5 The reciprocal space | 26 |
| 2.1.6 Wavefunctions and physical observables | 30 |
| 2.1.7 Plane waves | 31 |
| 2.1.8 Bragg's law in real space | 32 |
| 2.1.9 Fourier analysis | 34 |

| | | |
|----------|---|-----------|
| 2.2 | Crystallographic computations in the hexagonal system | 35 |
| 2.2.1 | The direct metric tensor | 36 |
| 2.2.2 | The reciprocal metric tensor | 38 |
| 2.2.3 | The interplanar spacing | 39 |
| 2.2.4 | To the reciprocal space and back | 40 |
| 2.2.5 | Rotations in Cartesian frame | 42 |
| 2.2.6 | Crystal to Cartesian frame and the structure matrix | 45 |
| 2.2.7 | Metric tensor implementations | 47 |
| 2.3 | Wurtzite symmetry | 47 |
| 2.3.1 | The $P\bar{6}_3mc$ space group | 48 |
| 2.3.2 | Wurtzite crystal structure | 51 |
| 2.3.3 | Nitrides lattice parameters | 53 |
| 3 | Diffraction in a perfect crystal | 54 |
| 3.1 | Historical background | 55 |
| 3.2 | Kinematical versus dynamical theory | 61 |
| 3.3 | Diffraction geometry | 62 |
| 3.3.1 | Bragg's law in reciprocal space – Ewald sphere | 62 |
| 3.3.2 | Diffraction geometries | 64 |
| 3.4 | Diffraction intensity | 65 |
| 3.4.1 | X-ray scattering by electron charge density and the X-ray scattering factor | 66 |
| 3.4.2 | Electron scattering by a single atom and the electron scattering factor | 68 |
| 3.4.3 | Scattering by the unit cell and the electron structure factor | 73 |
| 3.4.4 | The structure factor in wurtzite nitrides | 75 |
| 3.4.5 | Scattering by an infinite crystal | 77 |
| 3.4.6 | Scattering by finite crystal | 79 |
| 3.4.7 | Treatment of absorption | 80 |
| 3.5 | Darwin-Howie-Whelan equations | 81 |
| 3.5.1 | The two beam case | 85 |
| 4 | Electron diffraction in an imperfect crystal – ECCI | 93 |
| 4.1 | Background | 94 |
| 4.2 | A word on <i>channelling</i> | 95 |
| 4.3 | Electron channelling contrast model | 100 |
| 4.4 | TDs displacement field for ECCI | 101 |
| 4.4.1 | Elasticity theory | 101 |

| | | |
|----------|---|------------|
| 4.4.2 | Semi-infinite screw dislocation | 104 |
| 4.4.3 | Semi-infinite edge dislocation | 105 |
| 4.5 | TD ECC-strain | 106 |
| 4.5.1 | The failure of the invisibility criterion for ECCI | 107 |
| 4.5.2 | ECC-strain profile for the forward scattering geometry | 108 |
| 4.5.3 | General coordinate transformation | 110 |
| 4.5.4 | β isosurfaces insights | 114 |
| 4.6 | Backscattering event model | 118 |
| 4.7 | Numerical simulation of electron diffraction model | 120 |
| 4.8 | Contrast predictions in GaN | 122 |
| 4.8.1 | Equivalence between contrast and ECC-strain | 126 |
| 4.9 | Conclusions | 129 |
| 5 | Electron diffraction in an imperfect crystal – TKD | 130 |
| 5.1 | Introduction | 131 |
| 5.1.1 | How does it work? | 131 |
| 5.1.2 | Kikuchi patterns – three ways | 133 |
| 5.1.3 | Interaction volume | 133 |
| 5.1.4 | TKD geometry | 135 |
| 5.1.5 | Why do we need a new model? | 136 |
| 5.1.6 | Electron scattering | 137 |
| 5.2 | Theoretical Model | 139 |
| 5.2.1 | Energy and diffraction distance integrated electron intensity . . | 140 |
| 5.2.2 | Monte Carlo Trajectory Simulations | 141 |
| 5.2.3 | Non uniform sampled MC | 144 |
| 5.2.4 | Sample thickness in TKD | 146 |
| 5.2.5 | Special sample-detector geometries and the master pattern . . | 148 |
| 5.3 | Results | 152 |
| 5.3.1 | Comparison between EBSD, ECP, and TKD master patterns . . | 152 |
| 5.3.2 | TKD patterns comparison with experiments | 155 |
| 5.4 | Discussion and conclusions | 157 |
| 6 | Summary, discussion and further work | 159 |
| 6.1 | Epilogue – Science as an incremental, open process | 161 |
| A | Implementations | 164 |
| B | Passive rotation matrices in the 3D Cartesian frame | 166 |

| | |
|---|------------|
| C Symmetry in crystallography | 167 |
| C.1 Symmetry operations | 168 |
| C.1.1 Operation of first kind: pure rotation | 168 |
| C.1.2 Operation of first kind: pure translation | 172 |
| C.1.3 Operation of second kind: pure reflection | 173 |
| C.1.4 Combination of rotation and translation | 174 |
| C.2 Point groups | 176 |
| C.2.1 6mm point group from generators | 178 |
| C.3 Space groups | 180 |
| C.3.1 <i>The International Tables for Crystallography, Volume A</i> | 181 |
| D TD strain tensor with surface relaxation | 185 |
| Bibliography | 188 |

List of Figures

| | | |
|------|---|----|
| 1.1 | SEM and electron diffraction Venn diagram. | 5 |
| 1.2 | SEM electrons energy spectrum. | 8 |
| 1.3 | SEM schematics in forward-scattering geometry. | 9 |
| 1.4 | AlGaN TEM. | 12 |
| 1.5 | GaN ECCI. | 12 |
| 2.1 | 2D crystal lattice definition. | 18 |
| 2.2 | Hexagonal 2D lattice. | 21 |
| 2.3 | 3D hexagonal crystal system. | 22 |
| 2.4 | Miller-Bravais basis vectors. | 24 |
| 2.5 | The $\langle 2\bar{1}\bar{1}0 \rangle$ direction family. | 24 |
| 2.6 | Common planes in hexagonal crystal structures. | 26 |
| 2.7 | Reciprocal 2D hexagonal lattice. | 29 |
| 2.8 | Real and reciprocal space hexagonal system basis sets. | 29 |
| 2.9 | Plane waves. | 32 |
| 2.10 | Bragg's equation in real space. | 32 |
| 2.11 | Graphical 3D representation of the 6₃mc symmetry. | 49 |
| 2.12 | Space group P6₃mc . | 50 |
| 2.13 | Wurzite unit cell crystallographic representation versus hcp structure. | 52 |
| 3.1 | Ewald sphere construction in the exact Bragg condition. | 63 |
| 3.2 | Electron diffraction scattering geometry. | 64 |
| 3.3 | Schematic diagram of scattering by an atom. | 67 |
| 3.4 | Atomic X-ray scattering factors. | 69 |
| 3.5 | Atomic electron scattering factors. | 71 |
| 3.6 | Relative atomic electron scattering factors. | 72 |
| 3.7 | What happens to the Bragg's law when we add an atom in between planes? | 73 |
| 3.8 | Ewald sphere construction for a positive deviation parameter s_g . | 80 |
| 3.9 | Thickness fringes. | 91 |

| | |
|--|-----|
| 3.10 Rocking curves. | 92 |
| 4.1 “Channels” | 96 |
| 4.2 Ion channelling. | 98 |
| 4.3 Stress distribution on an infinitesimal volume. | 102 |
| 4.4 Forward-scattering geometry. | 109 |
| 4.5 Rotation transformation of sample tilting. | 109 |
| 4.6 Planar edge TD β strain profile. | 111 |
| 4.7 Forward geometry reference frames. | 113 |
| 4.8 Edge TD ECC-strain field equidistant isosurfaces. | 115 |
| 4.9 Screw TD ECC-strain field equidistant isosurfaces. | 115 |
| 4.10 Mixed TD ECC-strain. | 116 |
| 4.11 Edge TD ECC-strain in different orientations. | 117 |
| 4.12 AlN ECCI in two diffraction conditions. | 117 |
| 4.13 Edge TD top view of equidistant ECC-strain isosurfaces. | 118 |
| 4.14 The code structure schematics for predicting TD contrast in ECCI . . | 121 |
| 4.15 Edge TD ECC-strain in different orientations. | 123 |
| 4.16 Predicted contrast comparison with experiments. | 125 |
| 4.17 ECC-strain vs contrast for a screw TD | 126 |
| 4.18 ECC-strain vs contrast for an edge TD | 128 |
| 4.19 Vanishing ECC-strain vs vanishing contrast for an edge TD | 128 |
| 5.1 EBSD, TKD and ECP set-up geometry. | 131 |
| 5.2 EBSD pattern of Ni northern hemisphere. | 132 |
| 5.3 Interaction volume | 134 |
| 5.4 Schematics of TKD set-up geometry | 135 |
| 5.5 Directional distributions of transmitted electrons intensity in TKD. . . | 142 |
| 5.6 Elastic scatter events distribution. | 144 |
| 5.7 Incoherent scatter probability. | 145 |
| 5.8 Estimated spatial distribution of diffraction out “sources”. | 146 |
| 5.9 KDE plots of electron energy versus escape distance distributions . . | 147 |
| 5.10 Energy distributions versus sample thickness. | 148 |
| 5.11 KDE plots of electron energy versus escape distance distributions . . | 149 |
| 5.12 Mean angular dependence of exit energies in TKD | 150 |
| 5.13 Master patterns for ECP, TKD and EBSD | 153 |
| 5.14 Line scans for previous maps and energy distributions | 154 |
| 5.15 Experimental TKD patterns. | 156 |
| 5.16 Dictionary indexing TKD pattern | 157 |

| | | |
|-----|--|-----|
| C.1 | Graphical representations of three-fold and six-fold pure rotations. | 169 |
| C.2 | Three-fold rotation around the third axis of a hexagonal basis set. | 171 |
| C.3 | $m(x, -x, z)$ mirror plane operation in a hexagonal basis set. | 174 |
| C.4 | Operations steps for screw axis. | 175 |
| C.5 | 2_1 screw axis operation in a hexagonal basis set. | 176 |
| C.6 | 6mm point group. | 178 |
| C.7 | Space group P6₃mc in <i>ITC</i> | 183 |
| D.1 | Screw TD strain tensor. | 186 |
| D.2 | Edge TD strain tensor. | 187 |

List of Tables

| | | |
|------|--|-----|
| 1.1 | Corrected and uncorrected electron wavelengths for voltages used in electron microscopy | 10 |
| 2.1 | Debye-Waller factor for cubic elemental crystals. | 19 |
| 2.2 | Debye-Waller factors for N in wurtzite materials. | 20 |
| 2.3 | Miller versus Miller-Bravais direction notation. | 25 |
| 2.4 | Miller versus Miller-Bravais planes notation. | 26 |
| 2.5 | Bragg angles for the most common planes in wurtzite materials for 20 keV incident electrons. | 33 |
| 2.6 | Calculated interplanar distances in wurtzite nitrides. | 40 |
| 2.8 | The P6₃mc space group number. | 50 |
| 2.9 | List of generators for wurtzite crystal structure. | 51 |
| 2.10 | Lattice parameters for some common wurtzite nitrides. | 53 |
| 3.1 | Scattering properties of particles used in diffraction. | 54 |
| 3.2 | Partial chronology of the history of diffraction. | 57 |
| 3.3 | Kinematical vs. dynamical diffraction theories. | 61 |
| 3.4 | Doyle & Turner atomic scattering parameters. | 68 |
| 3.5 | Structure factors for wurtzite nitrides. | 76 |
| 3.6 | Various dynamical models used in electron diffraction. | 81 |
| 4.1 | Critical channelling angle | 99 |
| 4.2 | Wurtzite GaN Voigt elastic constants. | 104 |
| 4.3 | Modelling parameters. | 124 |
| 5.1 | Calibration parameters. | 155 |
| C.1 | Examples of pure rotation symbols. | 169 |
| C.2 | Example of pure reflection symbols. | 173 |
| C.3 | Examples of screw axis symbols. | 175 |
| C.4 | Symmetry directions for the hexagonal crystal. | 178 |

List of Abbreviations

| | |
|-------------------|---|
| BSEs | Back Scattered Electrons |
| CSDA | Continuously Slowing Down Approximation |
| DW | Debye-Waller |
| EBSD | Electron Backscattered Diffraction |
| EBSP | Electron Backscattering Pattern |
| ECC | Electron Channelling Contrast |
| ECC-strain | Electron Channelling Contrast - strain |
| ECCI | Electron Channelling Contrast Imaging |
| ECP | Electron Channelling Pattern |
| EM | Electron Microscopy |
| FSEs | Forward Scattered Electrons |
| FE-SEM | Field Emission - Scanning Electron Microscopy |
| SEM | Scanning Electron Microscopy |
| SP | Stereographic Projection |
| TEM | Transmission Electron Microscopy |
| TKD | Transmission Kikuchi Diffraction |
| t-EBSB | transmission Electron Backscattered Diffraction |
| TD | Threading Dislocation |

Physical Constants

| | |
|--------------------------|---|
| Bohr radius | $a_0 = 5.291\,772\,10 \text{ \AA}$ |
| Electron rest mass | $m_e = 9.109\,383\,56 \times 10^{-31} \text{ kg}$ |
| Electron rest mass | $m_e = 0.510\,998\,94 \text{ MeV}/c_0^2$ |
| Electron volt | $eV = 1.602\,176\,62 \times 10^{-19} \text{ J}$ |
| Elementary charge | $e = 1.602\,176\,62 \times 10^{-19} \text{ C}$ |
| Permittivity of vacuum | $\epsilon_0 = 8.854\,187\,82 \times 10^{-12} \text{ F m}^{-1}$ |
| Permeability of vacuum | $\mu_0 = 1.256\,637\,06 \times 10^{-6} \text{ V s A}^{-1} \text{ m}^{-1}$ |
| Planck constant | $h = 6.626\,075 \times 10^{-34} \text{ Js}$ |
| Speed of light in vacuum | $c_0 = 299\,792\,458 \text{ m/s}$ |

List of Symbols

| Symbol | Name | Units used here |
|--|--|--|
| $\mathbf{a}, \mathbf{a}_i, \mathbf{b}, \mathbf{c}$ | Bravais lattice basis vectors | \AA |
| $\mathbf{a}^*, \mathbf{a}_i^*, \mathbf{b}^*, \mathbf{c}^*$ | Reciprocal basis vectors | \AA^{-1} |
| \mathbf{e}_i | Cartesian basis vectors | \AA |
| \mathbf{r} | General position vector | \AA |
| \mathbf{t} | Translation vector | \AA |
| \mathbf{g} | Reciprocal lattice vector | \AA^{-1} |
| \mathbf{g}_{hkl} | Reciprocal lattice translation vector | \AA^{-1} |
| \mathbf{k} | Wave vector | \AA^{-1} |
| $\{a, b, c, \alpha, \beta, \gamma\}$ | Lattice parameters | $\{\text{\AA}, \text{\AA}, \text{\AA}, ^\circ, ^\circ, ^\circ\}$ |
| d_{hkl} | Interplanar spacing for planes $(h k l)$ | \AA^{-1} |
| $f(s)$ | Atomic scattering factor | V\AA^3 |
| F_{hkl}, F_g | Structure factor for reflection hkl | V\AA^3 |
| V_g | Fourier coefficient of the crystal potential | V |
| θ_B | Bragg angle | $^\circ$ |
| Ω | Unit cell volume in real space | \AA^3 |
| \mathbf{u} | Displacement field | |
| s_g | Deviation parameter | |
| β (or ECC-strain) | Correction to s_g due to presence of defects | |
| $(h k i l), (h k . l)$ | Miller-Bravais plane indices | |
| $(h k l)$ | Miller indices of a plane | |
| $\{h k l\}$ | Family of planes | |
| $[u v t w]$ | Miller-Bravais direction indices | |
| $[u v w]$ | Miller direction indices | |
| $\langle u v w \rangle$ | Family of directions | |
| δ_{ij} | Kronecker delta | |

1 Introduction

1.1 The big picture

*Without microscopy, there is no modern science.
End of story.*

Dr. Alan Finkel, opening the 19th
International Microscopy Congress [Aus]

Alan went on to point out that a simple Google search of the word *scientist* returns two activities: people pouring coloured solutions into beakers and people looking down microscopes. Since Google recently improved the diversity of said people, the results make up a decent overview of the position microscopy has in science overall. The truth value of his statement can be quantified not only by the engagement it received on Twitter late last year, but also by the plethora of examples that back this claim.

Every high resolution image of bugs, cells, viruses you ever wondered at? Microscopy. Forensic science? Microscopy. Environmental scientists monitoring particles in air, water or soil? Microscopy. Identification of bacteria in food along its entire life cycle? Microscopy [Mic]. Weather scientists understanding the complicated behaviour of snow? Microscopy [LHH96].

And it doesn't stop at science. The art history world had been stuck for a while with four almost identical copies of a 16th century painting of "*Christ Driving the Traders from the Temple*" in various galleries around Europe [Cul19]. Three too many for unambiguously declaring one as the original. In 2009 an interdisciplinary research project was established with the purpose of applying, you guessed it, microscopy to characterise the pigments used, how they were ground and then how were applied to the wood. They use a combination of polarised microscopy to look at the pigments and stereomicroscopy to analyse the brushwork [Her12]. Unfortunately, they found that the copy in Glasgow, signed Hieronymus Bosch, appears to have been painted eighty years after his death.

Then, there is the world of nanotechnology including, at one end of the spectrum, the manufacturing of smaller and smaller devices and, at the other, the engineering at smaller and smaller scale of materials. No matter what quality control entails for a specific sub-field the task is the same: to characterise these materials. For instance, group-III nitrides are a type of very promising and exciting semiconductors, used in lights emitting diodes (LEDs) among others. In these materials dislocations reduce the luminescence output. Of course we want to improve the bang for our buck. The obvious way to understand and overcome the defect impact is, if you've been paying attention so far, by doing some microscopy. We will cover the details of this in Chapter 4.

But, just like there will likely not be one single cure for cancer, microscopy, this "cure" for many of our scientific problems, is in truth an umbrella term for quite a wide range of physical phenomena. From light polarisation to scattering and diffraction, all these different behaviours need then to be well understood if we are to apply them to probe nature. In the age of fast computers it becomes a no-brainer that we can afford to create numerically demanding models in order to increase the accuracy of our predictions.

The two main results chapters of this thesis are focused on developing models for two different characterisation techniques in the scanning electron microscope (SEM) based on diffraction. Chapter 4 will talk about electron channelling contrast imaging (ECCI) and Chapter 5 about transmission Kikuchi diffraction (TKD). I call both of these microscopy techniques novel, partly because they are relatively young (we will see in the respective chapters how that is something more of a stretch for ECCI), but more importantly because the physical mechanism behind these imaging techniques is not yet well understood. My definition of *well understood* involves having access to a model that predicts quantitatively the experiments, matching intensity values for all pixels and all conditions. We are probably at least a few PhDs away from that.

A question useful to look at when using ECCI is: *What does the dislocation contrast tell us?* Like many things in science the answer is "it's complicated". In Chapter 4 I try to unpack that and talk about the two main contributions: on one hand the electron beam-sample geometry and on the other the type of dislocation. Clearly this is an excellent problem to tackle with a model since one (me) can easily change a number of parameters and see how the results are affected. It turns out that tilting the sample, a tactic quite standard in the world of ECCI, increases the strain observed by the incident electrons for the specific type of dislocations common in group-III nitrides and, as a result, the contrast in the image and our chances to observe the defect.

Now, the relationship between dislocation type and how the contrast looks in the

ECCI, has become along the years a sort of holy grail of the field. A small one but a sacred one nevertheless. If this relationship would be undeniably established one could characterise dislocations in the SEM. This would be cheaper, faster with less work, with fewer doubts about sample integrity and better statistics for defect densities than the standard method used at the moment (TEM). Almost too good to be true. Perhaps, but it does look great on grants.

Like all good problems, answering it involves isolating a cause and effect from a number of possible causes; in this case the dislocation type and the (possibly unknown) diffraction condition will both affect the contrast features of the dislocation. Since there are no suggestions on how one would separate these effects with a backwards engineering approach, we are left with comparing against a number of possible features predicted by a forward model. I did not solve this problem, but I did make a dent in it. In this thesis, I proposed that the modelled strain profile of the limited number of possible dislocations in these materials will predict the observed contrast. Armed with this theory I went on to predict what affects the contrast more: the type of dislocation or the diffraction condition.

Talking of holy grails in the field of scanning electron microscopy, another interesting question is which backscattered electrons contribute to electron backscattered diffraction patterns. There are generally two schools of thought here: either a very narrow subset of electrons are allowed to diffract on the way out [Win+07], or all electrons are given a nonzero chance to do so [CDG13]. It might not sound so, but the difference becomes quite substantial especially when very small changes in the Kikuchi bands are being used as a method of strain characterisation. In Chapter 5 I show the predictions of EMsoft, an implemented model based on the second approach, where Monte Carlo models are used to estimate the statistical effect of electron scattering.

There are a number of electron diffraction modalities in the SEM, and each has its relative strengths and weaknesses. Transmission Kikuchi patterns, also known as transmission electron backscattering diffraction (t-EBSD) (to emphasise that the physics is similar for these transmitted diffracted electrons as it is for the more conventional backscattered ones) is a new addition to these modalities and the topic of Chapter 5. The interest in this novel technique is fuelled by the promise of high spatial resolution due to its geometry which allows for a smaller interaction volume.

Unlike the first type of models which ignore the backscattered electron source distribution, with our approach we can study the physics of these sources. We also show that the escape position actually changes with the thickness of the sample. Additionally, we can predict the energy and angular distribution of the electrons on the detector. All of these important details about the image ought to be well understood

if characterisation techniques reliant on small changes in images are to be developed. Which seems to be a trend not going away any time soon.

If you want to have a look at any of the code used in this thesis, you should; it's all on GitHub (<https://github.com/elenapascal/>). One thing I am pleased about is that I employed coordinate reference frames as objects, using a nifty SciPy library in Python [JOP+01], to make sense of them. Easy to read as well. Super important when you have about five of them to track during one computation. How does your local commercial software track reference frames? You probably don't know and that is a problem. In the best case scenario there is documentation, or even an actual paper about it. But can anyone be sure the implementation matches the documentation if no one but the vendor has access to the code? I vote no. I return to this in Section 6.1. For now let us come back to microscopy.

1.2 Diffraction and the SEM

The Venn diagram of electron diffraction and scanning electron microscopy (SEM), shown here in Fig. 1.1, is showing a very small overlap. Diffraction in general, and particularly that of electrons, which we will discuss in more details in Chapter 3 from page 54, is a mature and well understood subject. So is the now ubiquitous materials investigation tool that is the SEM, which we will briefly cover on page 6.

The group of people engaged in studying both these fields is a very select one. The techniques based on electrons diffraction in the SEM either do not have a dedicated conference such as the *channelling* family; this includes electron channelling patterns (ECPs) and electron channelling contrast imaging (ECCI) – which we will explore in Chapter 4 from page 93–, or do have dedicated conferences; this is the case for the backscattered/fore-scattered diffraction family which includes electron backscattered diffraction (EBSD) and, more recently, transmission Kikuchi diffraction (TKD), which will be described in Chapter 5 from page 130, but are dominated by material scientists interested more in understanding the materials rather than the physics of the characterisation technique.

Some of these techniques are more novel than the others, but all of them carry mysteries about aspects of the underlying physical processes. These unanswered questions are enticing not only from the aspect of fundamental physics, but also as a promise of more information that could be derived from these measurements. Building and implementing models that accurately predict these behaviours is, therefore, an important aspect of the field.

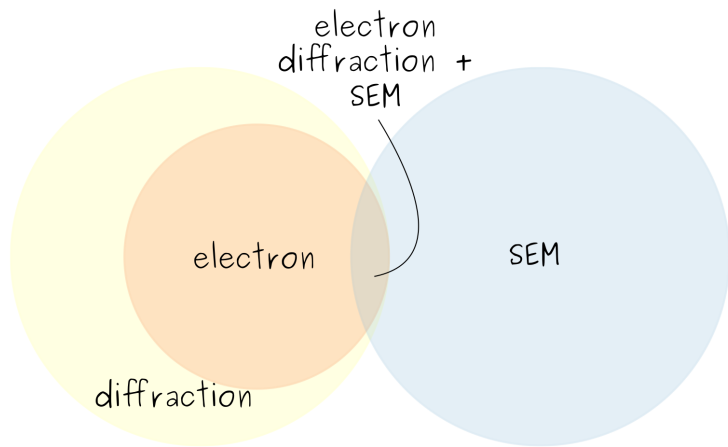


FIGURE 1.1: Venn diagram showing how many Google scholar results contain the keywords: diffraction (yellow), electron diffraction (orange) and SEM (blue). The small overlap summarises the topics addressed in this Thesis. The area of the circles is proportional to the number of search results.

In Chapter 4 I talk about ECCI, a SEM diffraction method well suited for the characterisation of threading dislocations (TDs) in nitrates. Then, in Chapter 5 I talk about TKD, a SEM diffraction technique optimised for the study of truly nano-crystalline materials.

1.2.1 Diffraction

Starting with page 54, I will spend the entire chapter 3 on the powerful characterisation technique that is diffraction. There are only handful more elegant ideas out there than the power of observing the reciprocal space of an ordered arrangement of atoms, taking us very quickly to the conundrum of why is maths such a good description of reality. But let us not digress.

The geometry of diffraction is beautifully simple in the form of Bragg's law. Perhaps less intuitive is the fact that Braggs law being satisfied is not a guarantee of non-zero diffracted intensity. This behaviour is going to depend not only on the crystal system as Bragg law does, but instead it is going to be a map of the space group symmetry of the material under investigation.

It is important to understand the basic diffraction behaviour in a material system before trying to derive information from a diffraction based technique applied to that

material system. I will show, in Chapter 3, theoretical predictions for electron diffraction relating parameters, such as scattering and structure factor, for a few group-III nitride materials: AlN, GaN and InN.

While all particles diffract in the same way, electrons interact more strongly with matter and simplifications that can be done in the more established case of X-ray diffraction predictions are not acceptable when it comes to electrons. In the rest of that Chapter 3 I will review the dynamical model of electron diffraction and show how it incorporates the diffraction parameters mentioned above.

Because we cannot talk about diffraction without some solid knowledge of crystallography, I cover extensively the basics of crystallography and crystallographic computations in Chapter 2. Since diffraction is the map of the crystal symmetry I examine in Appendix C on page 167 the full **P6₃mc** symmetry of the wurtzite system.

1.2.2 The scanning electron microscope

The phenomena described in the previous section occur at a scale too small to be measured by the naked eye. Luckily, development of science had brought us two main extensions to the range of scales we can study. On one hand, the telescope brings very distant objects closer and is optimised to collect as much light as possible and, on the other, the microscope makes very close objects appear many times larger. Interestingly, both these aids can be traced back to a 17th century event: the development of glass lenses used in spectacles. Fundamentally, both these visual extensions are governed by the same optics laws.

While modern light microscopes can commonly¹ showcase a magnification of about 2000 \times , their spatial resolution is limited by the wavelength of visible light, which is of the order of hundreds of nanometers, through Abbe's equation. One way around it is to use different imaging particles, for instance, X-rays or electrons which have significantly smaller wavelengths (see Table 3.1 for wavelength comparison between X-ray photons and electrons).

We will explore further the electron microscope, excellent detailed descriptions of which can be found in ref. [HSC72] and ref. [Rei98]. There are various ways of generating an electron beam. For instance, in our (FEI now Thermo Fisher) SEM, a field enhanced thermionic emission Schottky gun is used to generate a beam of electrons. This beam is then focused through a series of condenser lenses onto the surface of a sample such that the beam spot size on the sample can go down to 1 nm

¹ Developments in super resolution optical microscopy show that certain applications can overcome Abbe's limit.

in diameter in practice. After the beam is focused on the sample, scanning coils are used to deflect the beam on a set of orthogonal directions in a predefined manner.

Depending on the geometry of imaging² we can loosely classify electron microscopy into *transmission electron microscopy* (TEM) on one hand, where the image is formed by electrons which have travelled through a very thin sample, and *scanning electron microscopy* (SEM), where the imaging electrons come from the same, top surface of the sample with which the incident beam interacts³. Both of them have advantages and disadvantages. The TEM geometry minimises the lateral spread of the electron-sample interaction volume providing therefore higher spatial resolution, but it also limits its field of view. Additionally, thinning the sample to the sizes required by this geometry can be cumbersome, time consuming and irremediably damaging to the sample. There is also the additional question the microscopist must answer, whether the features observed are intrinsic to the sample or were introduced during the polishing process. On the other hand, for non-biological materials, the SEM requires minimal sample preparation since the thickness of the sample does not limit its capabilities. The downside, as we will see, is that the SEM is not optimised for diffraction contrast in the same way the TEM is.

Since electrons interact strongly with matter they can generate a plethora of signals for one to measure in the SEM using the right, specialised detector:

- Most commonly, low-energy ($<50\text{ eV}$) *secondary electrons* (SE) are ejected by those atoms with which the primary beam electrons have inelastically scattered. With such low energies these electrons cannot come from very deep in the sample, which means the interaction volume is narrow enough to provide a tool for high resolution surface imaging. These electrons are collected by attracting them to an electrically biased grid and then further accelerated towards a phosphor screen or scintillator, in what is known as a Everhart-Thornley detector [ET60].
- In addition to secondary electrons, excited atoms will also emit a variety of electromagnetic radiation such as characteristic X-rays which can provide information on the distribution of different elements in the sample as long as the SEM is equipped with wavelength dispersive X-ray spectrometers (WDS) or energy-dispersive X-ray spectroscopy (EDS).

² But also electron beam energy and sample preparation procedure.

³ Advances in both worlds make this distinction imperfect. There is an exception to the rule above, in the form of transmission SEM. To make things even harder to classify there is also scanning TEM.

- As the atoms relax back to their ground state after the encounter with the high energy electrons, they can generate light which can provide useful optical information in a technique known as *cathodoluminescence* (CL) [EM11].
- The primary beam electrons will also escape the sample, after having a range of energies through inelastic scattering. This implies, that, at some point in their trajectory, the incident electrons suffered a large angle elastic scattering event such that they turn back to the surface of entry. All the incident electrons that suffer an elastic scattering event and manage to escape through the entry surface are collectively known as *backscattered electrons* (BSE) and can be detected by a scintillator or a solid state detector. Since heavier atoms will elastically scatter electrons more strongly, BSEs can be used to detect contrast due different chemical compositions. Additionally, if the detector is not collecting a symmetric radial distribution of BSEs, then the image will also contain strong topographic contrast (for instance, think shadowing).

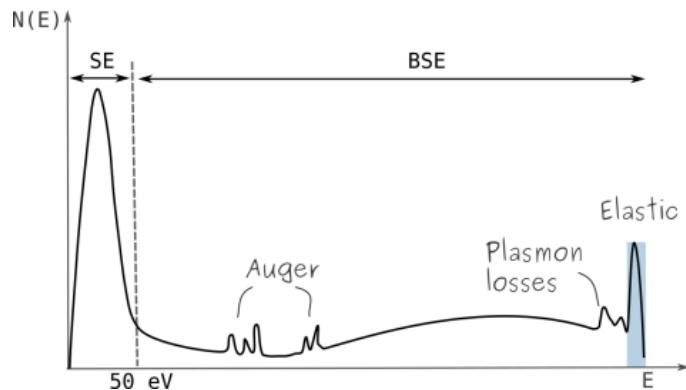


FIGURE 1.2: Schematic energy spectrum of secondary and backscattered electrons in an SEM [after [BE12]].

- Figure 1.2 shows the energy distribution of electrons reaching the BSE detector for an incident beam of energy E . Superimposed on the BSE energy curve are a few other signals but we will only talk here about the elastic peak as it is at the core of this work. A subset of BSEs will lose almost no energy before reaching the detector, either because they have been backscattered by the top layer of the sample, or, more likely, because they underwent diffraction, a case in which inelastic scattering processes are reduced (see the discussion on channelling on page 95). We will call these the *elastically BSEs*. This signal can provide information on the crystallographic orientation of a small region of the sample or about

small changes in local strain. More on this in Chapter 4 and Chapter 5. One could use energy sensitive detectors to select only this signal [Ves+15].

We will be concerned in this Thesis only with elastically scattered BSEs (in Chapter 5 we will also talk about forward scattered electrons (FSE)). The sample geometry optimised for this signal is shown below in Fig. 1.3. The sample is tilted with respect to the incident beam and the detector is positioned such that it can collect the solid angle of the backscattered electrons that provides the highest intensity. We call this geometry forward-scattering.

The method of operation of the SEM is shown Figure 1.3. A collimated beam of electrons is focused on the surface of a tilted sample. The beam is then scanned in a raster manner over the area of interest on the sample. The detector collects one pixel worth of BSEs intensity at a time. The beam is moved by the deflector coil to the next position on the sample defined by the step size. The resulting image is made up of the ordered collected pixels, and, at the end of the scan, has as many pixels as steps used in scanning.

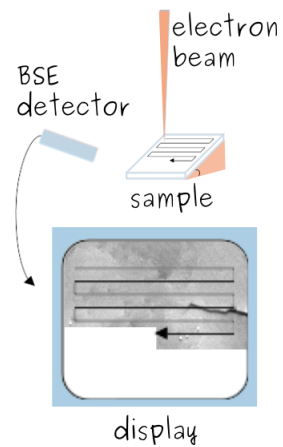


FIGURE 1.3: SEM schematics in forward-scattering geometry.

The tilt of the sample in the forward-scattered geometry in the SEM ensures that enough electrons reach the detector. It also makes the geometry of diffraction very different from that in the TEM. The sample's z-direction in the SEM is not the same as the beam direction which is the case for the TEM sample geometry. This means that if we are to use the diffraction models developed for TEM, they must be generalised for the sample tilt. More about this in the next chapter.

References [HSC72; Rei98] discuss the electron optics and we will not delve into here. We will however mention that the tilt of the sample affects the “squareness” of the scanned area. The trapezoidal area being scanned will produce a distorted image, which can be corrected to some degree using the tilt correction function (see page 50 in ref. [CG84] for tilt correction artefacts). The tilt can also change the shape of the beam on the sample which not only affects the imaging but also the diffraction interaction volume.

Let us briefly address relativistic corrections and the correction factor, γ , for electrons used in electron microscopy. The de Broglie equation for the relativistic electron

wavelength, λ , in Å, can be approximated in terms of the accelerating voltage V given in keV (equation 2.4 in [GH88]) as⁴:

$$\lambda \approx \sqrt{\frac{150}{V + 10^{-6} V^2}} \quad (1.1)$$

where the second term in the denominator is due to Lorentz factor and only becomes important for voltages greater than 20 keV as we can see in Table 1.1. For SEM applications discussed in this work we will focus on 20 keV incident electrons, and discard, quite acceptably, relativistic effects.

TABLE 1.1: Corrected and uncorrected electron wavelengths for voltages used in electron microscopy.

| Voltage [keV] | Lorentz factor γ | Wavelength λ [Å] | |
|----------------------|---|--|------------------|
| | | Uncorrected | Corrected |
| 20 | 1.04 | 0.086 | 0.086 |
| 100 | 1.20 | 0.039 | 0.037 |
| 1000 | 2.93 | 0.012 | 0.009 |

1.3 ECCI and the characterisation of TDs in nitrides

Over the past thirty years there has been no shortage of interest in electronic and light emitting devices based on semiconductors and, as a result, their impact on modern technologies has become notable. Brighter, more efficient and more reliable light sources have been developed. Specifically, the group III-nitride material systems and their alloys have been intensely studied due to a number of promising properties. We have witnessed an ever increasing span of emerging applications: from ultraviolet light water purification and hydrogen production, to high power electronics and novel optical communication systems [Kne+10]. The bottleneck of developing the next generation devices remains the material science of improving even further the efficiency for these devices.

The large difference in covalent bondings of the elements in these systems translates to greatly varying physical properties, including different lattice parameters and energy band gaps. The latter means that nitride alloy systems can offer a wide range

⁴Note that this is the result of an empirical fit and the dimensions of the parameters have not been taken into account. Changing the voltage units must be done with caution.

of direct energy-band gaps, *i.e.*, high intensity luminescence at a wide range of wavelengths (*e.g.* the band gap of InAlGaN systems ranges from infra-red to the ultraviolet region). In addition, their structural stability at high temperatures and good thermal conductivity make them ideal candidates for the fabrication of high power transistors. GaN is a binary system belonging to this material group and together with its cousins, InN and AlN, and their ternary and quaternary alloys are one of the semiconductors on top⁵ of material scientists minds, due to their many applications in optical and electrical devices.

Nevertheless, unlike Si and Ge, the group III-nitrides epitaxial growth is challenging due to the lack of a suitably lattice matched material. The lattice mismatch can be significant and the usual compromise between cost and growth impairment is sapphire (Al_2O_3), which at room temperature and along the *r*-plane has a lattice mismatch of $\sim 1.1\%$ even on a coincident lattice [Amb98] with GaN grown in the [0 0 0 1] direction. The epitaxial layers will be further strained during the cooling down stage, such that, at the end of the growth process, a thick layer can relax through the formation of dislocations along the interface of lattice mismatched materials.

An interface misfit dislocation introduces a discontinuous strain in the crystalline lattice, and the way to resolve the discontinuity is through the generation of *threading dislocations* (TDs) which run from the layer interface through the crystal up to its surface. Dislocations and line defects of crystalline solids can strongly affect the properties of the material and the performance of the devices we would like to use these materials for.

Surprisingly, the blue emitting devices based on III-nitrides are able to function even in the presence of TD densities of the order of $10^{11}cm^{-2}$, due to carrier localisation effects [Gra+05]. However, for a great number of devices, TDs prove to be problematic as they tend to be associated with impaired optical and electrical performances. For example, TDs correlate with increased leakage currents in green and blue light emitting diodes (LEDs) [Fer+07] and overall reduction in efficiency in near-UV LEDs [Kam+02]. Moreover, TDs can be blamed for reducing the lifespan of laser diodes as well as decreasing the electron mobility in high electron mobility transistors [Bou+05]. TDs can cause premature junction breakdowns as well as inhibiting high current gains in GaN based UV avalanche photodiodes [Lim+06]. They are also connected to the current collapse in GaN field-effect transistors [DSB06] and the general degradation in performance of high power GaN based devices. Therefore, the need to study the origin, development and impact of TDs becomes apparent if we are to optimise growth methods aimed at reducing the TDs density.

⁵After the big ones like Si and Ge and the more established systems of arsenides and phosphides

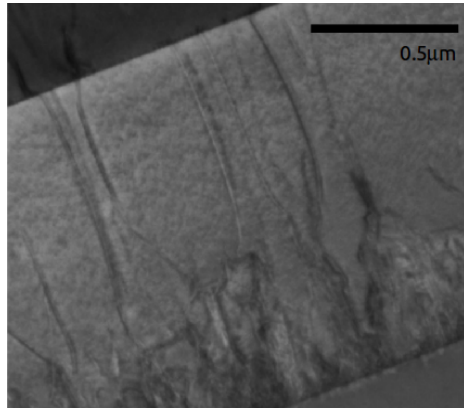


FIGURE 1.4: Transversal TEM image^a of an AlGaN on sapphire showing threading dislocations reaching an interface.

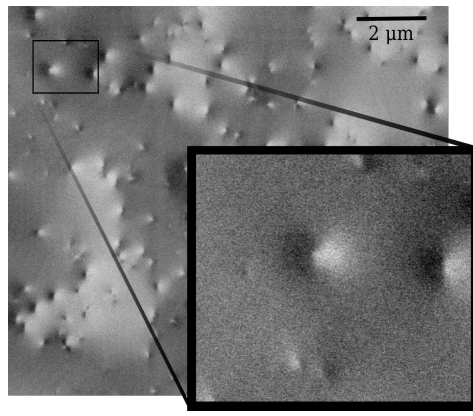


FIGURE 1.5: Plan view ECCI^a of a [0001] GaN on sapphire showing black-white contrast around threading dislocations.

^aTaken at the Kelvin Nanocharacterisation Center, University of Glasgow. By permission of David Thomson, University of Strathclyde

^aBy permission of Allehiani Nouf Mohammad, University of Strathclyde

Electron diffraction is one mechanism that is sensitive to the presence of strain due to dislocations in the crystal, facilitating therefore dislocation imaging. Transmission electron microscopy (TEM) has established itself as the default technique for the study of lattice deformations and for identifying defect types. We will talk more about dislocations in the next section but for now it is useful to know that two extreme [0001] threading dislocation characters can be distinguished: pure screw type (or *c-type*) where the Burgers vector (**b**) is aligned along the *c*-axis and pure edge dislocation (or *a-type*) when the Burgers vector is confined to the (0001) basal plane. If neither of these conditions is strictly met, the dislocation is called mixed, or *a+c type*.

TEM is especially reliable as a dislocation characterisation method as it can unambiguously identify the **c** and **a** components of a dislocation line running parallel to the imaged surface. This is achieved through the application of certain relationships between the diffraction vector **g**, Burgers vector **b** and the direction of the dislocation line **u_l** ($\mathbf{g} \cdot \mathbf{b} = 0$ and $\mathbf{g} \cdot \mathbf{b} \times \mathbf{u}_l = 0$), known as the *invisibility criteria*, for which no contrast associated with **c** or **a** components can be observed. This method has been applied broadly in the study and characterisation of dislocations in cross sectional GaN samples (*e.g.* [Hin+00]). For TDs which penetrate the sample surface normally (or almost normally) high resolution TEM (HRTEM) can provide direct observation of the Burgers vector direction of **a** type TDs. However, as the images are usually

acquired in plan view, the c components are invisible. The destructive TEM sample preparation and its limited field of view can also restrict the number of defects that can be observed and hence may impact the statistical limits on estimating defect densities, particularly for materials with lower numbers of dislocations.

There are characterisation methods which do not share TEM's requirements for sample preparation. These include atomic force microscopy (AFM), which can offer information on TDs associated with surface pits [Cra+02] (often after an etching or decoration treatment) or when terminating step edges. However, AFM can be sensitive to surface debris and may require extended periods of time to image even relatively small areas [KB97]. Alternatively, for larger area measurements, X-ray diffraction (XRD) [Hei+00] or cathodoluminescence [Ros+97] can provide information on the global material defect densities but can have serious limitations in terms of resolving individual dislocations, especially XRD.

An alternative to the above methods is the use of the electron channelling contrast imaging (ECCI) technique which can be employed within generally available field emission scanning electron microscopes (FE-SEMs). This approach can image defects with resolution of a few nanometers with a micrometer scale field of view, and is neither destructive nor based on direct sample contact. However, in order to obtain the maximum amount of information from these images, a thorough understanding of the contrast mechanisms is required.

Trager-Cowan *et al.* [TC+07] showed that using ECCI in the characterisation of nitrides is an excellent idea. ECCI has been used in the foreshatter geometry to reveal extended defects and morphological features of GaN samples while also delivering information about crystallographic orientation [Pic+07]. The electron channelling contrast images obtained in the SEM can provide structural information on dislocations interacting with the sample surface, particularly when obtained in highly diffracting channelling conditions [NK+12]. This information is shown in the form of variation in the electron backscattered contrast intensity around a dislocation – or dark-bright signal contrast on the micrograph. Because it can resolve individual dislocations while imaging larger areas (e.g. Nouf-Allehiani *et al.* [NA+rt] for material with TDs having a mean separation of ≈ 200 nm), ECCI is an ideal candidate for both precise and accurate number estimates for a wide range of TD densities (10^6 cm^{-2} – 10^{10} cm^{-2}).

1.3.1 Modelling of diffraction-in

In this work I continue on the path of analysing the ECCI as a TD characterisation technique. In Chapter 4 I look at the theoretical models that could be applied to predict the TD contrast in ECC images of [0001] grown GaN. It was clear that the contrast predictions methods used for TEM will be inappropriate when considering contrast in bulk samples. If a TD dislocation in a thin TEM sample will introduce two opposite, and cancelling in effect, surface relaxations on the top and bottom surface, a beam in ECCI will only image the top surface and therefore be far more sensitive to the top surface relaxation. A model for ECCI contrast should therefore take into account the surface relaxation, to begin with. The questions I followed were *What can a suitable model predict about the behaviour of the TD contrast?* and *What can we then learn from this predicted behaviour?*.

Since diffraction conditions in the SEM are more challenging to pinpoint than in the TEM, I wanted to remove this hard to determine variable from the predictions and look, qualitatively, at the behaviour of a property that causes the contrast in the first place: the strain flavoured parameter that quantifies the correction to the deviation parameter β due to the dislocation. I give it the name of *ECC-strain*.

By looking at isosurfaces of this newly minted ECC-strain for different types of dislocations in different conditions, I can make a few observations regarding the effect of geometry, the effect of dislocation type and the effect of diffraction condition on the imaged contrast. For instance, I predict that the contrast profile will depend firstly on the type of dislocation and its geometry and only secondly on the diffraction condition. These predictions could then be turned into recipes for contrast optimisation on one hand and dislocation characterisation on the other.

1.4 TKD and the study of truly nanostructured materials

Kikuchi patterns are another representation of the diffracting behaviour of electrons in the form of a variation in the angular distribution of escaping electrons undergoing diffraction, as we will see on page 133. We have already established that real materials are not perfect crystals. Dislocations are not the only imperfections that can dictate the properties of a carefully engineered material. The material structure can show features sometimes even at the nano scale level, in the form of crystal grains with more or less different crystal orientations from their neighbouring grains – what we call polycrystals.

The investigation and characterisation of the micro structure of new materials is a core aspect of materials science in particular but also fundamental science in general. Kikuchi diffraction became a widespread SEM technique, in the form of electron backscattered diffraction (EBSD), able to provide quantitative microstructural information about most inorganic crystalline materials. The history of Kikuchi diffraction patterns is almost ninety years old as we have seen on page 57, and the most applied version of it is in the form of EBSD.

However, recently, stimulated by the increased attention to nanostructured materials, which promise new and enhanced properties when compared to their larger scale counterparts, the interest in improving the resolution of established characterisation techniques has also expanded. The use of forward-scattered electrons (FSEs) through a thin sample as diffraction signal collected from the bottom of the foil has been shown to improve the lateral spatial resolution to below 10 nm [KG12; Tri12a]; this technique is commonly known as transmission Kikuchi diffraction (TKD) or transmission EBSD (t-EBSD).

1.4.1 Modelling of diffraction-out

The work described in Chapter 5 was the outcome of a collaboration with Prof. Marc De Graef's group from Carnegie Mellon University. The CMU group developed a vast, open-source software called EMsoft [DGG13] aimed at modelling a variety of diffraction techniques in the SEM including EBSD.

The aim of our particular project was to add a TKD modality implementation in EMsoft. Since EMsoft comes with energy filtering abilities we showed that it provides more accurate indexing of patterns than the commercially available software can achieve. But, more importantly, being an open software, it also give us large dataset of information from which we can learn about the physics of electron scattering.

In the resulting published paper [Pas+18b] we compare the energy distributions of the different diffraction modalities of the SEM: ECP, EBSD and TKD. While Kikuchi like lines in ECPs are the result of electrons with energies very close to the incident energy diffracting, in EBSD the relatively large interaction volume causes a spread of electron energies which in turn contributes to a blurring of the lines. On the other hand, for TKD we can predict that, in a sense, the sample thickness acts as an energy filtering mechanism. For samples thinner than the EBSD interaction volume the model predicts an increase in resolution of the Kikuchi bands which is observed experimentally.

2 Background and Basics

I often made the mistake to start talking about diffraction assuming the audience knows exactly what I mean. I'd like to rectify that here and introduce the concept and physics of *diffraction* in the SEM. I wrote this chapter as an introduction to theory the first year PhD me would have liked to have read, assuming the wisdom of today.

In this introductory chapter I will first lay out some key crystallography concepts such as the Bravais lattice (page 20), indices notations (page 24) and the reciprocal space (page 26). All these concepts will be illustrated by examples using the hexagonal lattice. In this way I can cover some basic physics concepts, introduce language and notations commonly used in this field but also evidence where some of the computations used in the later chapters come from.

Since we will make use of quantum mechanical notions such as the *wavefunction* I'll briefly lay out on page 30 what is meant by it in this document. Similarly, another useful concept used in diffraction, that of *plane waves* is outlined on page 32. I will remind the reader, on page 32, the condition for elastic coherent scattering along a set of crystal lattice planes or, more concisely, *Bragg's law*.

Next, starting with page 35, I will painstakingly go through the core algebra used in crystallography, both in the real and reciprocal space, covering notions such as the *metric tensor* and *structure matrix*. I will give examples from the hexagonal lattice to highlight the implications of these computations.

We cannot make a single dent in diffraction without a working knowledge of symmetry in crystallography, which is why I will take a few pages to explore *crystal symmetry* and *point group* analysis in Appendix C. Here I also will limit the examples to the wurtzite system to keep it relevant. On page 47, I go over the defining symmetry operation of wurtzite space group derived in this Appendix. These operations are defining the relative positions of the atoms in the unit cell and will be used in next chapter for computations of electron scattering factors.

2.1 Primer

But first things first. We need to define terms and notions that we've both seen before but maybe are not quite as within reach as they ought to be in order to comfortably embark on this journey. Better accounts of the basics covered here can be found in many textbooks [Hir+65; WC96; Rei98]. The following is only my attempt inspired in large parts by *Structure of materials: an introduction to crystallography, diffraction and symmetry* [DGM12] and *Introduction to Conventional Transmission Electron Microscopy* [DG03].

2.1.1 Crystal structure

At the atomic level many solids can be described as periodic and rigid arrangements of atoms. It is this periodicity that, as we will see, gives rise to diffraction phenomena which in turn allow us to observe and study very small features in solids. The *periodic arrangements of atoms or molecules* also constitutes the loose definition of a *crystal structure*.

The rigorous definition involves the mathematical construct of crystal *lattice* which characterises its translational symmetry. Figure 2.1 (b) shows an example of a lattice in 2D space (technically known as a *net*). Every point is identical to any other point. When the lattice is populated uniformly by the same fixed structure, or motif, we generate the periodic arrangement we mentioned previously. We show in Fig. 2.1 (a) a 4×4 square motif which, when applied to every point in the 2D lattice, generates the tessellation or regular structure in Fig. 2.1 (c)¹. If the motif is a unit cell made up of atoms or molecules then we can talk about making up a crystal structure.

2.1.2 Debye-Waller correction factor

When we say that a crystal is a rigid structure, we mean that over time the average positions of the atoms/molecules does not change. However, even at room temperature, the atoms exhibit thermal motion, small oscillations around their average “real values”. While this motion does not affect the crystal structure description (*i.e.*, we can ignore small thermal effects when describing the crystal structure), it must be taken into account when the the diffraction measurement is to be interpreted.

¹If you want to give 2D tessellation design a play here is a fun website: <http://gwydir.demon.co.uk/jo/tess/tess.htm>.

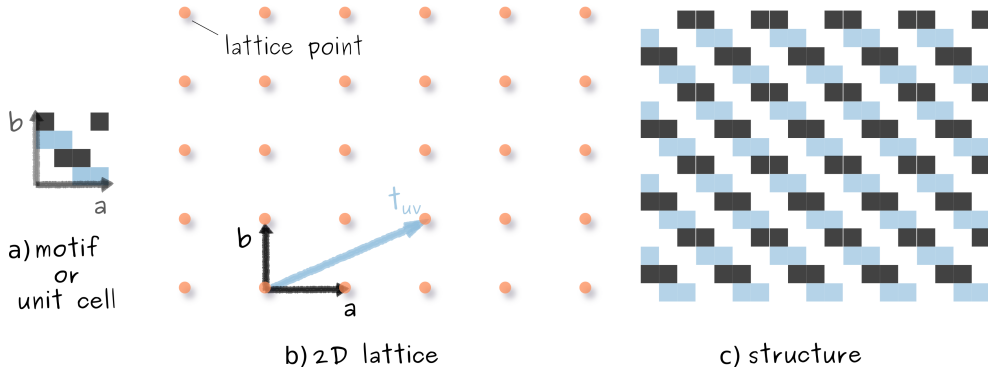


FIGURE 2.1: A periodic structure (c) showing copies of a 2D motif (a) at every lattice point on a 2D lattice. The translation vector t_{uv} moves the lattice to a position indistinguishable from the original one.

Due to these small vibrations, the electron cloud will spread over a larger space than a frozen atom would, which will reduce the electron density, and, for our purpose, will reduce or dampen the electron-electron scattering process. An adequate approximation when accounting for atomic thermal vibration is the Debye-Waller (DW) factor $B(T)$. If we assume the scattering probability for a certain set of planes is f_0 when the lattice is frozen in place, *i.e.*, at 0 K, then we can use the DW factor to correct the scattering probability f_T at temperature T :

$$f_T = f_0 e^{-B(T)s^2}, \quad \text{with} \quad s = \frac{\sin \theta_B}{\lambda} \quad (2.1)$$

where s is half of the inverse of interplanar distance d_{hkl} . We will see in the next chapter that f is commonly known as the scattering factor and how we can calculate its value. From dimensional analysis we can see that B is proportional to the mean square displacement of the atom in the direction normal to the Bragg plane. We can also read from this equation that the intensity of the diffracted beam is reduced by a factor $e^{-B(T)s^2}$ with respect to the intensity of the same beam interacting with the sample at 0 K.

A good approximation, and the one we will use here, is to assume that for close-packed structures the atomic vibration amplitude is isotropic, such that we only require one DW parameter for each element in the crystal structure. This is not a generally valid assumption, however, first principles phonon density calculations for wurtzite-type III-V semiconductors by Schowalter *et al.* [Sch+09a] showed that these materials have only small anisotropies of their Debye-Waller factors.

TABLE 2.1: Debye-Waller fitting parameters for cubic elemental crystals from [GP99] and the calculated DW values at 300K.

| Element | $a_0(\text{\AA}^2)$ | $a_1(\text{\AA}^2\text{K}^{-1})$ | $a_2(\text{\AA}^2\text{K}^{-2})$ | $a_3(\text{\AA}^2\text{K}^{-3})$ | $a_4(\text{\AA}^2\text{K}^{-4})$ | ME(%) | $B(\text{\AA}^2)$ |
|---------|---------------------|----------------------------------|----------------------------------|----------------------------------|----------------------------------|-------|-------------------|
| Al | 0.19 | 0.16e-2 | 0.25e-5 | -0.26e-8 | 0.10e-11 | 1.31 | 0.83 |
| Ga | 0.11 | 0.40e-3 | 0.66e-5 | -0.18e-7 | 0.19e-10 | 0.05 | 0.49 |
| In | 0.08 | 0.77e-2 | 0.48e-5 | -0.12e-7 | 0.11e-11 | 0.08 | 0.43 |

Gao and Peng [GP99] used a fourth degree polynomial regression fit to determine the temperature dependent DW factor for elemental cubic crystals from experimental data. These fit parameters (a_i) are shown in Table 2.1 for the metal elements Al, Ga and In together with their estimated maximum error (ME) values. The form of the polynomial fit function is shown below:

$$B(T) = a_0 + a_1 T + a_2 T^2 + a_3 T^3 + a_4 T^4$$

where the temperature is measured in Kelvin and B has units of \AA^2 .

We must note here that the assumption of isotropic vibrations is made for atoms in cubic elemental crystal. For non-cubic system we will depart from this approximation significantly. Not only this, but the measured Debye-Waller factors for defective materials will be different from that of perfect crystals since defects also scatter electrons. For this reason and the fact that first principles calculations can only be trusted if they predict experimental values, it is always a good rule to use experimental values wherever possible.

This being said, the literature on DW factors for nitrogen is limited and we must turn to theoretical predictions. Schowalter *et al.* [Sch+09a] calculated these values for a number of wurtzite structures. We show below, in Table 2.2, the values predicted for the DW factor of N in AlN, GaN and InN².

The Debye-Waller factor of an element, $B(\text{el.})$, is related to the electron static correlation function, $\langle u_\alpha(\text{el.}) \rangle$, which is the average displacement of an atom of el. in the direction α by:

$$B(\text{el.}) = \frac{8\pi^2}{3} (2 \langle u_{11}^2(\text{el.}) \rangle + \langle u_{33}^2(\text{el.}) \rangle).$$

² We will see later, that since N scatters electrons significantly less than the heavier metallic elements in the system, its DW factors will not carry great importance. However, we did include the computations here for completeness.

TABLE 2.2: Static correction functions for N in wurtzite materials from DFT LDA calculations [Sch+09a] at 300K and the predicted DW factor.

| N in Material | $\langle u_{11}^2(N) \rangle (\text{\AA}^2)$ | $\langle u_{33}^2(N) \rangle (\text{\AA}^2)$ | B(\AA^2) |
|---------------|--|--|---------------------|
| AlN | 0.0036 | 0.0034 | 0.28 |
| GaN | 0.0039 | 0.0037 | 0.29 |
| InN | 0.0065 | 0.0062 | 0.51 |

The computations that generated the values in the tables in this section can be conveniently found in the Jupyter Notebook titled `Debye-Waller.ipynb`.

2.1.3 *hP* Bravais lattice and the hexagonal crystal system

There are as many lattices as there are possible regular arrangements of lattice points and there are as many possible arrangements as variety of crystal forms observed in nature. In the example above we placed the motifs such that its four corners coincide with four lattice points. In this case the motif maps exactly to one lattice point. In 3D space, we would have had the option to map a 3D motif on one, two or three lattice points, defining lattices known as primitive (*P*), either body-centred (*I*) or base-centred (*C*), and face-centred (*F*), respectively. It is also easy to see that a motif with a very different shape will need a different arrangement of lattice points in order to cover the entire space neatly with no gaps or overlaps. We need, therefore, to unambiguously define both the lattice arrangement and the motif that define a crystal structure.

A specific arrangement of lattice points displays a unique translational symmetry which, in turn, can be characterised by a set of *basis vectors* usually denoted $\mathbf{a}, \mathbf{b}, \mathbf{c}$ for a 3D lattice. Fig. 2.1 (b) shows the two basis vectors \mathbf{a}, \mathbf{b} of the 2D lattice we used. We can think of them as having their origin in one of the corners of the motif structure and running along its edges. Together with the angle between them, the basis vectors can be used to define both the shape of the motif and lattice it can tessellate. We commonly define a unique 3D lattice by its lattice parameters $\{a, b, c, \alpha, \beta, \gamma\}$ where a, b, c are the lengths of the vectors $\mathbf{a}, \mathbf{b}, \mathbf{c}$, α is the angle between \mathbf{b} and \mathbf{c} , β is the angle between \mathbf{a} and \mathbf{c} and γ is the angle between \mathbf{a} and \mathbf{b} , respectively.

The volume described by the lattice parameters is known as the *unit cell* of the lattice. While, for any given lattice, we can always find a *primitive* unit cell, whose volume contains only one lattice point, in practice working with a high symmetry cell which reflects the point group symmetry of the crystal structure is preferred. We

will talk more about point and translation symmetry as applied to crystallographic symmetry in Appendix C on page 167.

We can now also identify the position of any point on the lattice with the help of the basis vectors. Let us introduce the *translation vector*, defined as the distance between any two points on the lattice. We can write it as $\mathbf{t}_{uv} = u\mathbf{a} + v\mathbf{b}$ in 2D (shown in Fig. 2.1 (b)), and $\mathbf{t}_{uvw} = u\mathbf{a} + v\mathbf{b} + w\mathbf{c}$ in 3D, where u, v, w are integers. Every point on an infinite lattice is equivalent to any other point, such that if one would be to move the structure by \mathbf{t}_{uv} while we weren't looking, we would not be able to tell anything had changed when we looked back. This means that all lattice points are identical and we can choose any of them as the origin. Such that, the position of any lattice point is an integer linear combination of basis vectors independent on the chosen origin.

If the lattice parameter values are chosen with no restriction, the resulting lattice has low symmetry. Conversely, let us select a 2D lattice with the two basis vectors equal in length, $|\mathbf{a}_1| = |\mathbf{a}_2| = a^3$, and the angle γ between them of 120° , as shown in Fig. 2.2. It is easy to notice that rotating this lattice by 60° around a lattice point picked as origin would produce the same lattice. Another way of saying this is that the lattice is invariant under a $2\pi/6$ rotation and by definition *hexagonal*. Notably, we could have chosen γ to be 60° and we would have ended up with the exact same lattice.

For every lattice with unique symmetry to be decorated with atoms, we talk about a specific *crystal system*. We've seen that the hexagonal 2D crystal system can be described in at least two ways. Similarly, we can construct a $2\pi/6$ rotation invariant lattice in 3D by selecting the following special values for the lattice parameters: $|\mathbf{a}| = |\mathbf{b}|$, $\alpha = \beta = 90^\circ$ and $\gamma = 120^\circ$ as shown in Fig. 2.3 (a). Here all we did was to add a \mathbf{c} axis normal to the 2D hexagonal lattice and set it as the rotation axis. This is easy to

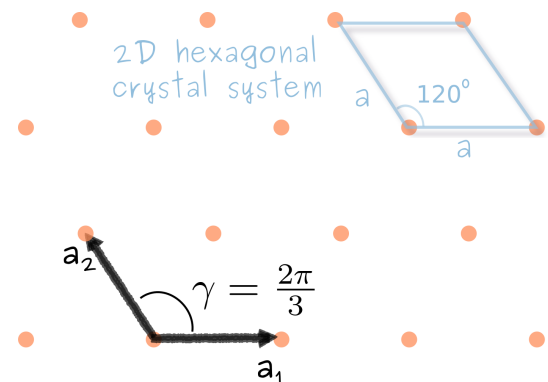


FIGURE 2.2: Hexagonal 2D lattice with basis vectors $\{\mathbf{a}_1, \mathbf{a}_2, \mathbf{c}\}$. The lattice parameters can be chosen to be $\{a, a, 2\pi/3\}$ or $\{a, a, \pi/3\}$.

³ A note about notation consistency. The general basis vectors of a lattice are $\{\mathbf{a}, \mathbf{b}, \mathbf{c}\}$. Whenever two or more vectors have the same magnitude we use the same letter and employ indices to differentiate between them such that the hexagonal lattice basis vectors are $\{\mathbf{a}_1, \mathbf{a}_2, \mathbf{c}\}$.

see when comparing the 2D and 3D hexagonal crystal system.

We defined our unit cell as having the edges at lattice points but we did not yet specified which lattice points. It is convenient to opt for a unit cell that is simple and describes the point symmetry of the underlying lattice. It is also useful to work with a small volume and, in practice, the smallest cell that reflects the full symmetry of the system is used. When the unit cell is small enough such that it only contains one full lattice point, *i.e.*, primitive cell, it is denoted by P as we have done in the choice of hexagonal unit cell shown in Fig. 2.3 (b) where h stands for hexagonal. Otherwise, the choice of unit cell is somewhat arbitrary, so much so that the Wigner-Seitz cell, which is centred on a lattice point and defined as the region of space closer to that lattice point than any other one, does not have edges aligned with lattice points.

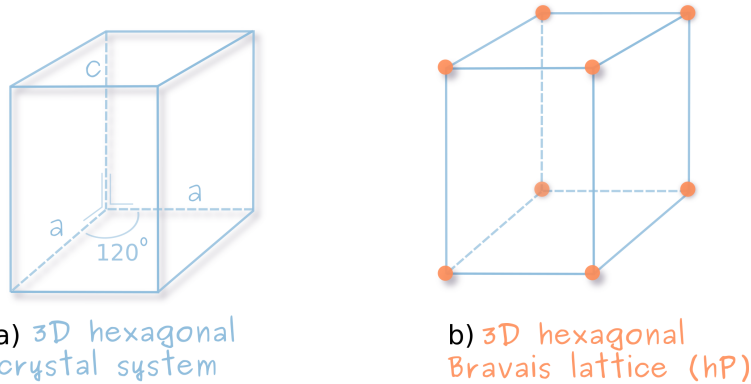


FIGURE 2.3: 3D hexagonal crystal system with lattice parameters $\{a, a, c, 90^\circ, 90^\circ, 120^\circ\}$ (a) and the 3D hexagonal primitive lattice (b).

The same crystal system can be populated with lattice points in different manners such that it ends up describing different lattices. However, the number of choices of unique lattice points arrangements is limited to 5 for 2D lattices and 14 for 3D lattices. These unique lattice generators are known as *Bravais*. The cubic crystal system (c), for instance, can be populated by a different number of lattice points: one to form the primitive cubic Bravais lattice (cP), two in the body centred lattice (cI)⁴ or three for the face centred one (cF). The hexagonal Bravais lattice (h) comes only in one type: primitive (hP), as shown in Fig. 2.3 (b).

We can also write out now, from geometry, the volume of a primitive hexagonal lattice Ω_{hex} which will become useful later:

$$\Omega_{hex} = a^2 \sin 60^\circ c \quad (2.2)$$

⁴ The label I comes from the German word for body centred *Innenzentriert*. See ref. [DW+85] for more information on lattice labels nomenclature.

With the notion of a hexagonal crystal system and its cell parameters well laid out, in the following section we will look at how we commonly label a certain plane or direction in this system.

2.1.4 Lattice planes and directions in the hexagonal system

There are in fact two ways we can refer to a given plane or direction in a hexagonal crystal. The usual, or *Miller* notation which applies to all the crystal systems, or the hexagonal symmetry friendly *Miller-Bravais* indexing method. The first is defined by three indices while the latter by four. For planes indexing, going from the four index notation to the three index one means dropping the redundant third index. However, for directions notations things are slightly more involved.

Miller indices

Miller wrote and taught extensively about a way to label crystal planes in terms of their intercepts with the crystal reference axes. It was because of this and his choice of h, k, l letters that the indexing method now bears his name: *Miller indexing*. The method is beautiful in its simplicity: find the intercept with the three basis vectors, invert the intercepts, and last but not least reduce to smallest relative primes. One can also obtain all the equivalent planes belonging to the same family by even permutations of the indices h, k, l . For the hexagonal system the $(h k l)$ indices correspond to the $\{\mathbf{a}_1, \mathbf{a}_2, \mathbf{c}\}$ basis vectors.

For directions, usually labelled $[u v w]$, the process is simpler; find the coordinates in the crystal frame of the vector pointing in that direction and reduce them to smallest relative primes. It is this latter step which prompts us to raise an important observation. The Miller notation for direction does not carry vector length information and should not be used for finding length information. This might sound obvious, yet the temptation to understand direction $[u v w]$ as vector \mathbf{t}_{uvw} is significant. The difference between the two becomes more apparent in the hexagonal system.

While the Miller indices notation is tremendously helpful when looking at families of planes in a cubic system, its powers become limited when tackling lower crystal symmetry. For instance in a system with lower than cubic symmetry, the family of planes for a given $(h k l)$ plane is no longer made up of *all* possible permutations of the Miller indices h, k and l .

Miller-Bravais indices

The hexagonal system indexing is a very different story. Usually treated as a special case in itself, the hexagonal system can keep the permutation equivalence property of Miller indexes as long as an extra, redundant basis vector is added. The new set of basis vectors, $\{\mathbf{A}_1, \mathbf{A}_2, \mathbf{A}_3, \mathbf{C}\}$, introduces 4-dimensional type vectors [Fra65] in what is called *Miller-Bravais indexing* [Nic66]. This notation replaces the rhombic prism primitive unit cell with a hexagonal one made up of three primitive hexagonal Bravais lattices (hP), as seen in Fig. 2.4. We show here the three-vectors basis set together with the four-vector one.

Three of the Miller-Bravais basis vectors are the Miller basis vectors: $\mathbf{A}_1 = \mathbf{a}_1$, $\mathbf{A}_2 = \mathbf{a}_2$ and $\mathbf{C} = \mathbf{c}$. The extra basis vector is co-planar with the first two and, therefore, linearly dependent on them:

$$\mathbf{A}_3 = -(\mathbf{a}_1 + \mathbf{a}_2) = -(\mathbf{A}_1 + \mathbf{A}_2). \quad (2.3)$$

A vector \mathbf{p} in this system is defined as $\mathbf{p} = p_1\mathbf{A}_1 + p_2\mathbf{A}_2 + p'\mathbf{A}_3 + p_3\mathbf{C}$. When coordinates $\{p_1, p_2, p_3, p'\}$ are integers, \mathbf{p} becomes the translation vector \mathbf{t} which shows a common direction in the crystal system. If we take this a step further and reduce the coordinates to relative primes then we obtain the reduced vector \mathbf{t}_{uvtw} where indices u, v, t, w form the Miller-Bravais notation.

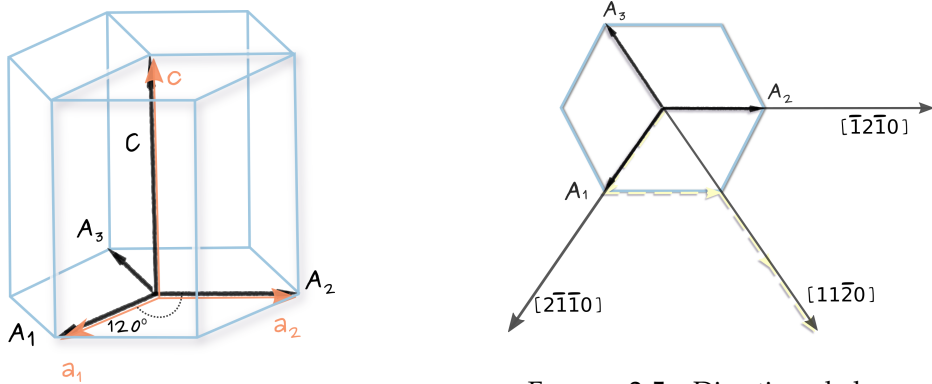


FIGURE 2.4: Hexagonal prism unit cell and the Miller-Bravais basis vectors $\{\mathbf{A}_1, \mathbf{A}_2, \mathbf{A}_3, \mathbf{C}\}$.

FIGURE 2.5: Directions belonging to the $\langle 2\bar{1}\bar{1}0 \rangle$ family. The yellow line shows the formation of the vector $\mathbf{t}_{[11\bar{2}0]}$.

Directions in the four-index notations are of the form $u\mathbf{A}_1 + v\mathbf{A}_2 + t\mathbf{A}_3 + w\mathbf{C}$ and written as $[u\ v\ t\ w]$, where $u, v, t, w \in \mathbb{Z}$ and are relative primes. Comparing this expression to the same direction written with the three Miller basis vectors, $U\mathbf{a} + V\mathbf{b} + W\mathbf{c}$, yields the following true relations:

$$U = 2u + v, \quad V = 2v + u, \quad W = w, \quad (2.4)$$

and also

$$t = -(u + v).$$

Because the first three basis vectors are not linearly independent, writing out their Miller-Bravais indices is somewhat awkward as seen in Fig. 2.5. The three co-planar vectors ensure that any given direction will have at least two non-zero components, and the \mathbf{A}_i basis vectors themselves have three non-zero components. While the Miller direction vectors corresponding to the basis vectors directions have the same lengths as the basis vectors themselves, this is not the case in the Miller-Bravais notation, see vector $\mathbf{t}_{[11\bar{2}0]}$. Nevertheless, we can find families of directions through the usual permutations which would not be possible using the Miller notation as we can see from Table 2.3.

TABLE 2.3: Some common directions in hexagonal system given in Miller and Miller-Bravais notation.

| Family | Miller-Bravais | Miller | Family | Miller-Bravais | Miller |
|------------------------------------|-----------------------|----------------|------------------------------------|-----------------------|----------------------|
| | [2 $\bar{1}\bar{1}0]$ | [100] | | (cont...) | |
| $\langle 2\bar{1}\bar{1}0 \rangle$ | [11 $\bar{2}0]$ | [110] | $\langle 2\bar{1}\bar{1}0 \rangle$ | [$\bar{1}\bar{1}20]$ | [$\bar{1}\bar{1}0]$ |
| | [$\bar{1}2\bar{1}0]$ | [010] | | [1 $\bar{2}10]$ | [010] |
| | [$\bar{2}110]$ | [$\bar{1}00]$ | $\langle 0001 \rangle$ | [0001] | [001] |

A plane description in the new basis set will be of the form $(h k i l)$ where i can be found from $i = -(h + k)$ and, bearing no unique information, can be omitted from the notation: $(h k .l)$. A family of planes is then given by the permutations of the first three Miller-Bravais indices including their negative values:

$$\{h k i l\} = \{(h k i l), (i h k l), (k i h l) (\bar{h} \bar{k} \bar{i} l), (\bar{i} \bar{h} \bar{k} l), (\bar{k} \bar{i} \bar{h} l)\}.$$

Table 2.4 shows a list of commonly used families of planes in a hexagonal system. A graphical representation of these planes is shown in Fig. 2.6. The Miller indices are counter-intuitive in this system and often the Miller-Bravais notation is preferred. We also mention the polarity of each family of planes but we will postpone the explanation of polarity for the point group discussion on page 178.

TABLE 2.4: Common planes in hexagonal system given in Miller and Miller-Bravais notation.

| Family | Miller-Bravais | Miller | Family | Miller-Bravais | Miller |
|--------------------------------------|----------------|--------|---------------------------------------|----------------|--------|
| <i>m-plane</i> <i>(non-polar)</i> | (1̄100) | (1̄10) | <i>a-plane</i> <i>(non-polar)</i> | (01̄10) | (010) |
| | (1̄010) | (1̄00) | | (1̄100) | (1̄10) |
| | (1̄100) | (1̄10) | | (01̄10) | (010) |
| | (01̄10) | (01̄0) | | (10̄10) | (100) |
| | (10̄10) | (100) | <i>r-plane</i> <i>(semi-polar)</i> | (11̄20) | (110) |
| | (12̄10) | (120) | | (12̄10) | (120) |
| <i>a-plane</i> <i>(non-polar)</i> | (2̄110) | (2̄10) | | (1̄120) | (1̄12) |
| | (1̄120) | (1̄10) | | (01̄12) | (012) |
| | | | <i>c-plane (polar)</i> | (10̄12) | (102) |
| | | | | (1102) | (112) |
| | | | | (01̄12) | (012) |
| | | | | (1012) | (102) |
| | | | <i>c-plane (polar)</i> | (0001) | (001) |

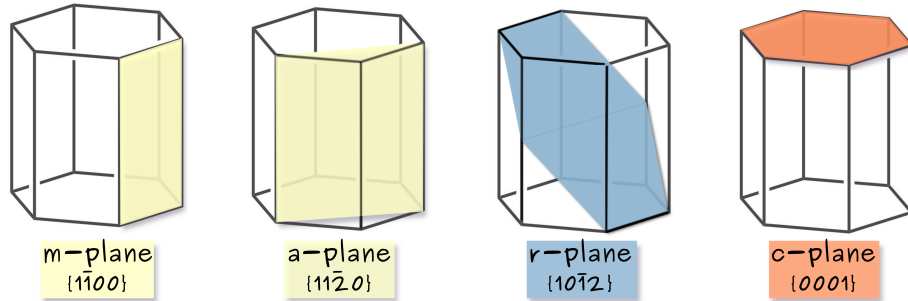


FIGURE 2.6: Common planes in hexagonal crystal structures.

We can also expand the *zone axis* definition, which tells us what $(h k l)$ planes belong to direction or zone, $[u v w]$, given in Miller indices as $hu + kv + lw = 0$ to the Miller-Bravais notation:

$$hu + kv + it + lw = 0 \quad (2.5)$$

2.1.5 The reciprocal space

We have all the Bravais lattice basis set mathematical framework of dealing with vectorial quantities in a crystal frame and yet we had to introduce Miller and Miller-Bravais indices which don't really fit in this vector space. This leads us to why crystallographers like to employ a very different vector space to ease computations, namely

the *reciprocal space*. So then, any vectorial quantities in a crystal (*i.e.*, position, direction, strain) can be defined in real space in terms of the basis vectors of its Bravais lattice, $\{\mathbf{a}, \mathbf{b}, \mathbf{c}\}$, or, conversely, in the reciprocal space in terms of a new set of basis vectors defined such that the components of a direction vector are the Miller indices, $(h k l)$, of the plane normal to that vector, $\{\mathbf{a}^*, \mathbf{b}^*, \mathbf{c}^*\}$. To be on the safe side we usually denote vectors defined in the reciprocal space with \mathbf{g} and the translation vector in reciprocal space by \mathbf{g}_{hkl} :

$$\mathbf{g}_{hkl} = h\mathbf{a}^* + k\mathbf{b}^* + l\mathbf{c}^*, \quad (2.6)$$

$$\text{where it must be true that: } \mathbf{a}^* = \frac{\mathbf{b} \times \mathbf{c}}{\Omega}, \quad \mathbf{b}^* = \frac{\mathbf{c} \times \mathbf{a}}{\Omega}, \quad \mathbf{c}^* = \frac{\mathbf{a} \times \mathbf{b}}{\Omega}. \quad (2.7)$$

with Ω being the volume of the unit cell, $\Omega = \mathbf{a} \cdot (\mathbf{b} \times \mathbf{c})$. Note, that both the dot and the cross products here must be generalised to non-Cartesian crystal frames and I show how to do that in next section, Section 2.2 on page 35.

A few observations can be made straight away at this point:

- From dimensional analysis we can tell that the length of a reciprocal space vector, $|\mathbf{g}|$, will be measured in units of $\langle \text{length}^{-1} \rangle$.
- The reciprocal lattice parameters are going to be $\{a^*, b^*, c^*, \alpha, \beta, \gamma\}$ with the same angle definition as before.
- The dot product of a real space basis vector with its reciprocal space basis vector will yield zeros except for: $\mathbf{a} \cdot \mathbf{a}^* = \mathbf{b} \cdot \mathbf{b}^* = \mathbf{c} \cdot \mathbf{c}^* = 1$ or:

$$\mathbf{a}_i \cdot \mathbf{a}_j^* = \delta_{ij} \quad (2.8)$$

A less intuitive observation on this different perspective of the crystal space leads to some upside-down-world-like properties. If we consider a distance vector with components known in relation to a real space basis set, and want to transform it to another real space basis with basis vectors smaller in magnitude, in order to keep the magnitude of the vector we must increase its components values. This property of some vector to counter-vary the change in basis with an inverse change in their components we call *contravariance*. If for the same vector which tells a distance in real space, we do the same exercise in reciprocal space, we find that that a decrease of

the basis set gives smaller vector components. This vector behaviour is called *covariance*. The fact that the same vector can have opposite properties in these two different vector spaces tells us that the spaces themselves are reciprocal to each other.

You're welcome reader, you're now almost a crystallographer. The missing bit of information for being a full-fledged one is the Bragg diffraction condition which will be discussed on page 32. It is because the Bragg's diffraction condition depends on the lattice plane orientation with respect to the incident beam and the distance between the set of planes under scrutiny, that having an easy way of finding the normal to a plane (hkl) in the reciprocal space vector \mathbf{g}_{hkl} becomes valuable in crystallography. Not least due to the vector \mathbf{g}_{hkl} property of having its length equal to the inverse of the distance between the set of planes $\{hkl\}$:

$$d_{hkl} = \frac{1}{|\mathbf{g}_{hkl}|}. \quad (2.9)$$

The reciprocal hexagonal lattice

I will have to just state for now the form of reciprocal basis vectors for the hexagonal lattice. We will suspend the disbelief until page 41 of *Crystallographic Computations* sections, where I show how one could get the general form of the cross product. Let us then assume that we can find the reciprocal lattice vectors $\{\mathbf{a}_1^*, \mathbf{a}_2^*, \mathbf{c}^*\}$ to be in terms of the real space hexagonal lattice basis set, $\{\mathbf{a}_1, \mathbf{a}_2, \mathbf{c}\}$ to be:

$$\mathbf{a}_1^* = \frac{4}{3a^2} \mathbf{a}_1 + \frac{2}{3a^2} \mathbf{a}_2, \quad \mathbf{a}_2^* = \frac{2}{3a^2} \mathbf{a}_1 + \frac{4}{3a^2} \mathbf{a}_2, \quad \mathbf{c}^* = \frac{1}{c^2} \mathbf{c}. \quad (2.10)$$

Where the reciprocal hexagonal lattice translational vector is, from Eq. 2.6:

$${}^{hex} \mathbf{g}_{hkl} = h\mathbf{a}_1^* + k\mathbf{a}_2^* + l\mathbf{c}^*. \quad (2.11)$$

Another noteworthy property of the reciprocal space is that the reciprocal crystal lattice must also be one of the 14 Bravais lattices. We have already seen in the discussion of Fig. 2.2 that the hexagonal lattice can be mapped by two lattice parameters sets. It turns out that the reciprocal hexagonal lattice has the same symmetry as the real space hexagonal lattice mapped by the other set of lattice parameters. Fig. 2.7 (a) shows the reciprocal 2D lattice with parameters $\{a^*, a^*, 60^\circ\}$ which is comparable to Fig. 2.2. The 3D reciprocal hexagonal system is the same hexagonal prism as in the real space with the lattice parameters $\{a^*, a^*, c^*, 60^\circ, 90^\circ, 90^\circ\}$ as can be seen in Fig. 2.7 (b).

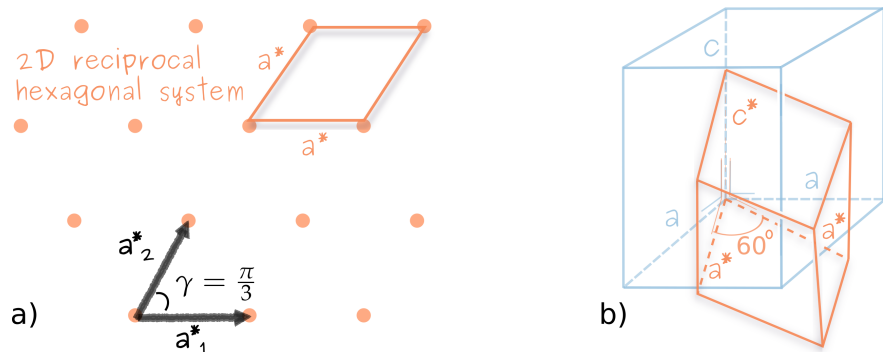


FIGURE 2.7: Reciprocal 2D hexagonal lattice with basis vectors $\{a_1^*, a_2^*\}$ and lattice parameters $\{a^*, a^*, 60^\circ\}$ (a) and the 3D reciprocal hexagonal crystal system with lattice parameters $\{a^*, a^*, c^*, 60^\circ, 90^\circ, 90^\circ\}$ overlaid on the real space one while keeping the same origin (b).

The first two vectors in both the real and reciprocal hexagonal system basis sets, $\{a_1, a_2\}$ and $\{a_1^*, a_2^*\}$, respectively, do not align with each other as Fig. 2.7 indicates and Fig. 2.8 emphasises. This is the case for the 3-index notation. When the fourth index is added to form the reciprocal basis set $\{A_1^*, A_2^*, A_3^*, C^*\}$ defining a lattice with parameters $\{A^*, A^*, A^*, C^*, 120^\circ, 120^\circ, 120^\circ, 90^\circ, 90^\circ, 90^\circ\}$ things get even more confusing. While the Miller-Bravais real and reciprocal co-planar hexagonal basis vectors, $\{A_i\}$ and $\{A_i^*\}$, are parallel to each other, the two reciprocal basis sets, $\{a_i^*\}$ and $\{A_i^*\}$, are not. Figure 2.8 should make that somewhat more clear.

The four reciprocal basis vectors can be found in terms of the four real space basis vector to be:

$$\begin{aligned} A_1^* &= \frac{2}{3a^2} a_1, & A_2^* &= \frac{2}{3a^2} a_2 \\ A_3^* &= \frac{2}{3a^2} a_3, & C^* &= \frac{1}{c^2} c. \end{aligned} \quad (2.12)$$

Where the four index reciprocal space translation vector is:

$${}^{hex}g_{hkl} = hA_1^* + kA_2^* + iA_3^* + lC^* = {}^{hex}g_{hkl}.$$

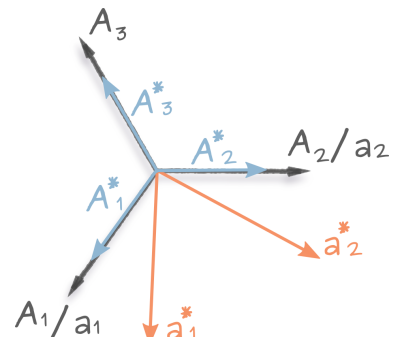


FIGURE 2.8: Relationship between real and reciprocal space hexagonal system basis sets.

The crystallographer must always be extra careful if using both notations. The two reciprocal basis vectors notations are not even describing exactly the same lattice. A

closer inspection of Eq. 2.10 and Eq. 2.12, tells us that the four-index reciprocal lattice is three times more dense than the three-index reciprocal one. Nevertheless, all the discussion about Miller-Bravais index notation still hold, *i.e.*, Eq. 2.3 is still valid, and the reciprocal space properties, including Eq. 2.8, still apply.

We will explore, in more depth, crystallographic computations in the hexagonal system, both in the real and the reciprocal space in Section 2.2 on page 35.

2.1.6 Wavefunctions and physical observables

In the language of quantum mechanics, physical quantities are described via operators. The allowed values of the physical quantities are then eigenvalues of these operators. One must find the eigenfunctions of the corresponding operator in order to compute the value of a certain physical observable (*i.e.*, one must solve the equation $\hat{f} |\Psi\rangle = f |\Psi\rangle$).

For a free particle the momentum operator is $\hat{p} = i\hbar\nabla$ where \hbar is the reduced Planck's constant ($\hbar = h/2\pi$). The eigenvalues \mathbf{p} and eigenfunctions $|\Psi\rangle$ of the momentum operator are defined by the equation:

$$-i\hbar\nabla |\Psi\rangle = \mathbf{p} |\Psi\rangle .$$

Which has solutions of the form:

$$\Psi(\mathbf{r}) = C e^{\frac{i}{\hbar} \mathbf{p} \cdot \mathbf{r}},$$

where C is a normalisation constant. We can now use Louis de Broglie's relationship to relate momentum p of a particle to a wavelength λ : $\lambda = h/p$. If the wave number k is introduced, $k = 1/\lambda$, then we can write in vector form $\mathbf{p} = \hbar\mathbf{k}$.⁵ Using this we can rewrite the wave function of a particle as a linear superposition of momentum eigenfunctions:

$$\Psi(\mathbf{r}) = \sum_{\mathbf{k}} \psi_{\mathbf{k}} e^{2\pi i \mathbf{k} \cdot \mathbf{r}}, \quad (2.13)$$

where the C has been absorbed into the coefficients $\psi_{\mathbf{k}}$.

We will see in the next chapter that this expansion of the wave function in terms of plane waves makes the foundation of electron diffraction modelling.

⁵ It is a consequence of the de Broglie formula that the momentum space is equivalent to the reciprocal space, apart from a scaling factor \hbar .

2.1.7 Plane waves

Let us explore further the equation 2.13 above where \mathbf{k} is the wave vector denoting the direction of travel of the wave and \mathbf{r} is the position vector a point P (see Fig. 2.9). Applying dimensional analysis for the exponent, one can show that, if the position vector \mathbf{r} has components $\{r_1, r_2, r_3\}$ with respect to the real space basis vectors $\{\mathbf{a}, \mathbf{b}, \mathbf{c}\}$:

$$\mathbf{r} = r_1 \mathbf{a} + r_2 \mathbf{b} + r_3 \mathbf{c},$$

then the components of the wave vector \mathbf{k} must be given with respect to the reciprocal basis vectors and, therefore, \mathbf{k} must be a reciprocal space vector:

$$\mathbf{k} = k_1 \mathbf{a}^* + k_2 \mathbf{b}^* + k_3 \mathbf{c}^*.$$

We will use this opportunity to quickly introduce a useful shorthand notation that allows crystallographers to be economic with their symbols. For this we have to slightly adjust the basis vector notation⁶:

$$\mathbf{r} = r_1 \mathbf{a}_1 + r_2 \mathbf{a}_2 + r_3 \mathbf{a}_3 = \sum_{i=1}^3 r_i \mathbf{a}_i \equiv r_i \mathbf{a}_i$$

Since most of crystallography happens in 3D space we will always assume that the sum goes from $i = 1$ to $i = 3$ even when the limits are not written and the sum symbol, \sum , is dropped altogether. This is known as the *Einstein summation convention* and its rule is that summation is implied over every pair of subscripts which appears on the same side of the equation. Using the Einstein summation convention the dot product $\mathbf{k} \cdot \mathbf{r}$ can be written as:

$$\mathbf{k} \cdot \mathbf{r} = (k_i \mathbf{a}_i^*) \cdot (r_i \mathbf{a}_i) = k_i r_j \delta_{ij} = k_i r_i,$$

where we made use of the definition of the reciprocal lattice: $\mathbf{a}_i \cdot \mathbf{a}_j^* = \delta_{ij}$.

⁶ Another note on basis vector notation. Unfortunately, the letter \mathbf{a} is overused in crystallography and can bear different meanings. Here we are using \mathbf{a}_i to denote one component from a generic basis set in which all vectors are labelled with the same symbol but different subscripts. Real space basis in this notation is $\{\mathbf{a}_i, i \in (1, 2, 3)\}$ and reciprocal space basis vectors are $\{\mathbf{a}_i^*, i \in (1, 2, 3)\}$.

If we now ask the question of where in the real space is the wave going to have constant phase we can easily spot the required condition to be:

$$\mathbf{k} \cdot \mathbf{r} = k_1 r_1 + k_2 r_2 + k_3 r_3 = \text{const.},$$

$$\forall \mathbf{r} = r_1 \mathbf{a}_1 + r_2 \mathbf{a}_2 + r_3 \mathbf{a}_3$$

Which looks a lot like the equation of a plane:

$$\mathbf{k}(\mathbf{r} - \mathbf{r}_0) = 0$$

where \mathbf{r}_0 is the position vector of the origin of the wave vector \mathbf{k} as shown in the figure to the right. The distance between consecutive planes with same phase will be given by $\lambda = 1/|\mathbf{k}|$.

We can then say that the totality of points with the same phase form an infinite plane in the real space. Another way to say this is that the particle wave will exhibit in the real space planar surfaces of same phase, oriented normal to the travelling direction $\hat{\mathbf{k}}$. Hence the name of *plane waves* which we will use from now on to refer to expressions of the form:

$$e^{2\pi i \mathbf{k} \cdot \mathbf{r}} \quad (2.14)$$

2.1.8 Bragg's law in real space

Consider the drawing in Fig. 2.10. A plane wave of wavelength λ and wave vector \mathbf{k} is incident with incidence angle θ on a set of parallel plane with Miller indices (hkl) . The planes are partially transparent and partially reflective, such that the reflected beam together with the incident one and the normal vector to the planes are co-planar. We ask the question: “What is the condition that two reflected plane waves (1) and (2) will be in phase?”.

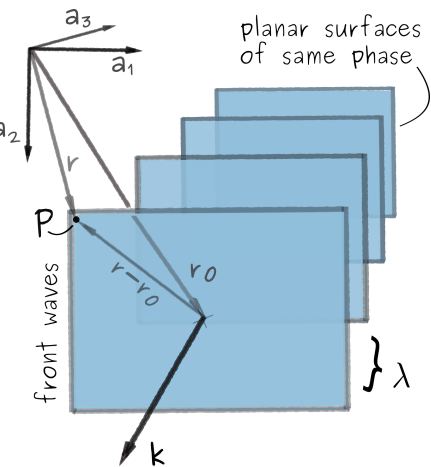


FIGURE 2.9: Schematic drawing of plane waves and the vectors considered in this section.

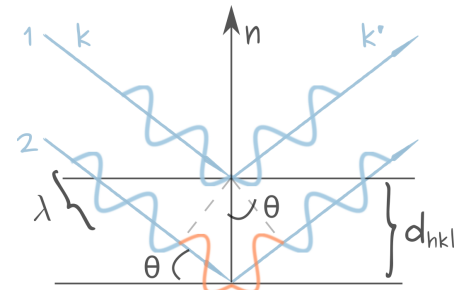


FIGURE 2.10: Geometrical representation of Bragg's equation in real space. The path difference of the reflected plane wave (2) with respect to (1) is shown in orange.

The answer is straightforward. The path difference between waves (1) and (2), shown in orange, must equal an integer number of wavelengths [BB13]:

$$2d_{hkl} \sin \theta = n\lambda.$$

Do note that Fig. 2.10 is a planar section of the diffraction geometry. The diffracted beam \mathbf{k}' will travel in a direction contained by a conical surface of opening angle $\pi/2 - \theta$ centred around the plane normal. For every plane (hkl) in a crystal there will be a conical surface of diffracted beams, with parameters determined by the inter-planar spacing d_{hkl} and the radiation wavelength λ .

In common practice we will only consider first order diffraction; instead of talking about n order diffraction from planes (hkl) we will talk about first order diffraction from planes $(nk\bar{nh}nl)$. The reader will recall that the planes with Miller indices $(nk\bar{nh}nl)$ are parallel to the planes (hkl) but with an inter-planar spacing given by $d_{nhnkl} = d_{hkl}/n$. The version of Bragg law used in diffraction is then:

$$2d_{hkl} \sin \theta_B = \lambda. \quad (2.15)$$

The angle θ for which constructive interference occurs is known as *Bragg angle*, θ_B . Table 2.5 shows the Bragg angles for 20 keV electrons diffracting from common wurtzite crystal planes (shown in Fig. 2.9). Recall that the formula for inter-planar spacing in hexagonal unit cells is given in Eq. 2.30.

TABLE 2.5: Bragg angles for the most common planes in wurtzite materials for 20 keV incident electrons.

| planes | (hkl) | d_{hkl} | $AlN\theta_B$ | $GaN\theta_B$ | $InN\theta_B$ |
|---------|-------|---------------|---------------|---------------|---------------|
| m-plane | (100) | $\sqrt{3}a/2$ | 2.74° | 2.67° | 2.42° |
| c-plane | (001) | c | 0.49° | 0.47° | 0.43° |
| a-plane | (110) | $a/2$ | 1.58° | 1.54° | 1.39° |

Note that while the Bragg equation describes the geometric condition for diffraction as constructive interference to occur, it does not, however, provide any information on the intensity (if any) of the diffracted beam. The real space form of this equation is only useful in determining the Bragg angles for a given wavelength and crystal structure as we have done here. More useful is the study of the direction of the diffracted beam for a given crystal structure which requires the expression of some reference frame. In order to tackle this problem, it is common to express the Bragg

equation to the reciprocal reference frame and introduce the Ewald sphere, as we will do in the next section.

2.1.9 Fourier analysis

We have introduced the notions of crystal lattice and talked about its translational invariance under a translation vector $\mathbf{t} = u\mathbf{e}_1 + v\mathbf{e}_2 + w\mathbf{e}_3$ where u, v, w are constants. We have also introduced the reciprocal space and that of plane waves. What is left is to tie everything together through the introduction of Fourier transform which in turn will lead us to the mathematical formulation of diffraction.

Considering the wave function description of a particle as a superposition of momentum eigenfunctions described by vector \mathbf{k} , we now want to ask the question: “*What is the relative contribution of a specific wave vector to the total function $\Psi(\mathbf{r})$?*”. This is a very similar question to “*What is the contribution of the basis vector \mathbf{e}_1 to a given vector $\mathbf{t} = u\mathbf{e}_1 + v\mathbf{e}_2 + w\mathbf{e}_3$?*”. We know the answer to that to be u ; easily derived from the dot product $\mathbf{t} \cdot \mathbf{e}_1$. Similarly, we can use the dot product for continuous functions of the plane wave form $\Phi = e^{2\pi i \mathbf{k} \cdot \mathbf{r}}$ and $\Phi' = e^{2\pi i \mathbf{k}' \cdot \mathbf{r}}$. In the bra-ket notation this is defined as:

$$\langle e^{2\pi i \mathbf{k} \cdot \mathbf{r}} | e^{2\pi i \mathbf{k}' \cdot \mathbf{r}} \rangle = \iiint e^{2\pi i (\mathbf{k}' - \mathbf{k}) \cdot \mathbf{r}} d\mathbf{r} = \delta(\mathbf{k}' - \mathbf{k})$$

where the integral is over all 3D space. The delta function form underlines the fact that Φ and Φ' are orthogonal functions whenever $\mathbf{k}' \neq \mathbf{k}$ leading to the scalar product of plane wave functions to be zero.

Then, the contribution of a wave vector \mathbf{k} to the wave function $\Psi(\mathbf{r})$ is the projection of the wave function on the momentum eigenfunction corresponding to \mathbf{k} . This also happens to be the definition of the *direct Fourier transform*:

$$\Psi(\mathbf{k}) = \langle e^{2\pi i \mathbf{k} \cdot \mathbf{r}} | \Psi(\mathbf{r}) \rangle = \iiint \Psi(\mathbf{r}) e^{-2\pi i \mathbf{k} \cdot \mathbf{r}} d\mathbf{r} \equiv \mathcal{F}[\Psi(\mathbf{r})] \quad (2.16)$$

The Fourier Transform \mathcal{F} allows us to transform a wave function from the real space, $\Psi(\mathbf{r})$, to the momentum space, $\Psi(\mathbf{k})$, by using the equation above.⁷ The reciprocal relationship is defined by the *inverse Fourier transform*:

⁷ Note on the sign convention chosen: the sign of Fourier function in Eq. 2.16 is due to the order chosen in the bra-ket and it is opposite from the crystallographic sign convention. Also note on the wave vector definition convention used here lacking the factor of 2π ($|\mathbf{k}| = 1/\lambda$) which shows up sometimes in solid state physics. Consistent with this choice, the Fourier transform definition used here

$$\Psi(\mathbf{r}) = \mathcal{F}^{-1}[\Psi(\mathbf{k})] \equiv \iiint \Psi(\mathbf{k}) e^{2\pi i \mathbf{k} \cdot \mathbf{r}} d\mathbf{k} \quad (2.17)$$

While the general analytical form of Eq. 2.16 does not look overly complicated, it does involve, somewhat inconveniently, a triple integral over the entire space. In the special case when the function to study is periodic, we can simplify this expression and reduce it to a discrete sum, or what is known as a *Fourier series*. Any physical property of the crystal, such as charge density, carries the property of translational invariance under \mathbf{t} , which means the function for the entire crystal is periodic and can be written as an expansion of complex functions weighted by their Fourier coefficients. For instance, the direct space crystal potential can be written as the discrete inverse Fourier transform version of Eq. 2.17 :

$$V(\mathbf{r}) = \sum_{\mathbf{k}} V_{\mathbf{k}} e^{2\pi i \mathbf{k} \cdot \mathbf{r}}, \quad (2.18)$$

and we will show that the Fourier coefficient $V_{\mathbf{k}}$ are related to the diffracted wave amplitudes.

2.2 Crystallographic computations in the hexagonal system

In the previous Section we covered the hexagonal crystal system (page 20) together with its basis vectors in both real (page 23) and reciprocal space (page 26). We should be ready now to tackle vectorial computations in these reference frames except for one difficulty. None of the seven crystal systems have Cartesian basis vectors and the hexagonal system is certainly not the exception. Even the cubic system is defined by non-unitary vectors. Therefore none of the usual vector identities applies.

In the following we will use the direct metric tensor to generalise the dot product for a given (non-Cartesian) crystal system both in the real and reciprocal space. We will then cover the equations for distances and angles between directions in a hexagonal system. For a good number of derivations shown here I follow the microscopy friendly textbooks [DG03] and [DGM12].

On page 40 we discuss the real to reciprocal space and inverse transformations. These are useful manipulations when it comes to combining information defined in

is missing the $1/2\pi$ pre-factor and reader should pay attention to the convention used when comparing with the form of these formulas with literature.

the reciprocal space, like the diffraction condition, with information defined in real space, like position vectors in the sample. This applies, indeed, to computations of highly position-dependent diffraction information, like in the case of a polycrystalline material or defected crystal.

The alternative to using the metric tensor is to transform the parameters of interest from the crystal frame to Cartesian frame and perform the computations in the usual manner and, only after, translate the result back into the crystal frame if needed. We will use this latter approach for rotation operations which we define in the Cartesian frame on page 42. There is another reason, besides reduction in abstraction, for wanting to move computations to a Cartesian frame or at least orthogonal frame. Regardless of the sample information we are interested in computing, the sample, the SEM geometry and the detector are all rectangular.

2.2.1 The direct metric tensor

Let us start by considering a vector \mathbf{p} defined in a crystal frame with basis vectors $\{\mathbf{a}_1, \mathbf{a}_2, \mathbf{a}_3\}$ by coordinates $\{p_1, p_2, p_3\}$:

$$\mathbf{p} = p_1 \mathbf{a}_1 + p_2 \mathbf{a}_2 + p_3 \mathbf{a}_3$$

Back to the vector \mathbf{p} this time defined in a crystal system with basis vectors $\{\mathbf{a}_i, i \in \{1, 2, 3\}\}$ and angles $\{\alpha, \beta, \gamma\}$ (the list of six lattice parameters). If we are interested in finding its length we know we can use the dot product definition:

$$\mathbf{p} \cdot \mathbf{p} = |\mathbf{p}|^2 \cos(\theta = 0)$$

$$\therefore |\mathbf{p}| = \sqrt{\mathbf{p} \cdot \mathbf{p}} = \sqrt{p_i \mathbf{a}_i \cdot p_j \mathbf{a}_j} = \sqrt{p_i p_j \mathbf{a}_i \cdot \mathbf{a}_j}$$

If we were in a Cartesian frame $\{\mathbf{e}_1, \mathbf{e}_2, \mathbf{e}_3\}$ we would have known that the result of the last dot product is non-zero only when $i \neq j$, i.e., $\mathbf{a}_i \cdot \mathbf{a}_j = \mathbf{e}_i \cdot \mathbf{e}_j = \delta_{ij}$, and therefore $\mathbf{p} = \sqrt{p_1^2 + p_2^2 + p_3^2}$. But we are not and we don't (I didn't). Which is why we need to introduce a more general result for the dot product between two vectors.

$$\mathbf{a}_i \cdot \mathbf{a}_j = |\mathbf{a}_i| |\mathbf{a}_j| \cos \theta_{ij} \equiv g_{ij},$$

where θ_{ij} is the usual angle between basis vectors \mathbf{a}_i and \mathbf{a}_j and we introduced component ij of the the *direct metric tensor* g . The full 3×3 matrix form of the metric tensor can be written in terms of the six lattice parameters of a triclinic system as follows:

$$g = \begin{bmatrix} \mathbf{a}_1 \cdot \mathbf{a}_1 & \mathbf{a}_1 \cdot \mathbf{a}_2 & \mathbf{a}_1 \cdot \mathbf{a}_3 \\ \mathbf{a}_2 \cdot \mathbf{a}_1 & \mathbf{a}_2 \cdot \mathbf{a}_2 & \mathbf{a}_2 \cdot \mathbf{a}_3 \\ \mathbf{a}_3 \cdot \mathbf{a}_1 & \mathbf{a}_3 \cdot \mathbf{a}_2 & \mathbf{a}_3 \cdot \mathbf{a}_3 \end{bmatrix} = \begin{bmatrix} a_1^2 & a_1 a_2 \cos \gamma & a_1 a_3 \cos \beta \\ a_2 a_1 \cos \gamma & a_2^2 & a_2 a_3 \cos \alpha \\ a_3 a_1 \cos \beta & a_3 a_2 \cos \alpha & a_3^2 \end{bmatrix}. \quad (2.19)$$

For a system with higher symmetry, like the hexagonal Bravais lattice, hP , with lattice parameters $\{a, a, c, 90^\circ, 90^\circ, 120^\circ\}$, the form above reduces to:

$${}^{hex}g = \frac{a^2}{2} \begin{bmatrix} 2 & -1 & 0 \\ -1 & 2 & 0 \\ 0 & 0 & c^2/2a^2 \end{bmatrix}. \quad (2.20)$$

We are finally ready to calculate the magnitude of a vector, \mathbf{p} , defined in a hexagonal crystal system, $\mathbf{p} = p_1 \mathbf{a}_1 + p_2 \mathbf{a}_2 + p_3 \mathbf{c}$:

$$|\mathbf{p}| = \sqrt{{}^{hex}g_{ij} p_i p_j} = \sqrt{(a^2(p_1^2 - p_1 p_2 + p_2^2) + c^2 p_3^2)}, \quad (2.21)$$

the general dot product between two vectors, \mathbf{p} and \mathbf{q} , defined in the same hexagonal crystal system, $\mathbf{q} = q_1 \mathbf{a}_1 + q_2 \mathbf{a}_2 + q_3 \mathbf{c}$:

$$\mathbf{p} \cdot \mathbf{q} = p_i {}^{hex}g_{ij} q_j, \quad (2.22)$$

and the angle θ between the same two vectors:

$$\cos \theta = \frac{p_i {}^{hex}g_{ij} q_j}{|\mathbf{p}| |\mathbf{q}|} = \frac{a^2 (p_1 q_1 + p_2 q_2 - \frac{1}{2}(p_1 q_2 + p_2 q_1)) + c^2 p_3 q_3}{|\mathbf{p}| |\mathbf{q}|}. \quad (2.23)$$

It is common to ask about angles between directions rather than specific vectors. In this case it is just a matter of replacing the components p_i, q_i with the reduced prime integers of the Miller indices of the given directions $[u v w]$.

What about the Miller-Bravais indexing? I hear you ask. Not to worry, we can apply an identical derivation for the four index notation hexagonal basis set $\{\mathbf{A}_1, \mathbf{A}_2, \mathbf{A}_3, \mathbf{C}\}$. We will denote the four-index metric tensor with G and follow ref. [OT68] to write:

$${}^{\text{hex}}\mathbf{G} = \begin{bmatrix} \mathbf{A}_1 \cdot \mathbf{A}_1 & \mathbf{A}_1 \cdot \mathbf{A}_2 & \mathbf{A}_1 \cdot \mathbf{A}_3 & \mathbf{A}_1 \cdot \mathbf{C} \\ \mathbf{A}_2 \cdot \mathbf{A}_1 & \mathbf{A}_2 \cdot \mathbf{A}_2 & \mathbf{A}_2 \cdot \mathbf{A}_3 & \mathbf{A}_2 \cdot \mathbf{C} \\ \mathbf{A}_3 \cdot \mathbf{A}_1 & \mathbf{A}_3 \cdot \mathbf{A}_2 & \mathbf{A}_3 \cdot \mathbf{A}_3 & \mathbf{A}_3 \cdot \mathbf{C} \\ \mathbf{C} \cdot \mathbf{A}_1 & \mathbf{C} \cdot \mathbf{A}_2 & \mathbf{C} \cdot \mathbf{A}_3 & \mathbf{C} \cdot \mathbf{C} \end{bmatrix} = \frac{a^2}{2} \begin{bmatrix} 2 & -1 & -1 & 0 \\ -1 & 2 & -1 & 0 \\ -1 & -1 & 2 & 0 \\ 0 & 0 & 0 & 2c^2/a^2 \end{bmatrix} \quad (2.24)$$

The magnitude of the same vector \mathbf{p} this time with components $\{P_1, P_2, P', P_3\}$ corresponding to the four-vector basis, $\mathbf{p} = P_1\mathbf{A}_1 + P_2\mathbf{A}_2 + P'\mathbf{A}_3 + P_3\mathbf{C}$ is:

$$|\mathbf{p}| = \sqrt{P_i {}^{\text{hex}}\mathbf{G}_{ij} P_j} = \sqrt{(3a^2(P_1^2 + P_1P_2 + P_2^2) + c^2P_3^2)}, \quad (2.25)$$

which is similar but not the same as Eq. 2.21, note the sign difference. For the same vector the coordinates in four-vector basis are going to be smaller than the coordinates in the three-vector basis, since there are more vectors to contribute. A word of advice for the reader, don't be tempted to apply the vector length derivation to the Miller and Miller-Bravais notation of directions, remember the discussion on page 23.

The angle between two vectors, $\mathbf{p} = P_i\mathbf{A}_i$ and $\mathbf{q} = Q_i\mathbf{A}_i$, defined using the four-vector basis of a hexagonal lattice is then, similarly to Eq. 2.23:

$$\cos \theta = \frac{P_i {}^{\text{hex}}\mathbf{G}_{ij} Q_j}{|\mathbf{p}| |\mathbf{q}|} = \frac{a^2 (3(P_1Q_1 + P_2Q_2) + \frac{3}{2}(P_1Q_2 + P_2Q_1)) + C^2P_3Q_3}{|\mathbf{p}| |\mathbf{q}|}. \quad (2.26)$$

2.2.2 The reciprocal metric tensor

On page 28 we covered, to some extent, the reciprocal hexagonal lattice and its basis vectors in both the linearly independent form of $\{\mathbf{a}_1^*, \mathbf{a}_2^*, \mathbf{c}^*\}$ and the linearly dependent $\{\mathbf{A}_1^*, \mathbf{A}_2^*, \mathbf{A}_3^*, \mathbf{c}^*\}$.

The *reciprocal metric tensor*, can be derived in much the same way as the real space one, by doing the dot product between all the pairs of basis vectors: $\mathbf{g}_{ij}^* = \mathbf{a}_i^* \cdot \mathbf{a}_j^*$. It is also, quite conveniently, the inverse of the real space metric tensor: $\mathbf{g}_{ij}^* = (\mathbf{g}_{ij})^{-1}$, such that for the reciprocal hexagonal lattice with parameters $\{a^*, a^*, c^*, 90^\circ, 90^\circ, 60^\circ\}$ can easily be written out to be:

$${}^{\text{hex}}\mathbf{g}^* = \begin{bmatrix} \mathbf{a}_1^* \cdot \mathbf{a}_1^* & \mathbf{a}_1^* \cdot \mathbf{a}_2^* & \mathbf{a}_1^* \cdot \mathbf{c}^* \\ \mathbf{a}_2^* \cdot \mathbf{a}_1^* & \mathbf{a}_2^* \cdot \mathbf{a}_2^* & \mathbf{a}_2^* \cdot \mathbf{c}^* \\ \mathbf{c}^* \cdot \mathbf{a}_1^* & \mathbf{c}^* \cdot \mathbf{a}_2^* & \mathbf{c}^* \cdot \mathbf{c}^* \end{bmatrix} = ({}^{\text{hex}}\mathbf{g})^{-1} = \frac{2}{3a^2} \begin{bmatrix} 2 & 1 & 0 \\ 1 & 2 & 0 \\ 0 & 0 & 3a^2/2c^2 \end{bmatrix} \quad (2.27)$$

The lattice parameters are inverted with respect to the real metric tensor given in Eq. 2.20, as expected, and we also gained a normalisation factor of 1/3 from the determinant. But more notably, the form of the matrix is different to all the other hexagonal metric tensors. The minus signs present in 1) Eq. 2.20, 2) Eq. 2.24 and, as we will see, in 3) Eq. 2.29 are missing here. This observation is consistent with the comments made for Fig. 2.8 on page 29, namely that the hexagonal reciprocal space lattice defined by three basis vectors is different 1) the real space hexagonal lattice defined with three basis vectors 2) the one defined with four basis vectors and 3) the reciprocal hexagonal lattice defined with four basis vectors. Just to reiterate, interchanging between basis sets needs a bit of thought.

We can write out, similarly to equation 2.21, the length of a generic reciprocal space vector $\mathbf{g} = g_1 \mathbf{a}_1^* + g_2 \mathbf{a}_2^* + g_3 \mathbf{a}_2^*$ (written conveniently for Einstein summation) from the dot product with itself:

$$|\mathbf{g}| = \sqrt{g_i g_{ij}^* g_j} \quad (2.28)$$

In terms of the four index notation, the reciprocal metric tensor G^* is:

$${}^{\text{hex}}G^* = \frac{2}{9a^2} \begin{bmatrix} 2 & -1 & -1 & 0 \\ -1 & 2 & -1 & 0 \\ -1 & -1 & 2 & 0 \\ 0 & 0 & 0 & 9a^2/2c^2 \end{bmatrix} \quad (2.29)$$

Which looks very similar to the real space four-index notation metric tensor ${}^{\text{hex}}G$ in Eq. 2.24 with inverse lattice parameters; as expected, since the real and reciprocal four-basis vectors are parallel to one other.

2.2.3 The interplanar spacing

We now have all the tools to calculate the length of the translation vector in the hexagonal system reciprocal lattice, $\mathbf{g}_{hkl} = h\mathbf{a}_1^* + k\mathbf{a}_2^* + l\mathbf{c}^*$ defined in Eq. 2.6. The identity in Eq. 2.28 reduces to:

$$|\mathbf{g}_{hkl}| = \sqrt{\frac{4}{3a^2}(h^2 + k^2 + hk) + \frac{1}{c^2}l^2}$$

Such that we could, finally, derive the expression for the distance between a set of planes $\{h k l\}$ in a hexagonal system defined in Eq. 2.9:

$${}^{hex}d_{hkl} = \frac{1}{\sqrt{\frac{4}{3a^2}(h^2 + k^2 + hk) + \frac{1}{c^2}l^2}} \quad (2.30)$$

We can also find the distance between a set of hexagonal system planes $\{h k i l\}$ given in Miller-Bravais notation:

$${}^{hex}d_{hkil} = \frac{1}{\sqrt{\frac{4}{3a^2}(h^2 + k^2 + i^2 + hk + ki + ih) + \frac{1}{c^2}l^2}} \quad (2.31)$$

Table 2.6 shows a few examples of calculated interplanar distances for common families of planes in wurtzite nitride systems (see Fig. 2.6). Spot that the distance between consecutive *c-planes* is the lattice parameter *c* while the one between *a-planes* is half the lattice parameter *a*.

TABLE 2.6: Calculated interplanar distances in wurtzite nitrides.

| System (a[Å], c[Å]) | Interplanar spacing for set of planes $\{h k l\}$ [Å] | | | |
|---------------------|---|-------------------------|-------------------|-------------------|
| | a-plane $\{110\}$ | r-plane $\{1\bar{1}2\}$ | m-plane $\{100\}$ | c-plane $\{001\}$ |
| AlN (3.11, 4.98) | 1.56 | 1.83 | 2.69 | 4.98 |
| GaN (3.19, 5.19) | 1.60 | 1.89 | 2.76 | 5.19 |
| InN (3.53, 5.70) | 1.77 | 2.08 | 3.07 | 5.70 |

2.2.4 To the reciprocal space and back

While the equivalence between reciprocal vector absolute value and inverse of the distance between planes is clear, other transformations between the two vector spaces require a bit more work. Let us start with a vector \mathbf{p} with components $\{p_i, i \in (1, 2, 3)\}$ in the real space, $\mathbf{p} = p_i \mathbf{a}_i$. This vector must exist independent of the reference frame, so let us give it components $\{p_i^*, i \in (1, 2, 3)\}$ in the reciprocal space: $\mathbf{p} = p_i^* \mathbf{a}_i^*$ such that:

$$\mathbf{p} = p_i \mathbf{a}_i = p_i^* \mathbf{a}_i^*. \quad (2.32)$$

If, in the latter equality, we dot product both sides by \mathbf{a}_j and use both the property of the reciprocal lattice, given in Eq. 2.8, and the definition of the direct metric tensor, $g_{ij} = \mathbf{a}_i \cdot \mathbf{a}_j$ then we find that:

$$p_j^* = p_i g_{ij} \quad (2.33)$$

Which tells us how to find the components of the vector in the reciprocal space.

Alternatively, if we know the components of the vector in reciprocal space and want to define it in the real space, we dot product the right side of the last equality in Eq. 2.32 by \mathbf{a}_j^* , and use the definition of the reciprocal metric tensor this time, $g_{ij}^* = \mathbf{a}_i^* \cdot \mathbf{a}_j^*$, to find:

$$p_j = p_i^* g_{ij}^* \quad (2.34)$$

Similarly, if we are interested in finding the reciprocal basis vectors, \mathbf{a}_i^* , knowing the real space basis vectors \mathbf{a}_i , we replace p_i with the identity in Eq. 2.34 to find:

$$\mathbf{a}_i^* = g_{ij}^* \mathbf{a}_j, \quad (2.35)$$

and, inversely,

$$\mathbf{a}_i = g_{ij} \mathbf{a}_j^*. \quad (2.36)$$

Notice the difference in position of the metric tensor in equations 2.33 and 2.36. Another way to remember this is that the rows of the metric tensor are the components of the direct basis vector in terms of the reciprocal basis vectors, as explained in *Introduction to CTEM* pg. 17 [DG03], and the columns of the metric tensor contain the reciprocal components of a vector in terms of the real space components.

The reciprocal lattice basis vectors

On page 28 I made a promise to show where the form for the hexagonal reciprocal basis vectors (Eq. 2.10) comes from. Let us finally apply the reciprocal space vector definition in Eq. 2.7 to the hexagonal lattice. If we now make an attempt at writing out the cross products between two basis vectors of a crystal lattice, \mathbf{a}_p and \mathbf{a}_q ⁸:

$$\mathbf{a}_p \times \mathbf{a}_q = \Omega \epsilon_{ijk} \mathbf{a}_{p,i} \mathbf{a}_{q,j} \mathbf{a}^*_k$$

⁸ The index notation is going to be a bit crazy in this section; we are trying to annotate both different basis vectors and components of said vectors. The Einstein summation rules discussed on page 31 continue to apply.

where Ω is the volume of the unit cell. We have used a new symbol, ϵ_{ijk} , known as the *normalised permutation symbol* which can take three values depending on the order of indices $\{h, k, l\}$:

$$\epsilon_{ijk} = \begin{cases} +1, & \text{if } i, j, k \text{ are an even permutation of 123,} \\ -1, & \text{if } i, j, k \text{ are an odd permutation of 123,} \\ 0, & \text{otherwise.} \end{cases}$$

$\mathbf{a}_{\mathbf{p},i}$ is the component i of the basis vector $\mathbf{a}_{\mathbf{p}}$ and surely can only take the value 1 when $p = i$, i.e., $\mathbf{a}_{\mathbf{p},i} = \delta_{pi}$. In the same manner, $\mathbf{a}_{\mathbf{q},j} = \delta_{qj}$.

Since the cross product of two basis vectors points in a direction normal to both vectors, and since in a non-Cartesian system this will not necessarily coincide with the direction of the third basis vector, we had to use a different trick. Namely, the definition of the reciprocal basis vectors (Eq. 2.7) which is the reason why we ended up with a reciprocal vector component in the equation above in the first place anyway. Nevertheless, the equation above does not lead us very far in the attempt to write out the reciprocal basis vectors in terms of the real space one. We can however fix that by converting the components of this vector to the real space using Eq. 2.35 derived above.

Finally, we can write:

$$\mathbf{a}_{\mathbf{p}} \times \mathbf{a}_{\mathbf{q}} = \Omega \epsilon_{pqk} g_{km}^* \mathbf{a}_{\mathbf{m}}.$$

For the hexagonal lattice basis set we just replace the reciprocal metric tensor with the form given in Eq. 2.27. This would lead us end up with the reciprocal lattice vectors in on page 28.

2.2.5 Rotations in Cartesian frame

It is common in crystallographic calculations to want to express a tensor parameter known in one reference in a different reference frame; assuming we can figure out the position of the new reference frame in the old reference frame. For instance, mapping the electron beam scan in the sample frame (a task made especially challenging by the high sample tilt used in electron diffraction techniques, which the SEM is not very well designed to account for [Nol07]), involves moving electron scan positions between the beam frame and the sample frame. Assuming the scanning directions x and y are truly perpendicular, that the x scanning direction is indeed parallel to the

tilt axis of the sample and that the magnification and spot size are not significantly affected by the tilt (*i.e.*, parallel beam at high magnification) then the relationship between the basis vectors of two frames is a simple rotation. A similar transformation must be done for translating the escaping electron beam positions from the sample frame to the detector frame [Bri+16].

Unfortunately, simply calling an action “rotation” suffers from many ambiguities. In crystallography, when we talk about rotation we refer to a very well defined transformation. In a right handed system⁹ – first source of ambiguity – a rotation of the coordinate system (CS) around a given axis is the clockwise rotation in the plane normal to that axis as the viewer looks in the direction pointed by the axis. Another way of describing the clockwise rotation is the right hand rule, *i.e.*, holding the thumb in the direction of the chosen axis of rotation, the rest of the fingers point in the direction of rotation.

If you just looked at your right hand fingers going, in fact, anti-clockwise then you’ll understand why I call rotations confusing. It matters where the rotations axis, or finger is pointing – second source of confusion. You do need to align your viewing direction with the direction of the rotation axis, that is you need to awkwardly turn your right hand such that the thumb points to where you are looking. Voilà, clockwise rotation. Also, my activity for months during my PhD.

Another possible ambiguity is whether we refer to a *active* or a *passive* rotation:

- A passive, or alias transformation, like the one above, acts on the coordinate system. It rotates the CS clockwise around a given axis while keeping the position of the object of interest fixed.
- An active, or alibi transformation acts on the object. More explicitly, the active rotation affects the position vector of the object whose coordinates are described in a fixed CS. The direction of rotation is opposite to the passive one and therefore anticlockwise.

It should be obvious that a passive rotation of an object by an angle θ around a given axis is equivalent with a passive rotation of its coordinate frame by an angle $-\theta$ around the same axis.

The mathematical form of these transformations in 3D can be written as 3×3 matrices, \mathcal{R} . In the case in which the axis of rotation is one of the basis vectors we call the transformation a basic rotation.

Yet another source of ambiguity is the manner in which we apply the rotation matrix. Through this work we pre-multiply the rotation matrix with the position

⁹ (x, y, z) follow the thumb, index and middle fingers of the right hand

column vector: $\mathbf{v}' = \mathcal{R}(\theta)\mathbf{v}$. This leads us to the unambiguous definition of rotation we will use:

The anticlockwise rotation of a position vector in column form, \mathbf{v} , given in a right handed CS, around the rotation axis \mathbf{n} leads to a new position which can be calculated by pre-multiplying the rotation matrix $\mathcal{R}_{\mathbf{n}}$ by the position vector: $\mathcal{R}_{\mathbf{n}}\mathbf{v}$.

We will use the passive version of it when rotating reference frame, in which case we will also flip the definition of the axis of rotation ($\mathbf{v} = -\mathbf{v}$) such that we can use the same definition still. For any property in this definition changed, the rotation direction flips. For instance, post-multiplying the rotation matrix with row vector leads to a clockwise rotation. The tree passive rotation matrices for a right handed Cartesian frame are given in Appendix B.

A useful property of the rotation matrix is that the inverse of a rotation can be calculated by simply transposing the matrix ($\mathcal{R}\mathcal{R}^T = \mathcal{I}$). Another property is that the product of rotation matrices is yet another rotation matrix. Even in the case in which the rotation axis is not just a basis vector, the rotation can be broken down in maximum tree basic rotations.

This latter scenario describes another rotation formalism known as *Euler rotation* in terms of Euler angles; the rotation is given as a set of three angles which describe three successive rotations around a combination of the axes $\{\mathbf{x}, \mathbf{y}, \mathbf{z}\}$. Since matrix multiplication is not commutative, the order of the chosen axis is important and a lack of knowledge of the chosen convention makes the Euler notation ambiguous, in a yet different way. EBSD orientation mapping uses, for instance, the Bunge convention [Bun82], which orders the Euler angles as: (ϕ_1, ϕ_2, ϕ_3) around $(\mathbf{z}, \mathbf{x}, \mathbf{z})$, such that the total rotation is given by:

$${}^{Bunge}\mathcal{R}_{Euler}(\phi_1, \phi_2, \phi_3) = \mathcal{R}_z(\phi_3)\mathcal{R}_x(\phi_2)\mathcal{R}_z(\phi_1).$$

This series of rotations for a coordinate system from one position to another can be read as a rotation of ϕ_1 around the basis vector \mathbf{z} followed by ϕ_2 around \mathbf{x} and, finally, ϕ_3 around \mathbf{z} .

There are application for which neither the rotation matrix nor the Euler angle formalism are fully adequate, not least due to the ambiguities that need to be ironed out. One alternative is the *quaternion representation*. Quaternions are four-dimensional vectors, or can be seen as complex numbers with two extra non-real parts of the form $\hat{\mathbf{q}} = q_i\mathbf{i} + q_j\mathbf{j} + q_k\mathbf{k} + q_r = [q_i, q_j, q_k, q_r]$. A quaternion of this form describes a rotation around a rotation axis $\mathbf{n} = [n_x, n_y, n_z]$ by an angle θ such that $q_i = n_x \sin(\theta/2)$, $q_j = n_y \sin(\theta/2)$, $q_k = n_z \sin(\theta/2)$ and $q_r = \cos(\theta/2)$. Quaternion maths will be

faster on a computer compared to rotation matrices since the trigonometric functions are absent and it requires fewer operations per transformation.

Rowenhost *et al.* [Row+15] worked out the complete conversions between the rotation formalisms used in material science (including the Rodrigue-Frank vectors and homochronic vectors) and provided extensive open source Fortran-90 libraries with the implementations. The GitHub repository of Prof. De Graef [DGG14] contains Fortran95, IDL, MatLab, and C++ implementations for the rotations and conversions as well.

Now that we covered how to do rotations in a Cartesian frame we will go over transformations to and from the crystal frame.

2.2.6 Crystal to Cartesian frame and the structure matrix

While computations in the crystal frame conserve the symmetry of the crystal and keep the equations somewhat intuitive, there are undeniable benefits to bringing the calculations into the Cartesian frame as well. If only because implementing non Cartesian vectorial manipulation requires extra work, but ultimately because we want to project the information on a square detector or screen. We are interested in writing out the path of transforming from both the real and reciprocal hexagonal space to the Cartesian system.

The easiest and most common way of defining a Cartesian frame with basis vectors \mathbf{e}_i with respect to the crystal frame with basis vectors \mathbf{a}_i and corresponding reciprocal space vectors \mathbf{a}_i^* is as follows:

- \mathbf{e}_1 is the unit vector parallel to \mathbf{a}_1 :

$$\mathbf{e}_1 = \frac{\mathbf{a}_1}{|\mathbf{a}_1|} \quad (2.37)$$

- \mathbf{e}_3 is the unit vector parallel to \mathbf{a}_3^* :

$$\mathbf{e}_3 = \frac{\mathbf{a}_3^*}{|\mathbf{a}_3^*|} \quad (2.38)$$

- and \mathbf{e}_2 completes the right handed Cartesian reference frame:

$$\mathbf{e}_2 = \mathbf{e}_3 \times \mathbf{e}_1. \quad (2.39)$$

Let us consider a vector $\mathbf{p} = p_i \mathbf{a}_i$, whose components in the Cartesian frame are x_i^p . Since $\mathbf{p} = p_i \mathbf{a}_i = x_i^p \mathbf{e}_i$ it means that we could find a coordinate transformation matrix a_{ij} which relates the components p_i and x_i^p :

$$x_i^p = a_{ij} p_i \quad (2.40)$$

The components of the matrix a_{ij} can be found by rewriting the lengths of the lattice vectors in Eq.'s 2.37 to 2.39 in terms of the direct and reciprocal matrix tensors. For instance, $|\mathbf{a}_1| = \sqrt{g_{11}}$ (see Eq. 2.19). For the rest of the beautiful derivation we send the reader to page 140 of ref. [DGM12]. The final matrix will have elements containing both the direct and reciprocal metric tensor. We give here the form of matrix a_{ij} , also known as the *direct structure matrix*, for a hexagonal lattice:

$${}^{hex}a_{ij} = \begin{bmatrix} a & -\frac{a}{2} & 0 \\ 0 & \frac{\sqrt{3}a}{2} & 0 \\ 0 & 0 & c \end{bmatrix} \quad (2.41)$$

If we want to translate a reciprocal space vector to the same Cartesian frame, we have to introduce a second matrix b_{ij} known as the *reciprocal structure matrix*. We start now with a vector \mathbf{g} with components g_i in the reciprocal space: $\mathbf{g} = g_i \mathbf{a}_i^*$. The same vector will have components x_i^g in the Cartesian frame: $\mathbf{g} = x_i^g \mathbf{e}_i = g_i \mathbf{a}_i^*$ such that $x_i^g = b_{ij} g_i$. We can use the reciprocal structure matrix g_{ij}^* (Eq. 2.35) to rewrite the reciprocal basis vectors \mathbf{a}_i^* in terms of the real ones \mathbf{a}_j such that:

$$\mathbf{g} = x_i^g \mathbf{e}_i = g_i g_{ij}^* \mathbf{a}_j,$$

where we can now use the direct structure matrix a_{ij} (Eq. 2.40) to relate the quantities x_i^g and $g_l g_{lj}^*$:

$$x_i^g = a_{ij} g_l g_{lj}^* = a_{ij} g_{jl}^* g_l.$$

We can now define the reciprocal structure matrix for a hexagonal lattice, ${}^{hex}b_{ij}$:

$${}^{hex}b_{ij} = {}^{hex}a_{ij} {}^{hex}g_{jl}^* = \begin{bmatrix} \frac{1}{3a} & 0 & 0 \\ \frac{\sqrt{3}}{3a} & \frac{2\sqrt{3}}{3a} & 0 \\ 0 & 0 & \frac{1}{c} \end{bmatrix}. \quad (2.42)$$

2.2.7 Metric tensor implementations

I took the time to write out a good number of equations in this section. While these are well established and, probably, well understood vectorial manipulation in the world of X-ray diffraction, electron microscopists don't often incorporate basis transformation language in their work. I make this claim based on the observation that, while the implementation would be trivial, there is a lack of mature, accessible and easy to plug-and-play (ideally open) software out there to answer some of the crystallographic questions the material scientists might ask when using an SEM as a characterisation tool.

Until a *Python* library is available and documented for crystallographic basis set computations, I leave the reader with a web tool¹⁰, albeit limited in capabilities, written by Albes Koxhaj, an excellent summer project student in the SSD department who implemented a few of the equations here, and revised by me. The last two blocks of calculators in this tool were written to find the coordinates, in the crystal frame, of the normal direction on a given plane (hkl) or ($hkil$). For a hexagonal plane, we show that there are two special conditions in which the normal to a plane can be reduced to Miller indices $[uvw]$. The first case is when the \mathbf{c} -direction is parallel to the plane ($l = 0$) such that the lattice parameters can be removed from the indices and we are left with integer numbers. The second case is when the \mathbf{c} -direction is normal to the plane ($h = l = 0$ or $h = l = i = 0$), when the normal is along \mathbf{c} in both the real and reciprocal space. Any other case will keep coordinates dependent on the lattice parameters a, c which would make them unlikely to be reduced to integers.

I also wrote a few Python lines in the Jupyter notebook `grainNormal.ipynb`, showing the steps needed to calculate the surface normal in the crystal frame of individual grains from the Euler angles of an EBSD map by applying the identities in this section.

EMsoft [SRDG17] contains Fortran90 implementations of the metric tensor tensor formalism. The source code can be found in the `crystal.f90` and `symmetry.f90` modules in Source/EMsoftLib path on the GitHub page [DGG13].

2.3 Wurtzite symmetry

I wrote a somewhat comprehensive introduction to symmetry in the wurtzite system in Appendix C. This is aimed at a complete novice to crystallography which I was at

¹⁰ Link address is: <http://ssd.phys.strath.ac.uk/resources/crystallography/crystallographic-direction-calculator/>.

the beginning of this journey. I tried to keep it at textbook level by following the Symmetry chapter in *Structure of Material: An Introduction to Crystallography, Diffraction and Symmetry* [DGM12] and focusing on the symmetry operations relevant for this crystal system. Though it can look daunting and dry, I was told, I would recommend the reader to venture a look though it if they want to understand where the symmetry information in this section comes from. I believe it makes for a decent read and I added a lot of supporting figures and beautiful Rayshade¹¹ 3D renderings. I wrote my own input files for these renderings based on the input *.ray files¹² developed by Marc De Graef [DG98] with the purpose of teaching crystallography group symmetry [DG08]. My scripts can be found at this GitHub repository¹³.

On page 181 of the same Appendix, I also describe how to decipher the symbols in the *International Tables for Crystallography, Volume A* [Hit88], a skill indispensable to any crystallographer. Specifically, pages 584-858 of the *Tables*, covering space group **P6₃mc**, are explained in detail.

In the following section I will assume the reader has working knowledge of crystallographic language. You have been warned!

2.3.1 The P6₃mc space group

We talked in Appendix C about how one can determine the full symmetry of a space group by adding the point group operators to a compatible Bravais lattice. Indeed, the space group symbol itself is made up of the Bravais lattice information to which the point-group Hermann-Mauguin notation is added. Let us consider the space group **P6₃mc**. If we start with the primitive hexagonal Bravais lattice *hP* and add the **6mm** point group (see page 178) at every lattice point we obtain the **P6mm** space group. But we can generate a new group with a different symmetry if we replace the **6** symbol in the point group with a **6₃** screw axis operation (see page 174) and the second **m** with a glide plane **c** in the direction of basis vector **c**. The resulting symmetry group, **6₃mc**, is shown in Fig. 2.11. The blue planes are the mirror planes with normal {10.0} and, in between them, the grey planes represent the glide planes with normal {12.0}.

As before, the generating files can be found in *6_3mcPNG.ray* for the *.png image and *6_3mcGIF.ray* for the *.gif animation.

Note that this combination does not make up a point group as it does not present a unique symmetry. However, when adding the **6₃mc** symmetry at the lattice points on a hexagonal primitive Bravais lattice, it generates the brand new space group **P6₃mc**.

¹¹ Link is <https://sourceforge.net/projects/rayshade/>.

¹² Link is <http://som.web.cmu.edu/frames2.html>.

¹³ Link is https://github.com/elenapascal/SEM-diffraction/tree/master/Wurtzite_symmetry.

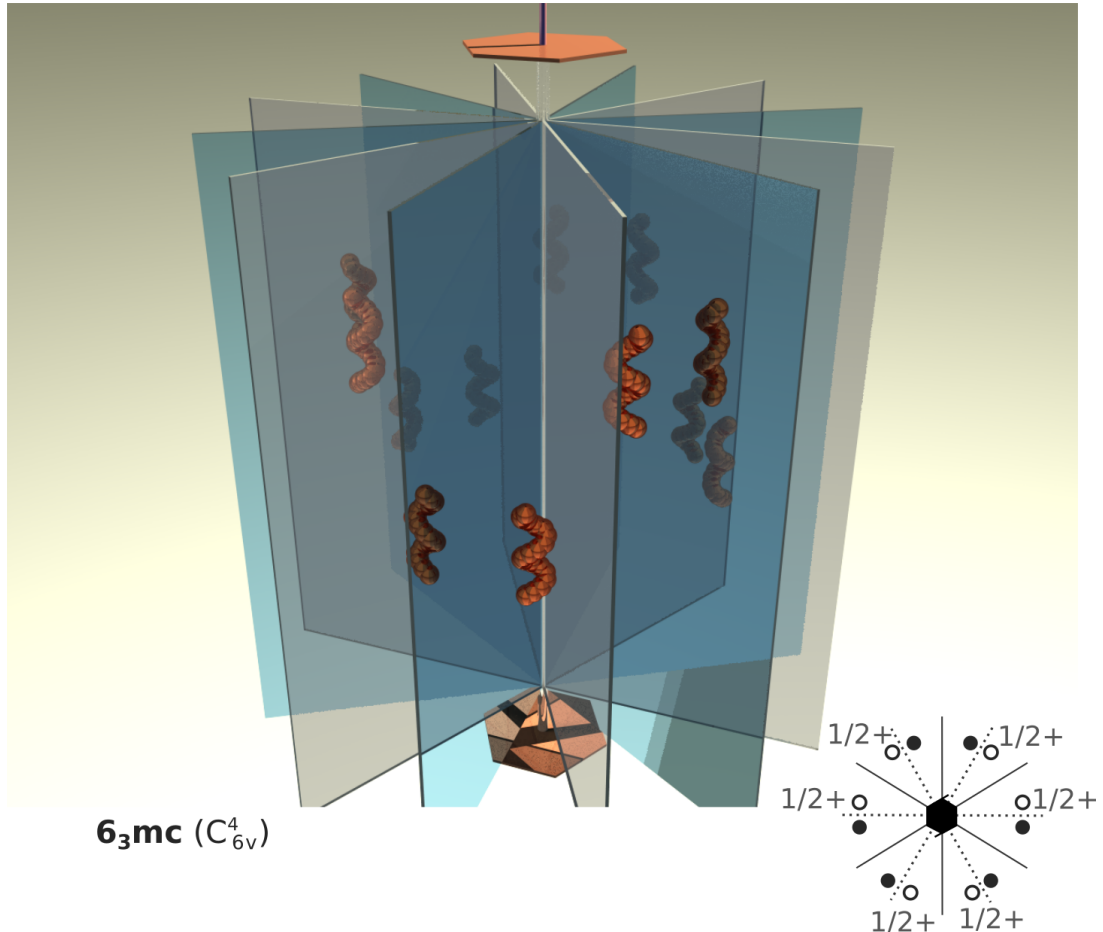


FIGURE 2.11: Graphical 3D representation of the **6₃mc** symmetry combination. Blue planes represent the mirror planes and the grey ones the glide planes. See Appendix C for discussion on squiggly objects. The 2D projection is shown in the bottom right corner. Filled circles indicate the object is in the plane of the drawing, open circles indicate the object is above the plane at the indicated height. Dotted lines represent a glide plane with translation normal to the drawing plane and solid lines are mirrors.

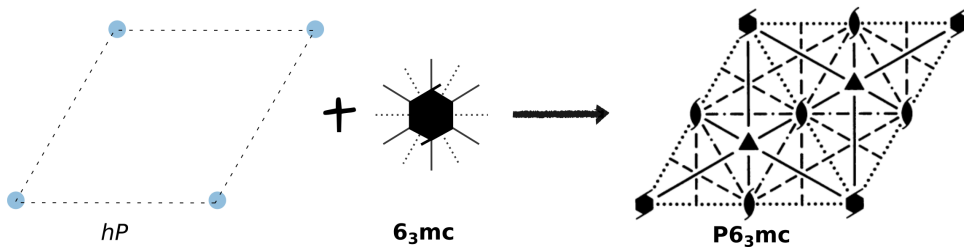


FIGURE 2.12: Top view construction of space group **P6₃mc** from the Bravais lattice **hP** combined with the symmetry combination **6₃mc**. [Right image taken from ref. [Hit88].]

TABLE 2.8: The **P6₃mc** space group with its corresponding number and crystallographic point group.

| Space group # | Point group | Space group symbol |
|---------------|-------------|-------------------------|
| 186 | 6mm | P6₃mc |

This is illustrated in Fig. 2.12, where the last image is taken from the *Tables* and shows the top view projection of the symmetry operators of this space group.

One can find the corresponding point group of a space group containing glide planes or screw axes (non-symmorphic) by simply replacing the glide planes by mirrors and the screw axes by regular rotations. We show in Table 2.8 the corresponding crystallographic point group together with the space group number as it is indexed in the *International Tables for Crystallography*. The important difference to keep in mind when comparing the space group **P6₃mc** with the corresponding point group **6mm** is that the space group symmetry includes translational vectors. And in this case, we are not only talking about the Bravais lattice translational vectors, but also about symmetry operators of the second kind, like screw and glide, that include translation. In mathematical language, this means that the point symmetry matrices $D^{(x)}$ are not sufficient for describing the symmetry of the the space group and we must turn to the 4×4 matrices, \mathcal{W} , which contain translation information as well. We showed on page 173 (Eq. C.4) how to write these matrices using the Seitz symbols: $\mathcal{W} = (D|\tau)$. The values of the relevant matrices D^x are given explicitly in Appendix C.

In Appendix C we derived the 12 symmetry operations of this space group. We also mentioned that these can also be found as a list in the *Tables*. We will need these symmetry operations in order to determine the equivalent positions of an atom in the unit cell, *i.e.*, for a given atom position apply all symmetry operations of the space group to this position and note all unique new coordinates inside the unit cell.

With the help of Appendix C we can read all the symmetry operations symbols in

TABLE 2.9: List of generators for wurtzite crystal structure.

| Operation # in Tables | Representation in Tables | Description (page discussed) | Graphical | Seitz symbol |
|--------------------------|--------------------------------|--------------------------------------|-----------|------------------------------|
| (1) | 1 | identity | | $(D^{(a)} 0)$ |
| (2) | $3^+ 0, 0, z$ | 3 fold rotation @ $[0\ 0\ 1]$ (168) | ▲ | $(D^{(n)} 0)$ |
| (4) | $2(0, 0, \frac{1}{2}) 0, 0, z$ | 2_1 screw axis @ $[0\ 0\ 1]$ (174) | ◆ | $(D^{(b)} \tau_{(0,0,1/2)})$ |
| (7) | $m x, \bar{x}, z$ | (1 1 0) mirror plane (173) | — | $(D^{(k)} 0)$ |

the right image of Fig. 2.12. Especially we can recognise the 4 group generators listed in the *Tables* (shown on page 183). Table 2.9 describes these generators and points to the Appendix pages where they are discussed. The table also gives us the matrices we need to apply to a position (x, y, z) when looking its symmetry equivalent places in the unit cell.

2.3.2 Wurtzite crystal structure

On page 20 we mentioned that a crystal structure is described by its space group, lattice parameters and atom positions in the asymmetric unit cell. We have covered group symmetries so far, and it is therefore time to place atoms on the lattice.

Unfortunately, some ambiguity about the positions of the wurtzite atoms in the unit cell exists. Figure 2.13 a) shows the common representation of a wurtzite unit cell. This is a didactically useful way to visualise the hexagonal close packing (hcp) structure that wurtzite exhibits. For this unit cell we can place an atom at $(0, 0, 0)$ and another, identical one at $(1/3, 2/3, 1/2)$. A pair of atoms of a different species can then be displaced by a value x in the *c-axis* direction with respect to the first two. For the perfect wurtzite structure $x = 3/8$. This unit cell will have the translational symmetry of the primitive hexagonal Bravais lattice, *hP*.

Nevertheless, this representation does not carry the symmetry of the space group **P6₃mc** to which wurtzite belongs. Figure 2.13 b), on the other hand, shows the unit cell of a **P6₃mc** space group structure exhibiting the full symmetry of this group. The atoms are now placed at the 2*b* Wyckoff positions given as fractional coordinates of the basis vectors:

$$\text{Ga}_1 : (1/3, 2/3, z = 0) \quad (2.43)$$

$$\text{N}_1 : (1/3, 2/3, z + x = 0 + x) \quad (2.44)$$

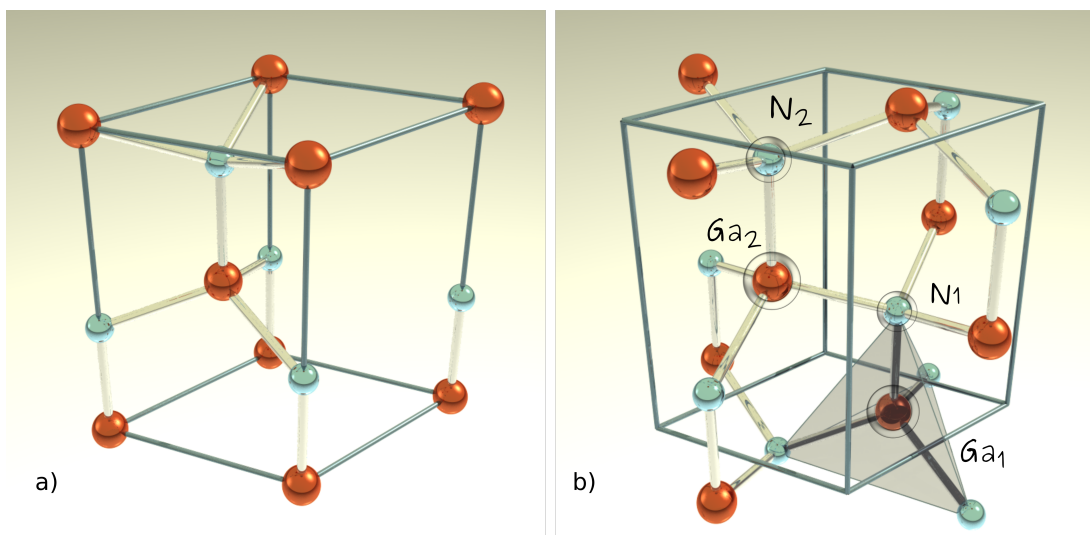


FIGURE 2.13: 3D render of: a) hexagonal unit cell representation of hcp structure of wurtzite, not respecting group symmetry; b) wurtzite crystal structure hexagonal primitive cell (*hP*) enclosed by blue edges and the tetrahedral asymmetric unit cell enclosed by glass faces. The 4 highlighted atoms are the ones contained by the primitive unit cell.

where $x = 3/8$ for the ideal wurtzite structure as before.

These two atoms are enough to define the asymmetric unit cell highlighted here by the tetrahedrally shaped grey box. Looking closer at the symmetry of the asymmetric cell we can recognise the glide, or, equivalently, screw symmetry we have seen in the **6₃mc** symmetry group render in Fig. 2.11. The mirror planes pass through the tetrahedral cells indicating the unit cell exhibits mirror symmetry, *i.e.*, we replace the pair of squiggly orange objects with the asymmetric unit cell. Any atom or group of atoms in the unit cell in 2.13 b) will satisfy all the symmetry operations of the space group shown in Fig. 2.12. Note that this is not the case for the unit cell in a).

The positions of the other atoms in the fundamental, hexagonal prism unit cell shown in Fig. 2.11 b) can be determined by applying the list of 12 symmetry operations of the space group to the positions inside the asymmetric unit cell given above. It turns out that we only need one operation to generate two new positions inside the unit cell. A number of operations can produce the two new positions, for instance the 2₁ screw operation with entry (4) in Table 2.9 with the origin the middle of the cell or a 6₃ screw with the origin at the origin of the cell.

$$\text{Ga}_2 : \mathcal{W}\text{Ga}_1 = (2/3, 1/3, z' = 1/2) \quad (2.45)$$

$$\text{N}_2 : \mathcal{W}\text{N}_1 = (2/3, 1/3, z' + x = 1/2 + x) \quad (2.46)$$

where $x = 3/8$ for the ideal wurtzite structure. The hexagonal unit cell is populated by the same 4 atoms as the one in Fig. 2.13 a). The two cells can generate the same structure, a) by translation only and b) by applying the generators of the space group. We will be using in this work exclusively the latter representation of this cell since the diffraction properties we are interested in are the result of the group symmetry.

The files used to render the `*.png` and `*.gif` versions of the images shown in this section are: `wurtzite_commonGIF.ray` for the first version of the cell shown in a) and `wurtzite_cellGIF.ray` for the latter.

2.3.3 Nitrides lattice parameters

Finally, the lattice parameters can be calculated from first principles and/or from diffraction experiments. I am showing in Table 2.10 the currently accepted lattice parameters for the three wurtzite systems we tackled in this work. The last entry shows the volume of the fundamental cell calculated using Eq. 2.2 derived on page 22.

TABLE 2.10: Lattice parameters and unit cell volume, Ω , for some common nitrides with wurtzite crystal structure.

| Wurtzite compound | a [\AA] | c [\AA] | Ω [\AA ³] |
|-------------------|-----------|-----------|------------------------------|
| AlN [Gol+01] | 3.11 | 4.98 | 41.71 |
| GaN [Les+94] | 3.19 | 5.19 | 45.74 |
| InN [Zub+01] | 3.53 | 5.70 | 61.51 |

3 Diffraction in a perfect crystal

In the previous chapter we have dusted off the tool-kit required to tackle diffraction. The current chapter deals with the theoretical formalism of electron diffraction and shows the explicit path of applying this formalism to group-III nitride compounds.

Since I believe some insight into the theory comes from the chronological development of the current accepted models, I'll treat my reader to the historical background of diffraction on page 55. Historically, diffraction is associated with X-rays, and we will end up using parts of the theories developed for X-ray diffraction when talking about electron diffraction.

While the phenomenon is described by the same physics regardless of the type of particles used, the way individual diffracting particles interact with matter can differ. While X-rays diffract from the electron density in the crystal, electrons are scattered elastically by the Coulomb potential. The latter is related to the electron density via the Poisson equation and, additionally, it also includes the nuclear contributions. Similarly, neutrons interact mainly with the nuclear potentials in the crystal sample. Table 3.1 shows the properties of the most common types of particles used in diffraction experiments together with their scattering sources.

TABLE 3.1: Particles used in diffraction experiments together with their scattering properties.

| Particle | λ [nm] | Charged? | Scattering object |
|--------------|----------------|----------|-------------------------------|
| X-ray photon | 0.01 – 1.0 | no | electron density distribution |
| neutron | ~ 0.1 | no | atomic nuclei distribution |
| electron | 0.001 – 0.1 | yes | atomic potential distribution |

Compared to X-rays, electrons have significantly shorter wavelengths and are scattered much more strongly by matter. This means that electrons convey information about much smaller crystal volumes than conventional X-ray microscopy, in other words, they promise better spatial resolution. It also means that effects which are negligible when it comes to the interaction of X-rays with matter, cannot be swept under the carpet and ignored when it comes to electrons. While we can use the geometrical, *i.e.*, kinematical, model for predicting X-ray diffraction intensities, we need

to take into account the fact that electrons will lose energy and coherence on their paths through the sample and that electron waves are more strongly coupled to each other. To do this we must turn to the dynamical theory for the prediction of scattered electrons intensities. More on that on page 61.

I have already made the note that diffraction is chiefly related to the wave behaviour of small particles like photons, electrons or neutrons. This behaviour is mathematically written in the form of a Bloch wave $\psi(\mathbf{r})$ whose squared amplitude, $|\psi(\mathbf{r})|^2$, describes the probability density of finding the particle at position \mathbf{r} . We will see on page 81 that these wavefunctions satisfy the Schrödinger's equation inside a crystal described by a periodic potential $V_C(\mathbf{r})$. Finding this crystal potential is the journey we will explore in the first part of this section.

In layman terms, diffraction is the phenomena of directional scattering arising as constructive interference along certain directions and destructive interference along others. From the intensity of the interfering waves one can derive information on the spatial distribution of the scattering centres and we will see how that relates to directional elastic scattering. We will talk chiefly about the crystal planes which dictate the Bragg scattering direction. I will also talk about the interaction of the electrons with the unit cell, which affects the intensity of the diffracting beam along chosen direction through the parameter known as the *scattering factor*. There are always these two conditions to take into account when figuring out the diffraction intensity along a certain direction. And both of these parameters (scattering angle from lattice plane and scattering factor) can have values for which the diffraction beam intensity vanishes. Which is why we divide the following sections into *Diffraction geometry* on page 62 and *Diffraction intensity* on page 65.

We will be covering some of the theoretical aspects of diffraction in this section. For a thorough and in-depth description of diffraction and it's application in crystallography we suggest the reader find a copy of the *International Tables of Crystallography Volume B: Reciprocal space* [Aut06; Cow+06].

3.1 Historical background

Soon after systematically experimenting with generating what will end up being known in the English languages as *X-rays*, the German physicist Wilhelm Röntgen used this new form of high energy radiation to "take a picture" of his wife's hand. To everyone's amazement the picture taken in 1895 showed the bones of her hand wearing her wedding ring. While the medical applications of X-rays are impressive

in their own right, a material scientist will claim that the best application of X-rays was yet to come.

Not even twenty years later, another German physicist, Max von Laue, decided to use this new radiation, which he'd probably called Röntgen rays, to "take a picture" of a crystal. He actually had a good reason to try that. Von Laue expected the wavelength of these radiations to be of the same order of magnitude as the distance between atoms in matter. If this criterion is met then the wave behaviour of the radiation will suffer constructive interference along directions dictated by the crystal lattice planes and we would call it diffraction. What he observed in his image was a series of ordered spots which would end up telling a story about the particular ordered arrangement of the crystal atoms. From here on things move rather quickly. Table 3.2 shows a quick overview over about a hundred years of historical events building to the development of electron diffraction techniques.

It is interesting to notice the interplay between experimental observations and theoretical predictions in the development of diffraction as a field. The observation of X-ray diffraction supported, first of all, the controversial wave-like behaviour of particles narrative, and, second of all, the description of crystalline materials as periodic lattice structures. It also led to the development of Bragg's law. Moreover, since the theory of space group symmetry had already been developed by the Russian crystallographer E. S. Fedorov, X-ray diffraction quickly became the structure analysis tool of choice of crystallography.

While Bragg's law was good enough to explain the geometry of the diffraction spots, it proved inconsistent in predicting experimental X-ray diffraction intensities. This lead C. G. Darwin to develop a first form of dynamical diffraction theory. He took into account the interaction of X-rays with matter as partially transmitted and partially reflected amplitudes at each lattice plane. His theory predicted correct values for the reflected intensities. Later, in 1917, P. P. Ewald introduced a new form of dynamical theory in which he considered the crystal to be a periodic distribution of dipoles excited by the incident wave. The new theory predicted both transmitted and reflected intensities. We will talk in the next section on page 61 on how the dynamical model can be reduced to the kinematical approximations when it is reasonable to assume independent direct and diffracted beams (for instance in cases where there would be maximum one inelastic coherent scattering event leading to the diffraction pattern).

There were still limitations in the dynamical theories. In 1930, J. A. Prins [Pri30] modified Darwin's theory to take into account the fact that the crystal is an absorbing medium. Just a year later, in 1931, von Laue showed that the interaction in Ewald's

TABLE 3.2: Partial chronology of the history of diffraction.

| Year | Event |
|--------|---|
| 1912 | First X-ray diffraction experiments by W. Friedrich, P. Knipping and M. von Laue |
| 1913 | Bragg family derives their name bearing law [BB13] to describe the geometry of diffraction spots. |
| 1914 | C. G. Darwin [Dar14] derives the first dynamical theory for the intensities of the diffraction spots. |
| 1924 | L. de Broglie hypothesises that particles should also behave as waves. |
| 1927 | Independently, G. P. Thomson [TR27] at the University of Aberdeen and C. J. Davisson and L. H Germer [DG27] at the Bell Labs, observe low energy electron diffraction spots through thin films. |
| 1928 | H. Bethe [Bet28] uses eigenvalue equations to explain and predict intensities in electron diffraction images. |
| 1928 | First electron diffraction patterns are recorded by S. Nishikawa and S. Kikuchi [NK28] from grazing incidence geometry and are described as “black and white lines in pairs due to multiple scattering and selective reflection”. |
| 1931-4 | E. Ruska and M. Knoll build the first electron microscope (EM), later known as a direct or transmission EM (TEM). |
| 1935-8 | M. Knoll suggests the idea of a scanning EM (SEM). M. von Ardenne [Ard38] constructs the first one. |
| 1961 | A. Howie and M. J. Whelan [HW61] expands Darwin’s theory to develop a simultaneous differential equation form for electron diffraction applicable for predicting diffraction contrast. |
| 1960-5 | P. B. Hirsch and co-workers at Cambridge [HHW60; Hir+65] develop the theory of electron diffraction contrast which can be used to identify line and planar defects in thin films in TEM images. |
| 1967 | D. G. Coates [Coa67] observes electron diffraction patterns in the SEM; later labelled electron channelling patterns (ECPs). G. R. Booker [Boo+67] provides a theoretical interpretation for the phenomena based on the Darwin-Howie-Whelan theory. |
| 1973 | J. A. Venables and C. J. Harland [VH73] describe another diffraction technique capable of providing local crystallographic information termed electron backscattering patterns (EBSP) or latter electron backscattered diffraction (EBS). |
| 1977-9 | 5 and 7 years, respectively, after Spencer <i>et al.</i> [SHH72] predicted from dynamical simulations that individual dislocation could be visible in a highly optimised SEM, Pitaval and Morin <i>et al.</i> [Mor+79] actually observed individual dislocations, developing a new technique of its own known as electron channelling contrast imaging (ECCI). |
| 2012 | The latest diffraction technique in the SEM with improved spatial resolution compared to EBSD is reported as transmission EBSD (t-EBSD) by R. R. Keller and R. H. Geiss [KG12] and Transmission Kikuchi Diffraction (TKD) by P. W. Trimby [Tri12a]. |

theory can be described by solving Maxwell's equations in a continuous medium with dielectric susceptibility distributed periodically in three dimensions. It is in this form that the dynamical diffraction theory is most used today and also the one we will use in this work.

The inverse effect, theory driving experimental observation this time, was triggered by de Broglie's doctoral thesis where he speculated that all particles ought to also behave as waves. Indeed, in just a couple of years, in 1927, G. P. Thomson [TR27] in UK pointed high energy electrons (10–60keV) at a thin film and recorded the results on a fluorescent screen placed underneath the sample. Not only did they observe a diffraction pattern which would confirm the wave like nature of electrons, but the diffraction behaviour obeyed the familiar Bragg law, albeit for a very small Bragg angle. Davisson and Germer [DG27] in US observed electrons diffraction using a remarkably different set up (and rather mechanically complex). They used low energy electrons (30–600 eV) which scattered, and diffracted from only the top layer of atoms of a crystalline sample. This approach placed the basis of what will become low energy electron diffraction (LEED) microscopy.

These observations provided the experimental means for the development of quantum mechanics, but more, more applicable to our story, marked the dawn of electron microscopy. Similarly to X-ray diffraction crystallography, electrons, with a wide range of energies and therefore wavelength, as we have seen, could now be used to study crystal structures. Electrons show a number of advantages over X-rays including the obvious smaller wavelengths meaning potential higher spatial resolution. From Thomson's experiment it becomes readily apparent also the fact that electrons are diffracted much more strongly than X-ray, requiring only small interaction volumes which means electron microscopy would easily lend itself applicable to the characterisation of micro-structures.

Before that would happen in practice, it became apparent that the diffraction theory must again be expanded to accommodate for this stronger and more complex interaction with matter of charged electrons. Indeed, a number of dynamical theories for electrons have been developed over the years all carrying the legacy of X-ray diffraction theoretical interpretations.

Electrons diffracting through crystals gives access to a plethora of information and diffraction signals. When, in 1928, Shoji Nishikawa and Seishi Kikuchi directed a beam of 50 keV electrons on a calcite sample at a grazing incidence of 6° diffraction was a phenomena associated with spots. But they have seen "... black and white lines in pairs due to multiple scattering and selective reflection" which we now recognise as diffraction patterns.

A number of studies quickly followed the investigation of these band features in electron diffraction. Notable here is that in 1937 Boersch [Boe37] (paper in German) already proposed that these observations could be explained using von Laue's dynamical theory of electron diffraction. By 1948, a number of models have already been proposed to explain the full range of features in the Kikuchi patterns. Artmann [Art48] (paper in German) used the reciprocity law and solved the Schrödinger equation for bound electrons in the three dimensional crystal potential to predict with good accuracy the intensity profile and geometry of Kikuchi bands.

While a beautiful physics experiment, electron diffraction would have lacked practical application before the development of the electron microscope; first the direct mode, where electrons penetrated through a sample and the image was collected on the other side (TEM) and, a few years later, the scanning mode, in which the incident electron beam scans over the sample in a raster manner and the backscattered electrons are recorded one "pixel" at a time to form an image (SEM). More insights could be derived now from the electron signal. The diffraction spots observed in the TEM or when at a grazing incidence angle in the SEM¹ were identified to be closely related to the crystal structure.

In 1967, yet another crystal structure signal was observed in the SEM by Coates [Coa67]: the dependence of the backscattered electron yield on the orientation of the crystal with respect to the incident beam; what future microscopists will label as electron channelling patterns (ECP). The same year Booker *et al.* [Boo+67] gave an qualitative explanation of the phenomenon, comparing the "bands of contrast" with fringes observed from bent thin foils in TEM. It was, nevertheless, clear that this measurement could provide information on the bulk crystal structure and orientation and expand the toolkit for material characterisation.

The timely development of models and computer-aided indexing solutions for patterns from all seven crystal systems meant that fully automated EBSD could replace X-ray pole figure measurements for texture analysis avoiding the limitation that come with X-ray analysis where the sample is tilted through large angles. The model developed by Howie and Whelan for electron diffraction intensity predictions in the TEM could be easily be modified and implemented on a computer, as Hirsch had shown, to account for dislocations displacement fields and therefore predict dislocation contrast in transmission mode open the world of defect characterisation.

However, it was not immediate that the spatial resolution of the SEM overtook that of the optical microscope; it was only in the late 1970 that we can talk about

¹ Both conditions in which the crystal volume with which the electron beam interacts is small enough to approximate the behaviour to kinematical diffraction.

high resolution SEM (HR-SEM) equipped with a field emission gun that could reach the same resolution as the TEM. Both of these developments were instrumental in achieving experimentally what Booker [Boo+67] predicted, namely the detection of individual dislocation in the SEM. We will talk more about the short history of ECCI in the next chapter.

It transpires that even far from perfect crystals, electron diffraction can provide great insight. By scanning over a micro-granular crystal in the SEM and recording the EBSD image for each pixel, one can pick up the orientation of individual grains using orientation indexing techniques. In the world of material science this is extremely powerful as a tool for mapping the quality of a new material in terms of its grains. If the detector is placed in the SEM such that mostly forward scattered electrons are collected, then one can obtain Kikuchi lines (EBSD) from a very small crystal volume or, in the language of microscopy, high spatial resolution. We will talk more in Chapter 5 about the novel Kikuchi diffraction technique, known as TKD, that can increase the spatial resolution even further allowing the study of truly nano-structural materials.

By the late 80s and early 90s, with the development of computers, we start talking about pattern indexing software systems. A number of companies have focused on developing modern EBSD systems packaged with indexing software appeared and experienced reasonable success catering to the industry's requirements. Unfortunately, it also marked the steady decline of academic interest in open electron diffraction software. In Chapter 5 I describe one such unicorn, and how the TKD modality was implemented and what the models are predicting.

In about the same time when EBSD was becoming popular in the world of material science, a new SEM diffraction technique was also gaining traction. If the geometry was such that the incident beam was close to a Bragg condition, high contrast around small crystallographic defects could be observed in the recorded images, similar to the case in TEM. This technique which will be known as electron channelling contrast imaging (ECCI). Since Booker already hinted at theoretical interpretation of these effects in relationship with the available Darwin-Howie-Whelan model, the next obvious step is to extend and implement the dynamical model such that it takes into account such small phase perturbations and can predict contrast profiles for dislocations observed in SEM. This is exactly what I endeavour to do in Chapter 4.

3.2 Kinematical versus dynamical theory

The geometrical or kinematical diffraction theory, developed for X-rays, assumes that each incident wave is scattered only once in the sample and all other interactions can be ignored. This, in turn, implies that 1) the amplitude incident on each of the diffraction centres is the same and 2) the sum of the diffracted amplitude is the sum of individual amplitudes diffracted by each diffraction centre. Therefore, the geometrical phase difference between diffracted beams is the main contributor to the diffraction pattern and the distribution of diffracted amplitudes in reciprocal space is the Fourier Transform of diffraction centres in real space.

The integrated elastically scattered intensities predicted by the kinematical theory are proportional to the square of the structure factor and also with the crystal volume with which the incident wave interacts. Because no loss of amplitude is taken into account, the kinematical theory predicts that as the interaction crystal volume increases to infinity so would the intensity of the diffracted beam. This is obviously nonsensical for anything but very small crystals. We can conclude that the kinematical approach holds well only for relatively weak interactions (X-ray interaction with matter) and/or small crystals. Darwin [Dar22] extended this theory and showed it can also be applied to large but defected crystals. Additionally, there is no phase information tracked in the kinematical theory and this becomes important for multiple reflections.

TABLE 3.3: Kinematical vs. dynamical diffraction theories.

| Kinematical theory | Dynamical theory |
|---|------------------------------------|
| weak interaction | strong interaction |
| small crystal OR large defected crystal | infinite crystal |
| single scattering | multiple scattering “pendellösung” |
| assumes no loss | takes loss into account |
| no phase information | carries information about phase |
| intensity $\propto F_{hkl} ^2$ | intensity $\propto \psi_g ^2$ |

Electrons manifest wave properties similar to those of X-rays and their diffraction behaviour in crystals is in many ways analogous to that of X-rays. Nevertheless, it should be obvious by now to the careful reader that the single scattering approximation of the kinematical theory will not be suitable for the strong interactions of electrons in crystals composed of more than a few layers. For these reasons the dynamical

diffraction theory for fast electrons has been developed and applied to quantitatively interpret electron diffraction patterns.

3.3 Diffraction geometry

Having set the context of diffraction as a means of identifying the crystal structures of elements and compounds, we will now explore further the governing rule of the phenomena, that of the Bragg's law. On page 32 I reminded the reader of the geometrical conditions for constructive interference to occur. The condition was given in terms of real space parameters which is why this form is also known as the real space Bragg's condition.

But we can translate the diffracted beam in Fig. 2.10 such that it has the same origin as the incident beam as shown in Fig. 3.1. Here we label the incident beam wave vector by \mathbf{k}_0 and the diffracted beam wave vector by \mathbf{k}_g . Their origin is denoted by C. From the definition of elastic scattering processes, we know that the length of wave vectors \mathbf{k}_0 and \mathbf{k}_g must be the same: $|\mathbf{k}_0| = |\mathbf{k}_g| = 1/\lambda$. It is interesting to write out the distance OG between the endpoints of these vectors:

$$OG = |\mathbf{k}_0| \sin \theta_B + |\mathbf{k}_0| \sin \theta_B = \frac{2 \sin \theta_B}{\lambda} = \frac{1}{d_{hkl}} = |\mathbf{g}_{hkl}|.$$

where we made use of Bragg's law in the penultimate equality.

3.3.1 Bragg's law in reciprocal space – Ewald sphere

Now that we have reviewed all the relevant physical names we can rewrite the Bragg's law in terms of parameters defined in the reciprocal space:

$$\mathbf{k}_g = \mathbf{k}_0 + \mathbf{g}. \quad (3.1)$$

With this equality Ewald showed that we can rephrase Bragg's equation to say: *If we consider a sphere of radius $|\mathbf{k}_0| = 1/\lambda$ centred at the origin of the incident beam vector, then a plane $(h k l)$ will diffract the beam if the reciprocal lattice point \mathbf{g}_{hkl} lies on that sphere.* This reciprocal space geometrical construction is known as the *Ewald sphere*. Even though we will relax this diffraction condition very soon, the Ewald sphere remains a core tool when talking about diffraction.

For instance, when we rotate or tilt the sample with respect to the incident beam until we hit a diffraction condition, we move the incident beam wave vector with

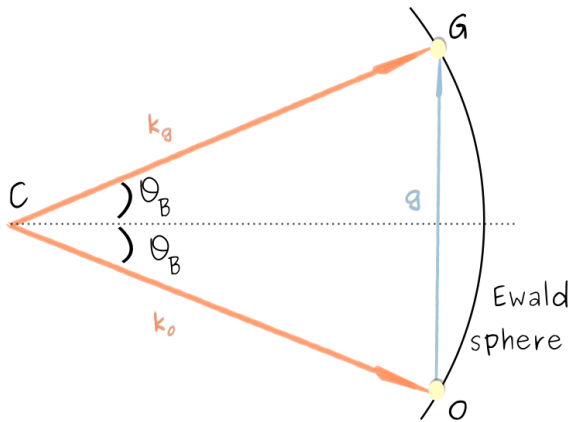


FIGURE 3.1: Ewald sphere construction in the exact Bragg condition.

respect to the lattice, and with it the Ewald sphere, until a reciprocal space lattice points lies on the the sphere. Note that this is a 3D construction and we only show in the figure above a 2D projection of it.

The lengths in Fig. 3.1 are also grossly exaggerated. For high energy electrons the wave vectors are long with respect to a much denser lattice than shown here. Drawn to scale, the portion of the Ewald sphere showing first order diffraction will be almost flat and the likelihood of multiple lattice points lying on the sphere would be somewhat increased.

Knowing all its parameters we can also write out the equation of the Ewald sphere. If we set the origin, O , to be to be the endpoint of the incident beam wave vector, then the centre of the sphere is at position $-k$. For any reciprocal lattice vector q , we can tell if it lies on the Ewald sphere if the following is true:

$$q \cdot (2k_0 + q) = 0.$$

When we enforce g to be on the Ewald sphere and use Eq. 3.1, the above becomes:

$$g \cdot (2k_0 + g) = g \cdot (k_0 + k_g) = 0. \quad (3.2)$$

This is known as the Bragg equation in reciprocal space and it tells us that the vector $k_0 + k_g$ must be on the plane normal to g for the exact Bragg condition to be met (see Chapter 2 in ref. [DG03] for more details).

As useful as the reciprocal space description of the diffraction condition is, we need to introduce a real space parameter which will prove essential: the normal to crystal sample surface.

3.3.2 Diffraction geometries

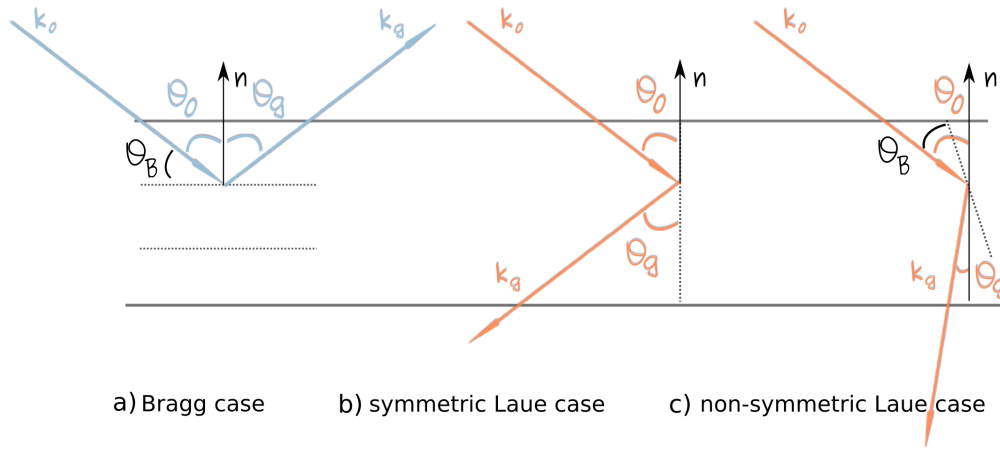


FIGURE 3.2: Scattering geometry cases relevant in electron diffraction.
The angles have been grossly exaggerated.

Let us introduce two new angles: θ_0 as the angle between the incident beam direction and the sample normal, \mathbf{n} , and, reversely, θ_g as the angle between the diffracted beam direction and the sample normal (see Fig. 3.2). Depending on the general direction of the diffraction planes with respect to the crystal sample surface, electron microscopists differentiate between:

- *symmetric Bragg case* (Fig. 3.2 a)) : when the diffracted beam escapes the sample through the same surface the incident beam entered. This geometry is defined by the film normal being also the normal to the diffracting planes $\{hkl\}$. The relationship between the angles is:

$$\theta_0 = \theta_g = \pi/2 - \theta_B.$$

- *symmetric Laue case* (Fig. 3.2 b)) : when the diffracted beam escapes from the bottom of the sample. This geometry is defined by the film normal being parallel to the diffracting planes $\{hkl\}$. The relationship between the angles is:

$$\theta_0 = \theta_g = \theta_B.$$

- *non-symmetric Laue case* (Fig. 3.2 c)) : is a generalised form of the one above. There is now a nontrivial angle between the diffracting planes and the surface normal. The only relationship we can write between the three angles is:

$$\theta_0 + \theta_g = 2\theta_B.$$

The form of dynamical theory commonly used in TEM diffraction contrast description is based on the symmetric Laue case [HW61]. This geometry is assumed valid for a large range of diffraction conditions that deviate from the perfect symmetric case. Whelan and Hirsch [WH57] showed that the angle of a stacking fault² introduced in a perfect crystal does not affect two beam dynamical calculations of diffraction intensities. Furthermore, Saldin *et al.* [SWR78] showed that the Darwin equations predict very small errors for a wide range of incident angles when the non-symmetric Laue case is approximated to a symmetric one. A good summary of this discussion was published by Sheinin and Jap [SJ79] who also took the conversation further. They used a Bloch wave formalism to test the limits of this approximation and concluded that for strong beams³ there is no significant difference between the predictions in the symmetric and non-symmetric Laue cases.

3.4 Diffraction intensity

We have explored so far the geometrical conditions for constructive interference, *i.e.*, diffraction, to occur in a crystal. But, as we will see on page 73, while a necessary condition, Bragg's law being satisfied is not sufficient for non zero intensity along a given direction. This is because Bragg's law gives us information only about the lattice orientation with respect to the incoming beam direction. However, we are free to decorate this lattice in more than one way, and the motif can end up scattering out of phase with the planes.

It therefore becomes important to understand the probability of scattering first from a single atom. Bragg's law remains the same for photons, electrons or neutrons even though the Bragg angles can vary greatly, depending, as they are, on the energy of the incoming beam. But the scattering physics and resulting intensity is dependent on the type of incident particle. We have seen in Table 3.1 on page 54 that while X-rays interact only with the electron cloud, electrons are scattered by both the cloud and the atom nuclei. In the next pages we will see how to calculate scattering probabilities, *i.e.*, *scattering factors*, for a number of common directions in binary group-III nitride systems.

²A stacking fault is a planar defect telling us that for a given set of planes of atoms there is an error in their stacking structure.

³Strong beams as opposed to weak beam conditions where the deviation from the exact Bragg condition is quite large. More about this on page 79.

Next, on page 73 we put all atoms on a unit cell and calculate the total scatter probability as a sum of all their contributions for a given direction. In the process we will introduce the useful mathematical concept of *structure factor* which describes how the positions of the atoms in the unit cell affect the intensity of the diffracted beam.

The high energy of the incoming beam simplifies the crystal to the behaviour of isolated spherical point scatterers. The parameters discussed in this sections are important because they constitute the only information we track about the crystal structure when we model electron diffraction. On page 77 we discuss how to calculate a crystal electrostatic potential that takes into account all this directional scattering information.

Finally, on page 75, we calculate the structure factors for a few nitride systems and discuss the systematic absences present in wurtzite.

3.4.1 X-ray scattering by electron charge density and the X-ray scattering factor

When a linearly polarised, monochromatic plane-wave X-ray beam is incident upon a stationary atom of atomic number Z , each of its Z electrons will scatter the X-ray waves. The oscillating electric field of the incident X-ray beam excites the individual electrons of mass m and charge e causing them to oscillate at the same frequency as the incident radiation. In turn, the individual electrons, now in the form of accelerated charge, will become a source of spherically radiated X-rays of frequency equal to the incident one. Multiple scattering processes can occur including incoherent scattering or Compton processes but for now we will only consider coherent scattering.

The intensity of a scattered radiation at a distance r from the scattering site of the individual electrons in terms of the incident radiation intensity I_0 and the scattering angle θ is well described by Thomson's equation:

$$I = I_0 \frac{K}{r^2} \sin^2 \theta, \quad (3.3)$$

which highlights the high directionality of coherent scattering. That is to say, most of the intensity of scattered X-rays will be in the forward direction. In the above equation K is a very small constant given by:

$$K = \left(\frac{\mu_0}{4\pi} \right)^2 \times \left(\frac{e^4}{m^2} \right) = 7.9 \times 10^{-30} \text{ m}^2$$

indicating that in practice scattering effects can become measurable only when a large number of electrons ($> 10^{23}$) are scattering.

In the forward direction, each of the Z electrons will scatter the X-rays beam with an identical phase change of π and no destructive interference (see Fig. 3.3 a)). Scattering in any other direction, $\theta \neq 0$, will result in pathway differences between X-rays scattered by different electrons. The loss of intensity due to destructive interference will translate to a reduced scattered intensity when compared to the forward scattered case (see Fig. 3.3 b)).

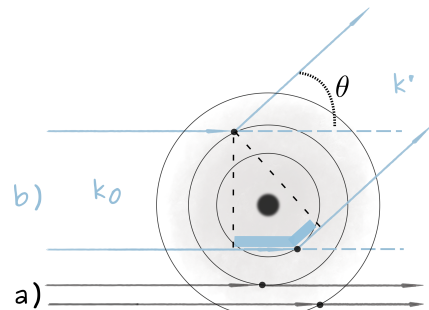


FIGURE 3.3: Schematic diagram of a) forward scattering and b) scattering by an angle θ . Note the pathway difference marked by thick blue line in b).

It is now time to introduce the atomic scattering factor, f^X , for a given direction θ and wavelength λ as the ratio of amplitude scattered by an entire atom to the amplitude scattered by only one electron in the same direction. Equivalently, the atomic scattering factor can be thought of as the probability amplitude that the atomic potential of an atom will scatter an incident wave with wave vector k_0 into the direction k' . But this probability is the Fourier transform of the atomic potential that does the scattering, which in the case of incident X-rays is the electron charge density. The *International Tables of Crystallography* [Aut06] contain tabulated calculated scattering intensity values for all atoms. Since it would be tedious to list the scattering factor values for all possible θ and λ , it is often more convenient to list them as curve fitting parameters. The scattering factor fitted function as a function of the variable $s = \sin \theta / \lambda$ is then given by:

$$f^X(s) = Z - 41.78214[\text{\AA}^2] s^2 \sum_{i=1}^N a_i e^{-b_i s^2} \quad (3.4)$$

Table 3.4 lists the dimensionless Doyle-Turner [DT68] a_i, b_i parameters values ($N = 4$) for a few group III-nitrides semiconductor elements: N, Al, Ga and In. Note that the values in the table are given assuming s is expressed in \AA^{-1} and λ is expressed in \AA .

The behaviour of the X-ray scattering factor, f_{el}^X , is shown in Figure 3.4 for N, Al, Ga and In. The coloured, vertical lines indicate the s values for the most common

TABLE 3.4: Doyle & Turner atomic scattering parameters [DT68] for a few elements. These values were calculated assuming that s is expressed in \AA^{-1} .

| Element | Z | a_1 | b_1 | a_2 | b_2 | a_3 | b_3 | a_4 | b_4 |
|---------|----|-------|--------|-------|--------|-------|-------|-------|-------|
| N | 7 | 0.572 | 28.847 | 1.043 | 9.052 | 0.465 | 2.421 | 0.131 | 0.317 |
| Al | 13 | 2.276 | 72.322 | 2.428 | 19.773 | 0.858 | 3.080 | 0.317 | 0.408 |
| Ga | 31 | 2.321 | 65.602 | 2.486 | 15.458 | 1.688 | 2.581 | 0.599 | 0.351 |
| In | 49 | 3.153 | 66.649 | 3.557 | 14.449 | 2.818 | 2.976 | 0.884 | 0.335 |

planes in wurtzite materials (see Fig. 2.6). For instance, the first vertical line (orange), reaching the In line, corresponds to the s value for the c-plane in InN. The scattering factor for $\theta = 0$ is the atomic number, and as expected, the curve decreases rapidly with increasing scattering angle (or decreasing wavelength) or, increasing interplanar distance, d_{hkl} . The code used for these plots and the interactive images can be found in the Jupyter notebook `scatterFactor.ipynb`.

We can observe that the light N atom will scatter fewer X-rays compared to the heavier elements, but at a rate that is consistently comparable to that from Al atoms. We can already conclude that the two species of atoms in AlN will scatter X-rays at comparable rates ($f_A^X l / f_N^X = 1 - 2$) and that this ratio depends only lightly on the crystal direction as the two curves are almost parallel. In the `scatterFactor.ipynb` I also plotted the scattering factors relative to f_N^X to make these ratios more readable.

In contrast, with the increase in mass of the group-III element ($M_{Al} < M_{Ga} < M_{In}$), the rate of scattering becomes significantly different, with Ga scattering X-rays 4-5 times more efficiently than Al, such that we can expect most of the signal to have scattered from the heavy element. Not only this, but for these heavier group-III elements compounds, the more closely packed the planes are (larger s) the more the scattering from the heavier element dominates when compared to scattering from N.

Note that I only show the curves here for values of $s \leq 0.5 \text{\AA}^{-1}$ ($d_{hkl} \geq 1 \text{\AA}$) which is large enough for some of the more common first order reflections. Bear in mind that if we were interested in scattering rates from the higher order reflections we would have to look further to the right on this graph (for AlN $s_{220} = 0.64 \text{\AA}^{-1}$).

3.4.2 Electron scattering by a single atom and the electron scattering factor

As far as the incoming electron beam is concerned, the electrostatic potential $V_{atom}(\mathbf{r})$ of one atom in the specimen is related to its spherically symmetric charge distribution through Poisson's equation:

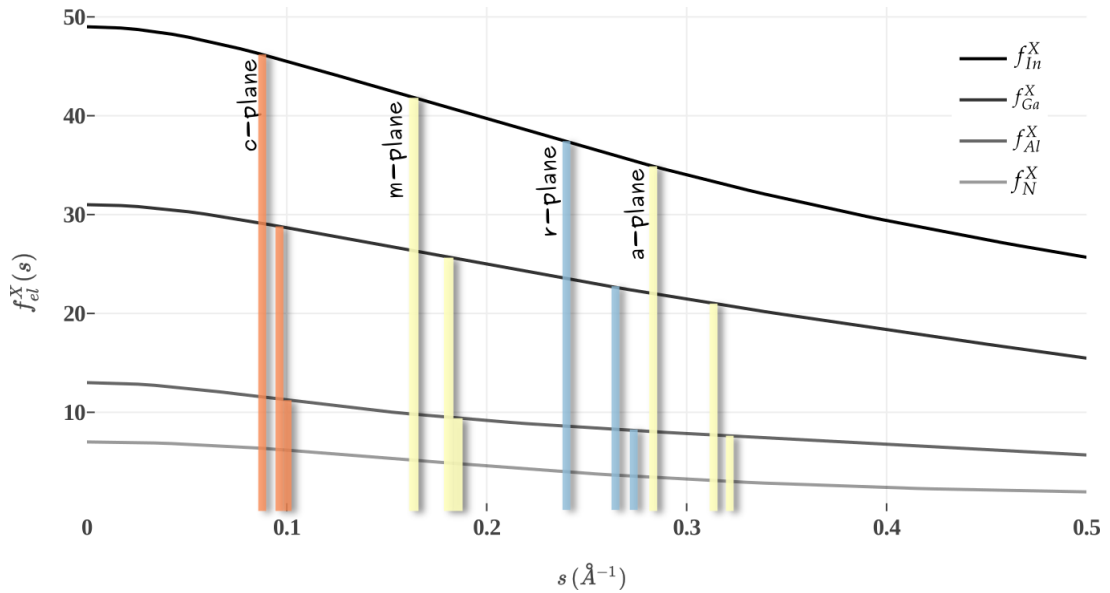


FIGURE 3.4: Atomic X-ray scattering factors for In, Ga, Al and N with superimposed vertical lines indicating the s -value for the most common planes in nitrides. The vertical line extend to the group III element curve which makes up the III_{el}N compound (*i.e.*, InN, GaN and AlN in this order) for which s_{hkl} was computed.

$$\Delta V_{atom}(\mathbf{r}) = -\frac{|e|}{\epsilon_0} (\rho_n(\mathbf{r}) - \rho_e(\mathbf{r})), \quad (3.5)$$

where Δ is the Laplacian (second order differential) operator. It will contain a contribution from the point charge nucleus ρ_n and a contribution from the electron cloud charge distribution ρ_e .

This does not take us very far since analytical solutions for the electron charge density can only be written for hydrogen. Luckily, the X-ray scattering amplitude calculated on the previous page (Eq. 3.4) is the Fourier transform of the electron charge density $\rho_r(\mathbf{r})$ so all that is left to do is to calculate the inverse Fourier transform of the X-ray diffraction amplitude.

We are now ready to define the *atomic scattering factor for an electron beam* $f^e(\Delta\mathbf{k})$, similarly to the case of an incident X-ray beam, as the probability that an incident plane wave with wave vector \mathbf{k}_0 is scattered by the atomic potential $V_{atom}(\mathbf{r})$ in the direction \mathbf{k}' . Where we introduced the momentum transfer vector $\Delta\mathbf{k} = \mathbf{k}' - \mathbf{k}_0$. Or, equivalently, we can write the probability as the Fourier transform of the atomic potential distribution $V_{atom}(\mathbf{r})$:

$$f^e(\Delta\mathbf{k}) \equiv \iiint V_{atom}(\mathbf{r}) e^{-2\pi i \Delta\mathbf{k} \cdot \mathbf{r}} d\mathbf{r} \quad (3.6)$$

Since the atoms studied are part of crystals we can use Bragg's condition, $\mathbf{k}' = \mathbf{k}_0 + g$. We will again make use of the useful variable transformation $s = \sin \theta / \lambda$, which at the Bragg angle has the magnitude:

$$|\mathbf{s}| = \frac{\sin \theta}{\lambda} = \frac{|\mathbf{g}_{hkl}|}{2} = \frac{1}{2d_{hkl}}. \quad (3.7)$$

Making the approximation that the nuclear charge density can be mathematically written as a delta function of weight Z, we are now ready to inverse Fourier transform all the quantities in Eq. 3.5 to obtain:

$$f^e(s) = \frac{|e|}{16\pi^2\epsilon_0} \frac{1}{|s|^2} [Z - f^X(s)]. \quad (3.8)$$

The reader might recognise equation 3.8 to be the Mott-Bethe formula. The use of the variable s defined in Eq. 3.7 means that for a given crystal structure the atomic scattering factor is only "sampled" at scattering vectors corresponding to half the reciprocal lattice vectors \mathbf{g}_{hkl} . It also means that, since for a given crystal structure the magnitude of \mathbf{s} is independent of the wavelength of electrons, the electron scattering factor is independent on the experimental conditions.

If we use the convenient Doyle-Turner parametrised form of the X-ray scattering factor given in Eq. 3.4 we can rewrite the Mott-Bethe formula to be:

$$f^e(s) = 0.04787801 [\text{V}\text{\AA}^3] \sum_{i=1}^{N=4} a_i e^{-b_i s^2}, \quad (3.9)$$

where we wrote the electron scattering function in units of $\text{V}\text{\AA}^3$ in this form.

This expansion is accurate for values of s up to 20 nm^{-1} . Values for the electron scattering factors in a large number of different materials can also be found in the *International Tables for Crystallography* [WP99]. Care must be taken when comparing values from different sources since the factor 0.0478701 can be present or not in the version of Mott-Bethe equation. Additionally, it is also possible for the pre-multiplier factor to be given in units of Vnm^3 resulting in the function having the same units.

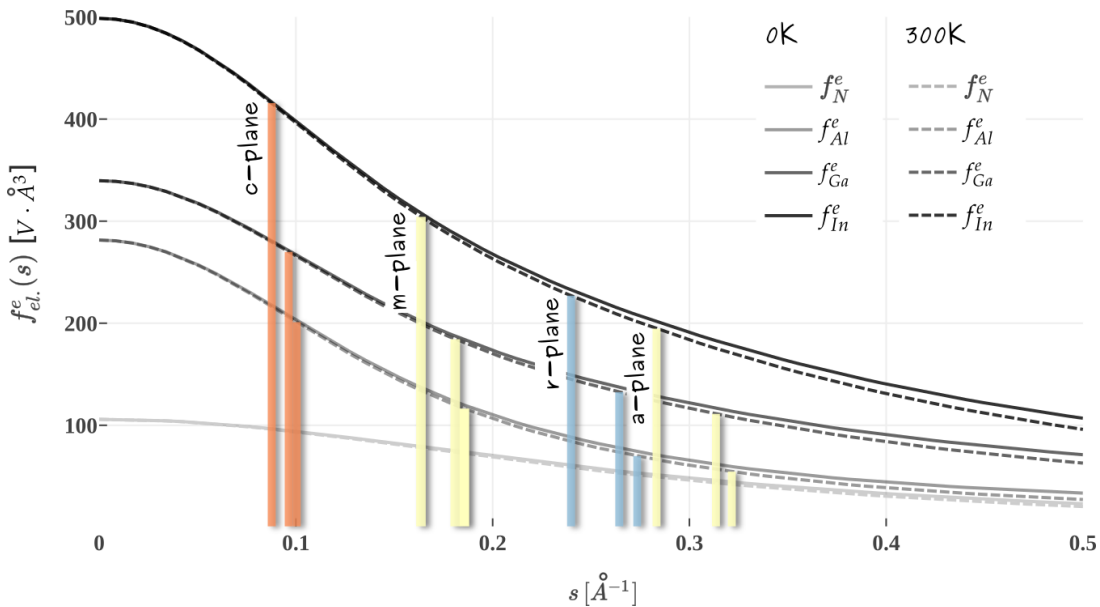


FIGURE 3.5: Atomic electron scattering factors for In, Ga, Al, N with superimposed coloured lines indicating the most common planes for nitrides (see Fig. 2.6).

The derivation of Eq. 3.9 made the assumption that the atom is completely still (or at temperature of 0 K). Nevertheless, we have already covered in Section 2.1.2 on page 17, that this is a very gross assumption and for any true attempt of understanding scattering we ought to take into account atomic vibrations. We therefore use Eq. 3.10 to correct the scattering factor for isotropic, thermal atomic vibrations so we can rewrite the corrected Mott-Bethe formula as:

$$f_T^e(s) = 0.04787801 \sum_{i=1}^{N=4} a_i e^{-b_i s^2} e^{-B_{el.} s^2}, \quad (3.10)$$

where $B_{el.}$ is the Debye-Waller factor for the given element which we calculated on page 17 for some of the nitride elements.

Figure 3.5 plots electron scattering factors (Eq. 3.9) for Al, Ga, In and N in continuous lines together with the DW corrected versions (Eq. 3.10) at 300 K in dashed lines. We can see the overall behaviour is not completely dissimilar from that of X-ray scattering in Fig. 3.4. See the description for that figure on how to read the vertical lines. The code used for this plot can be found, as well, in the Jupyter notebook `scatterFactor.ipynb`.

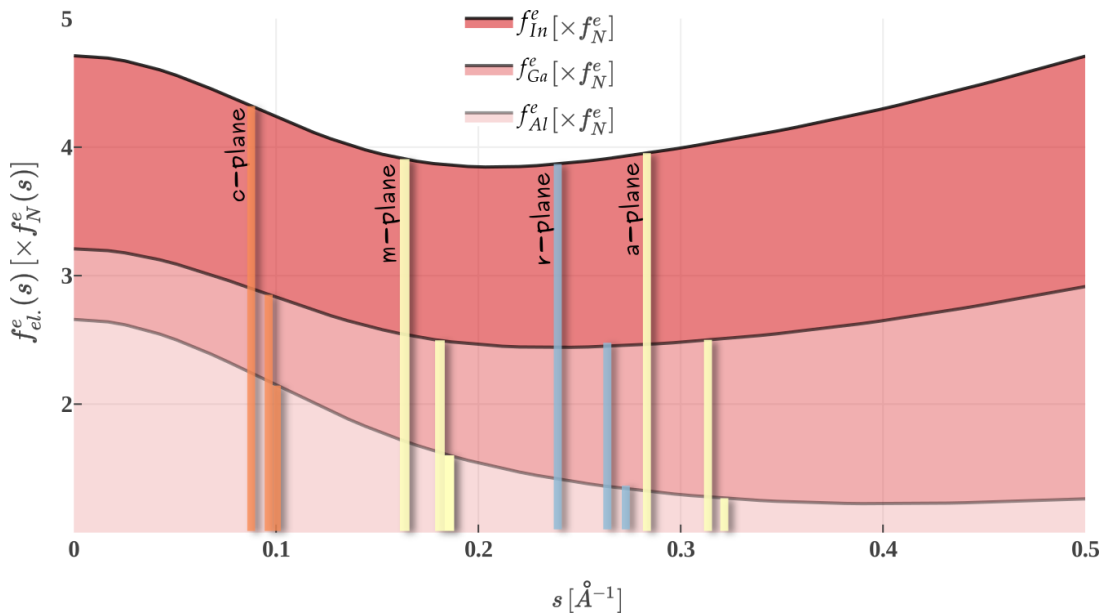


FIGURE 3.6: Relative atomic electron scattering factors for In, Ga, Al in terms of scattering from N atoms. The superimposed coloured lines indicating the most common planes for nitrides are the same as before.

As discussed on page 54 and showcased in Table 3.1, electron beams scatter significantly more in matter compared to X-rays which also transpires when comparing the values on the y-axes. This is due both to their smaller wavelengths and the fact that they interact with the entire atom not just the electric field. The added delta function-like nucleus potential makes the electron scattering factor much more sensitive to the direction of scattering and we can see the curve decays more rapidly than in the X-rays case.

The DW corrections become significant the more the interplanar distances are reduced. That is to be expected since the more comparable the interplanar distance becomes to the spatial range of the atom potential the more the point average position approximation breaks apart. The correction continues to become more significant as we go to higher values of reciprocal interplanar distances (s_{hkl}), e.g. for higher order reflections. The other factor that affects the correction factor is the size of the atom in the first place, with heavier atoms requiring larger correction factors. We can see that for the chosen range of s -values, the correction factor for N is about 1% and therefore almost indistinguishable in these figures. For In, however, it becomes close to 10% especially on the right side of the x-axis.

In Fig. 3.6 I show the same electron scattering factors from Al, In and Ga but this time relative to the scattering factor for N atoms in order to highlight how the rate of

scattering changes for different planes in binary compounds. For AlN the electrons scatter 1-3 times more frequently from the Al atoms than from the N atoms. This rate is highly sensitive to the direction of scattering such that for larger interplanar distances (*c*-plane) the scattering intensity is made up two parts from the group-III element scattering and one part from N. At smaller interplanar distances the scattering from N and Al is almost equal.

Because the electron scattering factor for N decays faster with s than that for Ga and In, the relative scattering for these heavier group III elements goes up after about $s = 0.2 \text{ \AA}$. Such that at small interplanar distances, *e.g.* higher order reflections, scattering from the heavier element in the compound dominates 3-7 times that from N atoms.

3.4.3 Scattering by the unit cell and the electron structure factor

Now that we know how charged particles scatter from a single atoms and from lattice planes, we can tackle a full unit cell by taking into account the relative positions of all the atoms in it. More practically, we need to address how we account for the relative phase of scattering from two atoms not belonging to the same family of planes. I'll show here the derivation from *Structure of Materials ...* [DGM12] pg. 298 which uses, as a working example, an atom places in between two planes.

Let us revisit Fig. 2.10, which I update here in Fig. 3.7. Beams 1) and 2), in blue, are scattered in phase since the incident angle $\theta = \theta_B$ satisfies Bragg condition. Let this set of planes be (100) . If we now add an atom at position r such that it lives on the orange plane, let it be (200) , in between the (100) , let us investigate how much destructive interference will it contribute to the scattered signal when a beam 3), in orange, scatters from it.

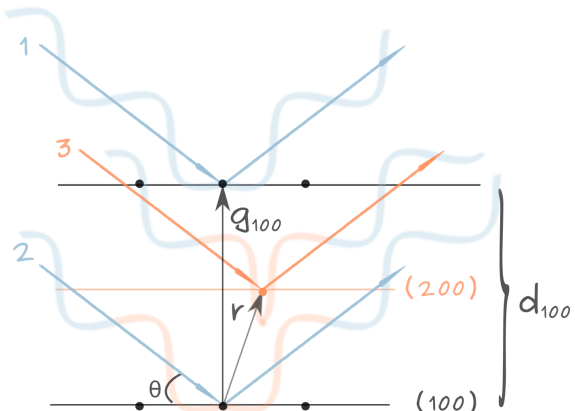


FIGURE 3.7: What happens to the Bragg's law when we add an atom in between planes? [Based on Fig. 12.4 in [DGM12]]

To answer this, section 2.1.8 on page 32 already prepared us to think about the difference in phase between beams 1) or 3) and beam 2). The path difference between the coherent scattered beams 1) and 2) is a full wavelength λ . It turns our that the difference in phase between beam 1) and 3) is independent on where on plane (200)

the atoms sits, all that matters is the distance to the planes (100). For plane (200) the extra atom sits at a distance $d_{hkl}/2$ from planes (100). This distance can be written as the projection of vector \mathbf{r} onto \mathbf{g}_{100} , *i.e.*, $\mathbf{g}_{100} \cdot \mathbf{r}$. We can then transform this distance to a phase by multiplying by 2π :

$$\phi_{1 \rightarrow 3} = 2\pi \mathbf{r} \cdot \mathbf{g}_{100} = \pi$$

This means the scattered beam 3) will be out of phase with 1) and 2), resulting in destructive interference. And this despite the fact that the Bragg condition is geometrically satisfied for (100) planes!

The phase equation above can be generalised to scattering from any atom at position $\mathbf{r} = (x, y, z)$ living outside a set of planes ($h k l$):

$$\phi = 2\pi \mathbf{r} \cdot \mathbf{g}_{hkl} = 2\pi(hx + ky + lz)$$

We are now ready to write out the full unit cell to the total scattering from planes ($h k l$) as the sum over the contributions of all the atoms:

$$F_{hkl} = \sum_{j=1}^N f_j^e(s) e^{i\phi_j} = \sum_{j=1}^N f_j^e(s) e^{2\pi i \mathbf{r}_j \cdot \mathbf{g}_{hkl}} = \sum_{j=1}^N f_j^e(s) e^{2\pi i (hx_j + ky_j + lz_j)} \quad (3.11)$$

where the index j in the sum goes over all the N atoms in the unit cell and $s = \frac{\theta_{hkl}}{\lambda}$.

We can generalise the sum over all the atoms in the fundamental unit cell, to be the sum over the atoms in the asymmetric unit cell, N_a , times a sum over all the equivalent positions of those atoms in the fundamental unit cell (*i.e.*, orbit)[DG03]. We can write the second sum with the help of the Seitz symbol ($D|\mathbf{t}$) (see page 172 in Appendix C):

$$F_{hkl} = \sum_{j=1}^{N_a} f_j^e(s) \sum_{(D|\mathbf{t})} e^{2\pi i \mathbf{g}_{hkl} \cdot (D|\mathbf{t})[\mathbf{r}_j]} \quad (3.12)$$

This sum is known as the *structure factor* and, as we have seen in Table 3.3 it is used in the kinematical model to predict the intensity of diffracted electrons. We will talk about its prediction for nitrides in the following section.

3.4.4 The structure factor in wurtzite nitrides

It is finally time to fill in Eq. 3.12 or Eq. 3.11 the position of the atoms in a wurtzite unit cell, Eq. 2.43 to Eq. 2.46 (given on page 51), and derive some structure factors for a few \mathbf{g}_{hkl} vectors:

$$\begin{aligned} \text{wurtzite } F_{hkl} &= f_{III_{el}}^e \left[(-1)^{2(\frac{h}{3} + \frac{2k}{3})} + (-1)^{2(\frac{2h}{3} + \frac{k}{3} + \frac{l}{2})} \right] \\ &\quad + f_N^e \left[(-1)^{2(\frac{h}{3} + \frac{2k}{3} + \frac{3l}{8})} + (-1)^{2(\frac{2h}{3} + \frac{k}{3} + \frac{7l}{8})} \right] \\ &= (-1)^{\frac{2h}{3}} (-1)^{\frac{4k}{3}} \left(f_{III_{el}}^e + (-1)^{\frac{3l}{8}} f_N^e \right) \left[1 + (-1)^{(\frac{2(h-k)}{3} + l)} \right] \end{aligned} \quad (3.13)$$

where $f_{III_{el}}^e$ is the scattering factor of the group-III element and we made use of the identity $e^{-i\pi n} = (-1)^n$ in the second step.

Table 3.5 shows computed values of F_{hkl} for the three nitride systems discussed so far in a number of orientations. These values are in general complex and I show them here in the Euler notation form $F_{hkl} = |F_{hkl}|e^{i\phi}$ where $|F_{hkl}|$ is the absolute value and ϕ the phase. If the reader is interested in calculating the structure factors for different directions, my script can be found in `structureFactor.ipynb` and it is just a matter of changing the h, k, l values. In the kinematical diffraction theory, often used in X-ray diffraction predictions, the diffracted intensity is simply:

$$I_{\mathbf{g}} = F_{\mathbf{g}} F_{\mathbf{g}}^* = |F_{\mathbf{g}}|^2 \quad (3.14)$$

It is important to acknowledge the limitations of these values since many assumptions were made to obtain them, not the least that the crystals in question are perfect. If this were the case, perfect semiconductor crystals being a common phenomenon, this entire project would be less worthwhile. The numbers in this tables are to be read as general behaviour, remembering that a different parametrisation would yield slightly different numbers (see chapter 7 in ref. [TC39] for longer discussion).

Another observation is that the phase remains the same for a family of planes of the same crystal structure regardless of the atoms that populate it and only the magnitude of the structure factor changes. This observation remains true for different multiplicities as well (see $(1\bar{1}.0)$ and $(2\bar{2}.0)$).

A first observation is that with the increase in the atomic mass of the group-III element, for the same set of planes, the structure factor increases, as we would expect from the scattering factor behaviour.

TABLE 3.5: Structure factors, $F_{hkl} = |F_{hkl}|e^{i\phi}$, for a few different planes in wurtzite nitride systems.

| $(h k l)$ | Structure factor F_{hkl} [VÅ ³] | | | | | |
|---------------------------|---|--------|-------------|--------|-------------|--------|
| | AlN | | GaN | | InN | |
| | $ F_{hkl} $ | ϕ | $ F_{hkl} $ | ϕ | $ F_{hkl} $ | ϕ |
| (0 0 0) | 774.67 | 0 | 891.01 | 0 | 1209.21 | 0 |
| (0 0 1) | 0 | 0 | 0 | 0 | 0 | 0 |
| (0 0 2) | 155.62 | 0.69 | 275.01 | 0.38 | 491.09 | 0.22 |
| ($\bar{2}$ 1 0) | 207.82 | 0 | 324.81 | 0 | 505.58 | 0 |
| (1 0 0) | 193.10 | 3.14 | 261.85 | 3.14 | 386.70 | 3.14 |
| (2 0 0) | 85.63 | 3.14 | 138.85 | 3.14 | 218.61 | 3.14 |
| (2 0 1) | 118.03 | -1.08 | 201.02 | -1.28 | 327.02 | -1.37 |
| ($\bar{2}$ 2 1) | 118.03 | 2.07 | 201.02 | -1.28 | 327.02 | -1.37 |
| ($\bar{2}$ 0 $\bar{1}$) | 118.03 | -2.07 | 201.02 | -1.86 | 327.02 | -1.78 |
| (1 $\bar{1}$ 2) | 52.57 | -2.34 | 105.50 | -2.76 | 194.67 | -2.92 |
| (3 0 1) | 0 | 0 | 0 | 0 | 0 | 0 |

Another observation would be that the scattering factor for planes belonging to the same family is not required to be the same. We can see that for (2 0 1) and ($\bar{2}$ 0 $\bar{1}$) planes which have the same absolute scattering factor value but do display different phases. This makes sense because for different planes, even those belonging to the same lattice symmetry, the atoms can be arranged at different positions.

A more subtle observation is that the interplanar distances are no longer a good indicator of the behaviour of the diffraction intensity behaviour (see Eq. 3.14). In this case, the *a-plane* (1 1 0) yields a higher scattering factor than *r-plane* (1 $\bar{1}$ 2) with lower interplanar distance. This is because some of the scattering on the *r-planes* leads to destructive interference as discussed in the previous section.

An important note we will address here is the symmetry of the structure factor. For this we will invoke *Friedel's law* and its application to non-centrosymmetric systems [Ser+73]. It is straightforward that $F_g = F_{-g}^*$ which can be rewritten as $F_g F_g^* = F_{-g}^* F_{-g}$ or $I_g = I_{-g}$. This is Friedel's law and it tells us that the intensity calculated as proportional to the structure factors absolute value will always show inversion symmetry. This is the behaviour seen for planes ($\bar{2}$ 0 $\bar{1}$) and (2 0 1). Nevertheless, for non-centrosymmetric systems, like the ones discussed here, this is not

what we expect. More generally, this kinematical description of the diffracted intensity, while suitable for predicting the scattering behaviour from a centrosymmetric system, fails to predict the break in symmetry of the non-centrosymmetric ones. This is yet another reason why we have to talk in the following sections about dynamical models for the wurtzite systems.

The last observation we will discuss here is that the structure factor is exactly zero for some of these planes ((0 0 .2) and (3 0 .1)) even if we are strictly respecting their Bragg condition. We will talk more *systematic absences* rules below.

Systematic absences

Looking at the last form of the equation and keeping in mind that $h, k, l \in \mathbb{Z}$ we can find the rules for vanishing scattering factors, *i.e.*, *extinction criterion*. The square bracket in Eq. 3.13 tells us that there is exactly one condition for the values h, k, l for which the value of the structure factor is zero, namely:

$$\frac{2(h-k)}{3} + l = 2n + 1 \quad (= \text{uneven})$$

For this sum to be uneven the first factor must be an integer, and can only be an even integer and, therefore, the second term must be even. We can then conclude that even when the Bragg condition is satisfied if the following relationships are satisfied simultaneously between the values h, k, l the diffraction intensity will be zero:

$$h - k = 3n \quad \text{AND} \quad l = 2m + 1$$

where $m, n \in \mathbb{N}$. In Table 3.5 we have seen that these conditions are met for (0 0 .1) and (3 0 .1).

Alternatively, we can say that for any departure from these conditions the structure factor will be non-zero, *i.e.*, *reflection criteria*:

$$h - k = 3n + 1 \quad \text{OR} \quad h - k = 3n + 2 \quad \text{OR} \quad l = 2m$$

These are, reassuringly, the same conditions given in the *Tables* for the space group **P6₃mc** (see page 183).

3.4.5 Scattering by an infinite crystal

We have previously talked about the interaction of a beam of high energy electrons with a crystalline sample as being mathematically represented in the Schrödinger's

equation by the electron interaction with the sample's electrostatic Coulomb potential $V(\mathbf{r})$. Finding the correct potential for a given crystalline structure is a fundamental problem in solid-state physics usually tackled by so-called first principles methods. These methods are notoriously expensive when solving even small systems since they aim to provide a solution for the many body problem that is the electron-electron interaction of the crystal structure. Fortunately for electron microscopists, the high energy of the incoming beam simplifies the crystal to the behaviour of isolated spherical point scatterers, where each scatterer is the potential of a single unit cell.

Since the unit cells live on the lattice, one way to write out an infinite lattice in maths form is as a set of unit-weight delta functions located at the lattice points:

$$\mathcal{L}(\mathbf{r}) = \sum_{u,v,w} \delta(\mathbf{r} - \mathbf{t}_{uvw}) = \begin{cases} 1 & \text{if } \exists u, v, w \in \mathbb{Z} \text{ such that } \mathbf{r} = \mathbf{t}_{uvw} \\ 0 & \text{otherwise} \end{cases} \quad (3.15)$$

where $\mathbf{t}_{uvw} = u\mathbf{a} + v\mathbf{b} + w\mathbf{c}$ is the translational lattice vector. The lattice points themselves correspond to single unit cells and their own potential is described by the N atoms in the unit cell located at positions \mathbf{r}_i :

$$V_{\text{unit cell}}(\mathbf{r}) = \sum_{i=1}^N V_{\text{atom}_i}(\mathbf{r} - \mathbf{r}_i) \quad (3.16)$$

The full lattice potential of an infinite crystal is an instance of the unit cell potential at each lattice point. This can be written as the convolution⁴ of the single unit cell potential with the area of delta functions potential of the crystal lattice:

$$V_{\text{IC}}(\mathbf{r}) = V_{\text{unit cell}}(\mathbf{r}) \circledast \mathcal{L}(\mathbf{r}) \quad (3.17)$$

By construction, $V_{\text{IC}}(\mathbf{r})$ has the periodicity of the underlying Bravais lattice:

$$V_{\text{IC}}(\mathbf{r}) = V_{\text{unit cell}}(\mathbf{r} + \mathbf{t}_{uvw}), \forall \text{ Bravais lattice vectors } \mathbf{t}_{uvw} = u\mathbf{a} + v\mathbf{b} + w\mathbf{c}. \quad (3.18)$$

This allows us to conveniently expand the potential as a discrete Fourier series.

⁴ Convolution with a delta function means "copying" the unit cell potential at the position of the delta function which, here, is every lattice site.

$$V_{IC}(\mathbf{r}) = \sum_{\mathbf{g}} V_{\mathbf{g}} e^{2\pi i \mathbf{g} \cdot \mathbf{r}} \quad (3.19)$$

where $V_{\mathbf{g}}$ are the Fourier coefficients of the electrostatic lattice potential corresponding to each set of planes \mathbf{g}_{hkl} in the crystal.

It is reasonable to choose $V_{\mathbf{g}}$ to be proportional to $F_{\mathbf{g}}$ since the structure factor carries the information about directional scattering we want the potential to have (see Appendix A.1 in Ref. [Rym70] for demonstration of the reasons):

$$V_{\mathbf{g}} = \frac{F_{\mathbf{g}}}{\Omega} = \frac{0.04787801}{\Omega} \sum_{j=1}^{N_a} e^{-B_{el,s^2}} \sum_{i=1}^{N=4} a_i^j e^{-b_i^j s^2} \sum_{(\mathbf{D}|\mathbf{t})} e^{2\pi i \mathbf{g}_{hkl} \cdot (\mathbf{D}|\mathbf{t})[\mathbf{r}_j]} \quad (3.20)$$

where Ω is the usual unit cell volume and we made use of Eq. 3.10 and Eq. 3.12. This implies the units for the Fourier coefficient will be $\langle V \rangle$.

3.4.6 Scattering by finite crystal

In practice crystals are not infinite, in fact they usually come in rather small sizes. This affects the form of the crystal potential. Mathematically this can be written as multiplication by a shape function which has non-zero value only inside the crystal. The reciprocal lattice points can no longer be represented by delta functions centred at the points but rather should be approximated to be three dimensional objects. It also means that the diffraction conditions become more relaxed as we can observe diffraction behaviour even when slightly off the Bragg angle.

The deviation parameters \mathbf{s}_g

It, therefore, becomes important to quantify the deviation from the Bragg condition since it is a core parameter in diffraction. For a thin foil the shape of the reciprocal lattice point becomes that of a relrod with one dimension of interest: $\mathbf{s} = s\mathbf{n}$. If we redraw Fig. 3.1 and allow a lattice point at distance s from the Ewald sphere in the direction of the lattice normal to contribute to diffraction we would end up with Fig 3.8. We can rewrite the Bragg condition (Eq. 3.1 on page 62) as:

$$\mathbf{k}_g - \mathbf{k}_0 = \mathbf{g} + \mathbf{s}, \quad (3.21)$$

such that the vector $\mathbf{g} + \mathbf{s}$ is now on the Ewald sphere. Rewriting Eq. 3.2 with this bit of information:

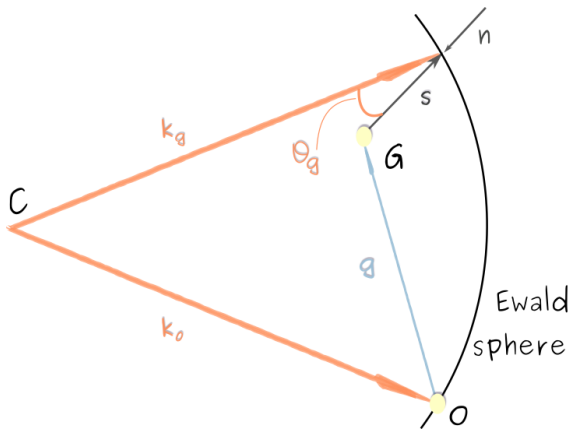


FIGURE 3.8: Ewald sphere construction for a positive deviation parameter s . \mathbf{n} is the normal to the foil.

$$(\mathbf{g} + \mathbf{s}) \cdot (2\mathbf{k}_0 + \mathbf{g} + \mathbf{s}) = 0$$

From this we can obtain the length of the vector \mathbf{s} which is usually repackaged in the following form:

$$s + \frac{s^2}{2|\mathbf{k}_0 + \mathbf{g}| \cos \theta_g} = \frac{-\mathbf{g} \cdot (2\mathbf{k}_0 + \mathbf{g})}{2|\mathbf{k}_0 + \mathbf{g}| \cos \theta_g} = \mathbf{s}_g$$

where \mathbf{s}_g is known as the *deviation parameter* and θ_g is the angle between the normal to the plane and \mathbf{k}_g . I will rewrite \mathbf{s}_g in a final form that would become useful later:

$$\mathbf{s}_g = \frac{k_0^2 - k_g^2}{2|\mathbf{k}_g| \cos \theta_g}. \quad (3.22)$$

3.4.7 Treatment of absorption

The discussion so far applies to perfectly elastic events. However, in real applications, electrons will have non-zero probability to lose energy during scattering events, what we call inelastic scattering processes. These electrons will not travel in the direction predicted by Bragg's equation but contribute to the image in the form of background instead.

In the absence of absorption the potential of the crystal will be a real value. In order to account for loss of electrons from the diffraction signal to inelastic scattering processes a complex optical potential can be introduced [GBA66]:

$$V_c(\mathbf{r}) = V + iW = \sum_{\mathbf{g}} V_{\mathbf{g}} e^{2\pi i \mathbf{g} \cdot \mathbf{r}} + i \sum_{\mathbf{g}} W_{\mathbf{g}} e^{2\pi i \mathbf{g} \cdot \mathbf{r}} \quad (3.23)$$

where the *absorption Fourier coefficient*, $W_{\mathbf{g}}$, can be shown to have a form similar to that of $V_{\mathbf{g}}$ in Eq. 3.20 where the scatter factor $f^e(s)$ is replaced by an absorptive factor $f'(s)$. The absorptive factor can also be parametrised, this time using the Weickenmeier and Kohl's parametrisation [WK91]. This formula I did not implement, but it can be found as part of *EMsoft* [DGG13] in `CalcUcg.f90`.

3.5 Darwin-Howie-Whelan equations

In this chapter we have alluded a few times at the limitations of the kinematical model and promised to explore a more robust model: the dynamical model. The dynamical model has, in fact, a long history and diverged into versions optimised for different applications. A few of these are given in Table 3.6.

TABLE 3.6: Various dynamical models used in electron diffraction.

| Model | Based on | Application |
|------------------------|-------------------------------------|---|
| Bethe's [Bet28] | eigenvalue equation | intensity of diffraction patterns |
| Cowley-Moddie's [CM57] | multi-slice approach | single crystal TEM |
| Howie-Whelan [HW61] | simultaneous differential equations | diffraction contrast |
| Van Dyck [VD80] | real space approach | improved accuracy on the multi-slice method |

For my intents and purposes, *i.e.*, diffraction intensity and contrast predictions, I will explore only the Howie-Whelan method (HW) in this work since the addition of dislocation strain is more straightforward than in the other models. For now we will focus on its predictions in a perfect crystal. Howie and Whelan followed Bethe's approach developed for the Bragg case in a perfect crystal with no absorption and generalised it. For this they needed to find the form of the wavelength of the diffracting particles as they travel in the crystal potential, *i.e.*, solve Schrödinger equation.

The time independent Schrödinger equation can be written for an electron wavefunction Ψ of energy eE in a periodic crystal potential $V(\mathbf{r})$ in the form known as the Helmholtz equation as:

$$\Delta\Psi(\mathbf{r}) + \frac{8\pi^2me}{\hbar^2} [E + V(\mathbf{r})] \Psi(\mathbf{r}) = 0, \quad (3.24)$$

where m, e, \hbar are the usual constants and Δ is the Laplace operator standing for:

$$\Delta\Psi = \frac{\partial^2\Psi}{\partial x^2} + \frac{\partial^2\Psi}{\partial y^2} + \frac{\partial^2\Psi}{\partial z^2}.$$

The meaning of Ψ is taken here to be that the value $\Psi\Psi^* d\tau$ is the probability of finding the electron in the volume $d\tau$.

Outside the crystal, where the potential term can be taken to be zero, the solution to the equation above will be in the form of a plane wave (see page 30): $\psi_0(\mathbf{r}) = e^{2\pi i \mathbf{k}_0 \cdot \mathbf{r}}$. Inside the crystal, the electrons are diffracted and follow a direction $\mathbf{k}_g = \mathbf{k}_0 + \mathbf{g}$ for every reciprocal lattice point \mathbf{g} on the Ewald sphere. The general solution to the equation above must then be a superposition of plane waves, one for each direction predicted by Bragg's law.

$$\Psi(\mathbf{r}) = \sum_{\mathbf{g}} \psi_g e^{2\pi i \mathbf{k}_g \cdot \mathbf{r}}, \quad (3.25)$$

where ψ_g is the complex amplitude of the Bragg plane wave \mathbf{g} and is the unknown to be determined.

The crystal potential $V(\mathbf{r})$ can be taken to have the form in Eq. 3.23. It is useful at this point to separate the zero-frequency real component V_0 out of the Fourier series as it represents the crystal's mean inner potential and a constant independent of the diffracting planes. This positive potential accelerates the electrons as they enter the crystal in a phenomenon known as *refraction*⁵.

$$V(\mathbf{r}) + iW(\mathbf{r}) = V_0 + \sum_{\mathbf{q} \neq 0} V_{\mathbf{q}} e^{2\pi i \mathbf{q} \cdot \mathbf{r}} + i \sum_{\mathbf{q}} W_{\mathbf{q}} e^{2\pi i \mathbf{q} \cdot \mathbf{r}}. \quad (3.26)$$

In the above we have changed the label of the general reciprocal lattice vector \mathbf{g} to \mathbf{q} in order to differentiate it from the reciprocal space lattice vector \mathbf{g} in Eq. 3.25.

We can also write out the wave vector of the incident electron beam corrected for refraction by the mean inner potential V_0 :

⁵ This is equivalent to the decrease in the speed of light as it enters a medium with a refractive index larger than that of vacuum.

$$|\mathbf{k}_0|^2 = k_0^2 = 2me(E + V_0)/h^2 \quad (3.27)$$

In preparation for the substitution of Eq. 3.26 in Eq. 3.24 we separate the term V_0 using the above identity and add the following shorthand notation:

$$U(\mathbf{r}) + iU'(\mathbf{r}) = \frac{2me}{h^2} \left\{ \sum_{\mathbf{q} \neq 0} V_{\mathbf{q}} e^{2\pi i \mathbf{q} \cdot \mathbf{r}} + i \sum_{\mathbf{q}} W_{\mathbf{q}} e^{2\pi i \mathbf{q} \cdot \mathbf{r}} \right\} \quad (3.28)$$

Using the 3.25 solution form in the master equation 3.24 and making substitution 3.26 we get the following:

$$\begin{aligned} \sum_{\mathbf{g}} \left\{ \Delta\psi_{\mathbf{g}} + i4\pi\mathbf{k}_g \cdot \nabla\psi_{\mathbf{g}} - 4\pi^2 |\mathbf{k}_g|^2 \psi_{\mathbf{g}} + \frac{8\pi^2 m_e}{h^2} (E + V_0) \right\} e^{2\pi i \mathbf{k}_g \cdot \mathbf{r}} \\ = 4\pi^2 \sum_{\mathbf{q} \neq 0} V_{\mathbf{q}} e^{2\pi i \mathbf{q} \cdot \mathbf{r}} + i4\pi^2 \sum_{\mathbf{q}} W_{\mathbf{q}} e^{2\pi i \mathbf{q} \cdot \mathbf{r}} \end{aligned} \quad (3.29)$$

Van Dyck [VD76] has shown that the second order derivative of the complex amplitude $\psi_{\mathbf{g}}$ is negligible for high energy electrons and we can drop it here. This is known as the *high-energy approximation* and Van Dyck showed that it holds for penetration depths up to a few hundred nanometres, depending on the average atomic number of the atoms in the crystal. For TEM high energy electrons, Howie [HW61] ignores the first derivative, $\nabla\psi_{\mathbf{g}}$ as well, but we will keep it. Rewriting the equation above with all these assumptions and using substitution 3.27 we finally obtain:

$$\sum_{\mathbf{g}} \left\{ i\mathbf{k}_g \cdot \nabla\psi_{\mathbf{g}} + \pi (k_0^2 - |\mathbf{k}_g|^2) \psi_{\mathbf{g}} \right\} e^{2\pi i \mathbf{k}_g \cdot \mathbf{r}} = -\pi \sum_{\mathbf{q}} \sum_{\mathbf{g}} [U_{\mathbf{q}} + iU'_{\mathbf{q}}] \psi_{\mathbf{g}} e^{2\pi i (\mathbf{q} + \mathbf{k}_g) \cdot \mathbf{r}} \quad (3.30)$$

Let us have a closer look at the $\mathbf{k}_g \cdot \nabla\psi_{\mathbf{g}}$ term in the Eq. 3.30 above. This term can be read as the directional derivative of the Bloch wave g in the direction \mathbf{k}_g when in perfect Bragg condition. This means we can reduce the grad operator to only one derivative with no loss of information. We will assign z_{beam} to be the electron beam propagation direction and can write the dot product as:

$$\mathbf{k}_g \cdot \nabla\psi_{\mathbf{g}} = |\mathbf{k}_g| \frac{d\psi_{\mathbf{g}}}{dz_{beam}} \cos\theta_B.$$

We have to make one final substitution in Eq. 3.30, a trick one. In the second term of this equation \mathbf{q} stands for a general reciprocal vector which could be replaced by $\mathbf{q} = \mathbf{g}' - \mathbf{g}$ for instance. This has the effect of changing the variable of the sum from $\sum_{\mathbf{q}}$ to $\sum_{\mathbf{g}'}$. The right hand side in Eq. 3.30 becomes:

$$RHS = -\pi \sum_{\mathbf{g}} \sum_{\mathbf{g}'} [U_{\mathbf{g}'-\mathbf{g}} + iU'_{\mathbf{g}'-\mathbf{g}}] \psi_{\mathbf{g}'} e^{2\pi i (\mathbf{k}_g) \cdot \mathbf{r}}$$

where we also interchanged the variables \mathbf{g} and \mathbf{g}' .

Both terms look now like a Fourier expansion with the same basis and the same number of terms. From the properties of Fourier series (see page 34) we know that the only way this is true is if the individual terms are equal to each other. Writing the equation above for every \mathbf{g} term in the sum and after some reordering we end up with:

$$\frac{d\psi_{\mathbf{g}}}{dz_{beam}} - 2\pi i \frac{k_0^2 - k_g^2}{2|\mathbf{k}_g| \cos \theta_B} \psi_{\mathbf{g}} = i\pi \sum_{\mathbf{g}'} \frac{U_{\mathbf{g}-\mathbf{g}'} + iU'_{\mathbf{g}-\mathbf{g}'}}{|\mathbf{k}_{\mathbf{g}'}| \cos \theta_B} \psi_{\mathbf{g}'}$$

This form already tells us that the change in amplitude of a diffracted wave, $\psi_{\mathbf{g}}$, with penetration depth in the crystal, z_{beam} , depends on its current value, $\psi_{\mathbf{g}}$, but also the amplitudes of all the other waves, $\psi_{\mathbf{g}'}$, that satisfy the Bragg condition. The complex electrostatic potential on the right hand side determines how strongly the excited waves are coupled to each other.

The second term on the left hand side in the equation above reminds us of the form of the deviation parameter, \mathbf{s}_g , given in Eq. 3.22 on page 80. The different angle showing up here ties in the discussion on page 3.2. Only for a symmetric Laue geometry we can replace $\theta_B = \theta_g$. Nevertheless, the error in approximating a non-symmetric Laue case to a symmetric Laue case is not significant for strong beams.

$$2\pi i \frac{k_0^2 - k_g^2}{2|\mathbf{k}_g| \cos \theta_B} \psi_{\mathbf{g}} = 2\pi i \mathbf{s}_g \psi_{\mathbf{g}}$$

Tilting or rotating the sample moves the Ewald sphere and with it the distance between the reciprocal lattice point and the sphere in the direction normal to the sample, *i.e.*, \mathbf{s}_g . For a set of diffracted waves only two non-collinear deviation parameters are independent of each other. But these independent parameters, which affect directly

the diffraction behaviour, are experimental variables set by the microscope operator and while easy to determine in a TEM, are, unfortunately, complete unknowns to the SEM operator.

Extinction distance and absorption length

We will introduce one final substitution. Dimensional analysis tells us that since the first term in the equation has units of reciprocal length so must have the last term. Whenever a term in an equation ends up having simple units, physicists will go and give it a name. In this case they split it in two and named the first term *extinction distance*, $\xi_{\mathbf{g}-\mathbf{g}'}$, and the second term *absorption length*, $\xi'_{\mathbf{g}-\mathbf{g}'}$, defined in terms of the Fourier coefficients of the real and imaginary parts of the lattice potential as follows:

$$\frac{1}{\xi_{\mathbf{g}-\mathbf{g}'}} \equiv \frac{|U_{\mathbf{g}-\mathbf{g}'}|}{|\mathbf{k}_{\mathbf{g}'}| \cos \theta_B} \quad (3.31)$$

$$\frac{1}{\xi'_{\mathbf{g}-\mathbf{g}'}} \equiv \frac{|U'_{\mathbf{g}-\mathbf{g}'}|}{|\mathbf{k}_{\mathbf{g}'}| \cos \theta_B} \quad (3.32)$$

where we used the fact that the complex Fourier coefficients of the electrostatic lattice potential can be written in terms of their modulus and phase angles, $\theta_{\mathbf{g}}$ and $\theta'_{\mathbf{g}}$:

$$U_{\mathbf{g}'-\mathbf{g}} = |U_{\mathbf{g}'-\mathbf{g}}| e^{i\theta_{\mathbf{g}-\mathbf{g}'}}; \quad U'_{\mathbf{g}'-\mathbf{g}} = |U'_{\mathbf{g}'-\mathbf{g}}| e^{i\theta'_{\mathbf{g}-\mathbf{g}'}}. \quad (3.33)$$

With the help of all these substitutions, we can finally write out the general form of the multibeam Darwin-Howie-Whelan equations [HW61] which describe the change in amplitude of electron diffracted beam with distance travelled inside the crystal:

$$\frac{d\psi_{\mathbf{g}}}{dz_{beam}} - 2\pi s_g \psi_{\mathbf{g}} = i\pi \sum_{\mathbf{g}'} \left(\frac{e^{i\theta_{\mathbf{g}-\mathbf{g}'}}}{\xi_{\mathbf{g}-\mathbf{g}'}} + i \frac{e^{i\theta'_{\mathbf{g}-\mathbf{g}'}}}{\xi'_{\mathbf{g}-\mathbf{g}'}} \right) \psi_{\mathbf{g}'}. \quad (3.34)$$

3.5.1 The two beam case

In the previous section, we started with a form of the Schrödinger's equation describing the electron wavefunction in a periodic, crystal potential. Using Bragg's law we expanded the wavefunction in plane waves and, separately, we Fourier expanded the complex crystal potential. The high energy approximation was applied. We equated

the individual harmonics terms in the Fourier expansion. We argued that the non-symmetric Laue geometry can be approximated with good confidence to the symmetric Laue case. We introduced the deviation parameter and the extinction distance and absorption length in the equations. Finally, we ended up with the multi beam form of the Howie-Whelan equations.

We will look now at the two beam case, when there is only one strong diffracted beam dominating diffraction behaviour, namely ψ_g in addition to the incident ψ_0 . Equation 3.34 becomes:

$$\begin{aligned} \frac{d\psi_0}{dz_{beam}} &= -\frac{\pi}{\xi'_0}\psi_0 + i\pi \left(\frac{e^{i\theta_g}}{\xi_g} + i\frac{e^{i\theta'_g}}{\xi'_g} \right) \psi_g \\ \frac{d\psi_g}{dz_{beam}} - 2\pi i s_g \psi_g &= i\pi \left(\frac{e^{i\theta_g}}{\xi_g} + i\frac{e^{i\theta'_g}}{\xi'_g} \right) \psi_0 - \frac{\pi}{\xi'_0} \psi_g \end{aligned} \quad (3.35)$$

On the left hand side there are two terms: the first is the contribution from the direct beam and the second is the contribution from the diffracted beam. Every beam equation has a contribution from all the beams, but the weighting factors will be different. On the right side of these equations there is a real term that depends on the normal absorption length, ξ'_0 , and a complex term telling us about the interaction with the other beam. For a centrosymmetric system ξ_g and ξ_{-g} are equal, but there we cannot expect this to hold for a non-centrosymmetric system, like wurtzite for instance. The round brackets can be simplified by introducing yet another parameter:

$$\frac{1}{q_g} = \frac{1}{\xi_g} + i\frac{e^{i(\theta'_g - \theta_g)}}{\xi_g}.$$

This has the benefit of simplifying the form of these equations and can be interpreted physically as the probability of scattering from one beam to the other.

It is common at this point to use the Ansatz that the solutions to these equations must be of plane wave form, for instance:

$$\begin{aligned} \psi_0 &= S_0(z_{beam}) e^{-\pi z_{beam}/\xi'_0} \\ \psi_g &= S_g(z_{beam}) e^{i\theta_g} e^{-\pi z_{beam}/\xi'_0} \end{aligned} \quad (3.36)$$

where we made use of the fact that the inner potential U_0 is real and therefore $\theta_0 = 0$. This substitution has the advantage of eliminating the ξ'_0 term.

The intensities of the direct and diffracted beam are then the square modulus of the direct and diffracted wavefunctions:

$$\begin{aligned} \text{direct beam: } I_0(z_{beam}) &= |\psi_0|^2 = |S_0(z_{beam})|^2 e^{-2\pi z_{beam}/\xi'_0} \\ \text{diffracted beam: } I_g(z_{beam}) &= |\psi_g|^2 = |S_g(z_{beam})|^2 e^{2i\theta_g} e^{-2\pi z_{beam}/\xi'_0} \end{aligned} \quad (3.37)$$

The equations 3.35 become⁶:

$$\begin{aligned} \frac{dS_0}{dz_{beam}} &= \frac{i\pi}{q_{-\mathbf{g}}} S_g \\ \frac{dS_g}{dz_{beam}} &= 2\pi i \mathbf{s}_g S_g + \frac{i\pi}{q_{\mathbf{g}}} S_0 \end{aligned} \quad (3.38)$$

There are a number of equivalent forms of these equations, but this is particularly useful one to generalise to imperfect crystals as we will see in the next chapter. The task is now to solve these coupled differential equations. There are a number of ways to do this. In the next pages we will cover the scattering matrix formalism and the analytical form.

The scattering matrix

There is another benefit to writing the equations in the form in Eq. 3.38. Namely, we can rewrite them in matrix form:

$$\frac{d\mathbf{S}}{dz_{beam}} = i\mathcal{A}\mathbf{S} \quad (3.39)$$

⁶ Here we made use of the identity $e^{i(\theta_{\mathbf{g}} + \theta_{-\mathbf{g}})} = 1$ which can be generalised to $e^{i\sum_{\mathbf{g}} \theta_{\mathbf{g}}}$, if $\sum_{\mathbf{g}} \mathbf{g} = 0$. This later statement can be verified using the definition of $\theta_{\mathbf{g}}$ from Eq. 3.33:

$$U_{\mathbf{g}} = \frac{2me}{h^2\sigma} \sum_j f_j^e e^{2\pi i \mathbf{g} \cdot \mathbf{r}_j} = U_{\mathbf{g}} e^{i\theta_{\mathbf{g}}}$$

where \mathbf{S} is the column vector $\mathbf{S} = \begin{pmatrix} S_0 \\ S_g \end{pmatrix}$, and \mathcal{A} is called *the scattering matrix* and is of the form:

$$\mathcal{A}(s_g) = \begin{pmatrix} 0 & \frac{\pi}{q_g} \\ \frac{\pi}{q_g} & 2\pi\mathbf{s}_g \end{pmatrix} \quad (3.40)$$

Computers are very good at dealing with matrices. Especially, if we were to consider many beams, the calculations time will scale up in a sensible manner, as apposed to the next approach we will be considering. But more important, the simple form of Eq. 3.39 is easy to solve. The amplitude of the scattering beam at distance z_{beam} inside the sample along the incident beam is the solution to this matrix equation:

$$\mathbf{S}(z_{beam}) = e^{i\mathcal{A}z_{beam}} \mathbf{S}(z_{beam} = 0) \equiv \mathcal{S}(z_{beam}) \mathbf{S}(0) \quad (3.41)$$

Where we can take at the entry in the sample, the direct beam amplitude to be 1 and the diffracted beam amplitude to be 0: $\mathbf{S} = \begin{pmatrix} 1 \\ 0 \end{pmatrix}$. Here we have introduced the definition of the *scattering matrix* \mathcal{S} . The scattering matrix can then be approximated using Taylor expansion:

$$\mathcal{S}(z_{beam}) = e^{i\mathcal{A}z_{beam}} = \sum_{n=0}^{\infty} \frac{i^n \mathcal{A}^n}{n!} z_{beam}^n \quad (3.42)$$

Knowing that for a very small z the Taylor expansion converges only after a few terms we can write out $z_{beam} = m\epsilon$ where ϵ is a very small value.

$$\mathcal{S}(z_{beam}) = \mathcal{S}(m\epsilon) = [\mathcal{S}(\epsilon)]^m \quad (3.43)$$

The procedure is then to split the total penetration depth into m small enough segments that the Taylor expansion converges to a set threshold. The lower the threshold the more accurate the calculations.

This approach had already been successfully applied to predictions of electron channelling contrast imaging of TDs coming at an angle to the surface [Pic+14].

Bloch wave formalism

The alternative path to finding a solution is analytically. Starting with Eq. 3.38 we can rewrite them, by substituting one in the other, in the form of a harmonic oscillator equation in S_0 :

$$\frac{d^2S_0}{dz_{beam}^2} - 2\pi i s_g + \frac{\pi^2}{q_g^2} S_0 = 0 \quad (3.44)$$

which will have solutions of the plane wave form, $e^{2\pi i \gamma z_{beam}}$, provided that

$$-\gamma^2 + s_g \gamma + \frac{1}{4q_g^2} = 0$$

This characteristic equations is satisfied by any of the two values::

$$\begin{aligned} \gamma^{(1)} &= \frac{s_g - \sqrt{s_g^2 + \frac{1}{q_g^2}}}{2} \\ \gamma^{(2)} &= \frac{s_g + \sqrt{s_g^2 + \frac{1}{q_g^2}}}{2} \end{aligned}$$

There are two independent solutions for the wave amplitudes:

$$\begin{aligned} S_0(z_{beam}) &= C_0^{(1)} \exp\left\{(2\pi i \gamma^{(1)} z_{beam})\right\} \\ S_0(z_{beam}) &= C_0^{(2)} \exp\left\{(2\pi i \gamma^{(2)} z_{beam})\right\} \end{aligned}$$

From substitution we get the two solutions of the diffracted beam amplitude:

$$\begin{aligned} S_g(z_{beam}) &= C_g^{(1)} \exp\left\{(2\pi i \gamma^{(1)} z_{beam})\right\} = 2C_0^{(1)} q_g \gamma^{(1)} \exp\left\{(2\pi i \gamma^{(1)} z_{beam})\right\} \\ S_g(z_{beam}) &= C_g^{(2)} \exp\left\{(2\pi i \gamma^{(2)} z_{beam})\right\} = 2C_0^{(2)} q_g \gamma^{(2)} \exp\left\{(2\pi i \gamma^{(1)} z_{beam})\right\} \end{aligned}$$

From which,

$$\frac{C_g^{(i)}}{C_0^{(i)}} = 2q_g \gamma^{(i)}$$

where $C_0^{(i)}$ and $C_g^{(i)}$ are constants to be determined from the boundary conditions:

$$\begin{aligned} S_0(0) &= C_0^{(1)} + C_0^{(2)} = 1 \\ S_g(0) &= C_g^{(1)} + C_g^{(2)} = 0 \end{aligned}$$

We find:

$$C_0^{(1)} = \frac{\gamma^{(2)}}{\gamma^{(2)} - \gamma^{(1)}} \quad (3.45)$$

$$C_0^{(2)} = \frac{\gamma^{(1)}}{\gamma^{(1)} - \gamma^{(2)}} \quad (3.46)$$

But this derivation can be used for a slightly different interpretation of diffraction and it has to do with the periodicity of the crystal and the steady state solutions of the electron wavefunction inside a periodic potential which are known as Bloch waves $\{\psi(\mathbf{r})\}$. For a two beam equation we can write out two Bloch waves:

$$\phi_0(\mathbf{r}) = C_0^{(1)} \psi^{(1)}(\mathbf{r}) + C_0^{(2)} \psi^{(2)}(\mathbf{r}) \quad (3.47)$$

$$\phi_g(\mathbf{r}) = C_g^{(1)} \psi^{(1)}(\mathbf{r}) \exp(i\mathbf{g} \cdot \mathbf{r}) + C_g^{(2)} \psi^{(2)}(\mathbf{r}) \exp(i\mathbf{g} \cdot \mathbf{r}) \quad (3.48)$$

with the boundary conditions:

$$\phi_0(0) = \sum_{i=1,2} \phi^{(i)} C_0^{(i)} = 1 \quad (3.49)$$

$$\phi_g(0) = \sum_{i=1,2} \phi^{(i)} C_g^{(i)} = 0 \quad (3.50)$$

The first Bloch wave (ψ_0) is defined such that its maxima are at interstices, while the second Bloch wave's (ψ_g) maxima occur on atom columns. We can also offer a more intuitive picture of the anomalous absorption in this frame since it is to be expected that the electrons from the second Bloch wave, that spend more time near the atomic nuclei will be more readily scattered than the ones contained in the first Bloch wave. And the best thing is that this description is equivalent to the one in Eq. 3.38 [Hir+65].

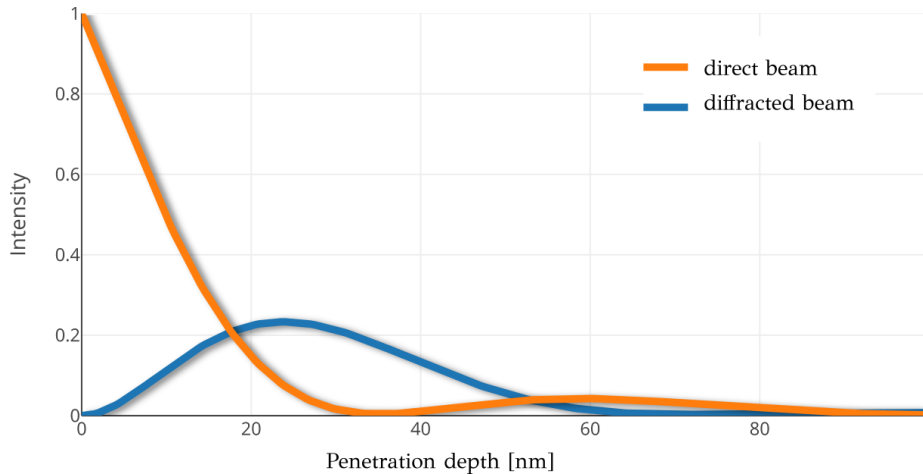


FIGURE 3.9: *Thickness fringes* for the direct and diffracted beams for a perfect centrosymmetric crystal.

Let us review what we have achieved so far. The dynamical theory solves the Schrödinger equation for the high energy electrons inside a crystal. The electrons see the perfect crystal as a periodic potential and their wavefunction is perturbed in such a way that if we consider a direct electron wavefunction and diffracted one, the amplitude will be dynamically transferred between these two waves as they travel through the crystal in a manner similar to the transfer of energy in the coupled pendulum oscillations.

Figure 3.9 shows exactly this periodic variation in the direct wave intensity (orange) and the diffracted beam (blue) with penetration depth in a film of Ni crystal. In the TEM world this plot is known as *thickness fringes*, since if one would be to measure

the transmitted or diffracted intensity through a wedge shaped crystal and plot it as a function of sample thickness the same image would result; the oscillations being a direct result of the change in crystal thickness. In the SEM case we can think of it as variation in the beams intensity as they travel inside the crystal. This plot can be achieved using any of the descriptions above. See `Task3.ipynb` for implementation details.

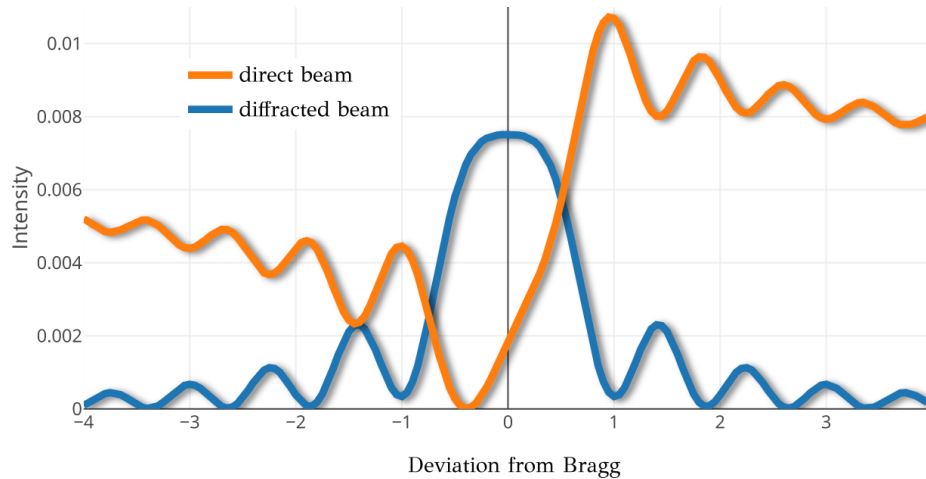


FIGURE 3.10: *Rocking curves* for the direct and diffracted beams for a perfect centrosymmetric crystal. Here, on the x-axis, I replaced the s_g with the dimensionless parameter $w = s_g \cdot \xi_g$.

A similarly oscillatory behaviour can be observed if we were to plot the intensity of the two beams as a function of deviation from the Bragg angle (“rocking”) as I did in Fig. 3.10. Notice that the diffracted beam contributes only when very close to the Bragg angle.

4 Electron diffraction in an imperfect crystal – ECCI

In this chapter we will explore the application of SEM electron diffraction to the study of imperfections in crystals, such as *threading dislocation* (TD) lines in the technique known as *Electron Channeling Contrast Imaging* (ECCI).

Back on page 10, I already covered why ECCI is a particularly interesting technique to apply to the relatively new world of group III-nitrides where defects tend to directly affect the efficiency of opto-electronic devices. Dislocation densities and distributions are particularly relevant when it comes to light emission since they seem to directly influence the incorporation of point defects and thus the parasitic defect luminescence [Kus+15]. It is known from the more established III-arsenide and phosphide materials that dislocations can act as non-radiative recombination centres for carriers in LEDs [Pen+05] as well as current leakage paths in power electronics. While dislocations in nitrides prove to be less effective centres of non-radiative recombination [Les+95], it is predicted that their density still ought to be reduced to below $\approx 10^7 \text{ cm}^{-2}$ [KM02].

In the previous chapter we covered how to solve the HDW equations for a perfect crystal and predict incident and diffracted beams intensities. These equations can easily accommodate crystallographic information for an introduced dislocation in the form of a strain profile. In this case, the crystal is subject to a deformation that moves an atom from the point \mathbf{r} to a point $\mathbf{r} + \mathbf{R}(\mathbf{r})$ and we expect the potential of the crystal to be changed by a factor $\{\exp(-2\pi i \mathbf{g} \cdot \mathbf{R}(\mathbf{r}))\}$. We will briefly talk about the derivation of the displacement field for threading dislocations normal to the surface on page 101.

In practice, this means that the diffraction condition is locally changed close to a crystal imperfection. One way to add this information in the Howie-Whelan equation is to correct the deviation from the Bragg angle, \mathbf{s}_g to contain also the dislocation displacement field. We will see how we can do that on page 106.

I will explore then what I have learned from looking at this correction factor, or what I call *ECC-strain*, including contrast relationship to the foreshatter SEM geometry

(page 108), TD contrast behaviour dependence on diffraction condition and dislocation type (page 114), as well as predictions of TD contrast in GaN and comparisons with experimental results (page 122). Part of the results shown in this chapter have previously been presented at the International Extended Defects in Semiconductors Conference 2016, and published as a proceedings paper [Pas+18a].

Before everything else, on page 95, I want to make very sure the reader is on board with the fact that every time we say *channelling* it should be read as *diffraction*, specifically, diffraction of the electron beam on the way into the sample.

But first, a bit of background.

4.1 Background

In the overview of diffraction related advancements on page 55, we left the story of ECCI development as a technique at Morin *et al.* [Mor+79] who were able to observe individual dislocations in Si using a cold field emission gun (FEG) attached to the SEM. Fast forward to 1990, FEG-SEM became commercial and also came with efficient BSE detector making ECCI less of a cutting edge technique and more of an integral capability of the standard SEM. This enabled Czenuszka *et al.* [Cze+90] to publish the first characterisation of individual dislocation in bulk material (Si) with ECCI.

Shortly after, Wilkinson [Wil+93] used ECCI to investigate clusters of misfit dislocations lying more than 1 μm underneath the surface at the interface of Si-Ge layers grown on Si. They noted that at this depth the spatial resolution is too low to resolve individual dislocations. However, they still concluded that the $\mathbf{g} \cdot \mathbf{b} = \mathbf{g} \cdot \mathbf{b} \times \mathbf{u} = 0$ invisibility criteria can be applied similarly to TEM. These pioneering ECCI investigations were made on highly tilted samples (40° - 70°), with side mounted BSE detectors, similarly to the EBSD set up.

When applied to metals ECCI tended to be used in a low tilt ($< 10^\circ$) configuration [SC99]. This set up offers a number of advantages: the standard Si-diode detector can be mounted on the pole piece offering a large BSE signal collection angle and the interaction volume is minimised granting higher spatial resolution. The downside to this geometry is the reduction in BSE signal which, for metals, is less of an issue than for semiconductors due to higher atomic numbers. A comprehensive overview of the applications of ECCI for metallic materials has been made by Weidner and Biermann [WB15].

From 2006 Trager-Cowan group [TC+06] showed that using ECCI in the characterisation of nitrides is an excellent idea. Since then ECCI has been used in the foreshatter geometry to reveal extended defects and morphological features of GaN

samples [Pic+07]. Picard *et al.* [Pic+09] also argued that the $\mathbf{g} \cdot \mathbf{b}$ dislocation type identification criterion can no longer be applied due to surface relaxation. They used simulations instead to determine the Burgers vectors of dislocations instead, laying the grounds for a non-destructive dislocation characterisation method.

Literature continues to call ECCI a new technique even though it has been around for almost forty years. There are a number of reasons for this including the fact that it resisted being standardised such that every group has their own method of acquiring ECC-images depending on the material studied, the SEM abilities and the available detectors. Different groups proposed flavours of ECCI to distinguish between procedures. Gutierrez-Urrutia *et al.* [GUZR09] and Zaafferer and Elhami [ZE14] coined the term *controlled ECCI* (cECCI) for a low tilt geometry ECCI aided by crystallographic information obtained from EBSD maps acquired at 70° tilt. Similarly, Mousour *et al.* [Man+15] used low tilt ECCI together with high resolution selected area channelling patterns to characterise dislocations in fine-grained Si steel and labelled it *accurate ECCI* (aECCI).

4.2 A word on channelling

Centuries after the decline of the Western Roman Empire, the allure of power and honour brought by the title of Roman Emperor was undiminished. While Irene of Athens, a female, was occupying the Roman throne, the pope crowned the king of Franks, Charlemagne, as Holy Roman Emperor – a new title Charlemagne found nifty enough to add to his already significant collection. But, as Voltaire reflected later on, the title, while maintained for an impressive span of a thousand years, had little practical significance: “[...] *the Holy Roman Empire was neither holy, nor Roman, nor an Empire*”. The title persisted even though the territory was not unified in religion and one of the emperors was even excommunicated by the pope. Rome was not by any stretch of imagination the centre of the *Holy Roman Empire*, in fact Italy eventually stopped being part of the empire with no effect on the Empire designation. While its border continued to change, the Holy Roman Empire was consistently made up of Germanic nations. Additionally, Latin was not a popular language across the territories. Finally, unlike the Roman Empire, the Holy Roman Empire was hardly an empire in the sense of a unitary legal entity and the absolute power the emperor would hold over its territories. Yet, the name prevailed, despite it being a gross misnomer¹, perhaps even an anachronism.

¹Here is another classic example: the Jerusalem artichoke is the root of a North American plant, in the sunflower family – the name is probably a corruption of the Italian for “sunflower”, *girasole*.

When it comes to the SEM techniques, their labels are also not terribly accurate. Some keep insisting calling the transmission diffraction mode in the SEM - transmission electron backscattered diffraction (t-EBSD), apparently oblivious to the oxymoron in the association. But, perhaps even more confusing, is the fact that, while some techniques carry in their name the type of electron interaction that generates the signal, EBS-Diffraction, TK-Diffraction, others do not. Electron channelling patterns (ECP) and electron channelling contrast imaging mislead the inexperienced reader to assume that the source of signal is fundamentally different, that in fact *channelling* might be the type of interaction to blame. These labels are the “Holy Roman Empire” of electron microscopy.

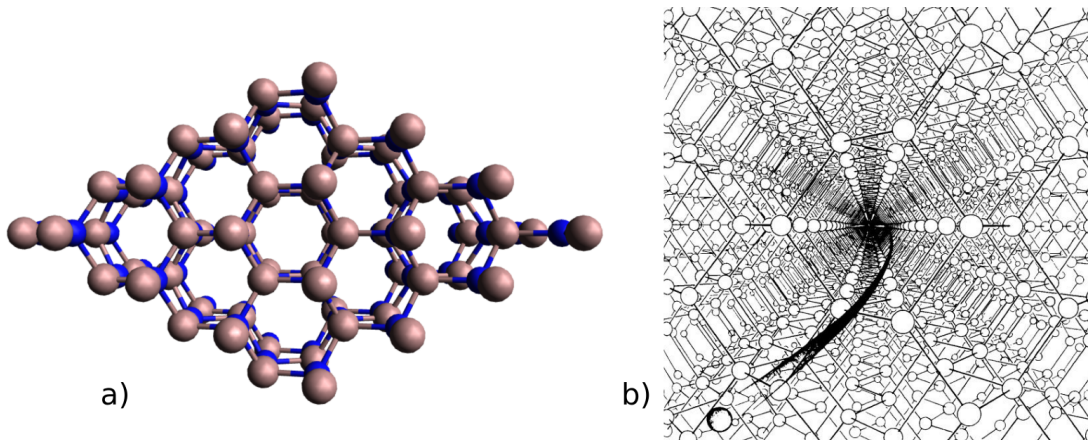


FIGURE 4.1: a) Open “channels” between rows of atoms along the main direction [001] in GaN – *not* responsible for what is sometimes called electron “channelling”. b) Artist’s impression of channelling of heavy charged particles, from [Bra68].

These two SEM techniques carry the word *channelling* for historical reasons. In early 1960s, before electrons became widely used in high resolution microscopy, ions were used in much the same way as electrons are in the scanning electron microscope. It was observed that the scattered secondary electron intensity depended on the ions’ incident direction [Dav83]. This was in sharp contradiction with the theory of scattering at the time which assumed the distribution of atoms in samples can be approximated to a dense gas. It became apparent that an incident ion beam aligned along any of the major axes of the crystal would yield longer penetration depths, would loose energy slower and would generate fewer secondary electrons close to the surface [Pie+63]. This was initially explained as simple geometrical transparency, *i.e.*, columns of empty space along major axes as shown in Fig. 4.1 a), such that the ions would simply suffer less scattering on their path as shown in the beautiful artist

render in Fig. 4.1 b) hence the name *channelling*.

Based on these observations, Linhard [Lin65] developed a classical mechanics explanation for incident particles with small and incoherent wavelengths such that effects such as interference patterns can be ignored. He defined the condition for the validity of this classical treatment through the requirement that the number of bound states in the atom string potential to be large compared to unity ($\nu_s \gg 1$). The full explanation of channelling is somewhat more involved than a simple geometrical transparency. The heavy particles, when incident at a direction close to a major crystallographic direction, behave as if focused by the total sum potential of the strings of atoms. Correlated deflection by the atoms in the strings protect the incident beam from penetrating close to the core of the atoms and suffer scattering. The resulting effect is that, in these special conditions, the incident particles can travel deeper in the sample and lose less energy, channelling, protected as they are by the potential of the string of atoms. Linhard then went on to establish an upper limit for stable channelling for the incidence angle relative to a major direction he called the *critical channelling angle*:

$$\theta_{chan} \leq \sqrt{\frac{2Ze^2}{Ed}} \quad (4.1)$$

where Z is the atomic number and E is the energy of the incident particle, e is the usual elementary charge and d is the distance between atoms in the string.

Not only strings of atoms but also lattice planes can channel a beam of incident charged particles. In *Notes on Channeling*, Andersen [And14] explains the qualitative image of planar channelling analogous to the string of atoms channelling. The planar potential can be thought of as a superposition of string potentials, allowing the incident beam particles to sneak in between two strings and still be protected by the deflection of correlated atom scattering. The dark spot in the centre of the angular flux distribution in Fig. 4.2 a) is due to lower scattering rates along the direction parallel to the $[001]$ axis, or string channelling. The dark lines are the result of planar channelling in the family of planes $\{100\}$ and $\{110\}$.

It was soon observed that the channelling extends to other charged particles like high energy protons [Dea+68] or alpha particles. For electrons and positrons, the first indications of crystal lattice influence on the scattering directions was given by observing emission yields from samples doped with β^+ emitters [UA68]. It appeared that the scattered yield increased when electrons were travelling along a lattice direction. These observations were later confirmed by Rutherford scattering experiments

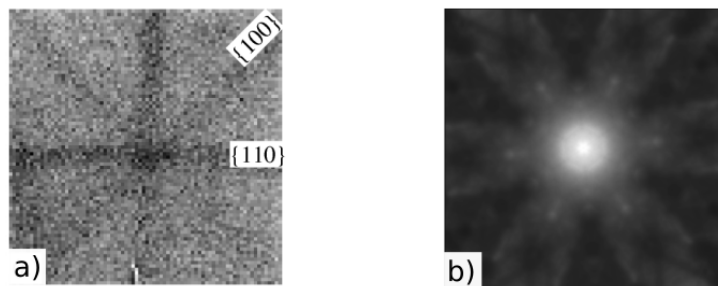


FIGURE 4.2: a) Flux distribution of heavy ions scattered from a transmitted beam through [001] Si crystal, from [Ass+99]. b) Simulated ECP pattern of [001] GaN using EMsoft [DGG13]. While the observed features are similar, a) is an effect of channelling and b) of diffraction.

of fast electrons incident on a sample [UF69]. It was only natural to make the parallel with ion scattering experiments and the so called phenomenon of *channelling*.

Mysterious is the fact that Coates had already published, two years previously, his observation of Kikuchi like patterns in the SEM [Coa67] – bright lines of increased electron backscatter intensity associated with lattice planes, yet the connection between the two phenomena was not made. By the time Joy wrote his significant contribution to the description and understanding of directional dependence of scattering in the SEM [JND82], the name of channelling had already gained traction and the phenomenon was known as an electron channelling pattern. When comparing the angular distribution of scattered ions (Fig. 4.2 a)) with that of electrons (Fig. 4.2 b)), the similarities are indeed indisputable. The contrasting lines in both cases are due to the lattice planes. In the first case the lines are dark indicating a lower scattering rate of ions when close to lattice directions and planes. However, in the electron case, the lines are bright, indicating an increase in scattering when electrons are close to the planes or directions.

For a polycrystalline sample, the contrast in intensity from one grain to the other seems similar when using ions [Fra+88] and electrons. Since for ions it was attributed to channelling it only made sense to blame channelling for a change in electron yield (contrast) for different orientated grains (Electron Channelling Contrast Imaging). When we say electron channelling we only mean channelling in the sense of a stable trajectory close to atoms and planes. Nevertheless, the underlying physics is different.

For MeV ions, with short wavelengths, the interference effects can be safely ignored since mean free path for inelastic scattering is as short as a few lattice spacings.

TABLE 4.1: Critical channelling angle θ_{chan} and Bragg angle θ_B for heavy ions and electrons travelling along (001) planes in a GaN sample. The number of bound states for strings ν_s and planes ν_p indicate the validity of the classical description of channelling.

| Particle | Energy [MeV] | ν_s (classical?) | ν_p (classical?) | θ^{chan} [°] | θ_B [°] |
|----------|--------------|-------------------------|----------------------|---------------------|----------------|
| C ion | 1 | > 10 (yes) | > 10 (yes) | ≤ 1.2 | $\leq 10^{-4}$ |
| electron | 1 | ≈ 4 (uncertain) | < 1 (no) | ≤ 0.1 | < 0.1 |
| electron | 0.02 | < 1 (no) | < 1 (no) | ≤ 0.9 | 0.5 |

Meanwhile, for fast electrons we cannot ignore that at Bragg angles their scatter amplitude will interfere constructively, which is what gives the strong, sharp peak in the scattered yield. The legitimacy of a classical description, such as channelling, for explaining these peaks is, nevertheless, doubtful.

In Table 4.1 I calculated the number of bound states, for both strings of atoms (ν_s) and planes (ν_p), for electrons at 1 MeV and 20 keV scattered along (001) planes in GaN. For electrons, the number of bound states in the string potential can be reduced from [Lin65] to:

$$\nu_s \approx \frac{1}{\sqrt{1 - \frac{v^2}{c^2}}} Z^{1/3} \frac{4a_0}{d}$$

and the number of bound states in a planar potential to:

$$\nu_p \approx \frac{0.4}{(1 - \frac{v^2}{c^2})^{1/4}}$$

where Z is the atomic number of the target material, a_0 is the Bohr radius, d is the distance between atoms in a string and v is the speed of the incident particle [UF69].

Diffraction and channelling are two separate but competing phenomena [Cha70]. They are defined by the Bragg and channelling angle, respectively, and looking at the range of these parameters we can decide which of these events dominates. For electrons with energies below 1 MeV the classical description is not appropriate, and the critical channelling angle is meaningless, which is why I wrote it in italics. But, for very high energy electrons, with energies above 1 MeV, channelling can become a relevant phenomena and will compete with the Bragg angle. We can see the situation is reversed for heavy ions, which are highly localised with numerous bound states, both in the string potential and the planar potential. However, the Bragg angle is vanishingly small for these heavy particles and therefore diffraction effects can be

ignored.

For SEM electron energies we are comfortable in the non-channelling range. Nevertheless, we will continue to use Holy-Roman-Empire-names of Electron Channelling Pattern and Electron Channelling Contrast Imaging and understand that the word channelling in these cases is different from the effect of ions channelling, referring instead to stable trajectories close to atomic nuclei for the electron Bloch waves.

Winkelmann and Vos [WSPW13] describe in detail the mechanism of *channelling in* means for ECPs and *channelling out* for EBSD.

4.3 Electron channelling contrast model

Dislocation contrast is a term coined for transmission electron microscopy. Defect characterisation in TEM is relatively well established. Both qualitative models such as the kinematical theory [HHW60], and more quantitative models in the form of the dynamical theory [HW61; CH71; SHH72] have been developed and successfully applied to predict dislocation contrast.

We have mentioned before that TEM samples must be prepared to be very thin. This is usually required in order to maximise the number of electrons that will escape from the bottom side of the sample. It is these very thin samples that minimise the interaction volume of the electrons that make the approximations in the original version of the dynamical theory pertinent.

For thicker samples than the ones used for TEM, inelastic scattering of electrons becomes impossible to ignore. When electron paths become long enough, a significant number of them are removed or “absorbed” from the diffracted beam through inelastic scattering. This loss becomes important when we take into account the dynamical pendellösung of intensities between the direct and diffracted beams. We will, therefore, always take into account absorption through the optical lattice potential discussed on page 80.

Otherwise, we will follow the path paved by TEM contrast simulations. This involves, simply correcting the deviation from the Bragg condition for the existence of a dislocation nearby. This correction, which we will call β , is, to a first approximation the directional derivative of the dislocation displacement field along the diffraction vector \mathbf{g} . We will see in Section 4.5 on page 106 that we will add a second order correction.

We then start again from the general Darwin-Howie-Whelan equation (Eq. 3.34), but this time we add the dislocation correction:

$$\frac{d\psi_{\mathbf{g}}}{dz_{beam}} - 2\pi(\mathbf{s}_g + \beta)\psi_{\mathbf{g}} = i\pi \sum_{\mathbf{g}'} \left(\frac{e^{i\theta_{\mathbf{g}-\mathbf{g}'}}}{\xi_{\mathbf{g}-\mathbf{g}'}} + i \frac{e^{i\theta'_{\mathbf{g}-\mathbf{g}'}}}{\xi'_{\mathbf{g}-\mathbf{g}'}} \right) \psi_{\mathbf{g}'}. \quad (4.2)$$

These equations, now become too complicated for an analytical solution and, as we will see in Section 4.7 on page 120, we need to use a computer to solve numerically.

Let us, in the following pages, talk about how to calculate the corrections needed for the DHW equations from the displacement field of dislocations.

4.4 TDs displacement field for ECCI

We are now tasked to calculate the displacement field introduced by a dislocation in a perfect crystal and for this we turn to elasticity theory.

Even one dislocation will disturb every single one of the $\approx 10^{11}$ atoms in one micrometer cube of the sample in a non trivial manner, the effects of this distortion can then affect the phase of the diffracting electrons and can be resolved in the SEM. In order to simulate this complex multi body problem it is not unwise to turn to a model that would strip down all unessential details to the bare physical properties that drive these interactions.

This branch of continuum mechanics developed specifically for the description of dislocations brings many elegant simplifications to the treatment of dislocations, but also some limitations. In the following subsections we are to direct our attention towards the derivation of strain fields produced by threading dislocations running normal to the surface of a sample using this mathematical formulation.

4.4.1 Elasticity theory

As part of continuum mechanics, elasticity theory ignores the fact that matter is made out of discrete particles and instead approximates it to be continuous and uniform even at the microscopic level. This conveniently enables us to ignore the very complicated interaction between the many atoms as well as any discontinuing properties at the microscopic level (including the actual dislocations!) simplifying the treatment a great deal. Instead, it entertains the more intuitive idea that matter fills the entire region of space it occupies in a continuous and homogeneous manner and that this holds true for any infinitesimal region of space. While this is not a rigorous description at the microscopic scale, for the micrometer level study of structural effects of dislocations, these crude assumptions will hold fully.

In this model all the specific physical properties of the continuum are exactly the same for any infinitesimal selected region. This facilitates the substitution of what would otherwise be discontinuous quantities with single valued, smooth fields representing the average value over that infinitesimal region of space of the property we would want to study.

In continuum mechanics we are concerned with the stress field applied to a material and the strain response of said material. Notice the word field in the previous statement. Many material properties are not simple scalars. In this case, both the strain and stress are tensors of rank 3 as shown in Fig. 4.3. Not all of the 3×3 matrix components are necessarily unique. In fact, it turns out that these entities are intrinsically symmetric² for a system at equilibrium, resulting therefore in only 6 unique components.

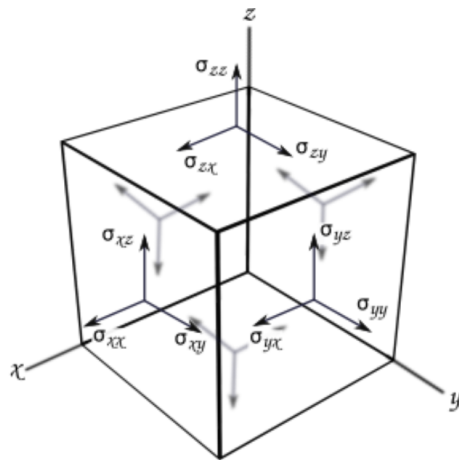


FIGURE 4.3: Stress distribution on an infinitesimal volume.

Within the framework of continuum mechanics we also make the assumptions of *linearity* and *perfect elasticity*. The final approximation we will introduce is that of *elastic isotropy*. We provide below the implications of these assumptions:

1. If a body returns to its original form completely after any deformation force is applied, we say that object possesses the property of *perfect elasticity*. Mathematically this is achieved by keeping the forces that produce the deformation below the plasticity region of the structural material of interest, or in other words very small (small enough).

²Onsager's Principle of Microscopic Reversibility [Cas45] can be used to show that principal transport properties are symmetrical tensors.

If we define σ_{ij} as the i^{th} component of the stress (force per unit area) on a plane whose normal is in the x_j direction as shown in Figure 4.3, and then consider that when acted upon by stress a body deforms such that the displacement at point \mathbf{r} is \mathbf{u} with component u_i we can define strain as:

$$\epsilon_{ij} = \frac{1}{2} \left(\frac{\partial u_i}{\partial x_j} + \frac{\partial u_j}{\partial x_i} \right) \quad (4.3)$$

2. In the equation above we have assumed the distortions are small enough that we can ignore all but first terms in the expansions of individual displacement components. This is also known as *linearity* and also produces a linear relation between stresses and deformations (Hooke's law):

$$\sigma_{ij} = c_{ijkl} \epsilon_{kl} \quad (4.4)$$

where the coefficients c_{ijkl} form a rank 4 tensor and are the elastic constants. For the most general case form a 6×6 matrix relating the six unique elements of σ_{ij} to the six elements of ϵ_{kl} .

3. The final assumption we make here is to state that our material can be reduced to *elastic isotropy* without impairing greatly the accuracy of the results. This is the property of a material whose elastic properties are independent on the orientation we study it in. This, in general, is not the case for none but a handful of cubic structures. For the wurtzite structure, Neumann's rule predicts all the symmetries of its point group. Additionally, since wurtzite is not that far crystallographically from zinc blende, it can be shown [Mar72] that one can reduce the wurtzite elastic constants to an effective cubic zinc blende tensor. This reduces the number of independent variables to three and we can rewrite Eq. 4.4 as:

$$\begin{bmatrix} \sigma_{11} \\ \sigma_{22} \\ \sigma_{33} \\ \sigma_{23} \\ \sigma_{13} \\ \sigma_{12} \end{bmatrix} = \begin{bmatrix} 2\mu + \lambda & \lambda & \lambda & 0 & 0 & 0 \\ \lambda & 2\mu + \lambda & \lambda & 0 & 0 & 0 \\ \lambda & \lambda & 2\mu + \lambda & 0 & 0 & 0 \\ 0 & 0 & 0 & \mu & 0 & 0 \\ 0 & 0 & 0 & 0 & \mu & 0 \\ 0 & 0 & 0 & 0 & 0 & \mu \end{bmatrix} \begin{bmatrix} \epsilon_{11} \\ \epsilon_{22} \\ \epsilon_{33} \\ 2\epsilon_{23} \\ 2\epsilon_{13} \\ 2\epsilon_{12} \end{bmatrix} \quad (4.5)$$

with μ known as the shear modulus and λ the Lamé constant. We can introduce another useful constant: the Poisson ratio, ν :

$$\nu = \frac{\mu}{2(\mu + \lambda)}$$

However, no crystal structure is truly isotropic with the wurtzite crystal system showing an anisotropy factor of 0.86 (compared to 1.0 for an isotropic system). Nevertheless, physics is all about approximating a complex system to a simple system and then adding corrections. This is exactly what the *Voigt* formula [HL82] achieves. In Table 4.2 I give the elastic parameters for GaN if we are to approximate it to be isotropic.

| Elastic constant | Symbol | Voigt approximation |
|------------------|-----------|---------------------|
| Shear modulus | μ | 121 GPa |
| Lamé constant | λ | 129 GPa |
| Poisson ratio | ν | 0.26 |

TABLE 4.2: Voigt approximation of elastic constants for isotropic wurtzite GaN.

4.4.2 Semi-infinite screw dislocation

A screw dislocation is a shear in the crystal with the edge of shear being the dislocation line itself. The amount of shear is quantified in terms of lattice parameters and is a vector along the dislocation line. This vector quantifying displacement is known as the *Burgers vector*, \mathbf{b} .

Let us work out the displacement introduced by a screw dislocation in a perfect crystal. The screw dislocation, let's say aligned with the z -axis, introduces displacement only along the dislocation line, as comprehensibly explained in *Theory of dislocations* [HL82]:

$$u_z = \frac{b}{2\pi} \arctan \frac{y}{x} \quad (4.6)$$

From Eq. 4.3 we can conclude that the only strain components produced by this displacement must be ϵ_{xz} and ϵ_{yz} . If we were now to consider a surface on which the dislocation is normal, both these strains will act on the surface and the surface itself will have an effect on the displacement field of the dislocation.

Saint-Venant's principle [Tou65] tells us that the forces exercised by a surface on an elastic body are equivalent to replacing the surface by an object impacting the same

force as long as the object is far away. So far this is not particularly unsettling. The beautiful approach based on this concept is that we can talk of the effect of surface relaxation around a dislocation as being derivable, similarly to the electrostatics world, by adding an imaginary field that ensures the surface “feels” zero strain.

In our case, for a screw dislocation normal to a surface, it is the out of plane stress that must be relaxed. The relaxation displacements in Cartesian coordinates was calculated by Eshelby and Stroh [ES51] to be simply:

$$u_x^i = \frac{b}{2\pi} \frac{y}{r-z} \quad (4.7)$$

$$u_y^i = -\frac{b}{2\pi} \frac{x}{r-z} \quad (4.8)$$

In the end, the total displacement introduced by a TD normal to a surface is made up of the *real + imaginary* displacement fields. In Appendix D, Fig. D.1 I show the elastic strain tensor components as contour plots for a screw TD in GaN using Eq. 4.3 with the displacements shown here.

4.4.3 Semi-infinite edge dislocation

An edge dislocation is the result of introducing an extra plane of atoms in a perfect crystal. The displacement field introduced is in plane and is given in Cartesian coordinates in the notation from [IL12] as:

$$u_x = \frac{b}{2\pi} \left[\arctan \frac{y}{x} + \frac{xy}{2(1-\nu)(x^2+y^2)} \right] \quad (4.9)$$

$$u_y = -\frac{b}{2\pi} \left[\frac{1-2\nu}{4(1-\nu)} \ln(x^2+y^2) + \frac{xy}{4(1-\nu)(x^2+y^2)} \right] \quad (4.10)$$

The surface relaxation is more involved in this case, but Yoffee derived an elegant solution [Yof61] for a dislocation interacting with a surface at a general angle:

$$u_x^i = \frac{\nu b}{4\pi(1-\nu)} \left[\frac{2xyz}{r(r-z)^2} + (1-2\nu) \frac{xy}{(r-z)^2} \right] \quad (4.11)$$

$$\begin{aligned} u_y^i &= \frac{\nu b}{4\pi(1-\nu)} \left[(1-2\nu) \log(r-z) - (3-2\nu) \frac{z}{r-z} \right. \\ &\quad \left. + (3-2\nu) \frac{y^2}{(r-z)^2} - \frac{2y^2}{r(r-z)} \right] \end{aligned} \quad (4.12)$$

$$u_z^i = \frac{\nu by}{2\pi(1-\nu)} \left[\frac{1}{r} + (1-2\nu) \frac{1}{r-z} \right] \quad (4.13)$$

Such that the total displacement components are: $u_x^t = u_x + u_x^i$, $u_y^t = u_y + u_y^i$, $u_z^t = u_z^i$. In Appendix D, Fig. D.2 I show the elastic strain tensor components as contours plots for an edge TD in GaN using Eq. 4.3 with the displacements shown here.

4.5 TD ECC-strain

The image of a single crystal surface in high magnification mode should consist of a constant backscattered electron yield as the near parallel beam is scanned over a small area. Around a dislocation line the crystal structure is distorted, which in turn affects the diffraction of the electron beam. The shift in diffraction behaviour close to the dislocation is observed as a change in the number of backscattered electrons originating from the distorted crystal region and provides direct information about departures from the perfect crystal structure in the ECCI micrograph. Similarly to the contrast mechanism in TEM described by Hirsch *et al.* [HHW60], the lattice curvature directly affects the distance by which the diffracting reciprocal lattice points deviate from the Bragg condition and is quantified by the deviation parameter \mathbf{s}_g . The correction needed to account for the distortion introduced by a lattice defect is then the change in the direction of the incident electron beam, \mathbf{r}_{inc} , of the component of the displacement field, \mathbf{u} , which is parallel to the reciprocal vector, \mathbf{g} , defining the diffraction condition. Tunstall *et al.* [THS64] showed geometrically that there is a second, smaller correction term which accounts for the change in lattice parameters close to the dislocation:

$$\mathbf{s}'_g = \mathbf{s}_g + \beta = \mathbf{s}_g + \hat{\mathbf{r}}_{inc} \cdot \nabla(\mathbf{u} \cdot \mathbf{g}) + \theta_B \hat{\mathbf{r}}_g \cdot \nabla(\mathbf{u} \cdot \mathbf{g}) \quad (4.14)$$

where θ_B is taken to be the Bragg angle and $\hat{\mathbf{r}}_g = \mathbf{r}_g / |\mathbf{r}_g|$ is the coordinate in the dislocation frame parallel to \mathbf{g} .

The new variable β , which I will also call *ECC-strain*, is the sum of all corrections to the deviation parameter due to the defect. If defined in an orthogonal coordinate system it can also be written as:

$$\boxed{\beta = \frac{\partial u_g}{\partial r_{inc}} + \theta_B \frac{\partial u_g}{\partial r_g}} \quad (4.15)$$

where u_g is the displacement field in the direction of \mathbf{g} .

If the displacement field is defined in a Cartesian reference frame in which \mathbf{g} is parallel to one of the axes then the corrections terms above can be considered as strain-like components since they measure displacements field gradients. Due to the θ_B weighting factor, the second strain-like term introduced by Tunstall is negligible and can be ignored whenever the first term is non-zero as we will see later. It is these strain-like components that disturb the electron diffraction as compared to a perfect crystal and generate the dark-bright contrast features associated with dislocations in ECCI images.

Note that the magnitude of β will be left as arbitrary more often than not since a one-to-one comparison against experimental results cannot be (yet) made. The comparisons I do make is against backscattered electron intensity, which in turn is also of arbitrary magnitude. What we are interested in instead, is how the change in strain compares with the change in contrast which I will investigate using contour plots.

4.5.1 The failure of the invisibility criterion for ECCI

We mentioned a few times that transmission electron microscopy has established itself as the default technique for the study of lattice deformations. It is especially reliable as a dislocation characterisation method as it can identify unambiguously the **c** and **a** components of a dislocation line running parallel to the imaged surface. This is achieved through the application of certain relationships between the diffraction vector \mathbf{g} , Burgers vector \mathbf{b} and the direction of the dislocation line \mathbf{u}_l ($\mathbf{g} \cdot \mathbf{b} = 0$ and $\mathbf{g} \cdot \mathbf{b} \times \mathbf{u}_l = 0$), known as the invisibility criteria, for which no contrast associated with **c** or **a** components, respectively, can be observed. This method has been applied broadly in the study and characterisation of dislocations in cross sectional GaN samples, *e.g.* [Hin+00].

Let us briefly discuss why, unlike the case for cross-section TEM, the invisibility criterion is not appropriate for dislocation identification in the foreshatter geometry

of ECCI especially in the absence of high resolution electron channelling patterns (ECPs).

The displacement in an infinite lattice due to a dislocation line of type **a** or **c** can be derived from elasticity theory in the linear regime (see for example Ref. [Rea53]). If the dislocation line interacts in any way with the free surface of the layer, the non-zero stresses at the interface have to be relaxed in order to obtain the full strain picture of the dislocation line. This relaxation in turn introduces extra displacements such that the total displacement at any point in the lattice is a sum of the “infinite-lattice” displacement and that due to the surface relaxation. Yoffe [Yof61] has calculated these surface relaxations due to general dislocations intersecting the surface at an arbitrary angle.

The importance of surface relaxation in the simulation of the electron channelling contrast micrograph has already been discussed by Wilkinson *et al.* [WH95] for dislocations running parallel to a nearby surface. Even for the diffraction conditions where the infinite-lattice model gives no ECCI strain-like components, the non vanishing surface strain terms ensure that the net contrast will never be truly zero. This effect will only increase for dislocation lines which penetrate the surface where the non-vanishing surface terms become even more significant. Even in the case where the Burgers vector is perpendicular to the **g** direction, the ECCI sampled strain will be smaller but still not zero.

This reduction in dislocation contrast at the invisibility criteria had been already used in literature [Mor+79; CSN01] to show that, at least phenomenologically, the same principle can be applied to ECCI. In practice care is advised when using this approach for the characterisation of dislocations. Unlike TEM which allows reasonable dislocation contrast to be acquired for a significant range of deviations from the Bragg condition, the contrast in ECC images is optimised at the exact Bragg condition, $s_g = 0$, and can change drastically on small variation from that condition. This can determine whether a dislocation is visible or not, even for diffraction conditions where we would expect to see good contrast (see also the discussion in Ref. [Cri06]).

4.5.2 ECC-strain profile for the forward scattering geometry

From Eq. 4.15 we can see that the strain profile imaged by ECCI, β , of the **a** character of a TD normal to the surface is sensitive to variations in the angle of incidence of the electron beam, r_{inc} . This is indeed the case for the forward-scattering SEM geometry; I show what I mean by this schematically in Fig. 4.4. This effect is especially strong for edge TDs because they introduce elastic displacement mostly in the plane

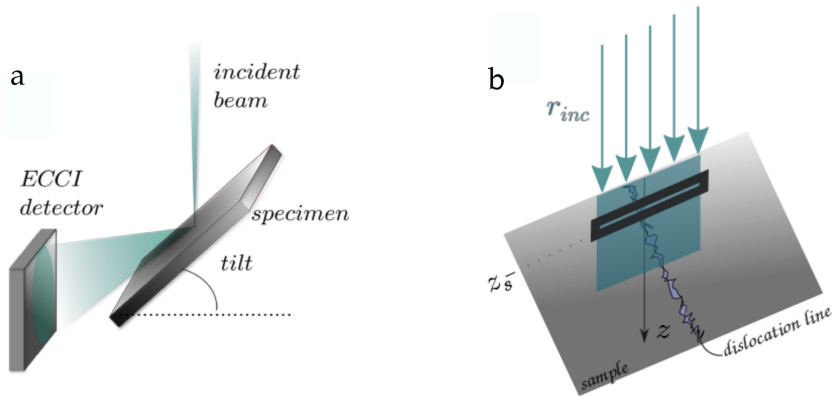


FIGURE 4.4: a) Schematic of forward-scattering geometry in the SEM. b) The geometry of the incident beam with respect to a tilted sample. The rectangular box shows the plane z_s which is considered in Fig. 4.6.

normal to the dislocation line and present almost no variation along a normally incident beam. Shown schematically in Fig. 4.5, the strain-like component only contains surface terms and anisotropy effects. Titling the sample (or the beam) translates to rotating the coordinate system in which the ECC-strain is defined, which means the tensor element in the new system will have to contain components from the plane normal to the dislocation line.

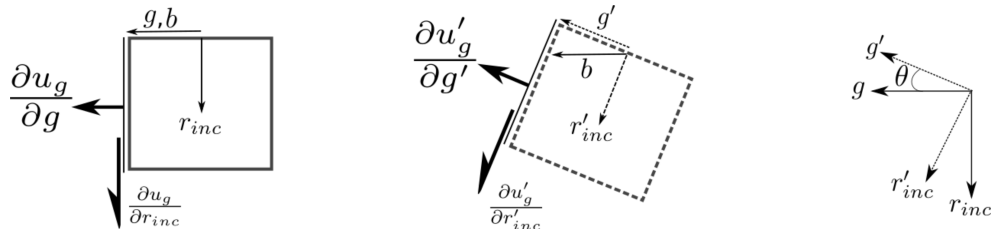


FIGURE 4.5: 2D diagram of rotation transformation in ECC-strain tensor. A θ anticlockwise rotation of the sample is equivalent to the same rotation of the coordinate system in which the strain components are defined.

The diagram in Fig. 4.6 illustrates this in two dimensions in the case when \mathbf{b} is parallel to \mathbf{g} . For a passive rotation of the sample around a direction normal to both the dislocation line and its \mathbf{b} , the first term of Eq. 4.15 in the new coordinate system will be:

$$\frac{\partial u'_g}{\partial r'_{inc}} = \cos^2 \theta \frac{\partial u_g}{\partial r_g} + \sin \theta \cos \theta \frac{\partial u_g}{\partial r_{inc}}$$

where the terms measuring the variation of the displacement field in the beam direction are ignored as they are very small. The first part in the equation above is the variation of the displacement field along \mathbf{b} (or \mathbf{g} in this case) and for reasons discussed above will be the dominant term in this strain expression. More about transformation of coordinates will be addressed in next subsection.

It is to be expected, then, that tilting the sample will improve the observed contrast of edge dislocations significantly. Fig. 4.6 a) to c) show how a small tilt can significantly change not only the intensity of the sampled strain but also the orientation of its high-low profile. This second effect has to do with the fact that our definition of β (Eq. 4.15) contains two strain-like components. Since the variation of displacement field along the line direction (the first term of Eq. 4.15) for the \mathbf{a} character of a threading dislocation is negligibly small, what we observe in Fig. 4.6 a) is purely the second strain-like component introduced by Tunstall. This strain profile closely resembles TEM bright field intensity maps for an edge dislocation normal to the foil surface computed by Tunstall *et al.* [THS64] with the high-low “butterfly” lobes oriented on each side of the Burgers vector.

However, Tunstall’s component is orders of magnitudes less significant than the first term of β , $\frac{\partial u_g}{\partial r_g}$. This means that when the foil is tilted, Tunstall’s strain profile will be replaced by the profile of the first term. It is remarkable that, in the case when the diffraction vector is aligned parallel with the Burgers vector, any amount of sample tilt will change the direction of the minimum-maximum strain direction from being perpendicular to \mathbf{b} to being parallel. When the full three dimensional displacement field is considered it becomes apparent that the variation of the field along the extra plane of atoms introduced by the edge dislocation dominates all other factors and this function has its maxima and minima along the Burgers vector. This contrast alignment was observed experimentally and reproduced by simulations for threading dislocations inclined to the surface by Picard *et al.* [Pic+07].

The images in Fig. 4.6 also highlight the ability of foreshatter geometry ECCI to access the TD strain profile for cases where plan view imaging might produce low signal to noise features. In general, the higher the tilt, the better the expected contrast of edge TDs will be.

4.5.3 General coordinate transformation

Eq. 4.14 contains mathematical objects specified in various reference frames and are therefore described using different basis sets. The \mathbf{g} vectors are described in the reciprocal crystal frame, the displacement field is defined in the dislocation frame and

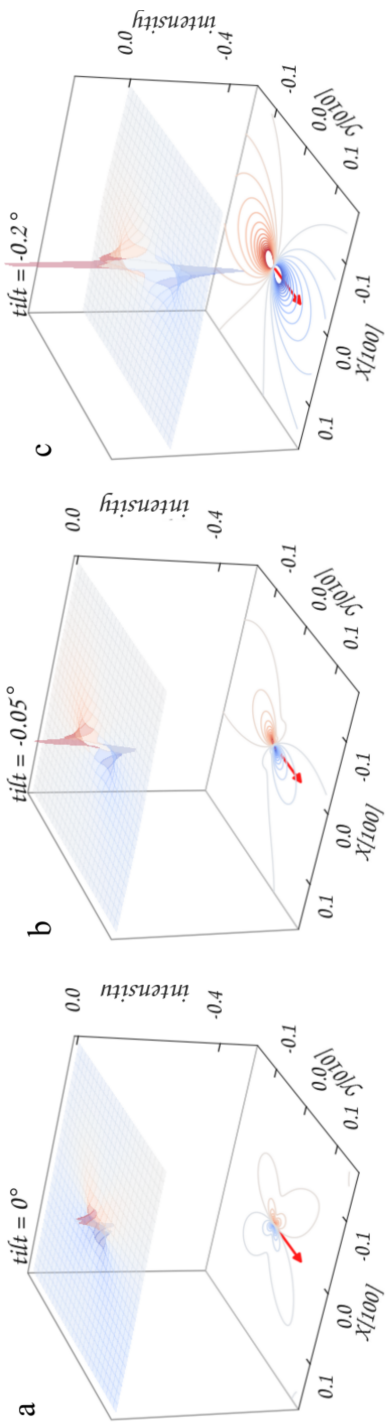


FIGURE 4.6: The β strain profile due to an edge TD in a cubic material shown in a plane z_s parallel to the surface for three electron beam incidence angles close to zero a) 0° , b) -0.05° and c) -0.2° . The red arrows show both the Burgers vector direction and the projection of \mathbf{g} .

the incident beam and sample orientation are usually given in lab coordinates. The first component of β in Eq. 4.14 for instance, can be written to show explicitly the relationship between reference frames, following the notation used by De Graef [DG03] as:

$$\frac{d\mathbf{u}(\mathbf{r}) \cdot \mathbf{g}}{dr_{inc}} = (r_{inc})_i^d \frac{\partial u_j^d}{\partial x_i} \mathcal{T}_{js}^{ds} B_{lm} g_m \quad (4.16)$$

where Einstein summation convention is used for repeating subscript indices. The superscripts indicate the reference frame in which the expression of the vector is known. B is the reciprocal structure matrix for the unit cell of the material. \mathcal{T}_{js}^{ds} is the coordinate transformation matrix which can be applied to a vector described in the dislocation frame (d) in order to be translated in the sample frame (s).

Fig. 4.7 shows the relationship between the lab frame, the sample frame and the dislocation frame as well as the rotations required to orient one with respect to the others. For instance, the sample is rotated anticlockwise with the angle α_{rot} about the x axis direction with respect to the lab frame.

If we define the coordinate frames used as meeting the following requirements:

- the sample tilt axis is aligned with its x axis as well as the lab x axis;
- the crystal is non polar so that the crystallographic Cartesian z can be aligned with the sample's z ;
- the anticlockwise rotation from the sample frame to the Cartesian crystal frame along z is given by α_{rot} ;
- the dislocation line frame is defined as the right handed counterpart of the dislocation frame defined by Tunstall [THS64], such that its z axis is anti-parallel with the crystal frame and the sample frame z axis,

then the transformation matrix from the dislocation reference frame to the sample reference frame can be written as:

$$\mathcal{T}_{ds} = \mathcal{R}^z(\alpha_{rot}) \mathcal{R}^x(\pi) \mathcal{R}^z(3\pi/4) \quad (4.17)$$

where $\mathcal{R}^w(\theta)$ is the passive anticlockwise rotation in a right handed coordinate system looking along w by an angle θ as discussed on page 42.

These transformations are implemented in this work using the *ReferenceFrame* class from Python's *sympy.physics.vector* module [Meu+17] which proved useful in

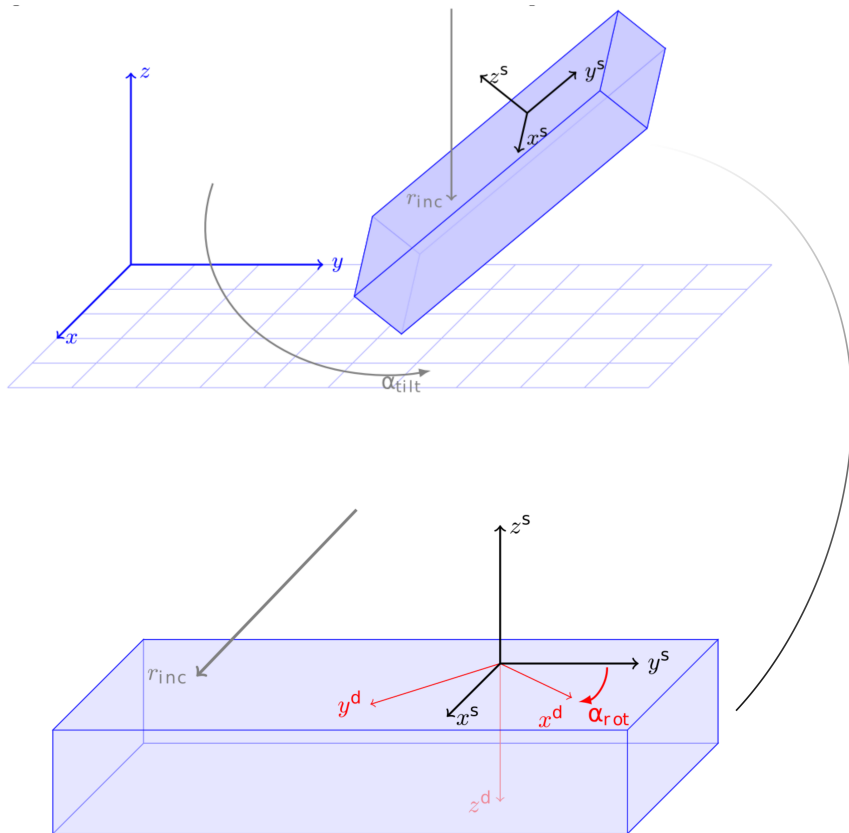


FIGURE 4.7: a) Tilted sample Cartesian frame (denoted by (s)) and incident beam direction in the lab frame used here as a reference frame. b) Relationship between the dislocation reference frame (denoted by d) and the sample reference frame. The crystal frame is defined as an anticlockwise rotation along z^s by α_{rot} and is not shown here.

keeping track of the frames in which vectors and fields are defined as well as the set of rotations between them. The total ECCI strain-like object is saved as a numerical function of x , y , z position in a Python generated Fortran routine that will be used later in the Howie-Whelan equations to calculate contrast.

For these plots I had to split the work in multiple files and all can be found in the “ecci-model” folder on the GitHub repository:

- `geometry.py` contains crystallographic calculus for a cubic or hexagonal crystal.
- `coordinates.py` contains the relationship between the different reference frames.
- `calculateBeta2.py` calculates the beta function as an object dependent on the position from the dislocation, the tilt and rotation of the sample, the diffraction condition.

- `generateBetaModules.py` uses previous function to create Fortran callable modules containing the beta function.
- `plotField.py` is used to the displacement field.
- `plotStrain.py` is used for a number of plots for the strain profile.

4.5.4 β isosurfaces insights

So far we have discussed the way to generate the strain components that affect the channelling contrast in the expression given in Eq. 4.15. Since this parameter has the form of strain ($\partial u / \partial x$), and, like the strain, it is dimensionless, I'm calling it here *ECC-strain*. Since we also covered the grounds of calculating this value in different coordinate system it is useful now to observe its behaviour more closely.

For the following calculations and plots I am considering a [0 0 1] grown GaN sample containing TDs coming normal to the surface. The sample is tilted with respect to the incident beam. I am plotting isosurfaces, that is surfaces of constant β value. Since it is common in this geometry for the ECC-strain to change sign around the dislocation (otherwise we would not have TD contrast), I plot both a positive β value isosurface, analogous to compressive strain, in red and a negative value, analogous to tensile strain, in blue. In their absolute, the positive and negative β values are chosen to be equal; I call them equidistant. Since the aim of this analysis is to observe the qualitative change in behaviour for different condition, for a series of images the β values are the same. The off-white isosurfaces show the zero value positions.

Screw versus Edge TD isosurfaces

There is insight that can be gained by looking at the shape of the strain components introduced by the threading dislocation in the Howie-Whelan two beam equations. I did that in Fig. 4.8 for an edge dislocation and Fig. 4.9 for an screw dislocation in a GaN sample tilted at 50 degree. Because strain is a three dimensional function it can be difficult to visualise, so what I did here is to plot only surfaces of constant strain component values (isosurfaces) both for a positive value (compressive strain) in red and a negative one (tensile strain) in blue, where the negative and positive values have the same absolute values. The isosurface values chosen are the same for the edge and screw dislocation. The white cylinder in the middle indicates the position of the dislocation line which runs along the z direction. The red rod shows the projection of the diffraction condition vector \mathbf{g} . The grey rod indicates the direction of the Burgers

vector \mathbf{b} , which is normal on the dislocation line for an edge dislocation and along the dislocation line, and here invisible, for a screw dislocation.

A first observation to draw here is that in a highly tilted sample, the ECC-strain introduced by an edge TD will generally be larger than that introduced by a screw dislocation far away from the surface. This relates back to the discussion we had in Section 4.5.2 on page 108 and has to do with unlocking larger strain components for an edge dislocation when tilting the sample.

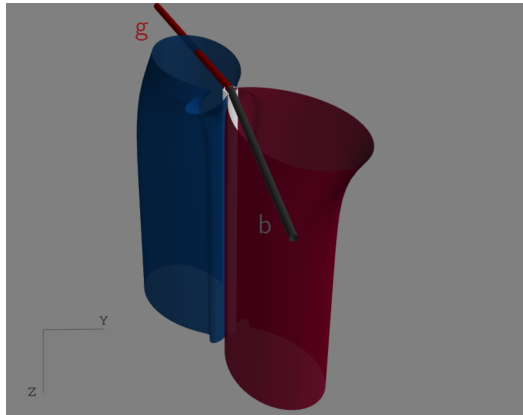


FIGURE 4.8: Edge TD ECC-strain field equidistant isosurfaces.

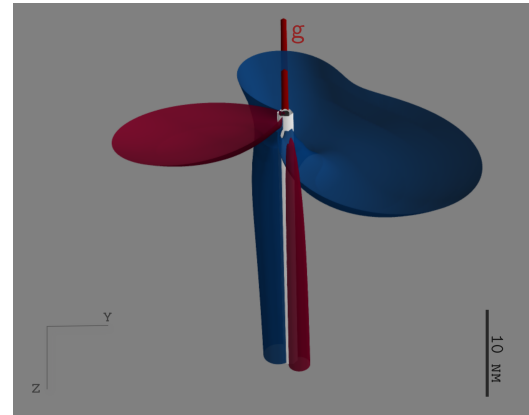


FIGURE 4.9: Screw TD ECC-strain field equidistant isosurfaces.

Another observation is that the surface relaxation affects ECC-strain of the two dislocation lines differently. At this high tilt there is little out of plane strain to relax for an edge dislocation and we can see the isosurfaces only curve a little at the top where the surface would be. The story is rather different for the screw dislocation in this specific diffraction condition. This time the isosurfaces make up large lobes close to the surface of the sample. Not only this, but we can observe an inversion of tensile-compressive strain as we follow the dislocation line to the surface.

Since in the end we must integrate the two beam equations downwards in the sample, what we could take home from this comparison is that it will be probably more likely to observe edge dislocation contrast in the SEM. The screw dislocation ECC-strain becomes comparable in effect only close to the surface, therefore we expect the TD contrast to be comparable only when we are confident the diffracting beam penetration depth is only a few nanometers.

Mixed TD isosurfaces

I want to quickly touch on how to predict mixed type dislocations. A mixed dislocation, in terms of continuum mechanics, is simply a linear combination of edge and

screw displacement fields. It will come as no surprise that the ECC-strain will also look like a linear combination of screw and edge ECC-strain. This can be seen in Fig. 4.10.

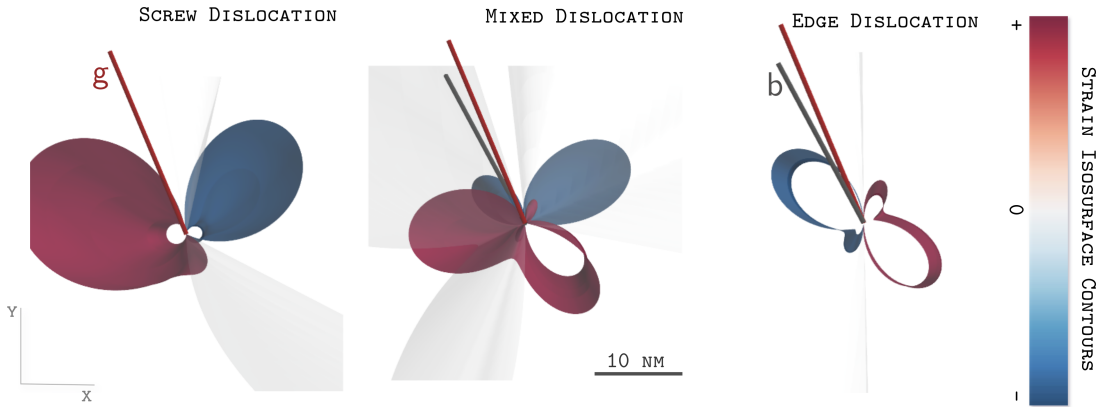


FIGURE 4.10: Top view of equidistant dimensionless ECC-strain isosurfaces for a pure screw dislocation, a mixed and a pure edge dislocation, respectively in GaN. The sample is tilted at 49.6° and rotated by 49.6° such that $\mathbf{g}=[7\ 5\ \bar{3}]$ is available.

The large surface relaxation is inherited from the screw dislocation displacement field, however the profile is complicated by the edge TD components. For a deep diffracting beam penetration depth we would expect the ECC-contrast to resemble mostly the edge dislocation since it has the dominant strain contribution.

Next, there is a critical question the channelling contrast literature is interested in: *Is the orientation of the dark-white contrast affected first by the diffraction condition or by the Burgers vector?*

Dependence on \mathbf{g}

In Fig. 4.11 I show the top of the sample view of the ECC-strain isosurfaces for an edge dislocation in three different diffraction conditions. The red rods indicate the projection of the \mathbf{g} vector and the grey rod shows the Burgers vector, \mathbf{b} . I kept the set of planes, and therefore the magnitude of \mathbf{g} the same, the red rods are projections and vary in size.

Relating to the size of the projection of the \mathbf{g} vector on the surface of the sample, the surface relaxation strain is larger or smaller. But the general geometry of the tensile-compressive strain, looking at the blue and red surface relaxation strain, does not seem terribly affected by which direction the reciprocal vector \mathbf{g} points to.

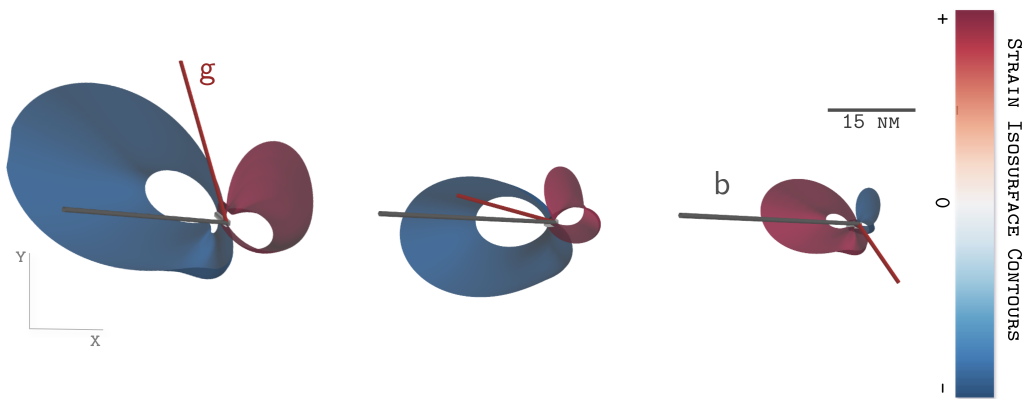


FIGURE 4.11: Top view of equidistant ECC-strain isosurfaces for a pure edge dislocation in different diffraction conditions given by the diffraction vector g (red rod).

To emphasise this point in practice, Gunnar Kusch took two ECC images, Fig. 4.12, from the same area of AlN in two different diffraction conditions shown in the bottom corner. While the directions of the projected g vectors is different the black-white dislocation contrasts direction remains the same if only fainter.

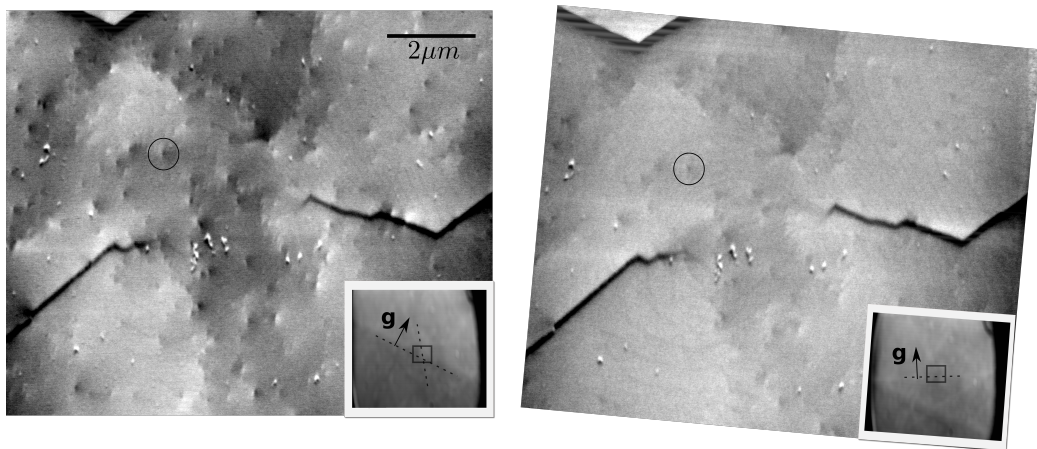


FIGURE 4.12: Forward geometry ECC image of AlN in two diffraction conditions shown by the ECPs inserts in the bottom corners.

Dependence on b

In Fig. 4.13 I show the top of the sample view of the ECC-strain isosurfaces for an edge dislocation in four different orientations of its Burgers vector. The red rods, like before, indicate the projection of the g vector and the grey rods show the Burgers

vector, \mathbf{b} . The diffraction condition remains the same in the first three panels and for the last panel is flipped to $-\mathbf{g}$. The off-white sections indicate the zero strain isosurface which looks complicated in the first panel.

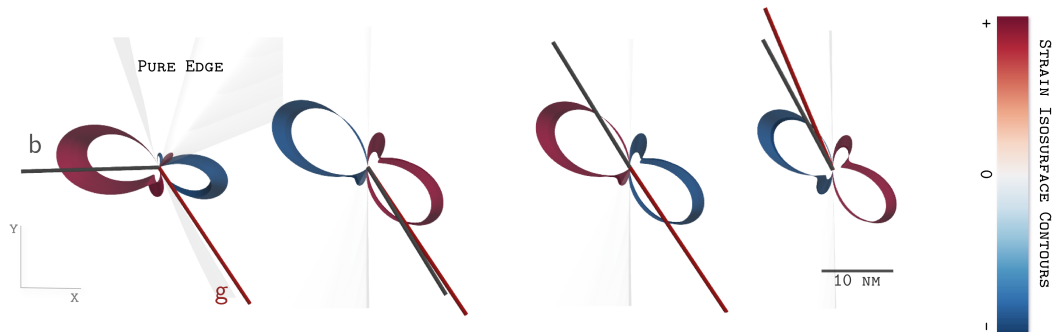


FIGURE 4.13: Top view of equidistant ECC-strain isosurfaces for a pure edge dislocation in different orientations indicated by the Burgers vector direction (grey rod).

Comparing the first two panels, where the Burgers vector, and essentially the dislocation, is rotated by about 120° in plane, we can observe that the tensile-compressive strain lobes rotate with \mathbf{b} . Rotating the dislocation by 180° , what I did in panels two and three, perfectly flips the tensile and compressive strain. This is unlike rotating the sample, but, somehow, not the dislocation, by 180° in a system with mirror symmetry such that we can hit $-\mathbf{g}$. I show this operation in panels three and four and while the tensile-compressive strain lobes do flip, their shape is slightly changed.

It is safe, therefore, to conclude that for the same diffraction condition the Burgers vector of an edge dislocation will dictate the ECC-strain geometry. This has been previously proposed by Naresh-Kumar *et al.* [NK+12].

4.6 Backscattering event model

For the backscattering process we follow the assumption made by Twigg *et al.* [TP09] that the contrast carrying signal comes from those electrons that leave the sample as soon as they suffer their first large angle scattering event, having previously suffered diffraction on their way in. The rest of the scattered electrons (making up the vast majority) will inelastically scatter multiple times on their way back out of the sample losing the contrast position information and only contributing to a uniform background.

Twigg *et al.* [TP09] follows Rossouw *et al.* [Ros+94], analogously to the simulation of Kikuchi bands by Winkelmann *et al.* [Win+07], and integrates the beams wavefunctions over depth to determine the probability of forward scattering at a certain penetration depth. Rossouw *et al.* [Ros+94] approximate the cross-section for localised scattering events, σ , for independent partial Bloch waves ϕ^i to be:

$$\sigma \approx A \sum_n Z_n^2 \sum_i |\phi^i(\tau_n)|^2 \exp\{-B_n\} \quad (4.18)$$

where the term A is:

$$A = \frac{2\pi N}{a_0^2 k^4} \frac{\cos \beta_1 - \cos \beta_2}{(1 - \cos \beta_1)(1 - \cos \beta_2)} \quad (4.19)$$

where β_1 and β_2 determine the minimum (β_1) and maximum (β_2) scattering angles allowed by the solid angle of the detector.

The BSE cross-section is proportional then to $P_n Z_n^2$ over all the atom sites in the volume of interaction, where $P_n = \sum_i |\phi^{(i)}(\tau_n)|^2$ is the probability density of electron backscattering from atom site τ_n smeared out by the Debye-Waller term B_n .

The trick now is to calculate the Bloch waves contributions in the equations above. Luckily we have the two beam differential equations 4.2 from which we could (we will see in next section how) calculate the intensities in the direct and diffracted beams. The columns approximation electron beams and electron Bloch waves are equivalent descriptions of the electron wavefunction in the crystal [HW61]:

$$\begin{aligned} \Psi(\mathbf{r}) &= \sum_i \alpha^{(i)} \phi^{(i)} = \sum_i \alpha^{(i)} \sum_{\mathbf{g}} C_{\mathbf{g}}^{(i)} \exp(2\pi i (\mathbf{k}^{(i)} + \mathbf{g}) \cdot \mathbf{r}) \\ &= \sum_{\mathbf{g}} \psi_{\mathbf{g}}(r_{inc}) \exp(2\pi i (\hat{\mathbf{r}_{inc}} + \mathbf{g}) \cdot \mathbf{r}) \end{aligned} \quad (4.20)$$

The first line is the electron wavefunction inside the crystal as superposition of Bloch waves of amplitudes $\alpha^{(i)}$ and partial Bloch waves components $\phi^{(i)}$, and the second line is in terms of beams for every diffraction condition \mathbf{g} . Note that in the equation above the wavefunction is given in terms of the position vector \mathbf{r} which needs to be replaced by the atoms positions τ_n for the probability computations.

The probability distribution function in terms of two beams is then:

$$|\Psi(\mathbf{r})|^2 = |\psi_0 \exp(2\pi i \mathbf{r}_{\text{inc}} \cdot \mathbf{r}) + \psi_g \exp(2\pi i (\mathbf{r}_{\text{inc}} + \mathbf{g}) \cdot \mathbf{r})|^2 \quad (4.21)$$

Note that both the direct and diffracted beam(s) contribute to the contrast and their backscattered cross sections and probabilities must be computed separate and added together thorough the equation above to calculate the total BSE contribution.

Twigg and Picard [TP09] used a slightly different approach, yielding very similar contrast predictions results. They assumed that the localisation of the backscattering process is implicit in the imaginary potential used to treat absorption. Therefore, they integrate the beam intensities along their path in order to calculate the probability of backscattering.

4.7 Numerical simulation of electron diffraction model

The dislocation line is placed in the centre of a square mesh. The pixels on the mesh are populated by columns aligned parallel to the incident beam and of length equal to the electron beam penetration depth. The HWD differential equations are then solved numerically step-wise for each column taking into account the variation of the displacement field along the column calculated previously. We use the Runge-Kutta algorithm available in the *zvode* library [Hin85] for the numerical integration which, even for stiff equations, can calculate the entire mesh in seconds when using a modern computer.

With the electron beam wavefunction numerically solved, I then “integrate along the beam” by summing up their squared values for the decided penetration depth. I then calculate for all the species in the sample the BSE cross section and the total BSE contribution for a pixel. After the backscattering event the electrons heading towards the detector are projected by yet another coordinate transformation on its surface.

The full code I used can be found in the “ecci-model” folder on the GitHub repository. The Howie-Whelan two beam integration is not particularly easy to read, neither is the backscattering process. I hope one day to make it readable, but until then, the schematics of it is shown in Fig. 4.14. I calculate the ECC-strain for each specific geometry and diffraction condition using Python and generate the long, unsimplifiable three dimensional numerical β function. These functions are turned to Fortran readable modules using the *codegen* function. Eventually, the β functions are fed into the Howie-Whelan ODEs, which are then integrated column-wise on a 2D mesh using the *zvode* library. There is an option to compare a TEM prediction to the ECCI one. The main file is *doHW.f90* which also contains all the hard-coded GaN parameters, the

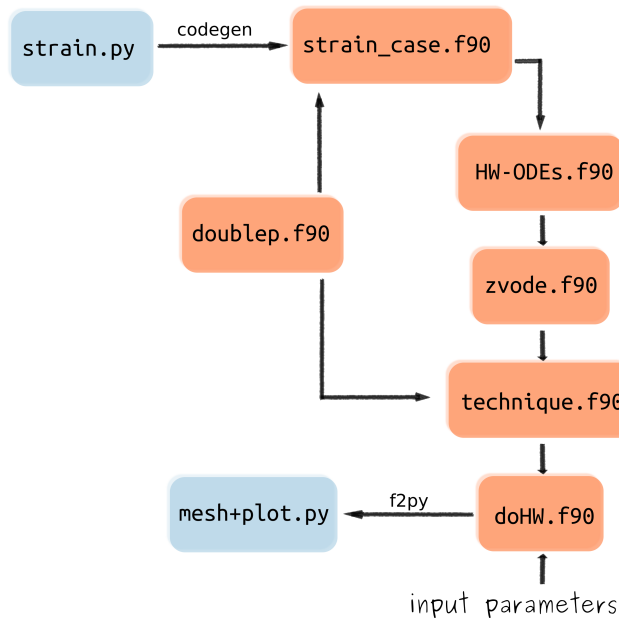


FIGURE 4.14: The code structure schematics for predicting TD contrast in ECCI .

depth of integration and the sample area considered. I wrote a `MAKEFILE` to control all of this. In the end, I obtain a file containing a two dimensional contrast function which could be plotted, for instance using more Python.

4.8 Contrast predictions in GaN

Dislocation analysis of GaN cross sections in TEM shows that the TDs predominantly show pure edge character with the dislocation line lying along the crystallographic c axis and the Burgers vector pertaining to the family $1/3\langle 11\bar{2}0 \rangle$ [Hin+00].

The ECC images of these types of TDs in the foreshatter geometry, with the film tilted at a high angle, will sample strain components which are not parallel to the dislocation line. While the plan view TEM images show TD black-white contrast being aligned perpendicularly to the Burgers vector of the dislocation, the geometry of the ECCI highlights a different set of strain components which can align the contrast direction along the Burgers vector.

In Fig. 4.15 I show possible strain profiles sampled in a plane 10 nm below the surface (similar to Fig. 4.5 for three geometries of orientation of an edge dislocation. The dislocation geometry is represented by the rotation of the vector \mathbf{b} with respect to \mathbf{g} . In Fig. 4.15 a) and c) the maximum variation in strain is somewhat aligned with the direction of the Burgers vector.

The image in Fig. 4.15 b) shows the invisibility criterion used in TEM, *i.e.* the case when vector \mathbf{g} is perpendicular to the Burgers vector \mathbf{b} . Note that the strain here is not exactly zero; in fact the maximum strain value is about a quarter of the value in the other two cases. Taking into account the exponential radial decay, this could be enough to suggest this geometry would be challenging to observe. But there is something else that contributes to the quasi-invisibility: there is a four dipole of strain variation, with alternating signs making it extra difficult to resolve the contrast.

Nevertheless, this is not the full picture of the contrast due to an edge TD. At 10 nm below the surface, we are sampling mostly infinite-lattice dislocation strain components. For a complete dislocation contrast picture, one would integrate over depth the relevant effect of the strain components.

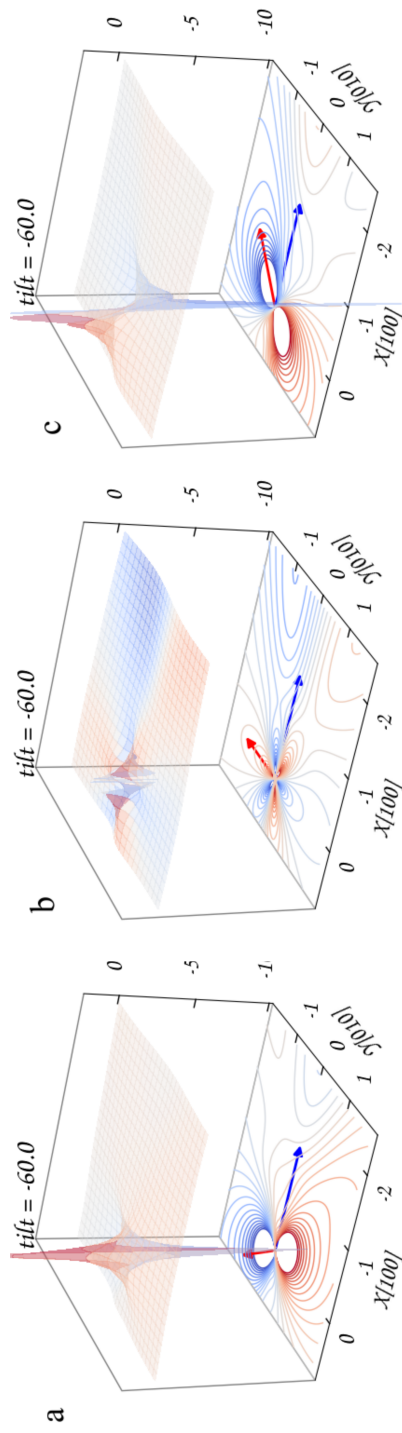


FIGURE 4.15: Accessible strain profiles for an edge TD in wurtzite GaN sampled in a plane parallel to the surface and 1 nm below the interface. The sample is tilted 60° from the original horizontal position. The marked red and blue arrows show the direction of the Burgers vector projection and the direction of the projection of \mathbf{g} , respectively. Vector \mathbf{g} remains the same across the three images while vector \mathbf{b} is rotated in increments in the same plane such that the angle between the vectors is: a) 30° , b) 90° , c) 150°

Two beam plan view ECC images were acquired by Naresh-Kumar [NK+12] using a 50° sample tilt together with electron channelling patterns from the same area for two different crystal rotation: $\mathbf{g}_a = [\bar{5}\bar{7}\bar{3}]$ and $\mathbf{g}_b = [7\bar{5}\bar{3}]$. This was achieved by tilting the crystal in plane with about 3°. The electron beam energy was 30 keV. The same small area from the two images is shown on the left in Fig. 4.16 a) and b) with the predicted dislocation contrast for three different possible Burgers vectors shown on the right. From the qualitative comparison we can determine which dislocations show similar behaviour to the model cases and assign Burgers vectors.

The modelling parameters used here are shown in the Table 4.3. The extinction distances are calculated numerically from the Fourier coefficient of the electrostatic potential of the crystal. The scattering factors of this potential are calculated using Weickenmeier-Kohl parametrisation as implemented in EMsoft [DGG13]. For the beam penetration depth calculation needed for the estimation of the diffraction columns integration depth we made use of a continuously slowing down inelastic scattering Monte Carlo model [Dro+07].

| Parameter | Symbol | Value |
|------------------------|-----------------|---------|
| Extinction distance | ξ_g | 29.6 nm |
| Beam penetration depth | r_{inc}^{max} | 80 nm |

TABLE 4.3: Modelling parameters for edge TDs in wurtzite GaN for the channelling conditions given in the text.

The predicted contrasts shown are plotted as variation from the perfect crystal BSE yield. Namely, the calculated BSE intensity is normalised with respect to the BSE yield far away from the dislocation. Normalisation is not used when comparing with the experimental contrast images. The intensity is plotted using the *BuPu* multi-hue colour scheme with white showing the highest intensity, blue - intermediate values, and dark purple the lowest intensity.

A very similar behaviour to the strain field profile in a plane is observed: the darker-lighter intensity appears to follow the Burgers vector direction. This points towards the fact that a qualitative prediction of TD behaviour can be achieved from a bare strain model correctly “sampled”. In order to reduce the characterisation uncertainty a larger number of different diffraction conditions should be acquired.

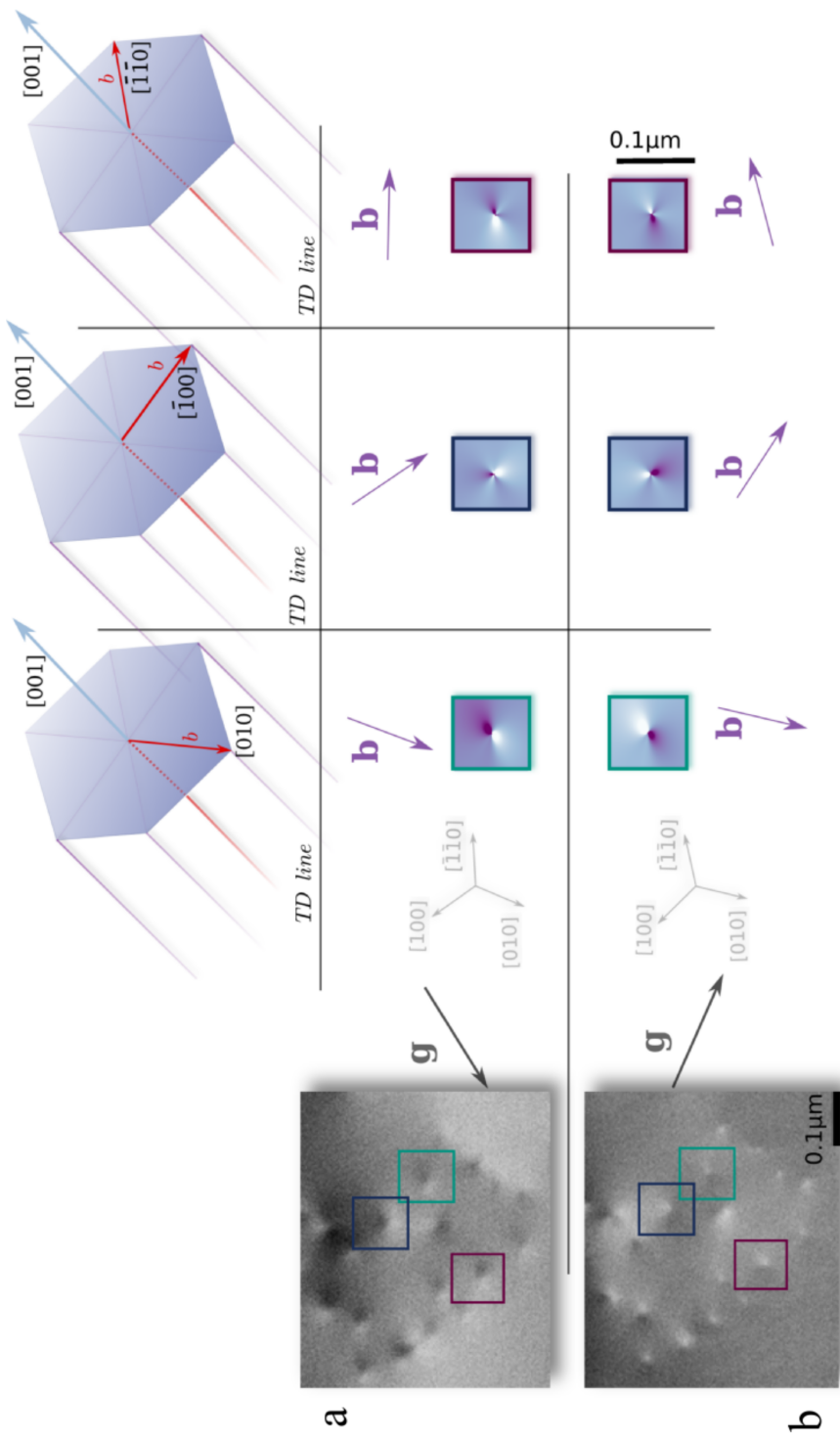


FIGURE 4.16: Experimental images on the left (see page 4.8 for details) versus predicted edge TD dark-bright contrast in ECC images on the right. The two experimental images a) and b) are from the same area but the crystal has been tilted a few degrees to access the new diffraction condition. The boxes correspond to the contrast produced by an edge TD with $\mathbf{b} = [010]$ (green box), $\mathbf{b} = [-100]$ (dark blue box), $\mathbf{b} = [-1-10]$ (purple box). See details in text. The Bravais three index notation was used throughout.

4.8.1 Equivalence between contrast and ECC-strain

In the end, the only change in the crystal is the dislocation displacement field, which will locally affect the phase of an incident electron beam. The β correction term is what tells the dynamical equations to locally change the position of the reciprocal lattice point closer to the Ewald sphere, resulting in an increase in intensity, or further from it, resulting in a decrease in intensity. This is what we see in the SEM micrograph as TD contrast.

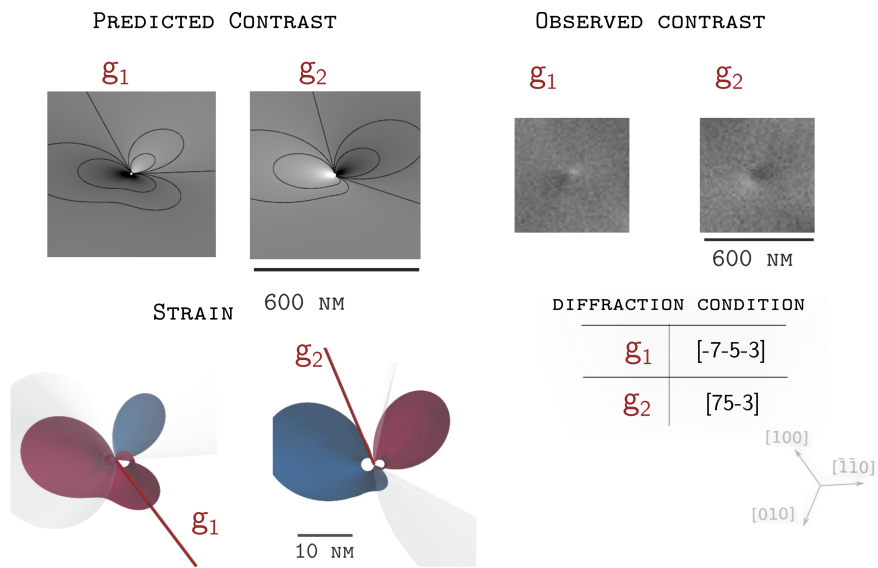


FIGURE 4.17: Comparison between ECC-strain (bottom left) and contrast (top left) for a screw TD in two different diffraction conditions g_1 and g_2 (given on the bottom right). On the top right two TDs from ECC images taken in the same conditions as the simulations are shown.

In the left columns of Fig. 4.17 and Fig. 4.18 I want to show that if I plot the ECC-strain isosurfaces and compare them to the two-beam dynamical simulation prediction of TD contrast they show the exact same geometry of features. Again, I compare the contrast prediction to selected TDs in ECC images taken in the same diffraction conditions as the simulations shown in the right column. The ECCIs were taken by Naresh-Kumar and can be found in this paper [NK+12].

Fig. 4.17 shows the top surface view strain isosurfaces (bottom) of a screw TD in two different diffraction conditions g_1 and g_2 , whose projections on the viewing plane is shown as red rods. Like before the modelled material is $[001]$ GaN and red strain isosurface indicated compressive strain (positive) while blue isosurface indicates tensile strain (negative). As discussed on page 115, for a screw TD in forward-scattering geometry the ECC-strain will be significant close to the surface.

The calculated dynamical contrast (top figures) follows very closely the surface relaxation isosurface profile, with high intensity mapping the tensile strain introduced by the dislocation, and low intensity matching the compressive part. This matching behaviour is not straightforward to generalise. Looking back at the rocking curves on page 92, Fig. 3.10, and remembering that the contrast in the SEM has contributions from both the incident and diffracted beam, we can see that small variations in intensity occur with deviation from Bragg condition in a complex manner. Additionally, the rocking curves will look different for different diffraction conditions and integration depths. My argument here is that the “proportionality factor” between ECC-strain and intensity is non-trivial and simulations are required in order to predict the correct contrast.

A very similar behaviour is observed for an edge TD and is shown in Fig. 4.18. This time the surface relaxation is not as prominent and we mostly see the infinite dislocation strain components. Nevertheless the features of these strain components can be rediscovered in the contrast simulations. The TDs in the experimental images show the same contrast geometry, perhaps with higher intensity than my predictions. Note that my simple simulations do not take into account any texture on surface of the sample, or perhaps more problematic, low angle grains between which the dislocations are commonly found. I will discuss more about this in Chapter 6 on page 159.

I conclude from these comparisons that it is the ECC-strain that gives the features of the contrast profile we observe in the SEM. If we are interested in understanding what the ECCI TD contrast tells us about the dislocation observed then we “simply” need to simulate the ECC-strain. The simulation involves juggling a number of different frames as we have seen on page 110 which, in turn, requires a good understanding not only of coordinates transformation calculations which we covered in the introductory chapter, but also of the diffraction condition and exact beam-sample-detector geometry. Unfortunately, none of these are obvious in an SEM since the SEM is not optimised for diffraction, especially not for channelling in the same way the TEM is. Everything from the small and controlled interaction volume designed for TEM to the detector position optimised to maximise diffraction signal in diffraction mode are incongruous with the SEM.

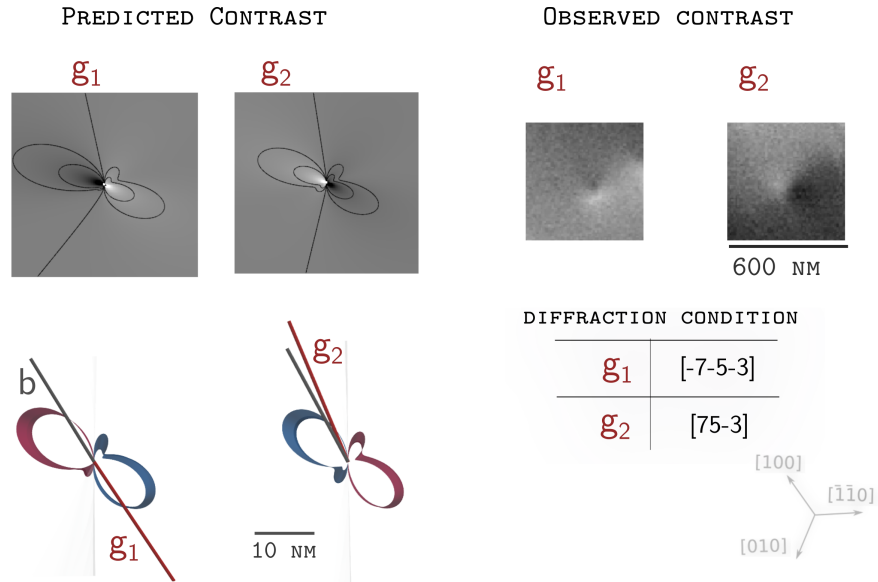


FIGURE 4.18: Comparison between ECC-strain (bottom left) and contrast (top left) for an edge TD in two different diffraction conditions g_1 and g_2 (given on the bottom right). On top right two TDs from ECC images taken in the same conditions as the simulations are shown.

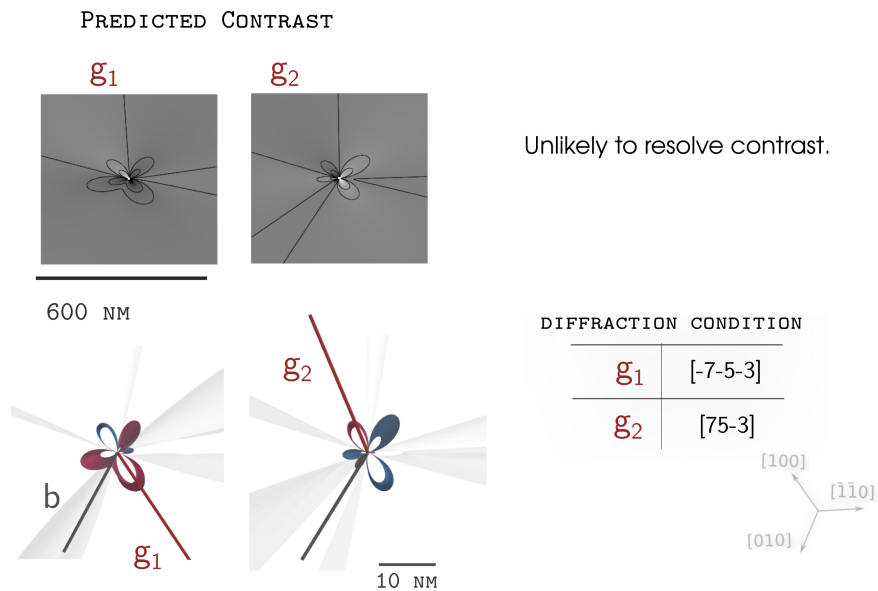


FIGURE 4.19: Comparison between vanishing ECC-strain (bottom left) and vanishing contrast (top left) for an edge TD in two different diffraction conditions g_1 and g_2 (given on the bottom right).

We can also see that for certain dislocation geometries like the one in Fig. 4.19 where the strain isosurfaces come very close to the core of the dislocation, *i.e.*, reduced ECC-strain, the contrast predicted will become faint. We do expect, then, that some dislocation can appear faint in the ECC images. If we were interested in a good approximation of their density, we would have to acquire multiple images in different diffraction conditions.

4.9 Conclusions

ECCI can be used as an alternative to, or jointly with, the established defect characterisation techniques. Since the usual defect identification procedure developed for TEM is not entirely appropriate for looking at TDs in ECCI, modelling the contrast predictions becomes critical.

The foreshatter ECC images provide TD contrast features as cumulative sampled strain components defined in the Cartesian frames selected by the imaging diffraction condition. While the characterisation is more involved than in TEM, which benefits from the applicability of the ‘invisibility criteria’, simulations of ECCI dislocation strain profile can predict the observed dislocation contrast. As these features are unique for different dislocation characters, this technique can be used to identify the type of imaged dislocations by comparison between measured and simulated TDs. We propose that the ECCI dislocation contrast is uniquely predicted by the ECCI strain profile. The equivalence between ECCI strain and ECCI contrast can aid not only the physical understanding of the observed images but can predict the behaviour of the contrast. For instance, we can predict that the contrast profile will always follow the edge component of the Burgers vector and that the diffraction condition will not affect its symmetry.

Finally, I show qualitative agreement between predictions of TD contrast in ECC images for two different diffraction conditions and the experimental images. These types of calculations can be used to unambiguously identify the type of dislocation observed in ECCIs.

If you can, reader, take an ECP before trying to find dislocation contrast in the SEM, even if it is poor quality you can use it to navigate towards a band, close to a Bragg condition and increase your chances of success.

5 Electron diffraction in an imperfect crystal – TKD

In the previous chapters we have established that the electron channelling (diffraction) contrast technique in the scanning electron microscope is a great tool to investigate dislocations close to a surface in crystalline materials. In this chapter we will explore different diffraction techniques used for the study of different kind of crystal imperfections.

So far, we have focused mostly on elastic, coherent scattering. We treated inelastic scattering as a channel of intensity loss in the diffraction beams and approximated its effect through the complex optical crystal potential. Since Kikuchi patterns are not only formed by electrons of incident energy, we need to take a closer look, on page 137, at models used to predict energy loss for high energy electrons.

While the physics of EBSD is somewhat well understood, the question explored in this chapter is whether the existing models can accommodate for the new geometry of the transmission-EBSD modality. In the following pages the implementation of diffraction pattern predictions of EMsoft software [SRDG17] is described (page 139). Then, I will talk about the difference in electron escape distances between the EBSD and TKD modalities, as predicted by Monte Carlo simulations, and why that matters on page 141.

The work I will show in this chapter was the outcome of a collaboration with Prof. Marc De Graef's group and parts of the results were published in *Energy-weighted dynamical scattering simulations of electron diffraction modalities in the scanning electron microscope* [Pas+18b].

In section 5.2 on page 139 we describe the typical geometries for EBSD, TKD and ECP data acquisition and formulate a general expression for the thickness integrated back-scattered electron intensity that is applicable to all three diffraction modalities. We describe the particulars of the Monte Carlo trajectory simulations in section 5.2.2, along with the resulting differences between the modalities. Master patterns for the three modalities are described and compared in section 5.3.1.

5.1 Introduction

5.1.1 How does it work?

Let us cover the grounds of the technique first. What we need for an electron backscatter pattern (EBSP) is a sample with a flat surface placed at a shallow angle of about 20° with respect to the incident electron beam as schematically shown in Fig. 5.1 a). The location where the 10 keV to 30 keV stationary beam is incident on the sample surface also marks the source of the spherically generated EBSD pattern.

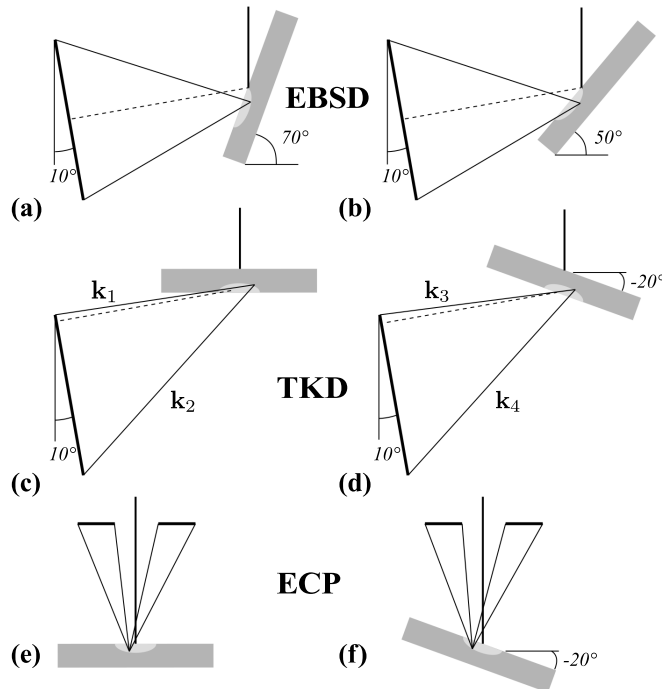


FIGURE 5.1: (a) and (b) EBSD geometry, with the sample inclined at 70° and 50° ; the detector is indicated by a thick line and is inclined by 10° with respect to the vertical direction. (c) and (d) show typical TKD geometries with a horizontal sample, and one inclined at -20° . (e) and (f) show typical ECP geometries with two different sample tilt angles.

Adapted from [Pas+18b].

An example of this is shown in Fig. 5.2 for a 20 keV electron beam incident on a Ni sample. The simulation was done using EMsoft [DGG13] and shows all possible independent exit directions in the Northern hemisphere as a stereographic projection (see ref. [CDG13]).

Primary beam electrons that have lost little energy on their way in the sample, have a chance to suffer diffraction at crystal planes on their way out of the sample.

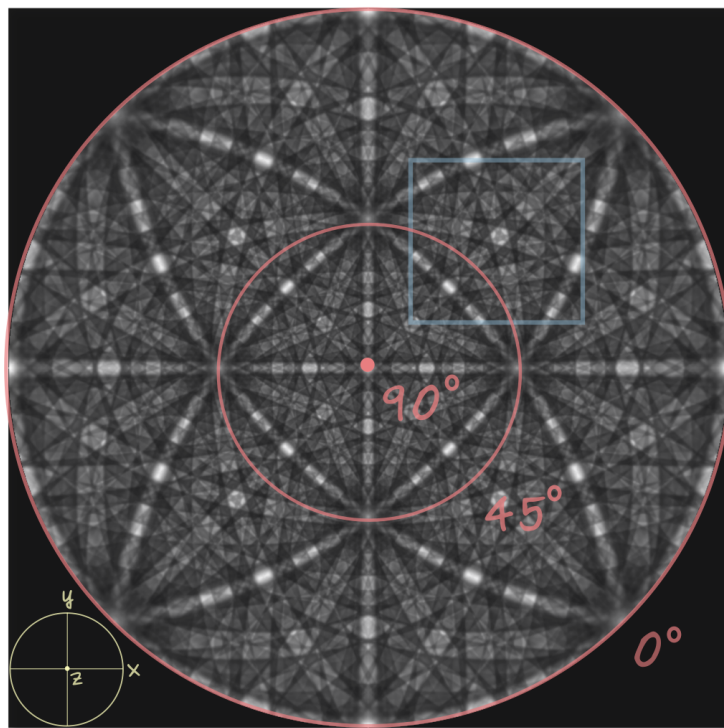


FIGURE 5.2: Simulated stereographic projection of the entire Northern hemisphere EBSD pattern of Ni using 20 keV incident electrons. The 90° represents the north pole and the 0° circle the equator and the geometry of the crystal is shown in the bottom left corner (see also Fig. 5.4 for coordinate frames geometry). The blue rectangle shows the area plotted in Fig. 5.13. Adapted from [Pas+18b].

The Kikuchi lines in the EBSD pattern tell us about the crystal planes in the sample we are probing with the electron beam.

If a phosphorous screen is placed close to the sample, on the path of the diffracting out electrons, then we can record a small solid angle of the pattern shown here. Nevertheless, with the help of careful analysis it will provide enough information to learn about the crystallography of this sample.

For a polycrystalline sample, using the scanning setting of the SEM one could record EBSD patterns for every single pixel and then analyse them to obtain texture information, misorientation or strain variation from one grain to the other. Automated pattern indexing software established this diffraction modality as one of the conventional tools of orientation mapping, phase identification and/or relative lattice strain estimation in crystalline materials [Sch+09b]. A better descriptions of this can be found in textbooks such as Chapter 2 in [MS07].

5.1.2 Kikuchi patterns – three ways

We can distinguish a number of different SEM modalities making use of the Kikuchi diffraction mechanism. If the recorded electrons are the backscattered ones (see Fig. 5.1 a), b)), then the technique is known as electron backscatter diffraction (EBSD) and the Kikuchi patterns obtained are called electron backscatter patterns (EBSP). In order to increase the diffraction signal in this mode, the popular approach has been to tilt the sample to about 70° from horizontal towards the detector, which guarantees a maximum backscattered electron yield. However, the high tilt will also spread out the information volume (or interaction volume) of the electrons within the sample, limiting the achievable spatial resolution.

The idea of questioning instead the electrons transmitted through a thin sample for diffraction information, as a method of improving the lateral spatial resolution, has attracted considerable attention in recent years [Tri12a; KG12]. In this case the detector is placed on the other side of a thin sample and transmission Kikuchi diffraction patterns are collected as seen in Fig. 5.1 c) and d).

The modalities above are sometimes referred to as “channelling out” diffraction techniques [Joy94] to suggest that the diffraction information has been sampled by electrons on their way out of the sample and that the volume from which the signal is collected is located close to the exit surface. The SEM can also be used in “channelling in” mode when electron channelling patterns (ECPs) are acquired [Coa67; JND82]. The usual set-up geometry is shown in Fig. 5.1 e) and f). In this case, Kikuchi-like diffraction patterns can also be obtained by varying the incident beam direction with respect to the crystal. Typically, those patterns have a smaller solid angle compared to their EBSD counterparts. Nevertheless, the physical scattering mechanisms that produce EBSPs and ECPs are related through the reciprocity principle [Rei98].

5.1.3 Interaction volume

As a SEM based technique, EBSD is limited in its spatial resolution by the SEM electron optics. When we talk of high resolution imaging of nano-grains, we imply the use of a high performance FE-SEM, short working distances, which in turns require small samples and small interaction volumes. We will see on page 136 that the latter argument motivates the need for the transmission mode of EBSD, namely transmission-EBSD or transmission Kikuchi diffraction (TKD). In conventional EBSD geometry the signal carrying electrons are the backscattered ones. These are electrons which can travel a significant distance before escaping the sample, “sampling” a rather broad interaction volume.

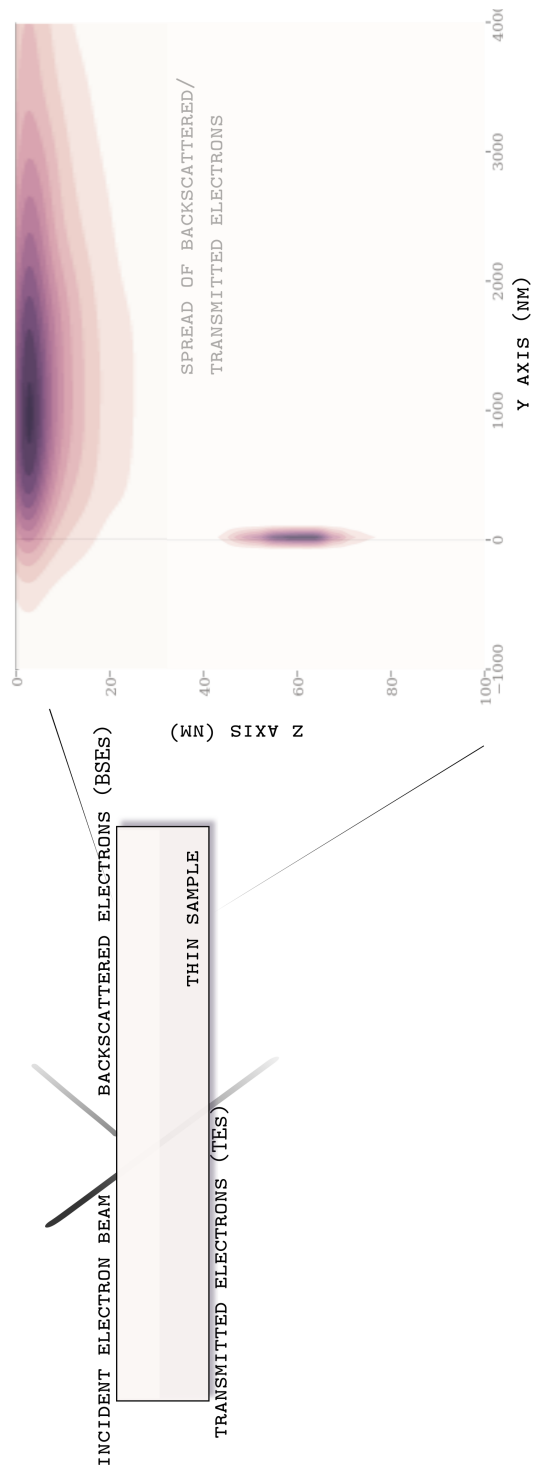


FIGURE 5.3: Interaction volume of backscattered (top images) and transmitted electrons (bottom images) shown here as kernel density estimates plots of the escaping electrons. The darker colour indicates larger probability of large angle elastic scattering event in that region.

The difference in interaction volume is shown in Fig. 5.3 as KDE plots [Sco92]. The position of escaping electrons is assumed to be the last scattering event before exiting the sample. The data was produced from Monte Carlo simulations using Casino [Dro+07] software for an incident beam of 30 keV on a 70° (EBSD – top figure) and a 20° (TKD – bottom figure) tilted sample of thin Si. I used different sample thicknesses in order to produce the same total number of backscattered and transmitted electrons. More about the description of the Monte Carlo method used on page 141.

5.1.4 TKD geometry

Following the EBSD experimental geometry described by Callahan [CDG13] we can derive the TKD sample-detector coordinates transformation.

For a translation vector \vec{t} which moves the origin of the detector frame O_d to the origin of the sample frame O_s defined as:

$$\vec{t} = (x_{PC}, y_{PC}, L),$$

the coordinates of a point $P(x_p, y_p)$ on the detector in the reference frame of the sample can be derived geometrically:

$$\vec{O_s P} = \mathcal{R}^{ds}(\vec{O_d P} - \vec{t})$$

where \mathcal{R}^{ds} is the coordinate transformation from the sample frame to the detector frame. Such that finally the direction cosines of a pixel on the screen in the sample frame is:

$$P^s = \begin{pmatrix} -\cos \alpha(y_d - y_{PC}) + L \sin \alpha \\ -(x_{PC} - x_d) \\ -\sin \alpha(y_d - y_{PC}) + \cos \alpha(z_d - L) \end{pmatrix},$$

$$\text{where } \alpha = \pi/2 + \theta_S + \theta_D.$$

For a given crystallographic orientation the direction cosines can be converted to the possible channelling out directions the pixels on a detector will register. This can

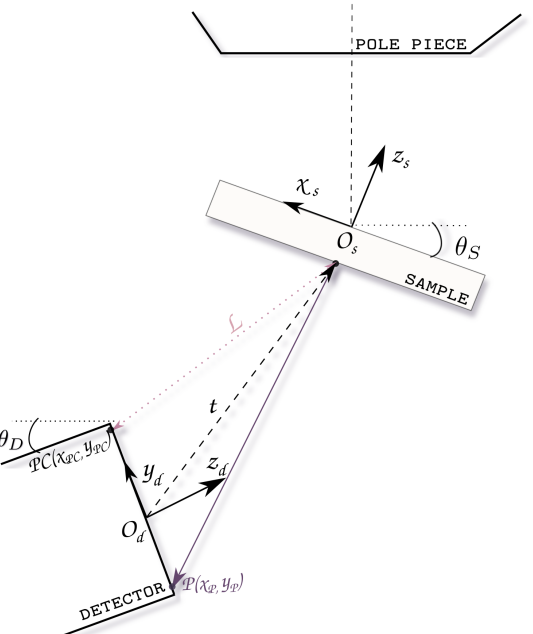


FIGURE 5.4: Schematics of TKD set-up geometry. PC denotes the pattern centre and L is the distance between the detector and the sample.

be done for all grains in a sample and the information can be stored in a look up table.

5.1.5 Why do we need a new model?

The geometry of the Kikuchi patterns is dictated by the unit cell of the crystal and its orientation. Other features, such as the width of the bands, for instance, are nevertheless influenced by the spatial distribution of diffracted electrons in the sample and their energy distribution. In the end, Kikuchi patterns offer a variety of information about the crystal structure of the material under investigation which is why they are widely used in the study of new materials. For a more complete discussion see ref. [Win+17].

Theoretical models have been developed and successfully applied to retrieve this wealth of information by taking into account the full dynamical behaviour of electron diffraction [Win+07; Pic+14; SDG16]. Electron diffraction calculations commonly handle inelastic scattering in a phenomenological way through the introduction of a complex optical crystal potential approximation. This assumption implies that inelastically scattered electrons, once they lose even a small amount of energy, will cease to contribute to the diffraction pattern. The predicted diffraction patterns based on this simplified model remain meaningful [How63] but, understandably, are lacking quantitative precision. Due to the strong interaction of incident beam electrons at SEM energies with matter, the inelastic cross section is always comparable to the elastic one, and a portion of inelastically scattered electrons will reach the detector and contributes to the imaged pattern.

Depending on the types of inelastic channels allowed, these electrons can suffer diffraction after losing a small amount of energy, contributing then to the diffuse-ness of the Kikuchi patterns. This process is especially relevant for “channelling out” modalities where electrons with energies lower than the incident energy can still contribute to the diffraction pattern. Alternatively, if electrons are scattered at a large angle multiple times such that memory of their original direction is lost, they will also contribute to the background intensity. This is the case for both channelling modalities. We call the later type of inelastically (back/forward-)scattered electrons (B/F)SE2 in order to differentiate them from (B/F)SE1 electrons carrying diffraction information.

It is therefore essential to explicitly consider inelastic scattering and its effects on the signal contributing electrons, such as their energy and spatial distributions [CDG13; Win+16]. This is especially important if finer features of the Kikuchi bands (size, absolute intensity relative to background, band edges) are to be correctly predicted. A

full account of the inelastic channels in electron diffraction poses a challenging problem. While general Schrödinger equation solutions for inelastic scattering in perfect crystals have been proposed by Yoshioka [Yos57] and solved for various electron microscopy applications (see Howie [How63] for small angle plasmon scattering and Forbes et al. [For11] for single thermal diffuse scattering events), to our knowledge, readily implementable solutions relevant for SEM electron energies have yet to be proposed.

In this work, we assume inelastic scattering events to be stochastic and that Monte Carlo (MC) technique can estimate both the trajectories of electrons that suffered such events as well as their energy distribution. Such models have been proposed and widely used to correctly predict distributions of backscattered electrons [Joy95]. The assumption that the distribution of escape energies and the trajectories of electrons carrying diffraction information can be estimated from the last elastic event predicted by MC models has already been successfully applied both for EBSPs [CDG13] and ECPs [SDG17].

The energy of the electron at the last elastic event before escaping the sample, is considered to be the energy for which the diffraction occurs. Similarly, the distance to the exit surface from the last elastic event, also known as the escape or exit distance, is used as the diffraction distance (electron path length over which coherence is not lost). Dynamical diffraction modelling is then applied for the full MC predicted electron energy and path distributions. Here, we extend this model to TKD patterns by considering the geometry of a thin film sample where the entry (top) and escape (bottom) surfaces are different such that the incoherent events acting as sources of diffracting electrons are scattering in a forward direction.

While this approach may not take into account the full extent of inelastic scattering effects on diffracted electrons proposed by the Yoshioka equations, it leads to a model of manageable complexity which is straightforward to implement and whose predictions are easily understood. Most importantly, it represents a step forward in taking into account the full physics of electron diffraction in matter by considering the full distribution of energies of channelling electrons and produces accurate predictions when compared to experimental patterns, as shown in section 5.3.1 on page 152.

5.1.6 Electron scattering

So far we have only talked about one type of electron scattering: the coherent, elastic type that is also known as diffraction. But electrons can scatter in a variety of ways.

Classically, the collision of particles is fully defined by their velocities and interaction parameters. However, high energy electrons are quantum mechanical objects. The notion of defined path for a particle with known velocity is meaningless in the Copenhagen interpretation of the quantum mechanical world¹. In any interpretation of quantum mechanics a version of the uncertainty principle limits us from knowing both the precise position and velocity of a particle, making the classical approach of predicting particle behaviour unfeasible at the scale of the very small. Instead, we are interested in defining the probability that, as a result of the collision, the particle will deviate by a given angle. This is what we mean by *scattering*.

For practical considerations it is common to classify the interaction of electrons with a crystal in two distinct processes:

- *Elastic scattering*, defined as a process which does not change the state of the crystal. Mostly made up by interactions with the nucleus. *Rutherford scattering* is the model commonly used to predict this behaviour and it does that by taking into account just Coulomb forces between the charged electron and the nucleus.

Let's say an elastic event will deviate the trajectory of an electron by a polar angle ϕ from its original trajectory. The probability of the electron being scattered in the solid angle $d\Omega$ is given by the angular differential form of the screened Rutherford cross section [RK76]:

$$\frac{d\sigma}{d\Omega} = \left(\frac{e^2}{4\pi\epsilon_0} \frac{Z}{4E} \right)^2 \frac{1}{\sin^2 \frac{\phi}{2} + \alpha} (\text{m}^{-2})$$

where E is the energy of the electron in keV and α is a screening factor accounting for the fact that some of the atomic charge is “screened” by the orbiting electrons from the perspective of the incident electrons.

As a result, it is common to assume that this scattering mechanism accounts for the bulk of angular scattering of electrons including the behaviour we call backscattering.

- *Inelastic scattering*, defined as the process in which the state of the crystal is modified by the interaction. An important contribution here is made by the electron-electron scattering which causes the incident beam electron to lose small amounts of energy to the crystal. The angular deflections caused by these events is relatively small allowing us to use, what is known as, the *continuously*

¹Note that in the Bohmian interpretation this is allowed [CMD18].

slowing down approximation (CSDA) to predict this particular type of inelastic scattering processes. We simply assume the electrons are carrying on the same path but slowly and continuously lose energy. The *Bethe's theory* describes electrons as a system of oscillators that lose energy due to excitations caused by the crystal and can predict a *stopping power* of inelastic events [JL89]:

$$\frac{dE}{ds} = -2\pi e^4 N_A \frac{Z\rho}{AE} \log \left(\frac{1.166E}{J} \right) \text{ (eV/Å)} \quad (5.1)$$

where E is the incident energy in units of eV, s is the path length along the trajectory (in Å), N_A is Avogadro's number, ρ is the density (in g/cm³), Z is the atomic number and A is the atomic weight of the target. J is an empirical parameter representing the mean ionisation potential, has units of eV and represents the effective average energy loss of the incident electron in the material. πe^4 is a common constant appearing in inelastic scattering cross sections and used in Gaussian units:

$$\pi e^4 = \pi(a_0 E_h)(\text{cm}^2 \text{eV}^2)$$

where a_0 is the Bohr radius and E_h is the Hartree constant. The pre-multiplying factors are sometimes written out explicitly as:

$$2\pi e^4 N_A = 784 \text{ (eV}^2 \text{cm}\text{\AA}/\text{mol}). \quad (5.2)$$

In order to predict the probability of electrons scattering in a certain direction and reach a certain energy, one has to combine the two scattering processes. When it comes to probability prediction, Monte Carlo methods are the answer as we will see on page 141.

5.2 Theoretical Model

This section will review the energy weighted dynamical theory implemented by EMsoft [DGG13].

5.2.1 Energy and diffraction distance integrated electron intensity

The simulation of the (back/forward-)scattered electron distribution emerging from a sample illuminated with a fine, nearly-parallel, electron probe can be achieved in general by integrating over both the energy range of the exiting electrons and the distance travelled in the sample between the scattering site and the sample surface. The probability of a (B/F)SE emerging from the sample in the direction $\hat{\mathbf{k}}$ (the hat indicates a unit vector) can be written as follows:

$$P(\hat{\mathbf{k}}) = \sum_{n \in \text{A.U.}} P_n(\hat{\mathbf{k}}), \quad (5.3)$$

where A.U. stands for asymmetric (primitive) unit and the index n runs over all positions in the asymmetric unit. The probability P_n is defined as:

$$P_n(\hat{\mathbf{k}}) = \sum_{j \in S_n} \sigma_j \int_{E_{\min}}^{E_{\max}} dE \int_0^{t_0(E)} dt \bar{\lambda}_{\hat{\mathbf{k}}}(E, t) |\Psi_{\hat{\mathbf{k}}}(\mathbf{r}_j; E, t)|^2. \quad (5.4)$$

Here, $\sigma_j = Z_j^2 D_j$ (with Z the atomic number and D the Debye-Waller factor) is the Rutherford scattering cross section for atom j in the set of equivalent positions S_n ; E_{\max} is the maximum energy (potentially the incident beam energy E_0) and E_{\min} the lowest energy considered in the calculation; t is the distance between the scattering site and the sample surface, measured along the exit direction; $t_0(E)$ is the maximum distance to be considered; $\bar{\lambda}_{\hat{\mathbf{k}}}(E, t)$ is a weighting function describing the fraction of incident electrons (per unit energy and per unit length) of energy E , originating a distance t from the sample surface and travelling in the direction $\hat{\mathbf{k}}$; the wave function $\Psi_{\hat{\mathbf{k}}}$ is evaluated for the equivalent atom positions \mathbf{r}_j and the parameters E and t . For the latter, one can use either the Bloch wave approach or the scattering matrix formalism. The weighting function $\bar{\lambda}$ is defined as:

$$\bar{\lambda}_{\hat{\mathbf{k}}}(E, t) \equiv \frac{\lambda_{\hat{\mathbf{k}}}(E, t)}{N t_0(E) (E_{\max} - E_{\min})}, \quad (5.5)$$

where $\lambda_{\hat{\mathbf{k}}}(E, t)$ represents an energy-depth-direction distribution obtained from Monte Carlo (MC) simulations, to be discussed in the following section, and N is the total number of incident beam electrons. The normalisation factor in the denominator renders the integrations in equation 5.4 dimensionless.

Equation 5.4 is valid for all (B/F)SE diffraction modalities, including EBSD, ECP and TKD. The differences between them lie in the nature of the sample (bulk vs. thin foil), the geometry of the scattering process (back-scattering vs. forward scattering),

and the subset of electrons carrying the coherent diffraction signal (all backscattered electrons vs. (B/F)SE1 electrons). These differences will be encoded in the geometry dependent weighting function $\bar{\lambda}$ for each of the modalities.

The Monte Carlo model enables us to predict how any of these system parameters influence the form of the weighting function. For instance, in the next section we discuss the impact of different sample geometries on TKD patterns, while in Section 5.2.4 the effect of foil thickness is investigated. Then, in Section 5.2.5 the sample-detector geometry is considered as a useful system parameter that can identify special cases for which the numerical solution of the scattering process can be simplified dramatically via the use of so-called *master patterns*.

5.2.2 Monte Carlo Trajectory Simulations

As we have seen in Section 5.1.6 on page 137, the information about scattering angles, direction and distances comes as a stochastic package. If we are to combine a number of scattering processes it would become cumbersome to keep track of all these probabilities and their predictions. Instead, it is more useful to use a random sampling approach with which we can run many simulations of the same process to predict its outcomes, like the Monte Carlo method.

The use of Monte Carlo simulations in predicting energy and spatial distribution for the incoherent electron sources is a field of great interest [Ren+98; TE04]. Its integration with the dynamical diffraction model has been described before for EBSPs [CDG13] and ECPs [SDG17] on bulk samples. These simulations employ Joy and Luo's [JL89] modified version of Bethe's continuous slowing down approximation (CSDA) as an empirical estimation for a sum of inelastic scattering processes probabilities. The probabilities of elastic scattering events are determined from the Rutherford scattering cross section in the single scattering approximation. Therefore, the loss of energy is uniquely determined by the CSDA while the angular deflections from the original direction are defined by the elastic scattering events. For further details on this simulation approach we refer to the book by Joy [Joy95].

In this work a similar approach is applied for the TKD modality with the modification that the sample is now a thin film and the escape surface is not the same as the entry one. A collimated beam of electrons with primary beam energy enter the top surface of a sample and start both losing energy and scattering away from their original trajectory. Eventually they will suffer one final forward-scattering event after which they will diffract on their way out of the bottom sample surface and reach the detector. The energy and depth distributions for each scattering direction of this last

event is predicted using the MC model since all events leading to it can be assumed to be stochastic. These distributions are then binned for easy storage and used as estimated values of the weighing function $\bar{\lambda}_{\hat{k}}(E, t)$.

Additionally, the Monte Carlo model can be used to predict general electron trajectories inside the sample and the system parameters that might affect them. In Fig. 5.5 we show angular (directional) distributions of escaping electrons predicted by the MC model for the TKD modality. The intensities are shown as stereographic projections (SPs) in the sample's southern hemisphere for a beam of 20 keV electrons incident on a 200 nm thick Ni foil. By binning the energy values of the electrons escaping from the bottom of the foil into high loss energy electrons (escape energy (E_e) < 17.5 keV), medium loss electrons ($17.5 \text{ keV} \leq E_e < 18.5 \text{ keV}$) and low-loss energy electrons ($E_e > 18.5 \text{ keV}$) we can show the effect of energy filtering and observe the behaviour of different energy electrons.

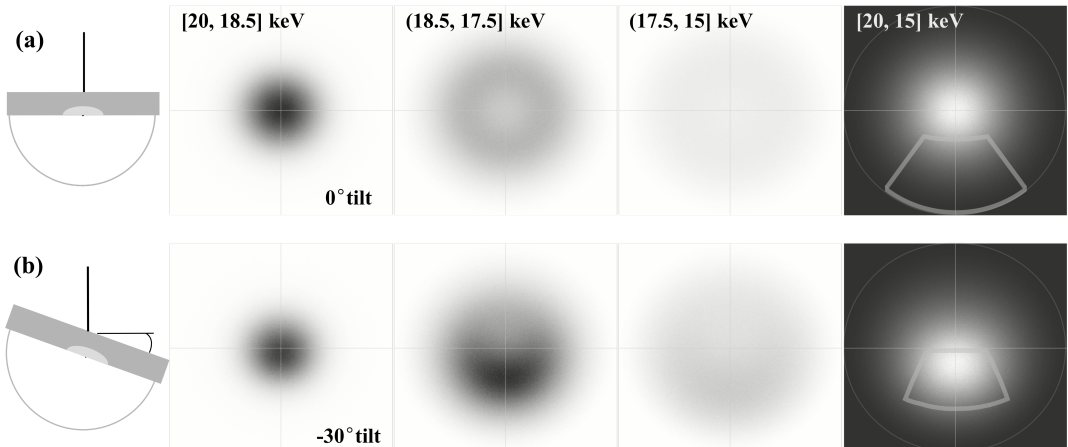


FIGURE 5.5: Directional distributions of transmitted electrons intensity in TKD geometry for two sample tilts (shown in the first column): 0° (a) and -30° (b). The intensities are shown here as stereographic projections where the intersection of the horizontal and vertical lines indicate the middle of the space (vertical line is the semicircle in the sketch). The first three images in each case are showing “energy filtered” electron intensities (reversed contrast) while the last column displays the total intensity distribution. Image adapted from [Pas+18b].

Fig. 5.5 (a) shows projections for the case when the sample is horizontal and the electron beam normal. Here we can observe, as expected, that higher energy transmitted electrons are much more focused in the middle of the southern hemisphere, which happens to coincide with the direction of the incident beam. With increased energy loss we can observe an increase in trajectory randomisation or diffuseness. This can be explained by considering the possible trajectories of electrons inside the sample and

their corresponding energy loss. Electrons escaping the sample with energies close to the incident beam will not have deviated far from the incident direction. Relative to this, high loss electrons are more likely to escape at large angles to their incident direction. High energy loss electrons appear to have no preferred escape direction and we can expect these electrons to only contribute to image background (FSE2).

In Fig. 5.5 (b) we investigate the effect of tilting the sample on the angular distribution of exiting electrons from the bottom surface. Similarly, the high energy electrons will not deviate far from their incident trajectories. However, in this case, the incident direction does not correspond to the centre of the stereographic projection space and we observe that the directional distribution of the low loss electrons clusters 30° below the SP horizon. The trajectories of higher loss electrons start to be randomised in the entire SP space. We can also observe in these images how the radial symmetry of electron scattering is broken by the tilt angle of the sample. Finally, the angular distribution of the highest loss electron distribution will look the same as for the flat sample as their “memory” of the incident direction is lost.

The outline in the rightmost column of Fig. 5.5 (a) and (b) depicts a typical detector projected onto the stereographic disk. The detector has dimensions $24 \times 36 \text{ mm}^2$ and is inclined by 10° from the vertical direction. The perpendicular distance from the exit point on the bottom of the sample to the detector is 20 mm, and the top edge of the detector lies in the sample plane for the 0° orientation. The detector bottom is closest to the centre of the stereographic projection. For 0° sample tilt, most of the scattered electrons miss the detector surface; for a -30° sample tilt, the intensity maximum moves upwards onto the lower part of the detector and at the same time the detector projection moves closer to the centre of the stereographic disk, indicating that a significantly larger number of electrons will reach the scintillator. It should also be noted that a typical raw TKD pattern will display a rather steep intensity gradient from top to bottom, in agreement with the intensity distribution inside the detector outline in Fig. 5.5 (b) (rightmost image).

It becomes apparent that the sample geometry constitutes an important parameter in the formation of the Kikuchi patterns. Similarly to the EBSD case, where the sample tilt determines the preferred trajectories of electrons of different energies scattering back from the sample [CDG13], the tilt of the thin film in TKD will directly influence the angular distribution of transmitted electrons suffering diffraction at different energies. In the following section we will carefully review the effect of another system parameter, the sample thickness, on the TKD diffraction patterns.

5.2.3 Non uniform sampled MC

Joy's Monte Carlo model [Joy95], as described in the previous section, is nothing more than an empirical fit for the energy and direction of backscattered electrons. This, in turn, makes a good start model for the prediction of energy and directions distributions of backscattered electron. The assumption we have made in incorporating the MC model with the dynamical simulations, is that the exit distances of electrons can also be predicted from the MC model. In the absence of a better model it seems adequate to use this approach and experimental results seem to agree to a first approximation [DHE08].

What I want to do in this section is to explore a different approach of sampling the MC predictions of escape distances. I will start by assuming the position in the sample of the primary electrons is well represented by the elastic events predicted by the MC model. I then run a large MC simulation of electron scattering in a Si sample and store energy, position and direction information for every elastic scattering event. I consider these events my data points.

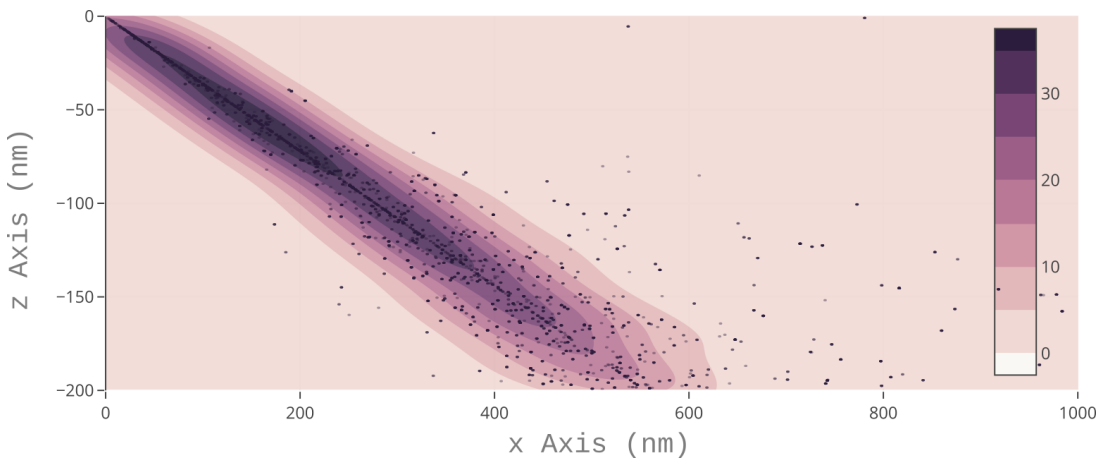


FIGURE 5.6: Visualisation of 10 keV primary electrons distribution in a Si sample tilted at 70°. The scatter points are elastic scattering positions as predicted by the MC model and the pink background is the KDE distribution plot with darker colours indicating higher probability in a linear manner as indicated by the legend in arbitrary units.

Fig. 5.6 shows a xz plane projection of primary electron positions. The scatter points plot is made up of random subset of about 1000 points taken from a simulation on 10.000 electrons. The MC simulation used here is the same as described in the previous section. Over-imposed on the scatter plot is a kernel density estimate map using the full data set and showing the areas with highest points density.

In the following I integrate the KDE map and use that as a weight in sampling, such that I sample more often from places with more points than from places with fewer points. The jupyter notebooks `TKD_distribution.ipynb` and `EBSD_distribution.ipynb` show all the steps described here for sampled MC for a TKD geometry case and a EBSD case, respectively.

I then define the probability of incoherent scattering to be proportional to the distance travelled by the electron until that point. This is in line with the continuous slowing down approximation for inelastic scattering which also scales with travelled distance. Fig. 5.7 is showing a weighted sample of 5000 positions and indicates the probability of incoherent scattering with different sized circles.

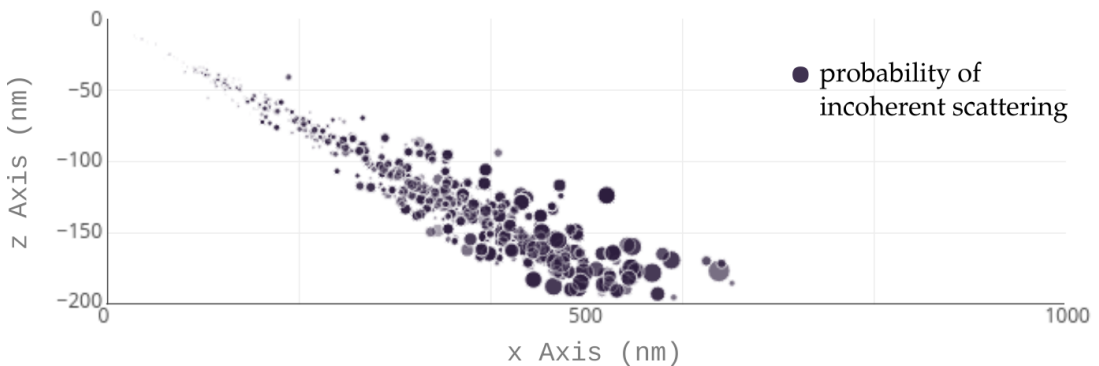


FIGURE 5.7: Probability of incoherent scattering of primary electrons on their trajectory in the sample. The probability scales with the size of the circle.

Not all these electrons will have the same chance to escape the sample without suffering significant loss of energy. The last bit of weighting that I introduce is an exponential distribution depending on distance to the exiting surface, z , where z is taken to be negative. In this case I'm considering the EBSD geometry where the exiting surface is also the entry surface. In effect, the exponential depth weighting is giving more weight to the positions closer to the surface than to those deeper in the sample. This is similar to the weighting factor proposed by Winkelmann *et al.* for localised BSE [WSPW13], defined as large angle scattering events followed by less than n_{ie} inelastic events, where n_{ie} is a user defined value.

The last two weighting procedures are competing with each other, the first one favouring data points deeper in the sample and the latter giving more weight to points closer to the surface. This explains why the resulting spatial distribution shown in Fig. 5.8 is significantly more localised than the original one in Fig. 5.6. More interestingly, it indicates a mean z of about 100-150 nm for 10 keV electrons incident at 70°

on a Si sample, significantly larger than the original model.

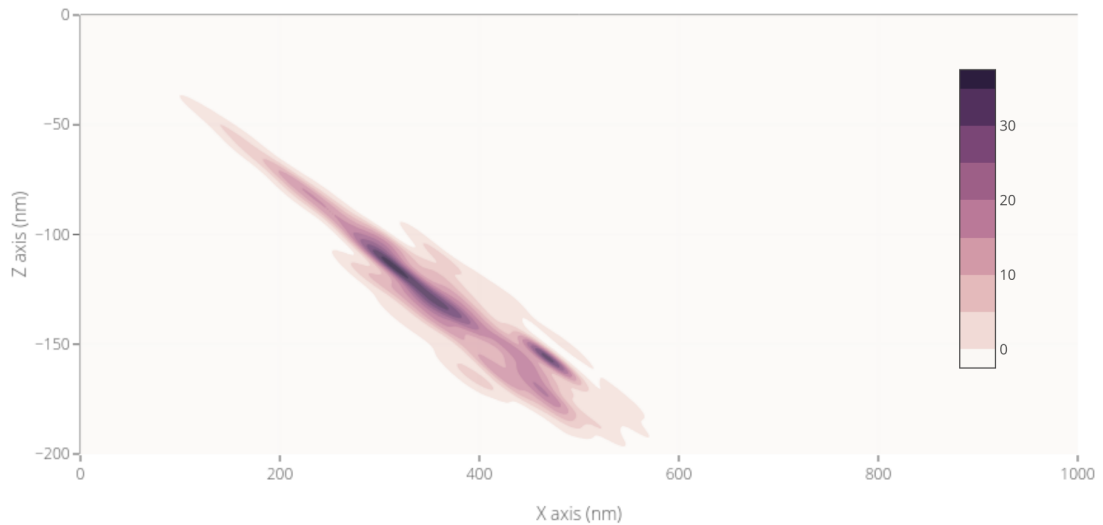


FIGURE 5.8: Estimated spatial distribution of “sources” of diffracting out electrons shown as KDE map. Like before, darker colours correspond to higher probability linearly for the colours in the legend.

5.2.4 Sample thickness in TKD

While for the EBSD and ECP modalities one only needs to run a single Monte Carlo simulation to obtain the energy-depth-direction histogram $\bar{\lambda}_k(E, t)$ for a bulk sample, for the TKD case, the MC simulation results depend on the thickness, t , of the sample. The larger the thickness, the more energy an electron will lose on its way to the exit surface, and this will shift the entire exit energy distribution to lower energies for increasing sample thickness.

This behaviour is shown in Fig. 5.9 as kernel density estimate (KDE) distributions [Sco92] of electron escape energy versus escape distance predicted information for two different Ni thin foil thicknesses, 100 nm and 200 nm respectively, in the TKD geometry. Darker colours show that more electrons are likely to escape the sample with the corresponding parameters. The likelihood across the two distributions has been normalised to the maximum value in Fig. 5.9 (a) such that the intensity across images can be compared. We also show the escape energy and distance region where 90% of electrons are expected to come from, which is indicated by the thick line. Comparing the two figures, 5.9 (a) and 5.9 (b), it is clear that the thickness of the thin sample strongly influences the shape of the distributions. Considering the y-axis, the energy range of the electrons exiting the sample broadens and the energy decreases

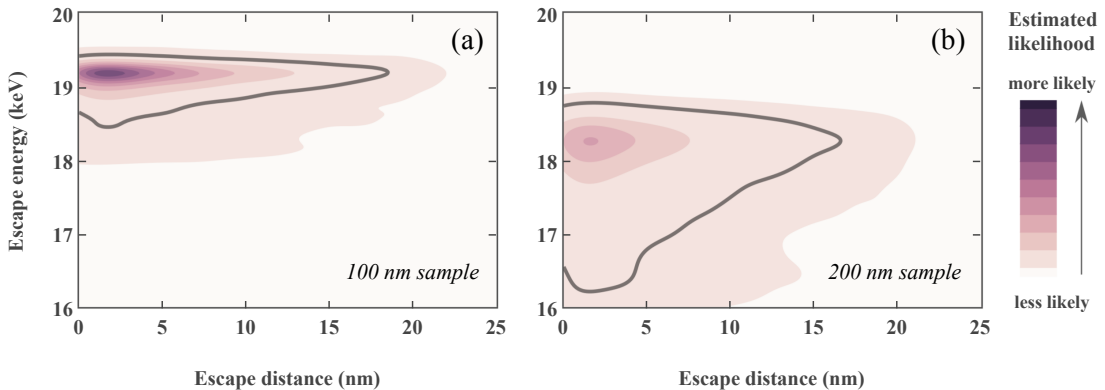


FIGURE 5.9: KDE plots of electron energy versus escape distance distributions as predicted by the MC model for TKD geometry for two sample thicknesses (a) 100 nm and (b) 200 nm. The area enclosed by the thick line contains 90% of events. See text for further details.

to significantly lower values as the thickness of the film increases. These observations already indicate that we should expect more diffuse diffraction patterns from thicker samples when compared to thinner ones. In general, the greater the interaction volume of electrons with the sample, the more energy will be lost by electrons before diffraction and the greater the diffuseness of the Kikuchi patterns; as supported by literature [RKS14].

Considering the x -axis, we observe that the escape depth profile resembles the usual power-law distribution [Win+16] with the bulk of the electrons carrying diffraction information originating from a few nm below the escape surface. It should be noted, that the MC model used in this study does not aim to predict the full depth of diffracting electrons or interaction volume. Instead, we make the assumption that the mean value of the full diffraction depth distribution can be estimated to be of the same order as the electron mean free path. Due to the power-law distribution rule, we can be confident that the vast majority of escape depths is considered in this model.

By comparing the two images in Fig. 5.9, we can see that the thickness of the samples impacts very directly the energy distribution of the escaping electrons. This linear correlation is shown more clearly as energy distributions of escaping electrons from a series of different thickness samples in Fig. 5.10. For very thin sample the energy distribution is narrow and we can expect sharp features while for thicker films energy absorption becomes more prominent and distributions will become broader with diffraction lines suffering blurring. The peak of the energy distribution is strongly influenced by sample thickness underlining the requirement for uniform thickness samples in TKD.

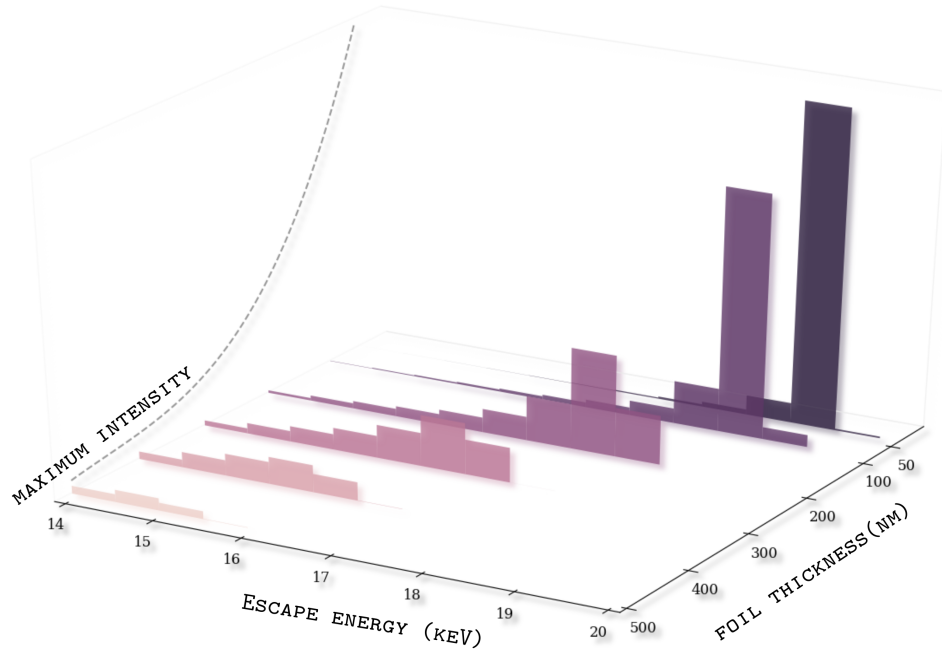


FIGURE 5.10: Energy distributions versus sample thickness for electrons exiting a 20° tilted Ni sample for a 20 keV primary beam. Image adapted from [Pas+18b].

It should be clear that accounting for the effect of sample thickness is essential when predicting accurate electron transmission diffraction patterns. In this model this is achieved by sampling the above likelihood distribution bin-wise and constructing the $\bar{\lambda}_k(E, z)$ weighting function as discussed in Section 5.2.1 on page 140.

In the next section, we will investigate special geometries for which electrons reaching different regions of the detector can be described by the same $\lambda_{\hat{k}}(E, t)$ function, simplifying the calculations significantly.

5.2.5 Special sample-detector geometries and the master pattern

Let us consider again the sample and detector geometries shown in Fig. 5.1 (a-f) back on page 131 where the lighter region on the samples depicts the volume in which electrons suffer scattering events. Different \mathbf{k} directions are indicated for which energy-distance KDEs distributions are shown in Figure 5.11. The top row shows two potential EBSD geometries, one with the sample tilted at the standard 70° angle with respect to the horizontal plane, the other with the sample tilted at 50° . As previously discussed, the sample geometry will determine the manner in which the radial symmetry of scattering will be broken. Nevertheless, the region of SP space sampled by

the position of the detector will also influence the uniformity (or lack thereof) of the electron energies and diffraction distances distributions. In Fig. 5.1 (a), the electrons that reach the top and bottom of the detector (thick line on the left, inclined at 10° from vertical) ought to have travelled approximately the same length inside the sample before channelling out; in Fig. 5.1 (b) on the other hand, the electrons that reach the bottom of the detector have travelled a significantly larger distance inside the sample.

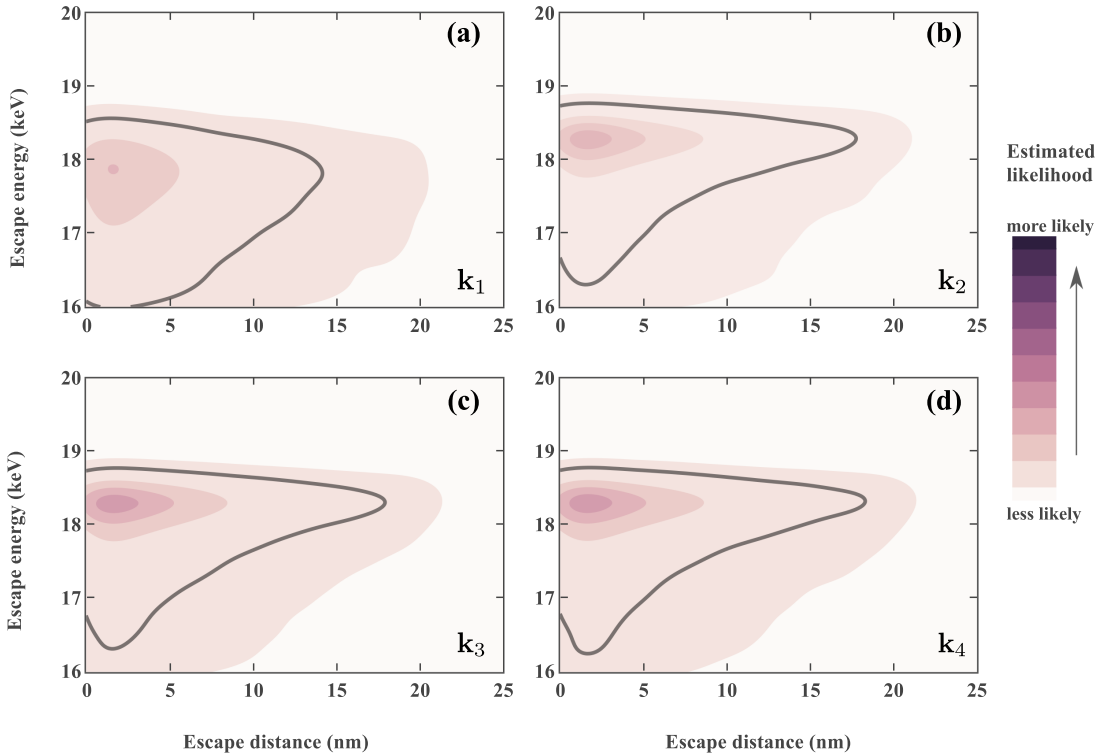


FIGURE 5.11: KDE plots of electron energy versus escape distance distributions as predicted by the Monte Carlo model for TKD geometries and directions \mathbf{k}_i shown in Figure 5.1 (c) and (d). The area enclosed by the thick line contains 90% of the events.

In TKD, the situation is similar: in Fig. 5.1 (c) the sample is horizontal and electrons that reach the top of the detector have travelled a much larger distance inside the sample before diffracting than electrons that reach the bottom. In the top row of Fig. 5.11, the escape energy-escape distance distributions are shown as KDE plots for electrons reaching the top (a) and the bottom (b) of the detector. We can observe qualitative differences in these distributions, especially for the escape energies. The electrons that travelled larger distances before diffracted lost more energy and therefore their energy distribution is shifted towards lower values. On the other hand, a small sample tilt of -30° shown in (d) reduces these differences. Fig. 5.11 (bottom

row) shows that the energy-distance distribution of electrons reaching the top of the detector (c) and the distribution of those reaching the bottom of the detector (d) is qualitatively the same. Note that figures 5.11 (b), (c) and (d) show similar distributions since all possible trajectories $\mathbf{k}_2, \mathbf{k}_3, \mathbf{k}_4$ have similar lengths in the sample.

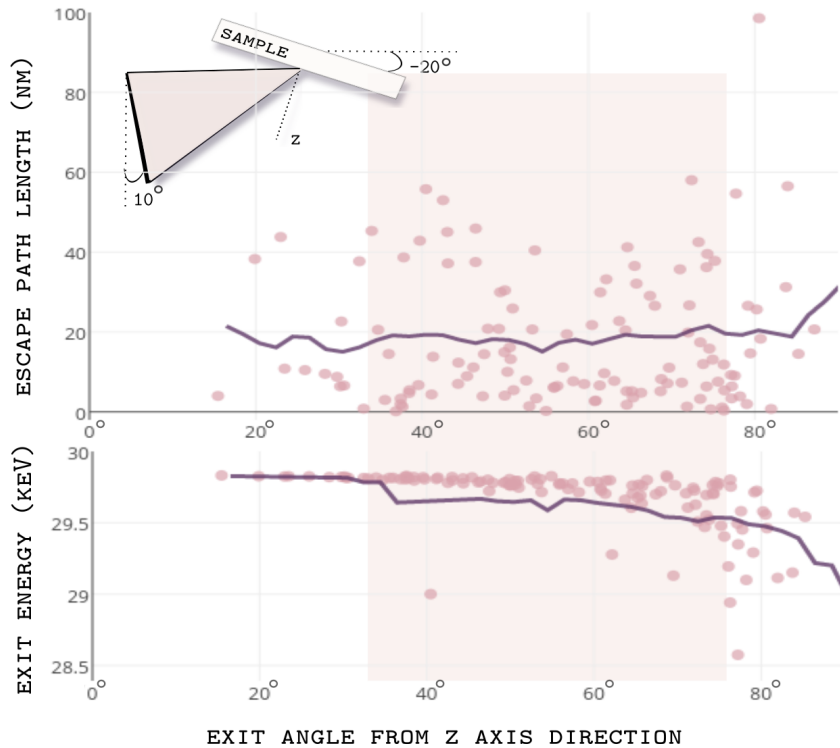


FIGURE 5.12: TKD electron escape path length (top) and electron exit energy (bottom) dependence on exit angle. Purple line shows the running mean values for more data points than shown. The pink coloured area indicated the solid angle of the detector as shown in the top left insert.

The conclusion we draw here is that in standard TKD geometry the path lengths and energies of electrons that reach the detector do not show strong dependency on the exit angle. To illustrate this even further, in Fig 5.12 I show another, more classical way to show this data, in the form of scatter plot, even though it now contains fewer data points. These are Monte Carlo results for 50000 electrons with incident energy of 30 keV travelling out of a 100 nm Si sample. Note, that I am showing a random sub-sample of 100 points. The angular dependence of both the exit energy (bottom) and the escape path length (top) shows a constant for the predicted solid angle of a detector (between 37° and 60° from the z-axis direction.)

Finally, for the ECP case illustrated in Fig. 5.1 (e) and (f), a small sample tilt does

not significantly change the distribution of path lengths inside the sample, and most trajectories have about the same path length.

This observation has consequences for the numerical approach to be used to obtain high quality simulated patterns. For special geometries, we can now approximate the weighting function $\bar{\lambda}$ by an effective (averaged) weighting function,

$$\bar{\lambda}_{\hat{\mathbf{k}}}(E, t) \rightarrow \bar{\lambda}(E, t), \quad (5.6)$$

which no longer depends on the electron direction \mathbf{k} . This has significant advantages numerically, since one can now pre-compute the probabilities $P(\mathbf{k})$ for a spherical sampling of incident beam orientations and store the resulting BSE yields in a master pattern (MP) that can be used to generate individual EBSD/TKD patterns by means of bi-linear interpolation, a fast and efficient way to compute many patterns in a short amount of time.

For EBSD and TKD simulations and sample orientations that deviate significantly from the standard orientations, one cannot apply the above approximation, since the range of distances travelled inside the sample is quite broad; thus, in these cases one must carry out the integrations of Eq. 5.4 for each individual EBSD/TKD pattern, which results in a slow computational tool.

For ECPs, the situation is quite different, since only BSE1 electrons carry coherent diffraction information; all other (BSE2) electrons only contribute to the background intensity. A BSE1 electron has nearly the same exit energy as the incident electron since the Rutherford backscatter event is the first major scattering event after entering the sample. Therefore, nearly all BSE1 electrons have the same exit energy and the energy integration can be eliminated, leading to the following expression which is valid for the ECP case only (with E_0 the incident electron energy):

$$P_n^{\text{ECP}}(\hat{\mathbf{k}}) = \sum_{j \in \mathcal{S}_n} \sigma_j \int_0^{t_0(E_0)} dt \bar{\lambda}(t) |\Psi_{\hat{\mathbf{k}}}(\mathbf{r}_j; E_0, t)|^2, \quad \text{with } \bar{\lambda}(t) \equiv \frac{\lambda(z)}{Nt_0(E_0)}. \quad (5.7)$$

Therefore, the master pattern approach is quite well suited for the ECP case as well. For standard geometry EBSD/TKD patterns and ECPs the master pattern is computed only once for a given crystal structure and microscope voltage, and can be used to compute individual patterns by interpolation.

TKD master pattern simulations proceed along lines similar to the previously published EBSD [CDG13] and ECP [SDG17] modelling approaches. A uniform grid of

points is generated on a spherical surface surrounding a hypothetical spherical crystal located at the centre; each sampling point represents one outgoing beam direction \mathbf{k} , and the radius of the sphere is the maximum integration depth $t_0(E)$. The sampling scheme employs the modified Lambert projection introduced in [Ros10; CDG13] in which a uniform grid on a square is mapped onto the sphere by means of an equal-area projection. For each beam direction, and for a given sample thickness, one carries out the integrals of equation 5.4, using the Monte Carlo $\lambda(E, t)$ weighting function determined for that sample thickness. In the following section, we show example TKD master patterns and compare them to similar patterns for the EBSD and ECP modalities.

5.3 Results

5.3.1 Comparison between EBSD, ECP, and TKD master patterns

The master pattern expression in Eq. 5.4 reveals that EBSD, ECP, and TKD master patterns have a lot in common; in particular, the dynamical scattering process that underlies the generation of Kikuchi bands is identical for the three diffraction modalities. The only differences occur in the directional, depth, and energy distributions of the B/FSEs that contribute to the patterns. To illustrate the similarity of the master patterns, Fig. 5.13 shows a portion of the upper right quadrant (centred on the [111] pole) of the energy-weighted silicon master patterns for (a) ECP, (b) and (c) TKD for two different foil thicknesses (50 and 250 nm) and (d) EBSD. The microscope voltage is 20 kV for all patterns, with a specimen tilt angle of 70° for EBSD, 0° for ECP, and –20° for TKD. The patterns are very similar but differ in small details. The TKD master patterns are plotted with added colour in order to highlight subtle differences.

Fig. 5.14 (a) shows line scans through each of the master patterns, slightly vertically offset to make the profiles more clearly visible. The differences in details across the patterns is seen here distinctly. The scan across the ECP pattern in Fig. 5.13 (a) displays significantly better resolved peaks compared to the EBSD one Fig. 5.13 (d), supporting the better resolution observed in the ECP master pattern. Since the main signal in the ECP case consists of BSE1 electrons which have lost only a small amount of energy in the sample before being backscattered, one can consider ECPs to be energy-filtered versions of EBSPs.

The line scans across the TKD patterns for different thickness films are more similar to each other, except for the shift in peaks in the zone axis (highlighted by the grey box). It is rather apparent that both the peak positions and the sharpness of the thin

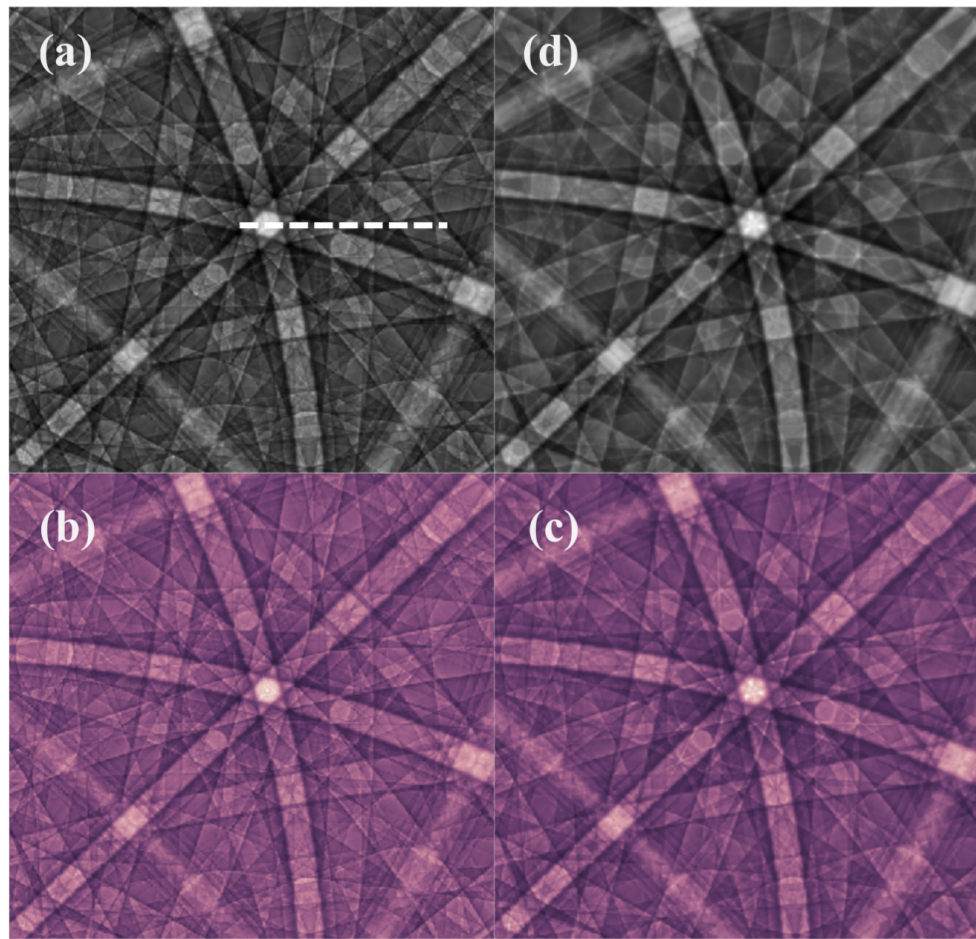


FIGURE 5.13: Portion of the stereographic projection shown in Fig. 5.2, centred on the [111] pole, of a master pattern for silicon for (a) ECP, (b) and (c) TKD for sample thicknesses of 50 and 250 nm and (d) EBSD.
Image adapted from [Pas+18b].

film (50 nm) TKD pattern are more similar to the ECP pattern, while the peaks and blurriness of the thick film TKD pattern are closer to those of the EBSPs. In effect, the Master Pattern for TKD on very thin samples is very similar to the ECP MP in similar geometry. If the sample is thicker, the blurriness in the MP for TKD reaches asymptotically the EBSD one.

We explain this behaviour by considering the energy loss of electrons contributing to the patterns in each case. The Monte Carlo predicted energy loss spectra for all four cases described above are shown in Fig. 5.14 (b) as fitted Poisson distribution curves. Thin film TKD patterns are produced by electrons with an energy range very close to the ECP case. Similarly, increasing the sample thickness causes the electron exit

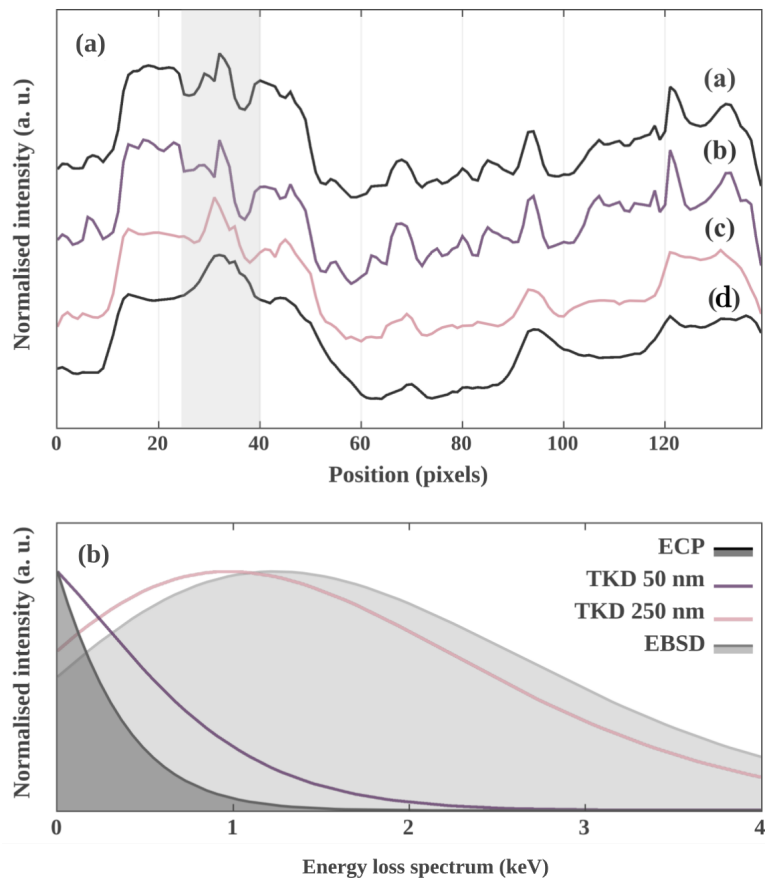


FIGURE 5.14: The profiles in (a) represent the intensity along the central line (marked as a dashed line in Fig. 5.13 (a)), for all four cases; the profiles have been offset vertically for clarity. The energy loss distribution estimated by the MC model for all four cases is shown in (b) as Poisson distribution fitted curves. Image adapted from [Pas+18b].

energy distribution to become wider and shift to lower energies, which corresponds to a broadening and slight blurring of the Kikuchi bands due to the increased Bragg angles; these phenomena are common to EBSPs and thick films TKD patterns.

It becomes apparent that the sample thickness can be seen as an energy filtering mechanism in TKD as we have seen in Fig. 5.10 on page 148. In terms of the traditional Hough-based indexing approach, one must thus select a butterfly mask of the appropriate width, depending on the sample thickness and incident electron energy. For the dictionary indexing approach [Mar+17], used by EMsoft, the pattern dictionary must be computed using the appropriate Monte Carlo and master pattern data, to ensure accurate matches between experimental and simulated patterns.

| x_{PC} (pixels) | y_{PC} (pixels) | ρ ($\mu\text{m}/\text{pixel}$) | L (μm) |
|-------------------|-------------------|---------------------------------------|-----------------------|
| 6.4406 | 264.1950 | 0.292 | 23471.48 |

TABLE 5.1: Pattern centre position (x_{PC}, y_{PC}) (given in the reference frame of the detector with origin in the middle as shown in Fig. 5.4), detector pixel size ρ and distance from sample to detector L for the TKD pattern shown in Fig. 5.15.

The EBSD master pattern is an energy-weighted average of individual master patterns and the integration over the electron energy gives rise to a continuous range of Bragg angles and, thus, a general blurring of the master pattern features compared to the ECP case. This will also be the case for individual diffraction patterns that are extracted from the master patterns via bilinear interpolation, as explained in [CDG13].

5.3.2 TKD patterns comparison with experiments

Patrick G. Callahan at University of California, Santa Barbara, acquired a number of experimental TKD patterns, an example of which is shown in Fig. 5.15 a) for a nanocrystalline Aluminum sample, acquired at 30 kV with a sample tilt of -18° in a FEI Teneo field emission scanning electron microscope, using the TSL Hikari EBSD detector system. The sample foil is approximately 150 nm thick. The calibration parameters are given in Table 5.1. I added axes showing the radial distance components from the pattern centre, r_x and r_y , respectively :

$$r_x = \tan(\theta_x) = \frac{(x - x_{PC})\rho}{L}$$

$$r_y = \tan(\theta_y) = \frac{(y - y_{PC})\rho}{L}$$

Fig. 5.15 b) shows the dictionary indexing simulations with this model and we can see that it matches the experimental patterns well. The dot product values between normalised patterns are equal to 0.881 which indicates a satisfactory match. For more details about the parameters that go into the simulation see the paper [Pas+18b].

Note that the only adjustments to the simulated patterns were brightness and contrast changes to maximise the visual agreement between the simulated and experimental patterns. The overall intensity gradient (from bright at the bottom of the pattern to dark at the top) follows directly from the use of the direction-dependent Monte Carlo statistical data, and is in good agreement with the intensity gradients

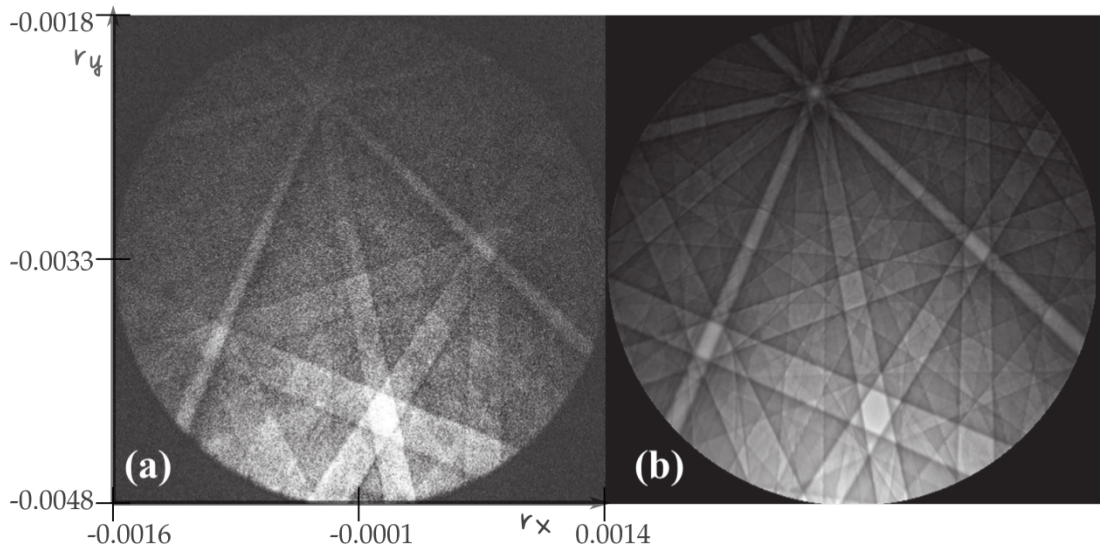


FIGURE 5.15: (a) Experimental TKD patterns for Al at 30 keV; brightness and contrast of the simulated patterns have been adjusted to better match the experimental patterns. The axes are showing the radial distance components from the pattern centre r_x and r_y . (b) Corresponding simulated patterns. Image adapted from [Pas+18b].

of the experimental patterns. The satisfactory agreement between simulated and experimental patterns indicates that the energy-weighted dynamical scattering model employed in the pattern simulations is sufficient to obtain realistic pattern simulations.

Next, he generated a TKD master pattern with the energy filtering model for an Al sample as shown in the paper. For all of the experimental patterns of an acquired TKD map of a nano-crystalline Al sample the dictionary indexing approach finds the simulated patterns from the MP that best matches it.

Fig. 5.16 a) shows an orientation similarity map. The dictionary indexing approach produces a list of the top N best matches (dictionary patterns with the N highest dot products, where N is typically set to 30). For each sampling point, the orientation similarity is computed by determining the average number of top matches that this sampling point has in common with its four nearest neighbours; this value is then displayed as a grey scale image. Since sampling points near grain boundaries will have fewer best matches in common with their neighbours, the orientation similarity map (OSM) provides an easy overview of the microstructure in which grain interiors have a uniform intensity level and all grain boundaries have lower intensity.

The [0 1 0] inverse pole figures in Fig. 5.16 b) and c) were obtained by the standard

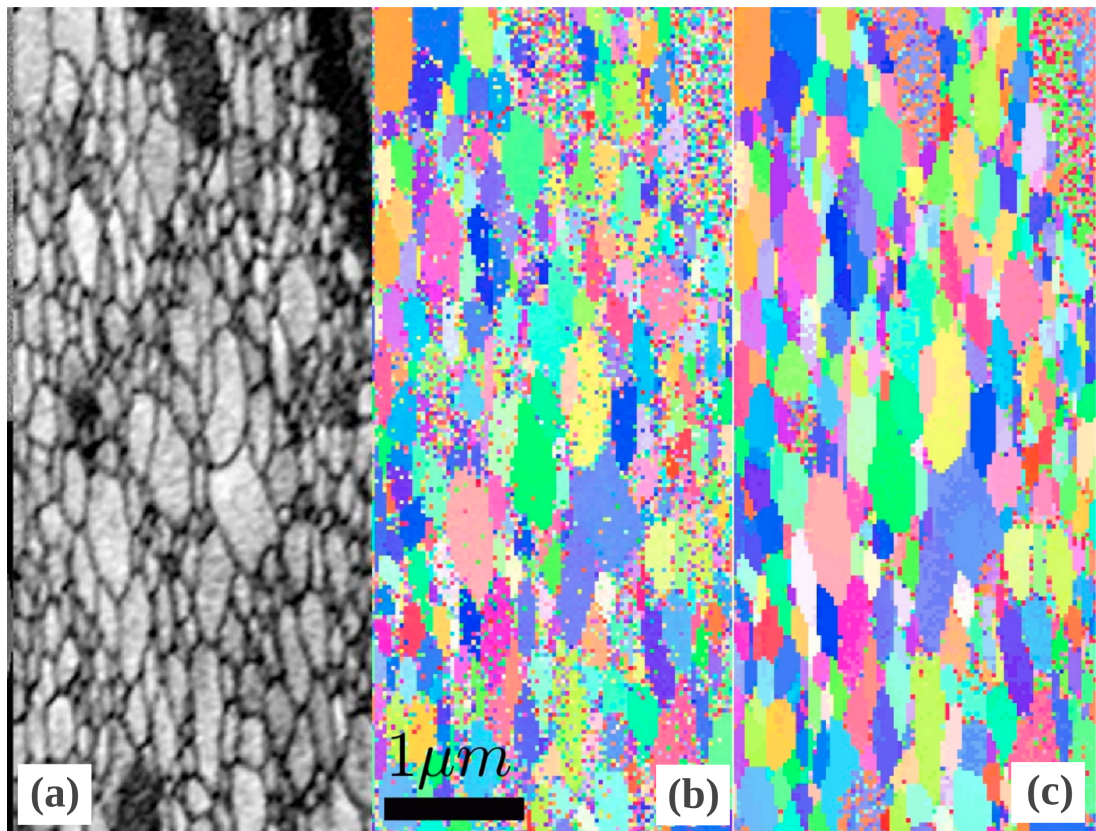


FIGURE 5.16: (a) Orientation similarity map (see text for details); (b) [010] inverse pole figure (IPF) obtained with the commercial OIM-8 indexing software; and (c) [010] IPF obtained using the dictionary indexing approach. Image adapted from [Pas+18b].

commercial OIM-8 indexing package and the dictionary indexing approach, respectively. The dark regions near the top of the field of view in Fig. 5.16 b) correspond to surface contamination from the XeF₂ etching step and result in clusters of incorrectly indexed or unindexable points in both indexing approaches; patterns were deemed to be unindexable when the Image Quality was low (according to the commercial software analysis package). However, overall, the dictionary indexing approach with the energy-weighted model has fewer undindexable or incorrectly indexed points, in particular near grain boundaries.

5.4 Discussion and conclusions

Inelastic scattering, a phenomenon usually discarded in diffraction simulations, has direct influence on the energy distribution of diffracting electrons and, consequently,

on the imaged Kikuchi patterns. The broader the energy distribution of diffracting electrons, the more diffuse the Kikuchi band edges. Using a Monte Carlo model we can observe that the length of electron trajectories before diffraction is a determining factor in the broadening of the energy distribution. This factor, in turn, can be controlled in the Transmission Kikuchi Diffraction modality through the thickness of the sample, acting effectively as an energy-filtering mechanism. Another determining factor for the energy distribution is the sample-detector geometry which influences both TKD and EBSD modalities.

We should note that the Monte Carlo model used in this work explicitly describes the lower escape distance values for the signal carrying electrons. A subset of electrons reaching the detector will, nevertheless, carry a probability of channelling over longer trajectories. Depending on their travel direction inside the crystal, these electrons are expected to give rise to contrast inversion of one or more Kikuchi bands (observed as dark instead of bright lines). This will occur when the distance travelled is of the order of, or larger than, the extinction distance for a particular plane. Contrast inversions are thus expected to occur for both EBSD and TKD modalities when the sample is tilted such that long electron trajectories are possible; in addition, the sample should have a crystal structure that gives rise to short extinction distances. For the ECP modality, contrast inversions are not expected to occur unless very large sample tilt angles are used, which is not practical due to the possibility of the sample hitting the back-scatter detector. Similarly, when the TKD detector is mounted horizontally, below the sample, the electron trajectories inside the sample will have a narrow range of escape distances, so that contrast inversions are also not expected to occur. A statistical model more sensitive to the outlier cases of long distance channelling electrons is therefore necessary if we are to correctly predict band contrast inversion.

The energy-weighted scattering model is shown to correctly predict Kikuchi bands sharpness (defined as signal to noise intensity) for the different SEM modalities. When used for the dictionary indexing approach it was shown to produce indexed TKD patterns with fewer incorrectly indexed points compared to commercial Hough transform based indexing software.

6 Summary, discussion and further work

In Chapter 3 I covered everything electron diffraction, including describing where the values of important diffraction parameters, like the structure factor, come from. I also took it upon myself to show graphs for scattering factors for group-III nitride systems (AlN, GaN and InN) and explain the insights they provide. Not only intuitive ones like the fact that the atoms in AlN will elastically scatter fewer electrons and, therefore, give a poorer signal to noise when it comes to ECC imaging, but also less intuitive aspects, such as families of planes that are more densely packed (such as the *a*-plane) scatter fewer electrons than their less packed counterparts (such as *c*-plane). This is somewhat unfortunate for the study of [0 0 1] wurtzite nitrides in the forward scatter geometry in the SEM.

I calculated the wurtzite structure factor in these systems and commented on their predictions, including the failure of Friedel's law for non-centrosymmetric systems and the systematic absences we can expect. Embarked with all these information I spend the rest of the chapter applying the Howie-Whelan dynamical model to the ECCI geometry. I make the argument the equations should still hold even if we replace the dependence on depth in the sample of the Bloch waves with that on the distance travelled by the primary beam.

Having the two beam dynamical equations laid out, in Chapter 4 I go over adding the displacement field introduced by a threading dislocation and using this model to predict the observed dislocation associated contrast in ECCI which I call *ECC-strain*. I spend some effort emphasising the importance of setting out the correct reference frame transformations. In the end, I argue, the contrast profile of a dislocation observed in ECCI is nothing more than a map of the strain projection selected by the diffraction conditions. Having worked out the complex relationship between the many frames involved, looking at the physics predicted by the strain profile of dislocations becomes a piece of cake.

For instance, I show how the sample tilt affects dramatically the surface relaxation of the ECC-strain and that, in turn, will enhance the contrast. I then interrogate the

ECC-strain for forward model geometry about whether the diffraction condition or the Burgers vector dominates the contrast profile. I conclude that edge TDs ECCI contrast profile generally follows the Burgers vector while the diffraction condition mostly affects its magnitude. I also compare these predictions with experimental data to confirm the behaviour.

All this analysis was done for a two beam dynamical model. This approach is a valid prediction of a strong two beam diffraction condition. This, in turn, is a likely condition to achieve for SEM electron energies which describe a smaller Ewald sphere, which will likely intersect a few reciprocal lattice points, as opposed to the large sphere the TEM electron energies correspond to. It would be interesting in future work, as already suggested by Prof. De Graef, to compare the two beam model prediction to the multi-beam one and assess how correct these assumptions are.

For a fact, the strong beam is not always fulfilled in ECC images either by chance in the absence of ECP navigating, or by choice since weak beam diffraction will give higher resolution as we know from TEM. It is my inkling that, in fact, ECC images showing only bright intensity at dislocation positions, mostly in metals, *e.g.* steel [GUZR09] or Al [BWV10], are obtained closer to weak beam conditions where the deviation from the Bragg angle, s_g is large. In this case, instead of bright-dark contrast, the dislocation moves locally the reciprocal lattice point closer to the Ewald sphere, showing as higher diffracted intensity on the micrograph. This is an interesting case especially because the Laue geometry approximation will become less feasible. To my knowledge, literature is yet to address the physics and possible models of predictions for, what is a common representation of ECCI, high intensity at dislocation positions in the SEM.

The fact of the matter is that ECCI models are nowhere near mature and here are two more points that I can think of where they are lacking. In terms of the TD displacement predictions, I approximated the anisotropy of wurtzite system to an isotropic one plus corrections. It would be more accurate to consider full anisotropy and models for that exist [BS71]. But this would make a small difference compared to introducing grains in the continuum model [RS50]. Dislocations on grain boundaries are ought to introduce a very different displacement field that is incomparable to that introduced by dislocations in a true continuous medium [VS02]. And we know plenty of dislocations lie on the grain boundaries. Grain boundaries facilitate dislocation pile-ups and influence directly the hardness of a material. Since TEM requires sample to be as thin as the size scale of grains, the sample preparation will introduce relaxation that will affect the grain structure. ECCI is therefore the only possible non-invasive imaging technique of dislocations at boundaries. Unfortunately, due to the

limited number of investigations we don't yet know how to use it precisely.

The other point of improvement is related to the Monte Carlo discussion in Chapter 5. I approximate the incident coherent beam penetration depth using Monte Carlo models that do not take into account diffraction whatsoever. I use the escape depth of low loss electrons, but the model does not know that diffracting electrons suffer less inelastic scattering and can travel further. Since the values I obtain are on the same scale as the literature offers, I think the values should be in the right ballpark, but it would be a worthwhile effort to quantitative study of how deep in the sample the ECC signal comes from.

Chapter 5 discusses the importance of taking into account multiple electron energies when modelling EBSD/TKD patterns. It shows that for the TKD geometry, the low side of the energy distribution of the low loss electrons contributing to the Kikuchi patterns will be highly anisotropic on the detector. In other words, not taking into account an energy distribution for the low loss electrons will fail to predict not only the intensity distribution along the Kikuchi lines, but also the their width variation as well as details.

We also show how the sample thickness acts in effect as an energy filtering mechanism for the diffracting electrons in TKD. In terms of comparing the Kikuchi patterns in all the diffraction mechanism in the SEM discussed in this Thesis, Fig. 5.13 on page 153 is an insightful one. Comparing the energy distribution of electrons contributing to ECP, TKD and EBSD patterns, and with it the resulting sharpness and details of the simulated Kikuchi lines on the MP, we conclude that the TKD modality is bridging the gap between the very narrow energy window of the ECPs and the broader energy range of EBSD.

6.1 Epilogue – Science as an incremental, open process

The history of science is all too often taught as a chronological list of discoveries. There is undeniable value in this approach as it reflects the arrow of complexity of notions. However, it leads to a very simplified image of the development of scientific knowledge: one big idea bringing over the next and so on. On page 57, I too show the history of diffraction as a table of chronological events. These are big shift events, which radically and permanently changed the way future science was to be done in this area. A good number of names in this table were awarded for their significant contribution with Nobel prizes. Nevertheless, the table is clearly a gross simplification of history, omitting, due to lack of space, the incremental refinement and maintenance work that supported and propelled the bigger ideas. It is quite common for

important work of individual voices to be wiped away from science history as we associate a breakthrough to a single name or even to a small group of people. Seeing the bigger picture is, undeniably, worthwhile, but we must not mistake it for the full picture.

The “unremarkable” work done by the rest of the community, not awarded prestigious prizes, is not less important for the advancement of science. Quite the opposite. Neither science nor culture truly advance in big steps. In a recent study published in *Nature*, Miu *et al.* [Miu+18] looked at the way pieces of software get improved by a community of developers in a simulation of cumulative cultural evolution. One of the observations was that the vast majority of advances are of an incremental type and not, as the scientific community expect, leaps in knowledge. Observing the strong positive breakthrough bias of scientific publishing, one would find it hard to assume that enough credit is given to the “tweakers”.

Another critical observation was that big changes in the paradigm are more likely to turn out unsuccessful than smaller tweaks. Remember the Nobel prize in medicine awarded for the “discovery” of brain lobotomies¹? Thankfully, neuroscience moved away from this particular scientific breakthrough. And it did that with small, incremental improvements on the understanding of the brain. Any sort of conversation about the development of science focused only on the leaps of knowledge must ultimately be misrepresenting the scientific process.

In this paradigm of scientific value misrepresentation, scientific code suffers perhaps even more. The philosopher Daniel C. Dennett, in his latest book *From bacteria to Bach and back* [Den17] makes the case that evolution is not only a good protocol for developing fit biological organisms but can, in fact, be successfully applied to a variety of concepts, perhaps, he argues, consciousness, the human mind and even code development. The latter analogy I find compelling. Similarly to adaptable organism having emerged from surviving a variety of conditions, the power of good code stands in the number of iterations it went through. Of course, we cannot wait around for functional code to “occur” as the results of tens of millions of years of iterations, and, after all, we expect developers to be somewhat wiser than the random processes occurring in nature. Nevertheless, in the end, each iterative step has the chance to rectify errors or limitations in the code, weed out unnecessary/old lines and replace them with new, more optimised, features. Established software tends to be software reviewed by many pairs of eyes. Yet, scientific software continues to be developed

¹ “for his discovery of the therapeutic value of leucotomy in certain psychoses” – The Nobel Prize in Physiology or Medicine 1949 [Nob49].

and maintained by small groups and destined to see the light of only a handful of iterations.

To add insult to injury, scientific code is rarely developed to be open and even more rarely made easily accessible. Here is another example of anecdotal evidence of why I think this a counter-intuitive way of following the scientific method. Two condensed matter groups set out, independently, to predict the behaviour of super-cooled water, and, even though they implemented the same method, their results contradicted each other for seven straight years [Sma18]. During this time, while the groups were in contact with one another, the actual lines of code never changed hands. When it finally did, a bug was discovered by the “competing” team in just a few months. I’m pointing out that we could have known in a few months, not seven long years, that water is predicted to change phase when supercooled. When scientific groups working in the same field do not collaborate with each other for whatever reason, it is science that suffers.

In the light of all these, I want my thesis work to make a positive tweak in the endeavour of making electron diffraction in the SEM a well-understood phenomena in the electron microscopy community. I aim for this work to aid the understanding of why we can observe and how we can study dislocations in the SEM and I do not expect it to be the definitive attempt. For these reasons I tried to make this document as accessible as possible for whoever wants to continue on this journey. I tried to explain in depth the building blocks I used and why I chose them, I provide access to whatever code I ran or wrote and I offer a small collection of extra materials. May your code and science be even a little bit better than mine!

A Implementations

I refer throughout this document to supplementary pieces of code, most in *Python* and some in *Fortran95*. I tried to describe in detail what they do, sometimes I included pseudocode and other times I just state the relevant equations. They can all be found on my, otherwise rather pristine, public GitHub repository [Pas15].

The Python scripts have been written in Python 2 which can be easily installed on Ubuntu machines (or most Linux flavours) from the package manager or by typing in 18.04 or later:

```
$ apt install python-minimal
```

Files containing Python script can be easily recognised from the *.py* file type and can be run with:

```
$ python filename.py
```

To run Fortran code on a Ubuntu machine use the *gfortran* compiler, which again can be found in the package manager or can be installed via:

```
$ apt install gfortran
```

For the Fortran files I wrote a *Makefile* that compiles the dependencies in the correct order. It can be run by simply typing *make* in the command line. Once everything is compiled it is just a matter of running the executable.

For the smaller scripts I use Jupyter [PG15] notebooks written in Python. I will assume the reader has Python 2.7 or greater installed. The Anaconda Python distribution [Ana] ships with Jupyter among other packages useful for scientific computation. However, if you have Python already installed then you can use the package manager *pip* to add new libraries:

```
$ pip install jupyter
```

To start a Jupyter notebook kernel you just type:

```
$ jupyter notebook
```

And navigate to the desired script file. Individual cells are compiled with Shift + Enter.

In some notebooks I use the `plotly` package [Inc15] for plotting. These figures are interactive but do require an account on the `plotly` website¹.

In Chapter 5 I talk about the open software implementation of electron and optical microscopy models EMsoft [SRDG17], which can be found on Prof. Marc De Graef's GitHub [DGG13] page where installation instructions are also given.

¹ Plotly website url is <https://plot.ly/>.

B Passive rotation matrices in the 3D Cartesian frame

As described in the main text, these are just the transpose of the active 3D rotations.

The passive, anticlockwise rotation of a Cartesian reference frame around the axis x is given in the pre-multiplication matrix form as:

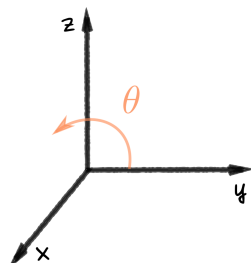
$$\mathcal{R}_x(\theta) = \begin{pmatrix} 1 & 0 & 0 \\ 0 & \cos \theta & \sin \theta \\ 0 & -\sin \theta & \cos \theta \end{pmatrix}$$

The passive, anticlockwise rotation of a Cartesian reference frame around the axis y is given in the pre-multiplication matrix form as:

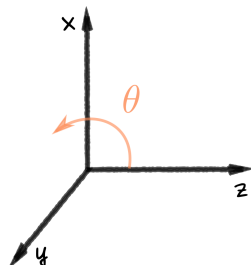
$$\mathcal{R}_y(\theta) = \begin{pmatrix} \cos \theta & 0 & -\sin \theta \\ 0 & 1 & 0 \\ \sin \theta & 0 & \cos \theta \end{pmatrix}$$

The passive, anticlockwise rotation of a Cartesian reference frame around the axis z in the pre-multiplication matrix form is:

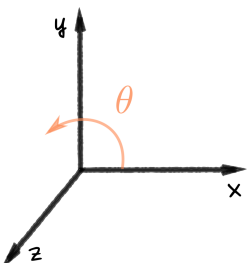
$$\mathcal{R}_z(\theta) = \begin{pmatrix} \cos \theta & \sin \theta & 0 \\ -\sin \theta & \cos \theta & 0 \\ 0 & 0 & 1 \end{pmatrix}$$



Basic rotation around x .



Basic rotation around y .



Basic rotation around z .

C Symmetry in crystallography

Many objects in nature exhibit symmetry of some sort. The human body has approximate mirror symmetry. A shamrock (the species of clover or trefoil used as the symbol of Ireland) has three-fold rotational symmetry (trefoil), and here's a bit of trivia to make you a star at the next British party, not four-fold symmetry as U.S. advertisements sometimes wrongly represents it. The reader might have noticed that the way we talk about object symmetry involves a motion action, which made upon the object would leave it unchanged. Indeed, the symmetry of an object will be defined by its *symmetry operations* that map the object onto itself. While for any motion one can find an object for which this is a symmetry motion, if we start with the object it is easy to start with these three basic actions to test its symmetry¹:

1. rotate
2. reflect
3. translate

If, after any one or a combination of 1, 2 and 3, the object looks the same as it originally looked than we talk about the object as being symmetric. There is a nuanced distinction between these operations since 1 and 3 can be physically realised and known as *proper* or first kind operations. Operations that involve 2 are *improper* or of second kind. Inversion is yet another improper operation that can be reduced in three dimensions to a rotation plus a reflection.

We will see that all this can be written in mathematical form with only minor adjustments. First, operation 3 can only truly be a symmetry operator for infinite objects which are not very common in everyday life. Second, the identity operator is also introduced as symmetry operator, such that, in the mathematical sense, all objects hold at least one symmetry property. Now there's nothing stopping you from being the soul of the party.

We will spend some time exploring a subset of symmetry operations chosen such that when combined can generate the entire symmetry of a wurtzite crystal. We

¹ Assuming we are to leave the metric properties of space undisturbed, *i.e.*, no stretching, bending, twisting, which should be easy to achieve in the physical world.

will follow closely the notation used in *International Tables for Crystallography, Volume A* [Hit88] described in some detail on page 181. We will use the two most common shorthand notations to write down symmetry operations: the *Hermann-Mauguin notation* also known as the *international notation* which is the standard one, and the *Schoenflies notation* which is widely used in Physics and Chemistry. We will also show the graphical symbols for the operations discussed.

C.1 Symmetry operations

The set of symmetry operations of a given object have noteworthy properties:

1. the application of two symmetry operations results in a third symmetry operator of that object
2. the inverse of an operation is also an operation of that object
3. all objects exhibit the identity operation
4. the associative law is valid when combining three or more operations.

These four properties are also the group axioms and tell us that the set of symmetry operations of a given object form a mathematical group. This will come in handy in the next section. For now it is worthwhile to look at how to write these operation in mathematical form.

In the following we will explore a non-exhaustive list of symmetry operations. We choose our examples such that they are relevant for generating the wurtzite crystal structure symmetry. Note that the basis vectors of a hexagonal lattice do not form a Cartesian frame. This means that the usual algebraic formulas used for transformation operations must be revised. We do expect the form of rotation, translation and reflection matrices to be therefore not as familiar, which is why we take the time to explore them here.

C.1.1 Operation of first kind: pure rotation

A pure rotation is fully determined by a rotation axis and a rotation angle which is chosen to be positive in the counter-clockwise direction. The rotation axis is given as a vector $[u\ v\ w]$ and the rotation angle is given as fraction of 2π . For instance a rotation of order three or three-fold rotation is a rotation by angle $2\pi/3$. In general an n -fold rotation is represented by symbol n (C_n) and Table C.1 shows examples for three-fold

TABLE C.1: Examples of pure rotation symbols.

| Name | Graphical | Hermann-Mauguin | Schoenflies |
|---------------------|-----------|-----------------|-------------|
| Three-fold rotation | ▲ | 3 | C_3 |
| Six-fold rotation | ◆ | 6 | C_6 |

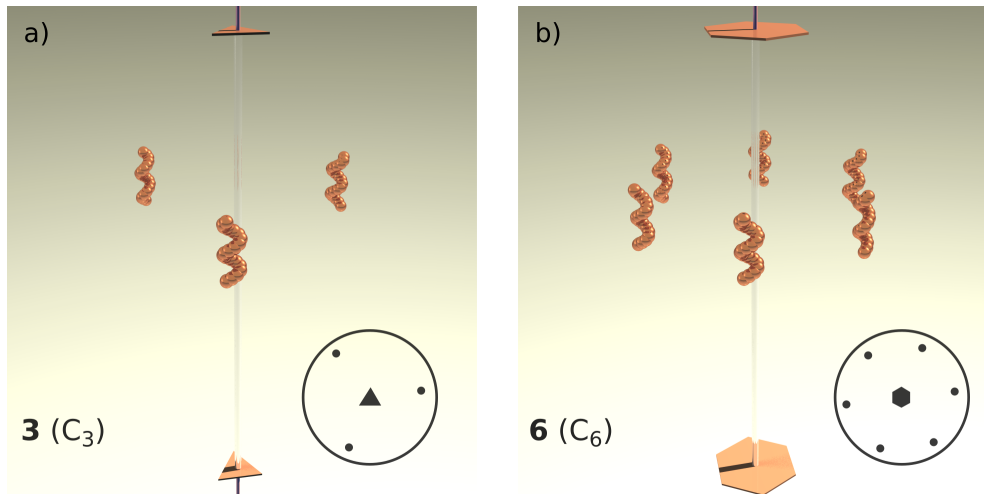


FIGURE C.1: Rendered 3D graphical representations of a) three-fold and b) six-fold pure rotations. The circles in the bottom right of the images represent the stereographic projections of the operators.

and six-fold rotations together with their graphical symbols which are filled polygons with n sides.

3D representations of the rotation operator are shown in Figure C.1 for rotations of order 3 in (a) and 6 in (b), respectively. The images have been rendered with the public domain software Rayshade 4.0.9 software². The input files I used are very closely based on the input *.ray files³ developed by Marc De Graef [DG98] with the purpose of teaching the crystallography group symmetry[DG08]. My scripts can be found at this GitHub repository⁴. The relevant files for this example are 3FoldPureRotationPNG.ray and 6FoldPureRotationPNG.ray and can be compiled on a Linux machine after the installation of Rayshade software (and making sure ImageMagick is available on the machine) by typing:

```
rayshade [filePNG].ray > [filePNG].mtv
convert [filePNG].mtv [file].png
```

² Link is <https://sourceforge.net/projects/rayshade/>.

³ Link is <http://som.web.cmu.edu/frames2.html>.

⁴ Link is https://github.com/elenapascal/SEM-diffraction/tree/master/Wurtzite_symmetry.

where [file] is the name of the file used. *.mtv files can also be converted to *.png or *.gif with ImageMagick. All the input scripts and resulting images and animated files can be found in the extra materials. To render the *.gifs one need more patience and has to do:

```
rayshade [fileGIF].ray > [fileGIF].mtv
convert [fileGIF].mtv [file].gif
```

The small helix object used by Marc De Graef in these images (made up of a helical string of spheres) was chosen such that it holds no rotational symmetry. The object also exhibits handedness and its mirror reflection will look different from the original object. Despite this, the entire system, the three objects in Fig. C.1 (a) or six objects in Fig. C.1 (b), looks indistinguishable from original when rotated $2\pi/3 = 120^\circ$ and $2\pi/6 = 60^\circ$, respectively, around the rotation axis. Similarly, a triangle prism will look the same after being rotated around the central axis by 120° and a hexagonal prism will look indistinguishable after being rotated 60° , respectively.

It is common for the axis of rotation to be the third basis vector *i.e.*, parallel to the crystallographic c-axis and, in those cases, the rotation axis to not be explicitly stated. In any other case, the rotation axis must be given, either in vector form $[uvw]$ or as the equation of the line coinciding with the axis. The latter notation method is the one used in the *International Tables for Crystallography*. As an example we can look at *Symmetry operation* (2) of a hexagonal lattice point group shown in Fig. C.7. $3^+(0,0,z)$ is a three-fold pure rotation around the [001] direction given here in line equation form. The $+$ sign informs us that the position of the point is elevated with respect to the drawing plane.

A three-fold symmetry of a lattice tells us that for every “motif” at position (x,y,z) we will find the same motif at the equivalent position (x',y',z') obtained through a 120° rotation around the central axis, here \mathbf{e}_z . In order to represent the rotation operation in mathematical form we must turn to rotation matrices. Unlike the somewhat intuitive form when used in an everyday orthonormal system, as seen on page 166, when derived for a general, non-orthonormal lattice the rotation matrices can become cumbersome and will obscure the symmetry (see ref. [Dav73]). Luckily, we can avoid that by considering the passive rotation of the system instead of the active rotation of the motif.

We want to find the rotation matrix $D(\theta)$ which, when applied to a set of (not necessary orthonormal) basis vectors $(\mathbf{e}_x, \mathbf{e}_y, \mathbf{e}_z)$ rotates them once around \mathbf{e}_z by an

angle θ to a new configuration (\mathbf{e}'_x , \mathbf{e}'_y , \mathbf{e}'_z). This passive rotation is defined in crystallography by the right hand rule⁵. It should be clear that this is equivalent to an active rotation (*i.e.*, rotating a vector defined in this basis) by the same angle anticlockwise around \mathbf{e}_z when looking in the direction of \mathbf{e}_z .

If the set of basis vectors describes a hexagonal lattice⁶ and the angle of rotation is 120° then the matrix $D^{\text{hex}}(120^\circ)[001] \equiv D^{(n)}$ is a three-fold rotation and can be derived by geometry as shown in Fig. C.2.

$$\begin{aligned} (\mathbf{e}'_x & \mathbf{e}'_y & \mathbf{e}'_z) = (\mathbf{e}_y & -\mathbf{e}_x - \mathbf{e}_y & \mathbf{e}_z) \\ &= (\mathbf{e}_x & \mathbf{e}_y & \mathbf{e}_z) D^{(n)} \end{aligned}$$

Which completely determines the matrix $D^{(n)}$ to be:

$$D^{(n)} = \begin{pmatrix} 0 & -1 & 0 \\ 1 & -1 & 0 \\ 0 & 0 & 1 \end{pmatrix} \quad (\text{C.1})$$

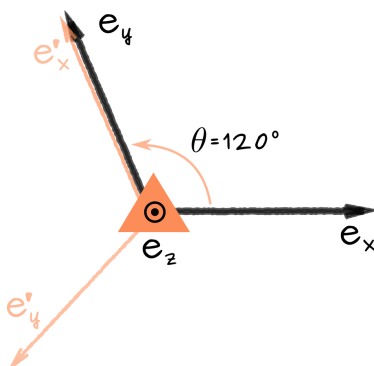


FIGURE C.2: Three-fold rotation around the third axis of a hexagonal basis set.

It is not only rotations that can be expressed in matrix form, reflections as well as any combination of reflection and rotation can be written down as matrix operations. Every possible symmetry operation a crystal holds, if it excludes translation, will be part of a finite and well determined group of 3×3 matrices. Only a subset of these matrices is really necessary to determine the entire group and these are known as *generators*. There are only 14 matrices $D^{(x)}$ that can act as generators, where (x) spans from (a) to (n) . Talking in detail about groups and space groups is beyond the purpose of this thesis, but a good introduction to crystallography for the electron microscopist can be found in *Structure of Materials; an introduction to crystallography, diffraction and symmetry* [DGM12] while an in-depth overview is given in the introduction to the *International Tables for Crystallography, Volume A* [Hit88] both of which we will reference throughout this section.

⁵ The right thumb points towards the direction line and the fingers indicate the positive rotation.

⁶ We have not explicitly shown that the hexagonal lattice is compatible with this symmetry operation but perhaps the reader will not be too suspicious of a hexagon showing three fold rotation symmetry.

C.1.2 Operation of first kind: pure translation

A pure translation is fully determined by translation vector $\mathbf{t} = u_1\mathbf{e}_1 + u_2\mathbf{e}_2 + u_3\mathbf{e}_3$. The lattice translation vector was introduced on page 20 and to it we can add the lattice centring vectors if present. The latter are useful for describing non-primitive lattices where lattice points exists not only at the corners of the crystal structure. The international symbol for translation is $t(u_1, u_2, u_3)$ as can be observed in the representation of the basis vectors given in the *Generators* list in Fig. C.7: $t(1, 0, 0)$, $t(0, 1, 0)$, $t(0, 0, 1)$.

Mathematically, a translation is just a vector addition:

$$\mathbf{r}' = \mathbf{r} + \mathbf{t}. \quad (\text{C.2})$$

However, we want to integrate this into the matrix formulation we developed for the rotation operation. To achieve this we introduce a 4D vector. By adding a trivial equation in the form of a fourth component which is just: 1 $(x_1, x_2, x_3) \rightarrow (x_1, x_2, x_3, 1)$. We also upgrade the Einstein notation to go from $i = 1$ to $i = 4$, such that Eq. C.2 becomes: $x'_i = x_i + u_i$ or in matrix form:

$$\begin{pmatrix} x'_1 \\ x'_2 \\ x'_3 \\ 1 \end{pmatrix} = \begin{pmatrix} 1 & 0 & 0 & u_1 \\ 0 & 1 & 0 & u_2 \\ 0 & 0 & 1 & u_3 \\ 0 & 0 & 0 & 1 \end{pmatrix} \begin{pmatrix} x_1 \\ x_2 \\ x_3 \\ 1 \end{pmatrix} \quad (\text{C.3})$$

The 4×4 matrix consists of the 3×3 rotation matrix $D_{ij}^{(i)}$ in the upper left corner, a 3×1 column vector containing the translation vector components on the right and a 1×4 row at the bottom, $(0 0 0 1)$, containing no useful information. We will introduce the symbol \mathcal{W} for the 4×4 matrix such that:

$$x'_i = \mathcal{W}_{ij} x_j.$$

In practice, it is more useful to denote the rotation matrix and translation vector that are implied, which is why the *Seitz symbol*, written as $(D|\mathbf{t})$, is more commonly used. For instance, the \mathcal{W} matrix in Eq. C.3 has the Seitz symbol $(E|\mathbf{t})$, where E is the identity matrix D . The \mathcal{W} matrix for a rotation plus translation is:

$$\mathcal{W} = (D|t) = \begin{pmatrix} D_{11} & D_{12} & D_{13} & u_1 \\ D_{21} & D_{22} & D_{23} & u_2 \\ D_{31} & D_{32} & D_{33} & u_3 \\ 0 & 0 & 0 & 1 \end{pmatrix}. \quad (C.4)$$

The pure rotation in Eq. C.1 has the Seitz symbol $(D^{(n)}|\mathbf{0})$ and as a 4×4 matrix becomes:

$$\mathcal{W}_\Delta = \begin{pmatrix} 0 & -1 & 0 & 0 \\ 1 & -1 & 0 & 0 \\ 0 & 0 & 1 & 0 \\ 0 & 0 & 0 & 1 \end{pmatrix}.$$

C.1.3 Operation of second kind: pure reflection

A pure reflection operation, more commonly known as a *mirror*, is characterised by the reflection plane. When it does not coincide with the plane of drawing, the mirror plane is schematically indicated by a solid line, as shown in Table C.2. The international notation for mirror plane provides also information on the orientation of the plane, usually by writing down the equation of the plane. For instance, the mirror plane parallel to (110) is written as $m(x, -x, z)$. We can find this symmetry operation at number (7) on page 584 of the *Tables*, shown in Fig. C.7.

TABLE C.2: Example of pure reflection symbols.

| Name | Graphical | Hermann-Mauguin | Schoenflies |
|--------------|-----------|-----------------|-------------|
| Mirror plane | — | m | σ |

Mirror operations can be represented by a matrix $D(m)$, which, analogous to the rotation matrix, can be determined from geometry. For the reflection operation in Fig. C.3:

$$\begin{aligned} (\mathbf{e}'_x & \mathbf{e}'_y & \mathbf{e}'_z) = (-\mathbf{e}_y & -\mathbf{e}_x & \mathbf{e}_z) \\ & = (\mathbf{e}_x & \mathbf{e}_y & \mathbf{e}_z) D(m) \end{aligned}$$

From which we find the set operation $D^{hex}(m_{(x, -x, z)}) \equiv D^{(k)}$ to be:

$$D^{(k)} = \begin{pmatrix} 0 & -1 & 0 \\ -1 & 0 & 0 \\ 0 & 0 & 1 \end{pmatrix}. \quad (C.5)$$

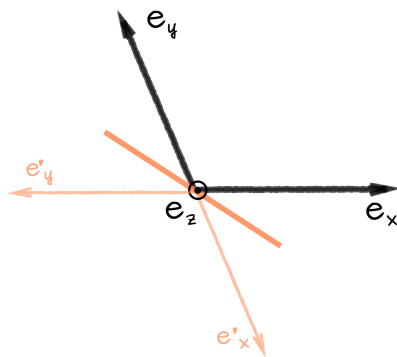


FIGURE C.3: $m(x, -x, z)$
mirror plane operation in
a hexagonal basis set.

Which, in turn, completely determines the matrix \mathcal{W}_m with Seitz symbol $(D^{(k)} | \mathbf{0})$.

C.1.4 Combination of rotation and translation

Combining translation with rotation yields a new type of symmetry operation, known as a *screw axis*. While applying a pure rotation of order n to an object we recover the original position after n successive operations, the extra translation operation in the screw axis renders this observation invalid. During a screw axis operation, the object is translated after every rotation step by a certain vector τ parallel to the rotation axis. We can see that in Fig. C.4. Input files used are `2_1PNG.ray` and `6_1PNG.ray` (see how to use them in the *Pure Rotation* subsection on page 169). For a 2_1 screw axis shown in Fig. C.4 a), after a two-fold ($2\pi/2 = 180^\circ$) rotation, the object is also translated by a vector τ from point **0** to point **1**. After $n = 2$ rotations it is translated 2τ in the direction of the screw axis to the point **2**. This position is identical to the original one except for a translation vector $m\mathbf{t}$ where \mathbf{t} is the smallest possible translation vector in the given direction and, in this case, $m = 1$. This is where the subscript $_1$ comes from in the notation 2_1 .

Generally, the notation for a screw axis is n_m where $n\tau = m\mathbf{t}$, which tells us that after n screw axis operations the original point is translated m lattice translation vectors in the direction of the screw axis. One screw axis operation involves an n -fold rotation plus a $\tau = m\mathbf{t}/n$ translation. Table C.3 shows the graphical and notation symbols for the relevant screw axis operations of the wurtzite crystal: 2_1 and 6_3 . The

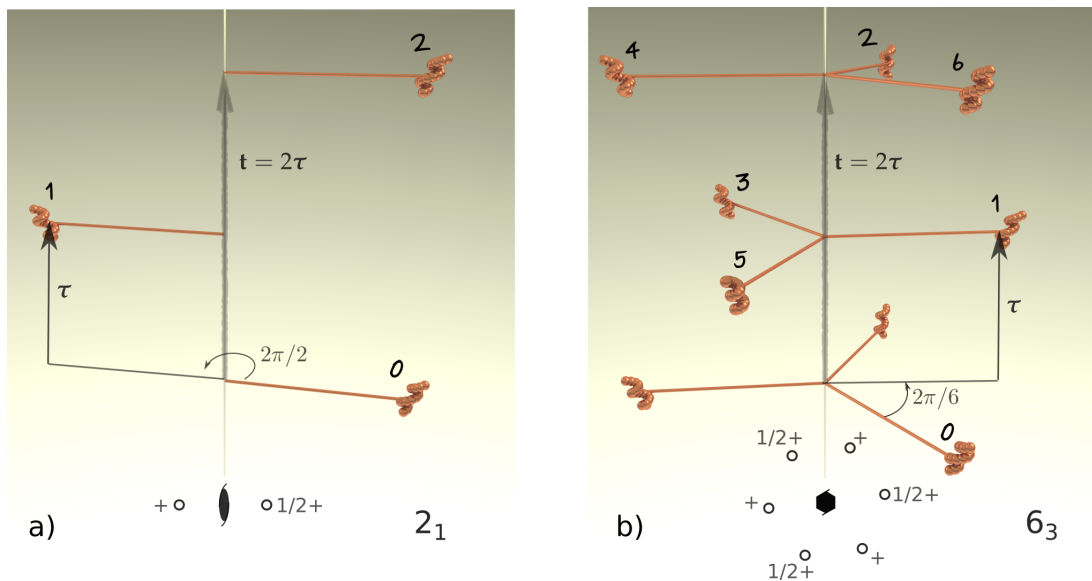


FIGURE C.4: Rendered 3D graphical representations and (sequentially numbered) operations involved in the construction of screw axis a) 2_1 and b) 6_3 . Standard 2D graphical projections are included at the bottom.

6_3 operation, shown in Fig. C.4 b), involves a $\tau = 3t/6 = t/2$ translation after each six-fold rotation, which takes the object on which it operates from point 0 to point 1 . After two 6_3 operations the object has been translated by a total vector equal to the lattice translation vector t . To obtain the next points, $3, 4$ and 6 , we must leave the unit cell in which we started. Because all unit cells must be the same, the screw rotation in the cell below dictates equivalent points in this cell corresponding to the position of points $3\text{-}6$.

The bottom of the images in Fig. C.4 contain standard graphical representation of the corresponding symmetry operations such that the axes of rotation are normal to the page. The open circles indicate that the objects are above the plane of drawing and the numbers next to the circle refer to the height of their positions.

TABLE C.3: Examples of screw axis symbols.

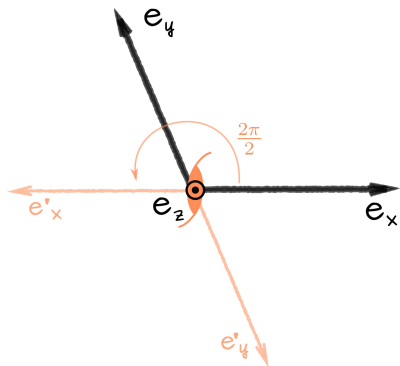
| Name | Graphical | Printed | Screw vector τ in units of t |
|---------------------|-----------|---------|-------------------------------------|
| Two-fold screw axis | ◐ | 2_1 | $1/2$ |
| Six-fold screw axis | ◑ | 6_3 | $1/2$ |

The *International Tables for Crystallography* denote the screw axis operations by the order of the rotation together with the translation vector τ : $n(\tau)$. The axis of rotation

is also added as it can be seen in the symmetry operations list on page 183. Operation (4), for instance, denotes a 2_1 screw axis around the **c**-axis in a hexagonal unit cell.

Mathematically, we can write this operation from geometry (see Fig. C.5) as:

$$\begin{aligned} (\mathbf{e}'_x & \mathbf{e}'_y & \mathbf{e}'_z) = (-\mathbf{e}_x & -\mathbf{e}_y & \mathbf{e}_z) \\ &= (\mathbf{e}_x & \mathbf{e}_y & \mathbf{e}_z) D^{(b)} \end{aligned}$$



From which we find the set operation $D^{(b)}$ to be:

$$D^{(b)} = \begin{pmatrix} -1 & 0 & 0 \\ 0 & -1 & 0 \\ 0 & 0 & 1 \end{pmatrix}. \quad (C.6)$$

FIGURE C.5: 2_1 screw axis operation in a hexagonal basis set.

Which completely determines the matrix \mathcal{W}_b with Seitz symbol $(D^{(b)} | \tau_{(0,0,1/2)})$:

$$\mathcal{W}_b = \begin{pmatrix} -1 & 0 & 0 & 0 \\ 0 & -1 & 0 & 0 \\ 0 & 0 & 1 & 1/2 \\ 0 & 0 & 0 & 1 \end{pmatrix}.$$

Now that we have written out the mathematical framework necessary for studying a number of different symmetries we can take a closer look at how to describe a crystal structure starting from the symmetry it manifests. More importantly, we want to answer the question “*What is the minimum number of symmetry operations from which a specific structure can be recovered?*”.

C.2 Point groups

It turns out maths already has the answer to that question and it can easily be applied to crystallography. If we forget for a moment about translations, then any of the remaining symmetry operators can be applied to an object and leave exactly one point invariant, namely the origin. For all the symmetry operations we talked about, the choice of the origin (a plane for reflection, an axis for rotation ...) was non-ambiguous. Another way of saying this is that all symmetry operators except translation overlap in exactly one point. All these operators can be expressed as 3×3

matrices D and carry the name of *point symmetries*. The total point symmetries of an object must also form a *group* with the properties given on page 168. If the object under consideration is a crystal structure, then those symmetry operations are selected such that they are compatible with the translational periodicity of its lattice. Starting, then, from a *point* one can derive 32 sets of consistent symmetry operations compatible with the Bravais lattices also known as crystallographic point groups (see Chapter 9 in [DGM12]).

Groups have several useful properties, including the fact that one can generate all elements of a group starting with a list of operations and constructing a multiplication table. The minimum symmetry operations needed to construct a full point group is known as a set of *generators*. There are only 14 total generators, a subset of which will produce any possible crystal symmetry. We have encountered three of them so far, denoted as $D^{(b)}$, $D^{(k)}$ and $D^{(n)}$. The matrices $D^{(i)}$ form the set of generators where (i) can go from (a) to (n) , $D^{(a)}$ being the identity matrix, which, as previously discussed, describes the symmetry of all systems and is always implied.

We keep on following the Hermann-Mauguin and Schoenflies notations for crystallographic point groups, with the latter shown in brackets. The Hermann-Mauguin notation for point groups has a maximum of three symbols, each corresponding to a particular direction in the Bravais lattice. Since the choice of origin is very specific when we consider the possible symmetries a crystal would exhibit, the possible axes of symmetry for a given crystal will be the directions used to describe the point group of a particular system.

Table C.4 shows the three directions for the three possible set of symbols describing the point group of a hexagonal crystal system. For instance, we can consider a group made up of only the identity operation and all powers⁷ of the rotation operator, we talked about rotation operations on page 168. The notation of this simple group will follow the notation of the operators, therefore, a six-fold rotational point group (also known as cyclic) is 6 or C_6 (C for cyclic).⁸ If a hexagonal crystal is known to be part of the crystallographic point group 6 then we can conclude it has six-fold rotational symmetry and can read from Table C.4 that the rotation axis must be [0 0 .1].

Now that we set the rules with the simplest of examples let's take a look at something a bit more involved. (1) *What happens if we combine the proper rotation group with reflection operations? and (2) How do we generate the full symmetry of such a group?*

⁷ An operator to power 2 simply means applying that operator twice in succession.

⁸ Note that we use the Sans Serif font for operators symbols and the Bold font for group notation.

TABLE C.4: Primary, secondary and tertiary symmetry directions (Miller-Bravais) for the hexagonal crystal.

| Crystal system | Primary $[u v . w]$ | Secondary $[u v . w]$ | Tertiary $[u v . w]$ |
|----------------|---------------------|-----------------------|----------------------|
| Hexagonal | $[0 0 . 1]$ | $\{1 0 . 0\}$ | $\{1 2 . 0\}$ |

C.2.1 6mm point group from generators

If we give a mirror plane (m) a six-fold rotation axis (6) then we end up with the point group shown in Fig. C.6. Notice the change of handedness (chirality) of the orange object as an indication of the reflection symmetry. The generating file is `6mm.PNG.ray`. It turns out that, for even rotation orders, an extra mirror symmetry appears. One can easily see that in the stereographic projection at the bottom of the image. Every second mirror is not generated by the rotation operation, however the structure clearly displays the extra reflections. This is why the group **6mm** has two ‘m’s in its notation. From Table C.4 we can read that the first set of mirrors have the normals $\{10.0\}$ while the second set of mirrors have the normals $\{12.0\}$. Similarly, the v in the Schoenflies notation C_{6v} indicates the vertical orientation of the mirror planes.

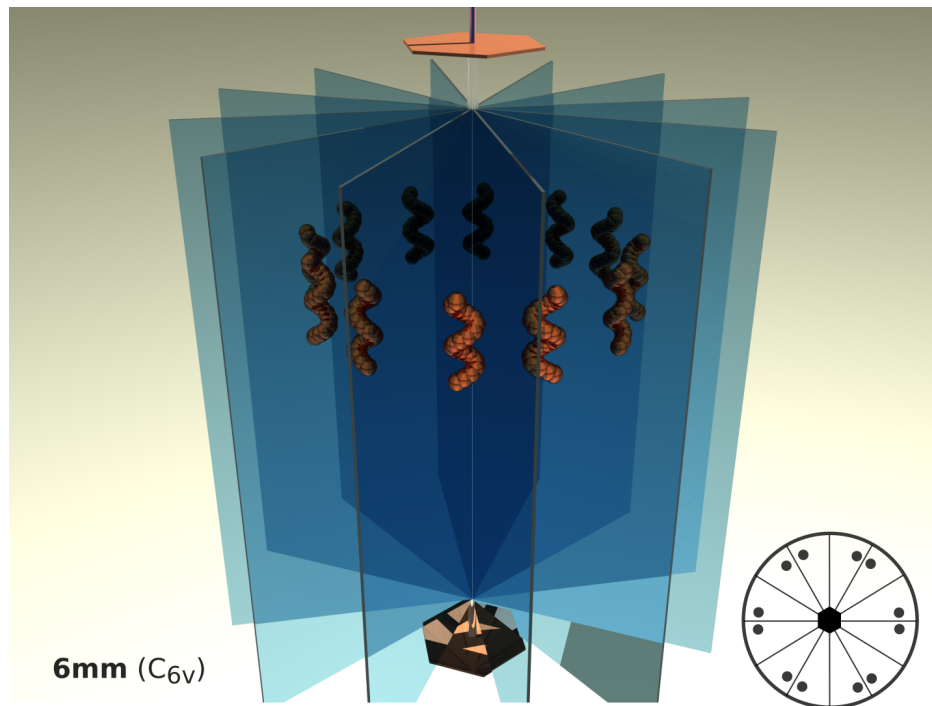


FIGURE C.6: Graphical 3D representation of **6mm** point group together with its stereographic projection in the bottom corner right.

The generators matrices of **6mm** point group are: $D^{(a)}$, $D^{(b)}$, $D^{(k)}$, $D^{(n)}$; where we denoted the identity operator with the label $D^{(a)}$. Conveniently, we have already derived the three 3×3 matrices corresponding to the last three of these operators: $D^{(b)}$ (Eq. C.6), $D^{(k)}$ (Eq. C.5), $D^{(n)}$ (Eq. C.1). We can find these matrices in the *International Tables for Crystallography, Volume A* [Hit88] in the *Generators* list of the space group (pages 584-585 shown here on page 183) as operations (1), (2), (4), (7). In order to find the full list of symmetry operators of the space group, we can read the *Symmetry operations* section from the *Tables* or we can multiply the generators among themselves until we find the full list of 12. We'll show here the hard way for the reader to use as a reference but also to somewhat demystify the origin of these matrices.

Before that we want to add a few notes on point group characteristics. The number 12 represents the size of the set of points in this group which have equivalent position. That is to say, if we start with an arbitrary position (x, y, z) how many new positions are generated when the full set of symmetry operations are applied. This is also known as the *order* of the group. We can then say that the **6mm** point group has order 12. Another point group property is that of *centrosymmetry*. If we define polarity as the property of a group in which directions \mathbf{t} and $-\mathbf{t}$ are not related to each other by any symmetry operation, then we can note that this group is only polar along the rotation axis. We can also conclude that this point group is not centrosymmetric.

To find the full symmetry of a point group starting with the list of generator matrices, we multiply each operator with itself and the others, remembering that matrix multiplication is not commutative. For every resulting matrix that is not the identity matrix we check if we already have it in the set. If not then we can add it and start the matrix multiplications again. When we did all the possible operations in a set without finding any new matrices we can stop looking and declare we found the full symmetry operations group. The *Python* style pseudocode for this is shown below in Algorithm 1. This function is implemented in the Jupyter notebook `Symmetry_matrices.ipynb`.

Using this implementation⁹ we find the following 12 symmetry matrices of the

⁹ Luckily, there is a good selection of mature or novel open software available to do these type of computations as well. Here are a few examples:

- GAP - provides an extensive computational group theory algebra library and tools.
- Mantid - available as a *Python* package, can handle crystallographic point and space group maths.
- spglib - another *Python* package, can do symmetry computations.
- EMsoft - the routine `CalcPositions` in the module `symmetry.f90` should do a generalised version of the implementation shown here.

```

def findSymMat(knownMat, *newMat):
    input : List of  $3 \times 3$  generator matrices
    output: Entire list of symmetry operators as  $3 \times 3$  matrices
    while still finding new matrices do
        for matrix_i in newMat do
            for matrix_j in knownMat do
                isThisNew = matrix_i  $\times$  matrix_j
                if isThisNew is not Identity Matrix and is not in knownMat then
                    add isThisNew to newMat
                    add isThisNew to knownMat
                else
                    | stop looking
                end
            end
        end
        if new matrix is found then
            | findSymMat (knownMat, newMat)
        end
    end
end

```

ALGORITHM 1: Recursive function to find the symmetry matrices of a space group starting from the list of generators.

6mm point group: $D^{(a)}$, $D^{(b)}$, $D^{(k)}$, $D^{(n)}$, $D^{(nn)}$, $D^{(nb)}$, $D^{(nk)}$, $D^{(kn)}$, $D^{(kb)}$, $D^{(b nk)}$, $D^{(n kk)}$, $D^{(k nk)}$ (not necessary in the same order as in the *Tables*). Here we used the notation: $D^{(nb)} = D^{(n)} \times D^{(b)}$ to represent a combination of operations applied in a specific order. For instance, $D^{(nn)}$ is a 3-fold rotation applied twice and it should come as no surprise that a 3-fold rotation applied three times is the identity operator: $D^{(nnn)} = D^{(a)}$. Similarly, $D^{(kk)}$ is a double reflection and, again, equals to the identity operator.

The equivalent positions in the space group can then be easily determined by simply applying these operators to a general position (x, y, z) .

C.3 Space groups

So far we have explored some possible symmetries of a system (motif) that are compatible with the hexagonal Bravais lattice of a crystal structure. It is time to add these

point group symmetries to the crystal lattice points and observe what new symmetries emerge. This simply involves combining the point group operators with the Bravais lattice translational vectors of a given crystal system. Every time this combination yields a new unique system then we can talk about a different symmetry group this time known as a *space group*.

There are 230 three dimensional space groups which might sound like a formidable result when we considered that we only combine 32 point groups with 14 Bravais lattices. However, bear in mind that there are more than one way of adding the point group symmetries at the lattice points. Additionally, combining symmetry operation can yield extra symmetries, just like the extra mirror planes “popped up” in the 6mm point group. Screw axes and glide planes¹⁰ are symmetry operators containing a translation vector and therefore not forming point groups. However, when used to point group symmetries, in combination with Bravais lattices, these operators will form new space groups.

The space group symbol is formed by combining the centring information of the Bravais lattice with the point group Hermann-Mauguin notation symbol. The information about the symmetry of the crystal system can be dropped since it will be implied in the point group symmetry. One can predict extra symmetry operations describing a unique space group by replacing one or more operations in the Hermann-Mauguin point group notation with a screw rotation or glide plane. It is entirely possible to end up with a situation in which the point group of a space group contains operations which do not occur in the space group at all.

Depending on whether or not the space group contains any glide planes or screw axis symmetry operations we differentiate between *non-symmorphic* and *symmorphic* space groups. Symmorphic space groups contain then only the point group operations and are easy to spot from their Hermann-Mauguin symbols.

C.3.1 The International Tables for Crystallography, Volume A

The series of volumes constituting the *International Tables for Crystallography* are a comprehensive database of crystallographic information relevant in the studies of the structure or properties of materials. *Volume A* [Hit88], specifically tackles the space groups. We have already referenced a few times to a specific page in *Volume A* which shows all the information needed for the study of the space group symmetry **P6₃mc**

¹⁰ We haven't explicitly talked about glide planes, but these are symmetry operations obtained by combining a mirror plane with translation over half the lattice vector parallel to the mirror plane. The symbol for a glide plane is *a*, *b* or *c* if the glide vector is $\mathbf{a}/2$, $\mathbf{b}/2$ or $\mathbf{c}/2$, respectively.

in tabulated form. It is a useful skill for a crystallographer to be able to read these pages.

- The top of the page holds the crystal system (hexagonal), the Patterson symmetry definition¹¹, the point group symmetry (6mm), the Schoenflies symbol (C_{6v}^4), the complete space group symbol ($P6_3mc$), the space group shorthand symbol **P6₃mc** and the space group number (186).
- Below, there is a drawing of the relative positions of the symmetry elements in the group, projected along the main direction (**c**), on the right. On the left, the equivalent positions are shown in the same projection.
- While the *Origin* of the group can be chosen arbitrarily, it is customary to choose the position with the highest symmetry of the group; here 6_3mc ¹². The symmetry is given in the usual point group notation following the system's symmetry directions (seen in Table C.4). To clarify the ambiguity a second set of symmetries is given $3m1$, where the 1 is a place-holder for no more than identity symmetry for this direction, to establish the origin in the upper left corner of the unit cell.
- The *Asymmetric unit* is the smallest volume of the unit cell that will completely and exactly fill the space when the group's symmetry operators are applied to it. It is defined in terms of the sides and vertices containing the volume, which in turn are the result of the intersecting symmetry planes bounding the cell. The volume of the asymmetric cell has the property of being the volume of the full unit cell divided by the product of the order of the point group, n , (for 6mm $n = 12$) and the number of centring operations plus one. For **P6₃mc** then, the volume of the asymmetric cell is $V_a = V/(12 \times 1) = V/12$.
- Below, the full list of *Symmetry operations* together with their positions is given and we have already shown how to read some of these operations. There are a total of 12 symmetry operators including the identity operator.
- From these operators only 4 make it to the list of *Generators*, (1), (2), (4), and (7), together with the basis translation vectors. Starting with these list of 4 operators the full previous list can be generated by matrix multiplication.

¹¹ The Patterson function is a mathematical construct of higher symmetry than the electron density function which it replaces in order to solve the phase problem in X-ray crystallography.

¹² Note that, while the notation is point group like, the origin position symmetries do not need to form a group and we do not keep the point group symbol notation.

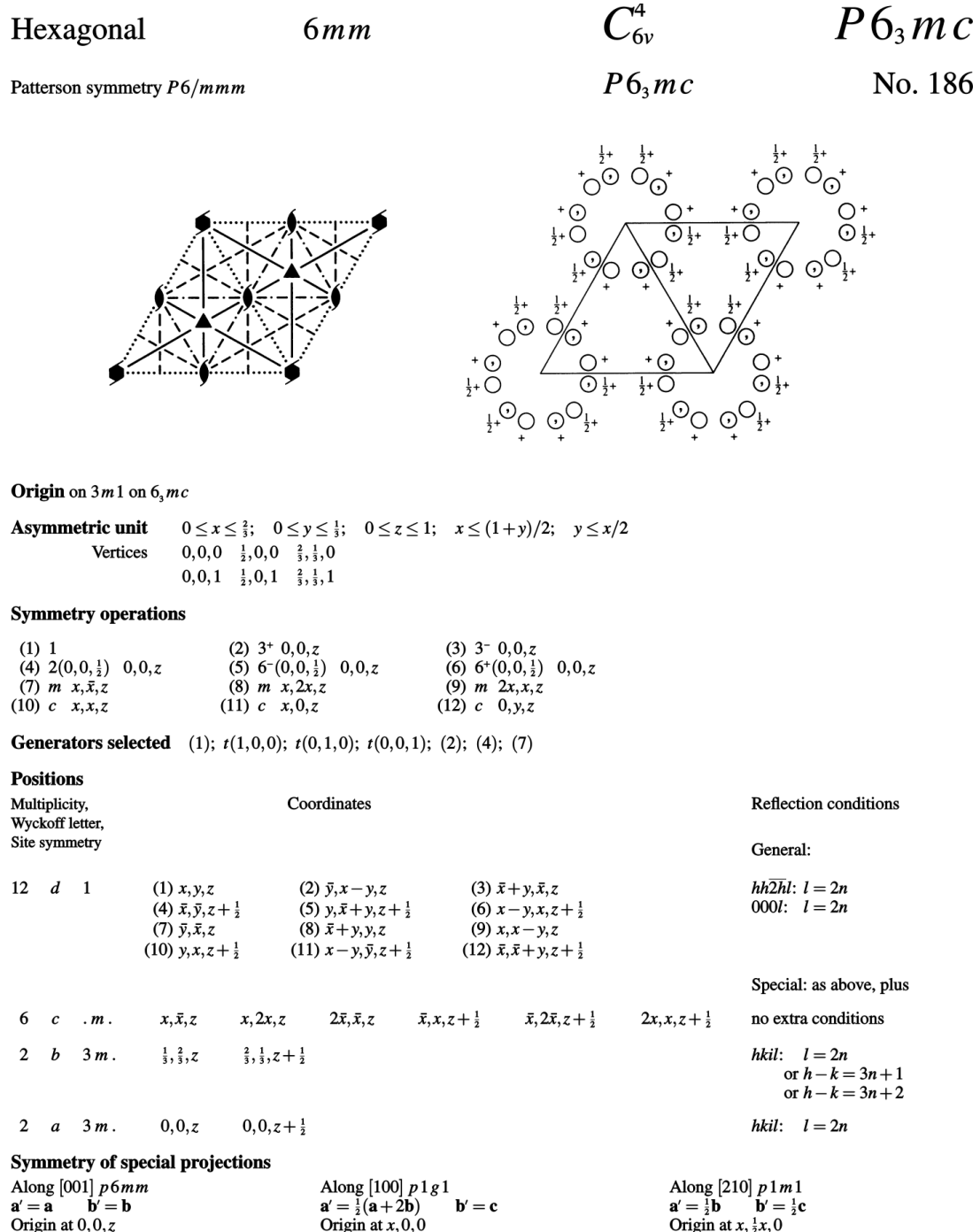


FIGURE C.7: Pages 584-585 (compressed here) of *International Tables for Crystallography, Volume A* [Hit88] describing the space group $P6_3mc$.

- The *Position* tables contain the symmetrically equivalent points in the crystal system divided between the general positions in the first block followed by the special positions blocks underneath. The general position is left invariant by the identity operator but no other symmetry operation of the space group, while the special positions are left invariant by at least one other symmetry operation in addition to the identity. All the symmetry operations that map a point onto itself form together a *site symmetry* group for that position given in the third column of the table. The coordinates for the general position, $(i)x', y', z'$, are the result of a symmetry operation (i) on the most general position x, y, z . These can also be viewed as a shorthand notation of the symmetry matrices of the group. The numbers in the first column indicate the number of equivalent points per unit cell or the *multiplicity* of the position. For the general position the multiplicity is the number of symmetry operators, while for the special positions each added site symmetry reduces the multiplicity by the order of symmetry. For instance, the second positions entry shows a mirror site symmetry which halves the multiplicity of the point to 6. The *Wyckoff letters* are labels for the Wyckoff positions, which in turn are a way of describing the positions of the atoms in the asymmetric unit. The last column in this table, entitled *reflection conditions*, is a list of diffraction information given as requirements for the structure factor to not be zero (conditions of occurrence) for the given position.
- The last section shown here is the *Symmetry of special projections* which contains two dimensional projection information of the unit cell along lattice directions. If the wurtzite unit cell is projected along the $[1\ 0\ 0]$ direction, then the resulting 2D object will have **p6mm** plane group symmetry and will be defined by the unit vectors \mathbf{a}' and \mathbf{b}' which in general are expected to be fractions of linear combinations of the original basis vectors. The origin of the 2D unit cell is also specified.

An account of crystal symmetry would be incomplete without referencing the *International Tables for Crystallography*. Now that we know how to read the *Tables* we can just read out the results of many of the derivations we have done in this Appendix.

D TD strain tensor with surface relaxation

The strain tensor of a semi-infinite threading dislocation normal to a surface, ϵ_{ij} , is shown below as contour plots for each strain tensor component. I'm showing these images in the strain tensor matrix form:

$$\epsilon_{ij} = \begin{pmatrix} \epsilon_{11} & \epsilon_{12} & \epsilon_{13} \\ \epsilon_{21} & \epsilon_{22} & \epsilon_{23} \\ \epsilon_{31} & \epsilon_{32} & \epsilon_{33} \end{pmatrix}.$$

Where the dislocation line is along z or index 3 in this notation. The elastic strain has the following property : $\epsilon_{ij} = \epsilon_{ji}$ making these matrices symmetric with respect to their diagonal, which is why there are only maximum 6 plots per image, *i.e.*, diagonal terms plus 3. Fig. D.1 shows the top view of strain components as contour plots for a screw threading dislocation and Fig. D.2 for an edge TD.

The colour map for all the plots in a matrix has the same limits for comparison. The ϵ_{31} and ϵ_{32} are the biggest components for the screw TD (Fig. D.1). This is perhaps not very easy to see because I choose I narrow colour range in order to pull out some features in the other images but it did mean, unfortunately that the peak in values in ϵ_{31} and ϵ_{32} is outside the colour range and shown here as white. Another way to read this matrix is to say that most of the strain of the screw threading dislocation in a semi-infinite medium is the shear strain normal to the plane xy. Nothing new so far.

Similarly, for the edge TD, shown in an identical manner in Fig. D.2, where I choose better colour map limits, the main components are ϵ_{11} , ϵ_{12} , ϵ_{22} , *i.e.*, all the strain contained entirely in the plane xy.

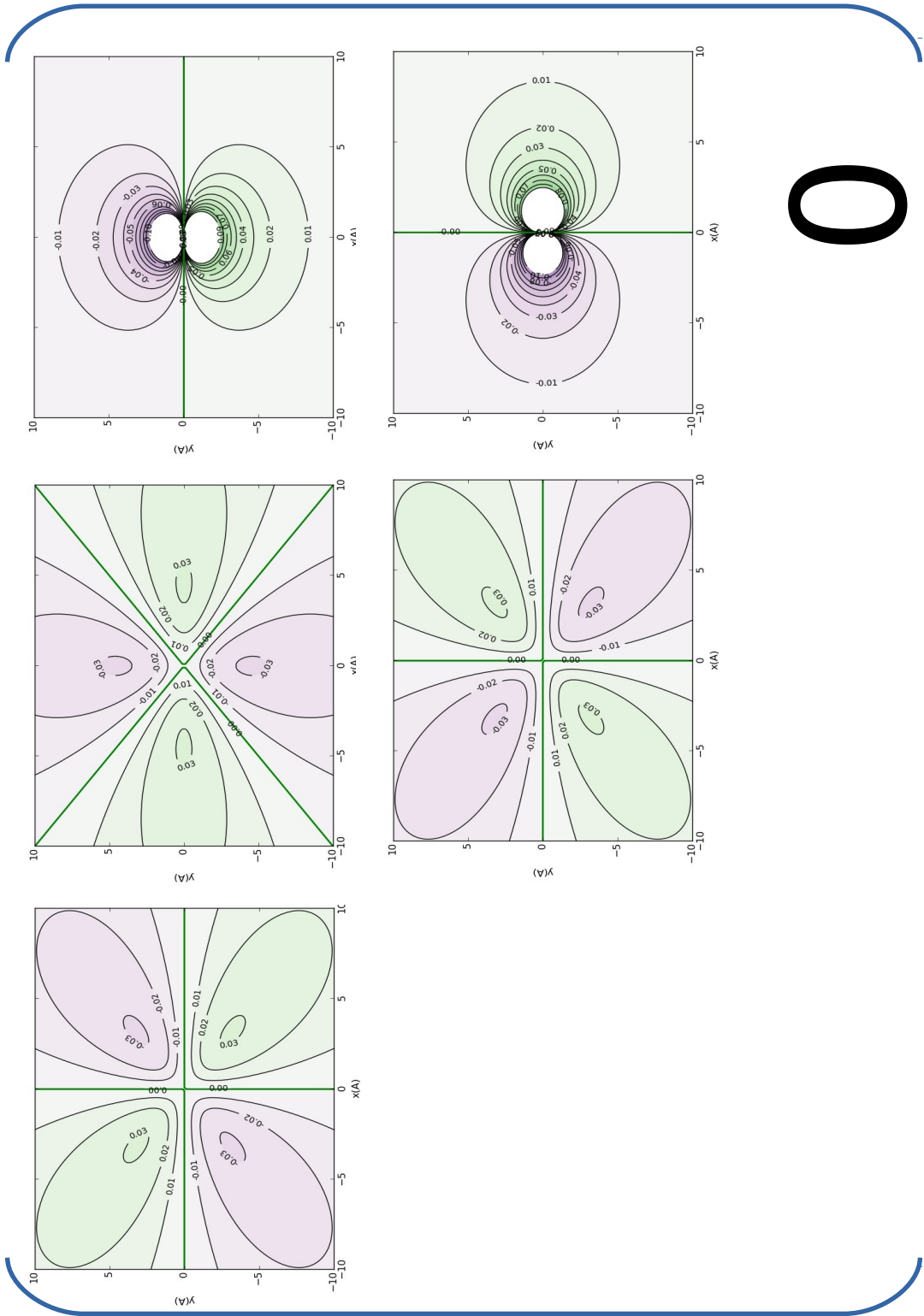


FIGURE D.1: Strain field tensor components of a screw TD in GaN normal to a surface as contour plots. The strain is plotted on a $10 \times 10 \text{ \AA}$ plane centred on the dislocation and 2 \AA below the surface.

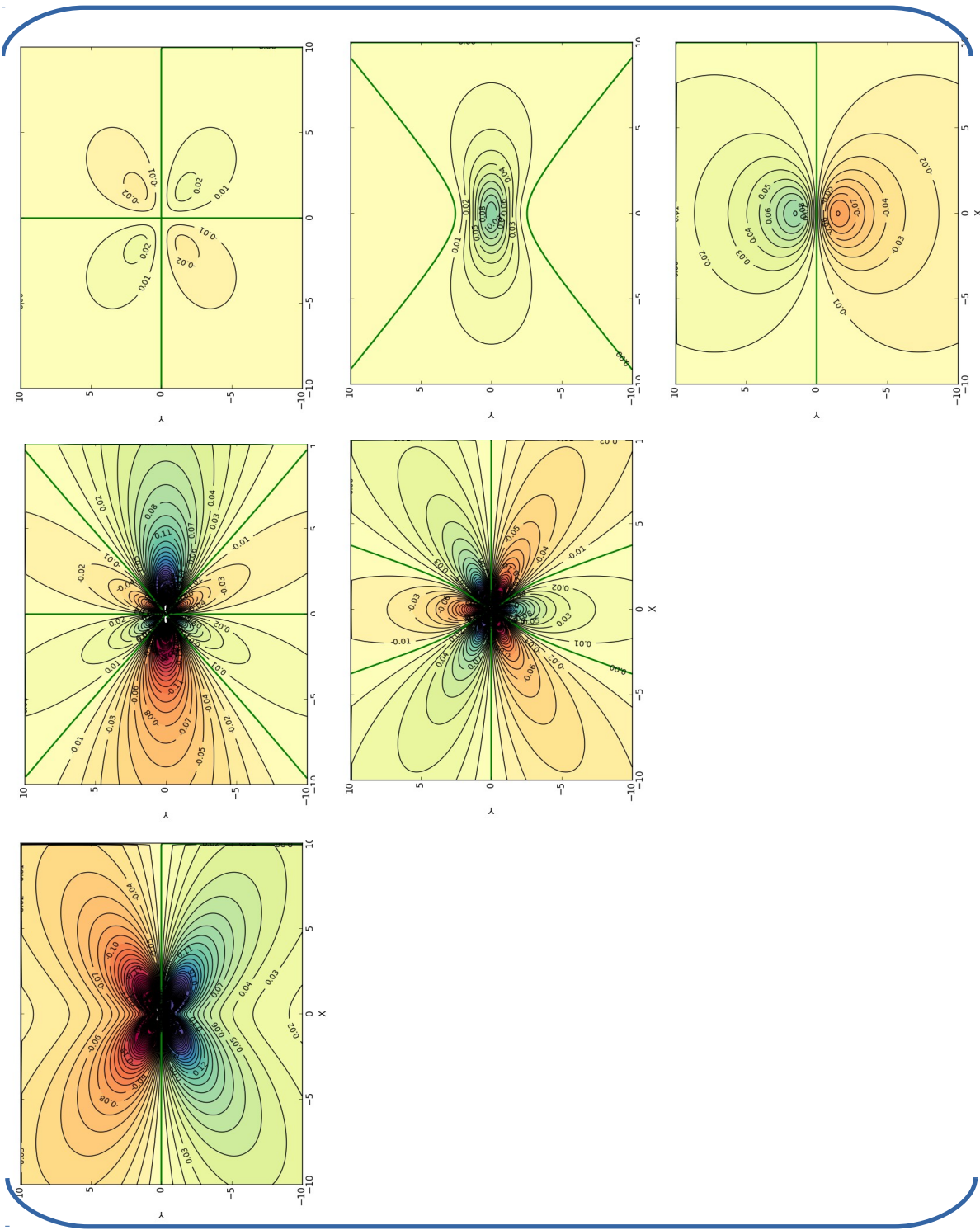


FIGURE D.2: Strain field tensor components of an edge TD in GaN normal to a surface as contour plots. The strain is plotted on a 10×10 Å plane centred on the dislocation and 2 Å below the surface.

Bibliography

- [Amb98] O. Ambacher. "Growth and applications of group III-nitrides". In: *Journal of Physics D: Applied Physics* 31.20 (1998), p. 2653.
- [Ana] Continuum Analytics. *Anaconda: Completely Free Enterprise-Ready Python Distribution for Large-Scale Data Processing, Predictive Analytics, and Scientific Computing*. URL: <https://www.anaconda.com/>.
- [And14] J. U. Andersen. *Notes on Channeling*. University of Aarhus, 2014.
- [Ard38] M. von Ardenne. "The Electron Scanning Microscope". In: *Journal of Physics* 109.9-10 (1938), pp. 553–572.
- [Art48] K. Artmann. "On the theory of the Kikuchi Bands". In: *Journal of Physics* 125.4-6 (1948), pp. 225–249.
- [Ass+99] W. Assmann, H. Huber, S. A. Karamian, F. Grüner, H. D. Mieskes, J. U. Andersen, M. Posselt, and B. Schmidt. "Transverse Cooling or Heating of Channeled Ions by Electron Capture and Loss". In: *Physical Review Letters* 83.9 (1999), p. 1759.
- [Aut06] A. Authier. "Dynamical theory of X-ray diffraction". In: *International Tables for Crystallography Volume B: Reciprocal space*. Springer, 2006.
- [BB13] W. H. Bragg and B.A. WL. Bragg. "The reflection of X-rays by crystals". In: *Proceedings of the Royal Society of London A* 88.605 (1913), pp. 428–438.
- [BE12] D. C. Bell and N. Erdman. *Low voltage electron microscopy: Principles and applications*. John Wiley & Sons, 2012.
- [Bet28] H. Bethe. "Theory on the diffraction of electrons in crystals". In: *Annalen der Physik* 392.17 (1928), pp. 55–129.
- [Boe37] H. Boersch. "About bands in electron diffraction". In: *Physikalische Zeitschrift* 38 (1937), pp. 1000–1004.
- [Boo+67] G. R. Booker, A. M. B. Shaw, M. J. Whelan, and P. B. Hirsch. "Some comments on the interpretation of the 'Kikuchi-like reflection patterns' observed by scanning electron microscopy". In: *Philosophical Magazine* 16.144 (1967), pp. 1185–1191.

- [Bou+05] Z. Bougrioua, M. Azize, P. Lorenzini, M. Laügt, and H. Haas. "Some benefits of Fe doped less dislocated GaN templates for AlGaN/GaN HEMTs grown by MOVPE". In: *Physica Status Solidi (a)* 202.4 (2005), pp. 536–544.
- [Bra68] W. Brandt. "Channeling in crystals". In: *Scientific American* 218.3 (1968), pp. 90–101.
- [Bri+16] T. B. Britton, J. Jiang, Y. Guo, A. Vilalta-Clemente, D. Wallis, L. N. Hansen, A. Winkelmann, and A. J. Wilkinson. "Tutorial: Crystal orientations and EBSD—Or which way is up?" In: *Materials Characterization* 117 (2016), pp. 113–126.
- [BS71] D. M. Barnett and L. A. Swasper. "The elastic energy of a straight dislocation in an infinite anisotropic elastic medium". In: *physica status solidi (b)* 48.1 (1971), pp. 419–428.
- [Bun82] H. J. Bunge. *Texture analysis in materials science: mathematical methods*. Butterworths, 1982.
- [BWV10] A. Barnoush, M. T. Welsch, and H. Vehoff. "Correlation between dislocation density and pop-in phenomena in aluminum studied by nanoin-dentation and electron channeling contrast imaging". In: *Scripta Materialia* 63.5 (2010), pp. 465–468.
- [Cas45] H. Casimir. "On Onsager's principle of microscopic reversibility". In: *Reviews of Modern Physics* 17.2-3 (1945), p. 343.
- [CDG13] P.G. Callahan and M. De Graef. "Dynamical EBSD Patterns Part I: Pattern Simulations". In: *Microscopy and MicroAnalysis* 19 (2013), pp. 1255–1265.
- [CG84] D. Chescoe and P. J. Goodhew. *The operation of the transmission electron microscope*. Oxford Univ. London, New York, etc.: Press & Royal Microscopical Soc, 1984.
- [CH71] D. R. Clarke and A. Howie. "Calculations of lattice defect images for scanning electron microscopy". In: *Philosophical Magazine* 24.190 (1971), pp. 959–971.
- [Cha70] L. T. Chadderton. "Diffraction and channeling". In: *Journal of Applied Crystallography* 3.6 (1970), pp. 429–465.
- [CM57] J. M. Cowley and A. F. Moodie. "The scattering of electrons by atoms and crystals. I. A new theoretical approach". In: *Acta Crystallographica* 10.10 (1957), pp. 609–619.

- [CMD18] L. Cheng, Y. Ming, and Z. J. Ding. “Bohmian trajectory-bloch wave approach to dynamical simulation of electron diffraction in crystal”. In: *New Journal of Physics* 20.11 (2018), p. 113004.
- [Coa67] D. G. Coates. “Kikuchi-like reflection patterns obtained with the scanning electron microscope”. In: *Philosophical Magazine* 16.144 (1967), pp. 1179–1184.
- [Cow+06] J. M. Cowley, P. Goodman, B. K. Vainshtein, B. B. Zvyagin, and D. L. Dorset. “Electron diffraction and electron microscopy in structure determination”. In: *International Tables for Crystallography Volume B: Reciprocal space*. Springer, 2006, pp. 276–345.
- [Cra+02] M. D. Craven, S. H. Lim, F. Wu, J. S. Speck, and S. P. DenBaars. “Structural characterization of nonpolar (1120) a-plane GaN thin films grown on (1102) r-plane sapphire”. In: *Applied Physics Letters* 81.3 (2002), pp. 469–471.
- [Cri06] M. A. Crimp. “Scanning electron microscopy imaging of dislocations in bulk materials, using electron channeling contrast”. In: *Microscopy Research and Technique* 69.5 (2006), pp. 374–381.
- [CSN01] M. A. Crimp, B. A. Simkin, and B. C. Ng. “Demonstration of the $g \cdot b \times u = 0$ edge dislocation invisibility criterion for electron channelling contrast imaging”. In: *Philosophical Magazine Letters* 81.12 (2001), pp. 833–837.
- [Cul19] Google Arts & Culture. *A scientific controversy*. 2019. URL: <https://arts.google.com/arts/QBqHqRLUMAKH2GDD6>.
- [Cze+90] J. T. Czernuszka, N. J. Long, E. D. Boyes, and P. B. Hirsch. “Imaging of dislocations using backscattered electrons in a scanning electron microscope”. In: *Philosophical Magazine Letters* 62.4 (1990), pp. 227–232.
- [Dar14] C. G. Darwin. “The theory of X-ray reflexion”. In: *The London, Edinburgh, and Dublin Philosophical Magazine and Journal of Science* 27.158 (1914), pp. 315–333.
- [Dar22] C. G. Darwin. “XCII. The reflexion of X-rays from imperfect crystals”. In: *The London, Edinburgh, and Dublin Philosophical Magazine and Journal of Science* 43.257 (1922), pp. 800–829.
- [Dav73] P. B. Davenport. “Rotation about nonorthogonal axes”. In: *American Institute of Aeronautics and Astronautics* 11.6 (1973), pp. 853–857.

- [Dav83] J.A. Davies. "The channeling phenomenon-and some of its applications". In: *Physica Scripta* 28.3 (1983), p. 294.
- [Dea+68] G. Dearnaley, I. V. Mitchell, R. S. Nelson, B. W. Farmery, and M. W. Thompson. "Proton channelling through thin crystals". In: *Philosophical Magazine* 18.155 (1968), pp. 985–1016.
- [Den17] D. C. Dennett. *From bacteria to Bach and back: The evolution of minds*. WW Norton & Company, 2017.
- [DG03] M. De Graef. *Introduction to transmission electron microscopy*. Cambridge university Press, New York, 2003.
- [DG08] M. De Graef. *Teaching crystallographic and magnetic point group symmetry using three-dimensional rendered visualizations*. International Union of Crystallography. 2008.
- [DG27] C. Davisson and L. H. Germer. "Diffraction of electrons by a crystal of nickel". In: *Physical Review* 30.6 (1927), p. 705.
- [DG98] M. De Graef. "A novel way to represent the 32 crystallographic point groups". In: *Journal of Matterials Education* 20 (1998), pp. 31–42.
- [DGG13] M. De Graef and Research Group. *EMsoft*. Carnegie Mellon University, 2013-2017. URL: <https://github.com/marcdegraef/EMsoft>.
- [DGG14] M. De Graef and Research Group. *3Drotations*. Carnegie Mellon University, 2014-2017. URL: <https://github.com/marcdegraef/3Drotations>.
- [DGM12] M. De Graef and M. E. McHenry. *Structure of Materials; an introduction to crystallography, diffraction and symmetry*. 2nd ed. Cambridge University Press, 2012.
- [DHE08] Andrew Deal, Tejpal Hooghan, and Alwyn Eades. "Energy-filtered electron backscatter diffraction". In: *Ultramicroscopy* 108.2 (2008), pp. 116–125.
- [Dro+07] D. Drouin, A. R. Couture, D. Joly, X. Tastet, Vincent Aimez, and Raynald Gauvin. "CASINO V2. 42—a fast and easy-to-use modeling tool for scanning electron microscopy and microanalysis users". In: *Scanning: The Journal of Scanning Microscopies* 29.3 (2007), pp. 92–101.
- [DSB06] D. W. DiSanto, H. F. Sun, and C. R. Bolognesi. "Ozone passivation of slow transient current collapse in AlGaN/ GaN field-effect transistors: The role of threading dislocations and the passivation mechanism". In: *Applied Physics Letters* 88.1 (2006), p. 013504.

- [DT68] P. A. Doyle and P. S. Turner. "Relativistic Hartree-Fock X-ray and electron scattering factors". In: *Acta Crystallographica* 24 (1968), pp. 390–397.
- [DW+85] P. M. De Wolff, N. V. Belov, E. F. Bertaut, M. J. Buerger, J. D. H. Donnay, W. Fischer, Th. Hahn, V. A. Koptsik, A. L. Mackay, H. Wondratschek, et al. "Nomenclature for crystal families, Bravais-lattice types and arithmetic classes. Report of the International Union of Crystallography Ad-Hoc Committee on the Nomenclature of Symmetry". In: *Acta Crystallographica Section A* 41.3 (1985), pp. 278–280.
- [EM11] P. R. Edwards and R. W. Martin. "Cathodoluminescence nano-characterization of semiconductors". In: *Semiconductor Science and Technology* 26.6 (2011), p. 064005.
- [ES51] J. D. Eshelby and A. N. Stroh. "CXL. Dislocations in thin plates". In: *The London, Edinburgh, and Dublin Philosophical Magazine and Journal of Science* 42.335 (1951), pp. 1401–1405.
- [ET60] T. E. Everhart and R. F. M. Thornley. "Wide-band detector for micro-microampere low-energy electron currents". In: *Journal of scientific instruments* 37.7 (1960), p. 246.
- [Fer+07] M. S. Ferdous, X. Wang, M. N. Fairchild, and S. D. Hersee. "Effect of threading defects on InGaN/GaN multiple quantum well light emitting diodes". In: *Applied Physics Letters* 91 (2007), p. 231107.
- [For11] B. D. Forbes. "Thermal diffuse scattering in transmission electron microscopy". In: *Ultramicroscopy* 111 (2011), pp. 1670–1680.
- [Fra+88] R. E. Franklin, E. C. G. Kirk, J. R. A. Cleaver, and H. Ahmed. "Channelling ion image contrast and sputtering in gold specimens observed in a high-resolution scanning ion microscope". In: *Journal of Materials Science Letters* 7.1 (1988), pp. 39–41.
- [Fra65] F. C. Frank. "On Miller-Bravais Indices and four-dimensional Vectors". In: *Acta Crystallographica* 18 (1965), pp. 862–866.
- [GBA66] R. Gevers, H. Blank, and S. Amelinckx. "Extension of the Howie-Whelan Equations for Electron Diffraction to Non-Centro Symmetrical Crystals". In: *physica status solidi (b)* 13.2 (1966), pp. 449–465.
- [GH88] P. J. Goodhew and F. J. Humphreys. *Electron microscopy and analysis*. 2nd ed. Taylor and Francis, 1988.

- [Gol+01] Y. Goldberg, M. E. Levinshtein, S. L. Rumyantsev, and M. S. Shur. "Properties of Advanced Semiconductor Materials GaN, AlN, InN, BN, SiC, SiGe". In: John Wiley & Sons, Inc., New York, 2001. Chap. Aluminum nitride, pp. 31–47.
- [GP99] H. X. Gao and L. M. Peng. "Parametrization of the temperature dependence of the Debye-Waller factor". In: *Acta Crystallographica A*.55 (1999), pp. 926–932.
- [Gra+05] D. M. Graham, A. Soltani-Vala, M. J. Dawson, T. M. Godfrey, J. S. Smeeton, M. J. Barnard, C. J. Kappers, Humphreys, and E. J. Thrush. "Optical and microstructural studies of InGaN/GaN single-quantum-well structures". In: *Journal of Applied Physics* 97 (2005), p. 103508.
- [GUZR09] I. Gutierrez-Urrutia, S. Zaefferer, and D. Raabe. "Electron channeling contrast imaging of twins and dislocations in twinning-induced plasticity steels under controlled diffraction conditions in a scanning electron microscope". In: *Scripta Materialia* 61.7 (2009), pp. 737–740.
- [Hei+00] H. Heinke, V. Kirchner, S. Einfeldt, and D. Hommel. "X-ray diffraction analysis of the defect structure in epitaxial GaN". In: *Applied Physics Letters* 77.14 (2000), pp. 2145–2147.
- [Her12] Erma Hermens. *On the trail of Bosch and Bruegel: four paintings united under cross-examination*. Archetype Publications, 2012.
- [HHW60] P. B. Hirsch, A. Howie, and M. J. Whelan. "A kinematical theory of diffraction contrast of electrons transmission microscope images of dislocations and other defects". In: *Philosophical Transactions A* 252 (1960), pp. 499–529.
- [Hin+00] T. Hino, S. Tomiya, T. Miyajima, K. Yanashima, S. Hashimoto, and M. Ikeda. "Characterization of threading dislocations in GaN epitaxial layers". In: *Applied Physics Letters* 76.23 (2000), pp. 3421–3423.
- [Hin85] A. C Hindmarsh. "Current methods for large stiff ODE systems". In: *Numerical Mathematics and Applications*. 1985, pp. 135–144.
- [Hir+65] P. B. Hirsch, A. Howie, R. B. Nicholson, and D. W. Pahley. *Electron microscopy of thin crystals*. London Butterworths, 1965.
- [Hit88] P. B Hitchcock. *International tables for crystallography volume A.:Space-group symmetry*. Ed. by T Hahn. 1988.
- [HL82] J. P. Hirth and J. Lothe. *Theory of dislocations*. Krieger publishing company, 1982.

- [How63] A. Howie. "Inelastic scattering of electrons by crystals I. The theory of small-angle inelastic scattering". In: *Proceedings of the Royal Society of London A: Mathematical, Physical and Engineering Sciences* 271 (1963), pp. 267–287.
- [HSC72] J. W. S. Hearle, J. T. Sparrow, and P. M. Cross. *The use of the scanning electron microscope*. Pergamon, 1972.
- [HW61] A. Howie and M. J. Whelan. "Diffraction contrast of electron microscope images of crystal lattice defects - II. The development of a dynamical theory". In: *Proceedings of Royal Society of London A*. Vol. 263. 1961, pp. 217–237.
- [IL12] V. L. Indenbom and J. Lothe. "Elastic strain fields and dislocation mobility". In: Elsevier, 2012. Chap. Dislocation interaction with surfaces.
- [Inc15] Plotly Technologies Inc. *Collaborative data science*. 2015. URL: <https://plot.ly>.
- [JL89] D. C. Joy and S. Luo. "An empirical stopping power relationship for low-energy electrons". In: *Scanning* 11 (1989), pp. 176–180.
- [JND82] D. C. Joy, D. E. Newbury, and D. L. Davidson. "Electron channeling patterns in the scanning electron microscope". In: *Journal of Applied Physics* 53.8 (1982), R81–R122.
- [JOP+01] Eric Jones, Travis Oliphant, Pearu Peterson, et al. *SciPy: Open source scientific tools for Python*. [Online; accessed <today>]. 2001–. URL: <http://www.scipy.org/>.
- [Joy94] D.C. Joy. "Channeling in and channeling out: The origins of electron backscattering and electron channeling contrast". In: *Proceedings of the annual meeting-Electrons Microscopy Society of America*. San Francisco Press. 1994, pp. 592–593.
- [Joy95] D.C. Joy. *Monte Carlo Modeling for Electron Microscopy and Microanalysis*. Oxford University Press, USA, 1995.
- [Kam+02] S. Kamiyama, M. Iwaya, S. Takanami, S. Terao, A. Miyazaki, H. Amano, and I. Akasaki. "UV Light-Emitting Diode Fabricated on Hetero-ELO-Grown Al_{0.22}Ga_{0.78}N with Low Dislocation Density". In: *Physica Status Solidi (a)* 192.2 (2002), pp. 296–300.

- [KB97] V. N. Koinkar and B. Bhushan. "Scanning and transmission electron microscopies of single-crystal silicon microworn/machined using atomic force microscopy". In: *Journal of Materials Research* 12.12 (1997), pp. 3219–3224.
- [KG11] R.R. Keller and R.H. Geiss. "Transmission EBSD from 10 nm domains in a scanning electron microscope". In: *Journal of Microscopy* 245 (2011), pp. 245–251.
- [KG12] R. R. Keller and R. H. Geiss. "Transmission EBSD from 10 nm domains in a scanning electron microscope". In: *Journal of Microscopy* 245.3 (2012), pp. 245–251.
- [KM02] S. Y. Karpov and Y. N. Makarov. "Dislocation effect on light emission efficiency in gallium nitride". In: *Applied Physics Letters* 81.25 (2002), pp. 4721–4723.
- [Kne+10] M. Kneissl, T. Kolbe, C. Chua, V. Kueller, N Lobo, J Stellmach, A Knauer, H Rodriguez, S Einfeldt, Z Yang, et al. "Advances in group III-nitride-based deep UV light-emitting diode technology". In: *Semiconductor Science and Technology* 26.1 (2010).
- [Kus+15] G. Kusch, M. Nouf-Allehiani, F. Mehnke, C. Kuhn, P. R. Edwards, T. Wernicke, A. Knauer, V. Kueller, G Naresh-Kumar, Markus Weyers, et al. "Spatial clustering of defect luminescence centers in Si-doped low resistivity Al_{0.82}Ga_{0.18}N". In: *Applied Physics Letters* 107.7 (2015), p. 072103.
- [Les+94] M. Leszczynski, T. Suski, H. Teisseire, P. Perlin, I. Grzegory, J. Jun, S. Porowski, and T. D. Moustakas. "Thermal expansion of gallium nitride". In: *Journal of Applied Physics* 76.8 (1994), pp. 4909–4911.
- [Les+95] S. D. Lester, F. A. Ponce, M. G. Crawford, and D. A. Steigerwald. "High dislocation densities in high efficiency GaN-based light-emitting diodes". In: *Applied Physics Letters* 66.10 (1995), pp. 1249–1251.
- [LHH96] Gary G Leppard, Andreas Heissenberger, and Gerhard J Herndl. "Ultrastructure of marine snow. I. Transmission electron microscopy methodology". In: *Marine Ecology Progress Series* 135 (1996), pp. 289–298.
- [Lim+06] J. B. Limb, D. Yoo, J. H. Ryou, W. Lee, S. C. Shen, R. D. Dupuis, M. L. Reed, C. J. Collins, M. Wraback, D. Hanser, et al. "GaN ultraviolet avalanche photodiodes with optical gain greater than 1000 grown on GaN substrates by metal-organic chemical vapor deposition". In: *Applied Physics Letters* 89.1 (2006), p. 011112.

- [Lin65] J. Lindhard. "Influence of Crystal Lattice on Motion of energetic charged particles". In: *Kgl. Danske Vidensk. Selskab. Mat. Fys. Medd* 34.14 (1965), p. 64.
- [Man+15] H. Mansour, M. A. Crimp, N. Gey, and N. Maloufi. "Accurate electron channeling contrast analysis of a low angle sub-grain boundary". In: *Scripta Materialia* 109 (2015), pp. 76–79.
- [Mar+17] K. Marquardt, M. De Graef, S. Singh, H. Marquardt, A. Rosenthal, and Sanae Koizuimi. "Quantitative electron backscatter diffraction (EBSD) data analyses using the dictionary indexing (DI) approach: Overcoming indexing difficulties on geological materials". In: *American Mineralogist* 102.9 (2017), pp. 1843–1855.
- [Mar72] R. M. Martin. "Relation between elastic tensors of wurtzite and zinc-blende structure materials". In: *Physical Review B* 6.12 (1972), p. 4546.
- [Meu+17] A. Meurer, C. P. Smith, M. Paprocki, Ondřej Čertík, Sergey B Kirpichev, Matthew Rocklin, AMiT Kumar, Sergiu Ivanov, Jason K Moore, Sartaj Singh, et al. "SymPy: symbolic computing in Python". In: *PeerJ Computer Science* 3 (2017), e103.
- [Mic] *Microscopy, A very Short Introduction*. Oxford University Press, 2015.
- [Miu+18] E. Miu, N. Gulley, K. N. Laland, and L Rendell. "Innovation and cumulative culture through tweaks and leaps in online programming contests". In: *Nature Communications* 9.2321 (2018).
- [Mor+79] P. Morin, M. Pitaval, D. Besnard, and G. Fontaine. "Electron–channelling imaging in scanning electron microscopy". In: *Philosophical Magazine A* 40.4 (1979), pp. 511–524.
- [MS07] T. Maitland and S. Sitzman. *Electron backscatter diffraction (EBSD) technique and materials characterization examples*. Vol. 14. Springer Berlin, 2007.
- [NA+rt] M. Nouf-Allehiani, G. Kusch, G. Naresh-Kumar, P. R. Edwards, E. Pascal, S. Kraeusel R. Johnston, B. Hourahine, and C. Trager-Cowan. In: *Phys. Rev. B* (forthcoming).
- [Nic66] J. F. Nicholas. "The simplicity of Miller-Bravais indexing". In: *Acta Crystallographica* 21.6 (1966), pp. 880–881.

- [NK+12] G. Naresh-Kumar, B. Hourahine, P. R. Edwards, A. P. Day, A. Winkelmann, A. J. Wilkinson, P. J. Parbrook, G. England, and C. Trager-Cowan. "Rapid nondestructive analysis of threading dislocations in wurtzite materials using the scanning electron microscope". In: *Physical Review Letters* 108.13 (2012), p. 135503.
- [NK28] S. Nishikawa and S. Kikuchi. "Diffraction of cathode rays by calcite". In: *Nature* 122.3080 (1928), p. 726.
- [Nob49] Nobelprize.org. *The Nobel Prize in Physiology or Medicine*. Web. 9 Aug 2018. 1949. URL: https://www.nobelprize.org/nobel_prizes/medicine/laureates/1949.
- [Nol07] G. Nolze. "Image distortions in SEM and their influences on EBSD measurements". In: *Ultramicroscopy* 107.2-3 (2007), pp. 172–183.
- [OT68] P. R. Okamoto and G. Thomas. "On the Four-Axis Hexagonal Reciprocal Lattice and its use in Indexing of Transmission Electron Diffraction Patterns". In: *physica status solidi (b)* 25 (1968), pp. 81–91.
- [Pas+18a] E. Pascal, B. Hourahine, G. Naresh-Kumar, K. Mingard, and C. Trager-Cowan. "Dislocation contrast in electron channelling contrast images as projections of strain-like components". In: *Materials Today: Proceedings* 5 (2018), pp. 14652–14661.
- [Pas+18b] E. Pascal, S. Singh, P. G. Callahan, B. Hourahine, Carol Trager-Cowan, and Marc De Graef. "Energy-weighted dynamical scattering simulations of electron diffraction modalities in the scanning electron microscope". In: *Ultramicroscopy* 187 (2018), pp. 98–106.
- [Pas15] E. Pascal. *SEM-diffraction*. University of Strathclyde, 2015-2018. URL: <https://github.com/elenapascal/SEM-diffraction>.
- [Pen+05] C. S. Peng, H. F. Liu, J. Konttinen, and M. Pessa. "Mechanism of photoluminescence blue shift in InGaAsN/GaAs quantum wells during annealing". In: *Journal of Crystal Growth* 278.1-4 (2005), pp. 259–263.
- [PG15] F. Perez and B. E. Granger. "Project Jupyter: Computational narratives as the engine of collaborative data science". In: *Retrieved September 11* (2015), p. 207.
- [Pic+07] Y. N. Picard, M. E. Twigg, J. D. Caldwell, C. R. Eddy Jr, PG Neudeck, AJ Trunek, and JA Powell. "Electron channeling contrast imaging of atomic steps and threading dislocations in 4 H-Si C". In: *Applied Physics Letters* 90.23 (2007), p. 234101.

- [Pic+09] Y. N. Picard, M. E. Twigg, J. D. Caldwell, CR Eddy Jr., MA Mastro, and RT Holm. "Resolving the Burgers vector for individual GaN dislocations by electron channeling contrast imaging". In: *Scripta Materialia* 61.8 (2009), pp. 773–776.
- [Pic+14] Y. N. Picard, M. Liu, J. Lammatao, R. Kamaladasa, and M. De Graef. "Theory of dynamical electron channeling contrast images of near-surface crystal defects". In: *Ultramicroscopy* 146 (2014), pp. 71–78.
- [Pie+63] G. R. Piercy, F. Brown, J. A. Davies, and M. McCargo. "Experimental evidence for the increase of heavy ion ranges by channeling in crystalline structure". In: *Physical Review Letters* 10.9 (1963), p. 399.
- [Pri30] J.A. Prins. "Die Reflexion von Röntgenstrahlen an absorbierenden idealen Kristallen". In: *Zeitschrift für Physik* 63.7-8 (1930), pp. 477–493.
- [Rea53] W. T. Read. *Dislocations in crystals*. Vol. 53. McGraw-Hill New York, 1953.
- [Rei98] L. Reimer. *Scanning Electron Microscopy – Physics of Image Formation and Microanalysis*. Springer, Berlin, 1998.
- [Ren+98] S. X. Ren, E. A. Kenik, K. B. Alexander, and A. Goyal. "Exploring spatial resolution in electron back-scattered diffraction experiments via Monte Carlo simulation". In: *Microscopy and Microanalysis* 4.1 (1998), pp. 15–22.
- [RK76] L. Reimer and E. R. Krefting. "The effect of scattering models on the results of Monte Carlo calculations". In: 460. 1976, p. 45.
- [RKS14] K. P. Rice, R. R. Keller, and M. P. Stokovich. "Specimen thickness effects on transmission Kikuchi patterns in the scanning electron microscope". In: *Journal of Microscopy* 254 (2014), pp. 129–131.
- [Ros+94] C. J. Rossouw, P. R. Miller, T. W. Josefsson, and L. J. Allen. "Zone-axis back-scattered electron contrast for fast electrons". In: *Philosophical Magazine A* 70.6 (1994), pp. 985–998.
- [Ros+97] S. J. Rosner, E. C. Carr, M. J. Ludowise, G. Girolami, and H. I. Erikson. "Correlation of cathodoluminescence inhomogeneity with microstructural defects in epitaxial GaN grown by metalorganic chemical-vapor deposition". In: *Applied Physics Letters* 70.4 (1997), pp. 420–422.
- [Ros10] D. Rosca. "New uniform grids on the sphere". In: *Astronomy & Astrophysics* 520 (2010), A63.

- [Row+15] D. Rowenhorst, A. D. Rollett, G. S. Rohrer, M. Groeber, M. Jackson, P. J. Konijnenberg, and M. De Graef. "Tutorial: Consistent representations of and conversions between 3D rotations". In: *Modelling and Simulation in Materials Science and Engineering* 23.8 (2015), p. 083501.
- [RS50] W. T. Read and W. Shockley. "Dislocation models of crystal grain boundaries". In: *Physical Review* 78.3 (1950), p. 275.
- [Rym70] T. B. Rymer. *Electron diffraction*. Vol. 108. Methuen, 1970.
- [SC99] B. A. Simkin and M. A. Crimp. "An experimentally convenient configuration for electron channeling contrast imaging". In: *Ultramicroscopy* 77.1-2 (1999), pp. 65–75.
- [Sch+09a] M. Schowalter, A. Rosenauer, J. T. Titantah, and D. Lamoen. "Temperature-dependent Debye-Waller factors for semiconductors with wurtzite-type structure". In: *Acta Crystallographica A*.65 (2009), pp. 227–231.
- [Sch+09b] A. J. Schwartz, M. Kumar, B. L. Adams, and D. P. Field. *Electron Backscatter Diffraction in Materials Science*. Springer, 2009.
- [Sco92] D.W. Scott. *Multivariate Density Estimation: Theory, Practice, and Visualization*. John Wiley & Sons, New York, Chichester, 1992.
- [SDG16] S. Singh and M. De Graef. "Orientation sampling for dictionary-based diffraction pattern indexing methods". In: *Modelling and Simulation in Material Science and Engineering* 24 (2016), p. 085013.
- [SDG17] S. Singh and M. De Graef. "Dictionary Indexing of Electron Channeling Patterns". In: *Microscoscopy and MicroAnalysis* 23 (2017), pp. 1–12.
- [Ser+73] R. Serneels, M. Snykers, P. Delavignette, R. Gevers, and S. Amelinckx. "Friedel's Law in Electron Diffraction as Applied to the Study of Domain Structures in Non-Centrosymmetrical Crystals". In: *physica status solidi (b)* 58.1 (1973), pp. 277–292.
- [SHH72] J. P. Spencer, C. J. Humphreys, and P. B. Hirsch. "A dynamical theory for the contrast of perfect and imperfect crystals in the scanning electron microscope using backscattered electrons". In: *Philosophical Magazine* 26.1 (1972), pp. 193–213.
- [SJ79] S. S. Sheinin and B. K. Jap. "On the validity of assuming symmetrical Laue diffraction conditions in calculations of diffraction contrast". In: *physica status solidi (b)* 91.2 (1979), pp. 407–412.

- [Sma18] A. G. Smart. *The war over supercooled water*. Ed. by Physics Today. 2018.
DOI: DOI:10.1063/PT.6.1.20180822a.
- [SRDG17] S. Singh, F. Ram, and M. De Graef. "EMsoft: open source software for electron diffraction/image simulations". In: *Microscopy and MicroAnalysis* 23.S1 (2017), 212—213.
- [SWR78] D. K. Saldin, M. J. Whelan, and C. J. Rossouw. "Electron Diffraction 1927–1977". In: *Inst. Phys. Conf. Set.* Vol. 41. 1978, pp. 50–56.
- [TC+06] C. Trager-Cowan, F. Sweeney, A. Winkelmann, A. J. Wilkinson, P. W. Trimby, A. P. Day, A. Gholinia, N. H. Schmidt, P. J. Parbrook, and I. M. Watson. "Characterisation of nitride thin films by electron backscatter diffraction and electron channelling contrast imaging". In: *Materials Science and Technology* 22.11 (2006), pp. 1352–1358.
- [TC+07] C. Trager-Cowan, F. Sweeney, P. W. Trimby, A. P. Day, A. Gholinia, N. H. Schmidt, P. J. Parbrook, A. J. Wilkinson, and I. M. Watson. "Electron backscatter diffraction and electron channeling contrast imaging of tilt and dislocations in nitride thin films". In: *Physical Review B* 75 (2007), p. 085301.
- [TC39] G. P. Thomson and W. Cochrane. *Theory and Practice of electron diffraction*. Macmillian and Co., 1939.
- [TE04] X. Tao and A. Eades. "Monte Carlo simulation for electron backscattering diffraction". In: *Microscopy and Microanalysis* 10.S02 (2004), pp. 940–941.
- [THS64] W. J. Tunstall, P. B. Hirsch, and J. Steeds. "Effects of surface stress relaxation on the electron microscope images of dislocations normal to thin metal foils". In: *Philosophical Magazine* 9.97 (1964), pp. 99–119.
- [Tou65] R. A. Toupin. "Saint-Venant's principle". In: *Archive for Rational Mechanics and Analysis* 18.2 (1965), pp. 83–96.
- [TP09] M. E. Twigg and Y. N. Picard. "Simulation and analysis of electron channelling contrast images of threading screw dislocations in 4 H-SiC". In: *Journal of Applied Physics* 105.9 (2009), p. 093520.
- [TR27] G. P. Thomson and A. Reid. "Diffraction of cathode rays by a thin film". In: *Nature* 119.3007 (1927), p. 890.
- [Tri12a] P. W. Trimby. "Orientation mapping of nanostructured materials using transmission Kikuchi diffraction in the scanning electron microscope". In: *Ultramicroscopy* 120 (2012), pp. 16–24.

- [Tri12b] P. W. Trimby. "Orientation mapping of nanostructured materials using transmission Kikuchi diffraction in the scanning electron microscope". In: *Ultramicroscopy* 120 (2012), pp. 16–24.
- [UA68] E. Uggerhøj and J. U. Andersen. "Influence of lattice structure on motion of positrons and electrons through single crystals". In: *Canadian Journal of Physics* 46.6 (1968), pp. 543–550.
- [UF69] E. Uggerhøj and F. Frandsen. "Fast-Electron Channeling investigated by means of Rutherford scattering". In: *Physical Review B* 2.3 (1969), pp. 582–590.
- [VD76] D. Van Dyck. "The importance of backscattering in high-energy electron diffraction calculations". In: *physica status solidi (b)* 77.1 (1976), pp. 301–308.
- [VD80] D. Van Dyck. "Fast computational procedures for the simulation of structure images in complex or disordered crystals: a new approach". In: *Journal of Microscopy* 119.1 (1980), pp. 141–152.
- [Ves+15] S. Vespucci, A. Winkelmann, G. Naresh-Kumar, K. P. Mingard, D. Maneuski, P. R. Edwards, A. P. Day, V. O'Shea, and C. Trager-Cowan. "Digital direct electron imaging of energy-filtered electron backscatter diffraction patterns". In: *Physical Review B* 92.20 (2015), p. 205301.
- [VH73] J. A. Venables and C. J. Harland. "Electron back-scattering patterns—A new technique for obtaining crystallographic information in the scanning electron microscope". In: *Philosophical Magazine* 27.5 (1973), pp. 1193–1200.
- [VS02] H. Van Swygenhoven. "Grain boundaries and dislocations". In: *Science* 296.5565 (2002), pp. 66–67.
- [WB15] A. Weidner and H. Biermann. "Case studies on the application of high-resolution electron channelling contrast imaging—investigation of defects and defect arrangements in metallic materials". In: *Philosophical Magazine* 95.7 (2015), pp. 759–793.
- [WC96] D. B. Williams and C. B. Carter. "The transmission electron microscope". In: *Transmission electron microscopy*. Springer, 1996, pp. 3–17.
- [WH57] M. J. Whelan and P. B. Hirsch. "Electron diffraction from crystals containing stacking faults: II". In: *Philosophical Magazine* 2.23 (1957), pp. 1303–1324.

- [WH95] A. J. Wilkinson and P. B. Hirsch. "The effects of surface stress relaxation on electron channelling contrast images of dislocations". In: *Philosophical Magazine A* 72.1 (1995), pp. 81–103.
- [Wil+93] A. J. Wilkinson, G. R. Anstis, J. T. Czernuszka, N. J. Long, and P. B. Hirsch. "Electron channelling contrast imaging of interfacial defects in strained silicon-germanium layers on silicon". In: *Philosophical Magazine A* 68.1 (1993), pp. 59–80.
- [Win+07] A. Winkelmann, C. Trager-Cowan, F. Sweeney, Austin P Day, and Peter Parbrook. "Many-beam dynamical simulation of electron backscatter diffraction patterns". In: *Ultramicroscopy* 107.4-5 (2007), pp. 414–421.
- [Win+16] A. Winkelmann, G. Nolze, M. Vos, F. Salvat-Pujol, and W.S.M. Werner. "Physics-based simulation models for EBSD: advances and challenges". In: *IOP Conference Series: Materials Science and Engineering* 109.1 (2016), p. 012018.
- [Win+17] A. Winkelmann, G Nolze, S Vespucci, G Naresh-Kumar, C. Trager-Cowan, A. Vilalta-Clemente, A.J. Wilkinson, and M. Vos. "Diffraction effects and inelastic electron transport in angle-resolved microscopic imaging applications". In: *Journal of Microscopy* 267 (2017), pp. 330–346.
- [WK91] A. Weickenmeier and H. Kohl. "Computation of absorptive form factors for high-energy electron diffraction". In: *Acta Crystallographica Section A* 47.5 (1991), pp. 590–597.
- [WP99] A. J. C. Wilson and E. Prince. *International Tables for Crystallography Vol. C, Mathematical, Physical and Chemical Tables*. Dordrecht, Holland, 1999.
- [WSPW13] A. Winkelmann, F. Salvat-Pujol, and W. Werner. "Monte Carlo Simulations for Applications in Electron Backscatter Diffraction". In: *Microscopy and Microanalysis* 19.S2 (2013), pp. 738–739.
- [Yof61] E. H. Yoffe. "A dislocation at a free surface". In: *Philosophical Magazine* 6.69 (1961), pp. 1147–1155.
- [Yos57] H. Yoshioka. "Effect of Inelastic Waves on Electron Diffraction". In: *J. Phys. Soc. Japan* 12 (1957), pp. 618–628.
- [ZE14] S. Zaeferer and N. Elhami. "Theory and application of electron channelling contrast imaging under controlled diffraction conditions". In: *Acta Materialia* 75 (2014), pp. 20–50.

- [Zub+01] A. Zubrilov, M. E. Levenshtein, SL Rumyantsev, and MS Shur. "Properties of Advanced Semiconductor Materials GaN, AlN, InN, BN, SiC, SiGe". In: John Wiley & Sons, Inc., New York, 2001. Chap. Indium nitride, pp. 49–66.
- [Aus] Australia's Chief Scientist. *SPEECH: PROGRESS IN VIEW*. <https://www.chiefscientist.gov.au/2018/09/speech-progress-in-view/?platform=hootsuite>. Online; accessed 29 March 2019.